



National Library
of Canada

Bibliothèque nationale
du Canada

Acquisitions and
Bibliographic Services Branch

Direction des acquisitions et
des services bibliographiques

385 Wellington Street
Ottawa, Ontario
K1A 0N4

385, rue Wellington
Ottawa (Ontario)
K1A 0N4

Titre No. / Titre / Numéro

Classe No. / Numéro / Classe

NOTICE

AVIS

The quality of this microform is heavily dependent upon the quality of the original thesis submitted for microfilming. Every effort has been made to ensure the highest quality of reproduction possible.

La qualité de cette microforme dépend grandement de la qualité de la thèse soumise au microfilmage. Nous avons tout fait pour assurer une qualité supérieure de reproduction.

If pages are missing, contact the university which granted the degree.

S'il manque des pages, veuillez communiquer avec l'université qui a conféré le grade.

Some pages may have indistinct print especially if the original pages were typed with a poor typewriter ribbon or if the university sent us an inferior photocopy.

La qualité d'impression de certaines pages peut laisser à désirer, surtout si les pages originales ont été dactylographiées à l'aide d'un ruban usé ou si l'université nous a fait parvenir une photocopie de qualité inférieure.

Reproduction in full or in part of this microform is governed by the Canadian Copyright Act, R.S.C. 1970, c. C-30, and subsequent amendments.

La reproduction, même partielle, de cette microforme est soumise à la Loi canadienne sur le droit d'auteur, SRC 1970, c. C-30, et ses amendements subséquents.

Canada

UNIVERSITY OF ALBERTA

**PROPAGATION AND ADSORPTION OF SURFACTANTS IN
CONSOLIDATED BEREA SANDSTONE WITH RADIAL FLOW**

BY



WELLINGTON YING-WEI KWOK

**A thesis to the Faculty of Graduate Studies and Research in partial
fulfillment of the requirements for the degree of Doctor of Philosophy.**

DEPARTMENT OF CHEMICAL ENGINEERING

**Edmonton, Alberta
Spring, 1994**



National Library
of Canada

Acquisitions and
Bibliographic Services Branch

395 Wellington Street
Ottawa, Ontario
K1A 0N4

Bibliothèque nationale
du Canada

Direction des acquisitions et
des services bibliographiques

395, rue Wellington
Ottawa (Ontario)
K1A 0N4

Your library's address

Your library's address

The author has granted an irrevocable non-exclusive licence allowing the National Library of Canada to reproduce, loan, distribute or sell copies of his/her thesis by any means and in any form or format, making this thesis available to interested persons.

L'auteur a accordé une licence irrévocable et non exclusive permettant à la Bibliothèque nationale du Canada de reproduire, prêter, distribuer ou vendre des copies de sa thèse de quelque manière et sous quelque forme que ce soit pour mettre des exemplaires de cette thèse à la disposition des personnes intéressées.

The author retains ownership of the copyright in his/her thesis. Neither the thesis nor substantial extracts from it may be printed or otherwise reproduced without his/her permission.

L'auteur conserve la propriété du droit d'auteur qui protège sa thèse. Ni la thèse ni des extraits substantiels de celle-ci ne doivent être imprimés ou autrement reproduits sans son autorisation.

ISBN 0-612-11266-7

Canada

UNIVERSITY OF ALBERTA

RELEASE FORM

NAME OF AUTHOR: WELLINGTON YING-WEI KWOK


TITLE OF THESIS: PROPAGATION AND ADSORPTION OF
SURFACTANTS IN CONSOLIDATED BEREA
SANDSTONE WITH RADIAL FLOW

DEGREE: DOCTOR OF PHILOSOPHY

YEAR THIS DEGREE GRANTED: SPRING, 1994

Permission is hereby granted to the University of Alberta Library to reproduce single copies of this thesis and to lend or sell such copies for private, scholarly or scientific research purposes only.

The author reserves all other publication and other rights in association with the copyright in the thesis, and except as hereinbefore provided neither the thesis nor any substantial portion thereof may be printed or otherwise reproduced in any material form whatever without the author's prior written permission.



WELLINGTON YING-WEI KWOK
1562 Mcgo Court
Samia, Ontario
CANADA N7S 4A8

December 15, 1993

UNIVERSITY OF ALBERTA

FACULTY OF GRADUATE STUDIES AND RESEARCH

The undersigned certify that they have read, and recommend to the Faculty of Graduate Studies and Research for acceptance, a thesis entitled **Propagation and Adsorption of Surfactants in Consolidated Berea Sandstone with Radial Flow** submitted by **Wellington Ying-wai Kwok** in partial fulfillment of the requirements for the degree of **Doctor of Philosophy**.



Dr. R.E. Hayes, Supervisor



Dr. R.G. Bentsen



Dr. M.N. Esmail, External Examiner



Dr. J.H. Masliyah



Dr. K. Nandakumar



Dr. H.A. Nasr-El-Din



Dr. J.T. Ryan

December 15, 1993

Abstract

Static and dynamic adsorption data are reported for two systems of surfactant solution and Berea sandstone. The surfactants used were Neodol® 25-3S (anionic) and Triton X-100® (non-ionic), which are commonly employed in enhanced oil recovery (EOR) processes. The purpose of this investigation was to examine the effect of physical parameters such as salinity, pH and injection flow rate on the propagation and adsorption of surfactants. A radial geometry was used so as to simulate the flow patterns near an injection wellbore.

It was observed that the equilibrium adsorption isotherms are of the simple Langmuir type for the anionic surfactant; and of the stepped Langmuir type for the non-ionic surfactant in agreement with the hemimicelle model. In addition, experimental results showed a dramatic surfactant loss and slower rate of surfactant propagation as salinity was increased. On the other hand, increasing pH (from 6 to 12) reduced the amount of adsorptive saturation. As shown in the results from the adsorption of non-ionic surfactant, this decrease was more pronounced under dynamic conditions. Surfactant loss was found to decrease as the injection flow rate was increased, and the maximum adsorptive capacity was consistently lower than that obtained from static tests at a given sodium chloride concentration and surfactant concentration.

For the anionic surfactant, at high surfactant concentration and over a narrow range of sodium chloride concentrations, a liquid crystal phase formed. The presence of this phase resulted in a higher apparent viscosity, a dramatic increase in the pressure drop across the core, and significant surfactant retention in the core. The latter was due to the formation of viscous fingers at the tail of the surfactant slug.

The effect of dispersion on the radial flow system was examined and the validity of various approximations and models for the dispersion coefficient is discussed. It is shown that the contribution of both molecular diffusion and mechanical dispersion are significant. The effect of boundary conditions at the injection wellbore and exit of the

core was also studied. It was observed that, for the ~~core d~~ ~~is~~ and range of flow rates used in the current study, the influence of boundary condition (Dirichlet or Cauchy condition) at the entrance on the simulated effluent ~~is~~ ~~important~~. It was, on the other hand, demonstrated that the use of a semi-infinite ~~(radius)~~ is necessary in order to preserve material balance in the simulation results.

A mathematical model based on the general ~~active-dispersive~~ transport equation of mass coupled with an equilibrium or a kinetic ~~adsorption~~ model was developed. Both linear and non-linear equilibrium models were found ~~unsuitable~~ for matching effluent profiles of surfactant propagation. Improved fits to the experimental data were obtained using a simple Langmuir-type kinetic model, but the amount of total adsorption was overestimated by such simulated profiles. It was apparent that the application of compound models, of combined kinetic expressions of rapid and slow adsorption processes, is required in order to provide a proper match to the experimental data. Very good fits were obtained for the effluent profiles of Neodol 25-3S using two-site and bilayer adsorption model, and for Triton X-100 using the kinetic hemimicelle model. For both types of adsorption models examined, an increase in the rate of adsorption was observed as the flow rate increased. Also, the adsorption kinetics appeared to depend significantly on the concentration or availability of monomers in solution, and the mass-transfer characteristics.

Acknowledgments

I wish to express my sincere gratitude and appreciation to Dr. Robert E. Hayes and Dr. Hisham A. Nasr-El-Din for providing timely support and guidance. Special thanks to the other members of my committee: Dr. A.E. Mather, Dr. Jacob H. Masliyah, Dr. K. Nandakumar and Dr. James T. Ryan, Professors of Chemical Engineering; Dr. R.G. Bentsen, Professor of Mining, Metallurgical and Petroleum Engineering; and Dr. H.N. Esmail, Professor and Chairman of Chemical Engineering at the University of Saskatchewan, for reviewing this manuscript.

I would also like to acknowledge Audrey Cameron, Kea Green and Tom Chee of the Petroleum Recovery Institute (PRI), and Bob Barton of the Data Acquisition & Control System (DACS) centre at the University of Alberta for their assistance and advice; Karin Mannhardt and Kevin Taylor of PRI for useful discussions; Shelley Laggitt, Rosemary French and Neil DeBree of the PRI Geology group for performing the x-ray diffraction analyses, scanning electron micrographs analyses and specific surface area measurements; and, most of all, Dr. Conrad Ayasse, Executive Director of PRI, for his permission to use all the laboratory facilities. Some of the experimental data were collected through the work of Dimpay Sethi (a summer trainee at PRI / University of Alberta) during the period of May-August, 1991.

Thanks are due to the Alberta Oil Sands Technology and Research Authority (AOSTRA) for financial support, Contract Agreement Number 886; Petroleum Recovery Institute for providing all laboratory facilities; Rheotek Incorporated for providing some of the software; Gulf Canada Resources Limited for the award of the Graduate Scholarship in Hydrocarbon Development; Petro-Canada for the award of the Graduate Scholarship in Petroleum Engineering; Natural Science and Engineering Research Council of Canada (NSERC), University of Alberta and Department of Chemical Engineering for their continuous financial support.

All the faculty and staff in the Department have provided invaluable assistance from time to time. Many thanks to Bob Barton, Cindy Hoister, Beverly Walker and Dr. Grant Fisher.

To Winnie and Allen Ho, for their guidance and for giving advice in time of need.

To Doris Leung, for being a good friend.

To Jean Corbin and Michael Kohlenberg, for being good friends also.

To all the people I have worked and interacted with in the Department as well as at the Petroleum Recovery Institute. It would be impossible to acknowledge all of them individually. I write their names below and hope that each one realizes her/his own contribution and significance to my work, and outside it. Thanks to:

Artin Afacan, Kay Atkinson, Alan Ayasse, Pranob Banerjee, Rudy Banert, Paul Barrow, Walter Boddez, Claudio Bordia, Mary Bourke, Dr. John Carroll, Jayant Chakravarty, Irene Comer, Richard Cooper, Marieta Cruz, Janet Cummings, Rame and Simarjit (Sam) Dhaliwal, Kevin Dorma, Sam Erlenbeck, Wendy Faid, Xiaosheng Fan, Dr. Khorashah Farhad, Doug Fisher, Jim Foti, Bev Fraser, Marcel Girard, Jon Goldman, Ravindra Gudi, Monty Hans, Blaine Hawkins, Laurie Heidebrecht, Amar Henni, Christine Ho, Gloria Hodges, Laurie Hodgins, Devon Husband, Andree Koenig, Dr. Sunil Koka, Shulamit Kuttner, Dr. Kun-Yu Kwok, Andrew Jenkins, Paula Jokuty, Yves Lacombe, Sreekanth Lalgudi, Tina Larson, Dr. Ai Dong Lea, George Lu, Mains (Mike) Macharia, Viral Maniar, Philip Mees, Alison Miller, Bill Morris, Joseph Najman, Dr. Mona Naar-El-Din, Dr. Paul Nawrocki, Fausto (Nick) Nicola, Wendy Novakowski, Dr. Jerry Novosad, Janet Noy, Trevor Parsons, Adam Rankin, Diane Reckhow, Keith Redford, Susan Richardson, Dr. Claudia Roe, Dr. Donald Ryland, Ramakant Sedhakar, Sean Sanders, Munawar Saudagar, Dr. Laurier Schramm, Jerry Shaw, K.N. (Avinash) Shanbhag, Ravi Sharma, Dr. David Shook, Henry Sit, Robert Spans, David Spagnolo, Murray Stevenson, Lynn Stony, Gail Swenson, Leanne Thomson, Dr. Yvon Theriault, Lyle Trytton, Alex Turta, Dr. Leigh Wardhaugh, Dr. Fred Wassmuth, Kendra Whitfield, Dorothy Wihlidal, and Birgitte Willumson.

Many thanks also to Judy Anne Craig, Lissa Haines M.D., Suzanne and Phil Langlois, Mary-Ann Miller, Janice Patel, James Rahob, Alicia Robinson, Nancy Scott, Tamir Sherif, John So, Jenny and Thomas Tsang, Suzanne Watson, Alanna Philip-Way, Michael Way and, in particular, Tammy Woods for their lasting friendships and support.

This thesis is dedicated to my parents, Josephine and Jack Kwok, for their love, support and encouragement, and to my dearest family ... Christina, Edmund and Candy.

Table of Contents

Abstract
Acknowledgments
Table of Contents
List of Tables
List of Figures
List of Plates
Nomenclature

Chapter 1

Introduction 1

Chapter 2

General Theories of Surfactant Adsorption on Mineral Surfaces 7

2.1 The Nature of Solid (Sandstone) Surfaces 7

2.1.1 Physical Properties of Clay Minerals 8

2.1.2 Surface Forces 9

2.1.3 Electrostatic Forces on Clay Surfaces 10

2.2 General Description of Adsorption Isotherm at the Solid-Liquid Interface ... 13

2.3 Properties of Surfactant in Aqueous Solutions 16

2.4 Mechanisms of Surfactant Adsorption 20

2.4.1 Adsorption of Non-Associated Surfactant Molecules at Low Concentration 23

2.4.2 Formation of Surface Aggregates: Hemimicelles 28

2.4.3 Formation of Surface Aggregates: Admicelles 30

2.5 General Isotherm Equations of Two-Step Adsorption 32

2.6 Important Factors Affecting the Adsorption of Surfactants 35

Chapter 3

Experimental Procedures and Set-up for Static and Dynamic Adsorption Studies 38

3.1 Materials 38

3.2 Analytical Methods 39

3.2.1 Analysis of Tracer Concentration 39

3.2.2 Analysis of Anionic Surfactant Concentration 40

3.2.3 Analysis of Non-ionic Surfactant Concentration	41
3.3 Measurements of the Physical Properties in Solutions	45
3.4 Geometric and Mineralogical Analyses of Berea Sandstone Samples	45
3.5 Static Adsorption Experiments	49
3.6 Dynamic Tests	49
3.6.1 Experimental Set-up	49
3.6.2 Procedure	50

Chapter 4

Propagation and Adsorption of NEODOL 25-3S (Anionic Surfactant)	54
4.1 Static Adsorption Isotherms	55
4.1.1 Liquid-to-Solid Ratios	55
4.1.2 Effect of Salinity	57
4.2 Dynamic Tests	59
4.2.1 Effect of Salinity	61
4.2.2 Effect of pH	70
4.2.3 Effect of Flow Rate	72

Chapter 5

Propagation and Adsorption of TRITON X-100 (Non-ionic Surfactant)	75
5.1 Equilibrium Static Adsorption Isotherms	76
5.1.1 Discussion of Errors in Adsorption Isotherms	76
5.1.2 Effect of Salinity	77
5.1.3 Effect of pH	80
5.2 Dynamic Tests	84
5.2.1 Effect of Salinity	84
5.2.2 Effect of Flow Rate	87
5.2.3 A Comparison between Static and Dynamic Adsorption	90
5.2.4 Effect of pH	96

Chapter 6

Dispersion in Consolidated Sandstone with Radial Flow	98
6.1 Advection, Diffusion and Dispersion	99
6.2 Dispersion in Porous Media with Radial Flow	102
6.2.1 Approximate and Analytical Solutions	102
6.3 Dispersion Characteristics of Tracer and Surfactant	110
6.4 Mathematical Description of the Experimental Data	114
6.5 Numerical Simulations of Dispersion with Radial Flow	114
6.5.1 Numerical Approximations and Errors	116
6.5.2 Comparison of Numerical Solution with Analytical Solutions	123
6.5.3 Boundary Condition at the Injection Wellbore	125

6.5.4 Boundary Condition at the Core Exit	127
6.6 Models of Dispersion Coefficient	130
6.6.1 Dispersion with Negligible Diffusion Effect	130
6.6.2 Dispersion Dominated by Diffusion	135
6.7 Dispersion with Mechanical Mixing and Diffusion	138
 Chapter 7	
Dynamic Adsorption of Surfactants	141
7.1 General Transport Equation for Dynamic Adsorption	143
7.2 Approximate Solution of Adsorption in an Advective-Dispersive System ...	144
7.3 Dynamic Effects on the Overall Adsorption	148
7.4 Compound Adsorption Model	154
7.5 Effects of the Solution Characteristics on Surfactant Adsorption	157
7.6 Bilayer Adsorption Model	163
7.7 Dynamic Adsorption at Higher Salinity	165
7.8 Effect of Flow Rate	168
7.9 Dynamic Adsorption of Non-Ionic Surfactant	173
7.10 Kinetic Adsorption of the Hemimicelle Model	173
 Chapter 8	
Conclusions and Recommendations	180
8.1 Propagation and Adsorption of Neodol 25-3S	180
8.2 Propagation and Adsorption of Triton X-100	181
8.3 Dispersion in Berea Sandstone Cores with Radial Flow	182
8.4 Dynamic Adsorption	183
8.5 Recommendations	185
References	186
 Appendix A	
Investigation of the Electrolyte Effect on Surfactant Aggregation	196
A.1 Viscosity Measurements	196
A.2 Effect of Salinity on the Apparent Viscosity of Surfactant Solutions	197
A.3 References	205
 Appendix B	
Mathematical Formulation of the Governing Transport Equations	206
B.1 General Description	206
B.2 Numerical Approximation	210

B.2.1 Interpolation Functions for One-Dimensional Elements	210
B.2.2 Interpolation Functions for Two-Dimensional Elements	211
B.2.3 Numerical Integration	214
B.2.4 Approximation of the Time Derivative	216
B.2.5 Boundary Conditions	216
B.3 Method of Solution	217
B.4 Adsorption Models	218
B.5 References	221

Appendix C

Summary of Experimental Data	222
C.1 Experimental run no. 91-042	223
C.2 Experimental run no. 90-009	225
C.3 Experimental run no. 90-022	227
C.4 Experimental run no. 91-046	229
C.5 Experimental run no. 91-045	231
C.6 Experimental run no. 90-010	233
C.7 Experimental run no. 90-021	235
C.8 Experimental run no. 90-006	237
C.9 Experimental run no. 90-018	239
C.10 Experimental run no. 90-025	241
C.11 Experimental run no. 90-014	243
C.12 Experimental run no. 91-043	245
C.13 Experimental run no. 90-020	247
C.14 Experimental run no. 91-044	249
C.15 Experimental run no. 91-036	251
C.16 Experimental run no. 91-034	253
C.17 Experimental run no. 91-035	255
C.18 Experimental run no. 91-041	257
C.19 Experimental run no. 91-033	259
C.20 Experimental run no. 91-039	261
C.21 Experimental run no. 91-040	263
C.22 Experimental run no. 91-038	265

List of Tables

Chapter 3

- 3-1. Mineralogical analysis of Berea sandstone as determined by X-ray diffraction 46**

Chapter 4

- 4-1. Effect of sodium chloride concentration on Langmuir isotherm parameters 59**
- 4-2. Summary of dynamic tests 60**

Chapter 5

- 5-1. Summary of model parameter for fitted adsorption isotherms. Equation (2-20), Ref. Zhu and Gu (1989, 1990) 83**
- 5-2. Summary of flow experiments on the propagation of Triton X-100 85**

Chapter 7

- 7-1. Summary of model parameters obtained using the equilibrium Langmuir adsorption model 152**
- 7-2. Summary of model parameters obtained using the kinetic Langmuir model 154**
- 7-3. Summary of model parameters obtained using the two-site model .. 157**
- 7-4. Summary of (a) individually fitted and (b) a common set of parameters obtained using the two-site model, for $c \leq 0.1$ wt.% 162**
- 7-5. Summary of model parameters obtained using the bilayer model, for $c \leq 0.1$ wt.% 165**

7-6.	Summary of model parameters obtained using the two-site model, for $c \leq 0.1$ wt.%. Surfactant slugs were prepared in 8 wt.% sodium chloride	166
7-7.	Summary of model parameters obtained using the two-site model, for $c \leq 0.1$ wt.%, showing the effect of flow rate on dynamic adsorption	171
7-8.	Summary of model parameters obtained using the two-site model, for (a) $c \leq 0.039$ wt.%, and (b) $c \leq 0.39$ wt.%	176
7-9.	Summary of model parameters obtained using the kinetic adsorption model, for hemimicelle formation (a) $c \leq 0.039$ wt.%, and (b) $c = c$	179

Appendix A

A-1.	Effect of sodium chloride concentration on the power-law constant, K , and index, n , of surfactant solutions containing 0.5 wt.% Neodol 25-3S	200
------	--	-----

Appendix B

B-1.	Interpolation results from Equation (B-16)	213
B-2.	Direct integration formulae for a triangle	215

List of Figures

Chapter 2

2-1.	Schematic diagram showing the compositional elements of sandstone	8
2-2.	Schematic diagram of a unit cell of kaolinite	9
2-3.	Dual charge on a kaolinite particle	11
2-4.	Structure of the electrical double layer near the clay-water interface	12
2-5.	Types of adsorption isotherms according to Brunauer <i>et al.</i> (1940)	17
2-6.	General classification of adsorption isotherms according to Giles <i>et al.</i> (1960)	18
2-7.	Stepped adsorption isotherm, showing the orientation of surfactant molecules and surface aggregates (hemimicelles)	22
2-8.	Adsorption isotherm and proposed mechanism for the formation of admicelle on solid surface	24
2-9.	Structures of (a) surface aggregates, (b) aggregates incorporating counterions, and (c) bilayer	29
2-10.	Adsorption isotherms with (a) heterogeneous and (b) homogeneous surfaces	31

Chapter 3

3-1.	A full scan of the absorbance spectrum for dilute Triton X-100 solutions showing two absorbance peaks at $\lambda = 224$ and 276 nm	42
3-2.	Effect of salt concentration on absorbance peak values at (a) 224 and (b) 276 nm	43
3-3.	Effect of pH on absorbance peak values at 224 and 276 nm	44
3-4.	Experimental set-up	51
3-5.	Schematic diagram of the radial core holder	52

Chapter 4

4-1.	Static adsorption isotherm of Neodol 25-3S as a function of solid-to-liquid ratio at a sodium chloride concentration of 3 wt.%	56
4-2.	Static adsorption isotherm of Neodol 25-3S on disaggregated Berea sandstone as a function of sodium chloride concentration	58
4-3.	Propagation of surfactant slug containing 0.45 wt.% Neodol 25-3S and 8 wt.% sodium chloride at 20 mL/h followed by negative salinity gradient drives	62
4-4.	Propagation of surfactant slug containing about 0.2 wt.% Neodol 25-3S and (a) 3, (b) 8 and (c) 12 wt.% sodium chloride at 20 mL/h	64
4-5.	Propagation of surfactant slug containing about 1 wt.% Neodol 25-3S and (a) 3 and (b) 12 wt.% sodium chloride at 20 mL/h	66
4-6.	Propagation of surfactant slug containing 1.85 wt.% Neodol 25-3S and 12 wt.% sodium chloride at 20 mL/h	68

4-7.	Pressure drop across the core as a function of core effluent volume for surfactant solutions containing 12 wt.% sodium chloride and various surfactant concentrations	69
4-8.	Propagation of surfactant slugs having about 0.5 wt.% Neodol 25-3S, 8 wt.% sodium chloride and pH of (a) 2.4, (b) 6.5 and (c) 12.3 at 20 mL/h	71
4-9.	Propagation of surfactant slugs containing about 0.5 wt.% Neodol 25-3S and 8 wt.% sodium chloride at (a) 5, (b) 20 and (c) 120 mL/h	73

Chapter 5

5-1.	Effect of sodium chloride on the equilibrium static adsorption of Triton X-100 on disaggregated Berea sandstone	79
5-2.	Effect of pH on the equilibrium static adsorption of Triton X-100 on disaggregated Berea sandstone from (a) 3 and (b) 8 wt.% sodium chloride solutions	81
5-3.	Surfactant propagation of 0.5 wt.% Triton X-100 in 3 wt.% sodium chloride at 20 mL/h, followed by a chase brine of 3 wt.% sodium chloride	86
5-4.	Effect of sodium chloride concentration on surfactant propagation with about 0.5 wt.% Triton X-100 in 3, 8 and 12 wt.% sodium chloride at 20 mL/h	88
5-5.	Propagation of surfactant of about 0.5 wt.% Triton X-100 in 3 wt.% sodium chloride at flow rates of 20 and 120 mL/h, (a) tracer and (b) surfactant	89
5-6.	Propagation of surfactant solution of about 0.5 wt.% Triton X-100 in (a) 3 and (b) 8 wt.% sodium chloride at flow rates of 20 and 80 mL/h	91

5-7.	Comparison of saturation adsorption of Triton X-100 under static and dynamic conditions	93
5-8.	Surfactant propagation of 0.49 wt.% Triton X-100 in 8 wt.% sodium chloride at 80 mL/h, followed by a chase brine of 8 wt.% sodium chloride	94
5-9.	Surfactant propagation of 0.47 wt.% Triton X-100 in 8 wt.% sodium chloride at 20 mL/h, followed by a chase brine of 8 wt.% sodium chloride	95
5-10.	Effect of pH on surfactant propagation with about 0.5 wt.% Triton X-100 in (a) 3 and (b) 8 wt.% sodium chloride at 20 mL/h, pH _i are 7 and 12	97

Chapter 6

6-1.	Dispersion regimes as a function of Péclet number (Fried and Combarous, 1971)	101
6-2.	Surfactant propagation in Berea sandstone core of 0.26/0.52 wt.% Triton X-100 (two-step injection) with 3 wt.% sodium chloride at 20 mL/h	112
6-3.	Dispersion of tracer and surfactant in Berea sandstone in the absence of adsorption	113
6-4.	Variation of pore velocity as a function of radial distance and fraction of pore volume	115
6-5.	Comparison of experimental data and numerical simulation with dispersion model: $D = \alpha u$ for $\alpha = 5.0 \times 10^{-4}$ m	118
6-6.	Effect of time step on the predicted concentration profiles, with dispersion defined as $D = \alpha u$ for $\alpha = 5.0 \times 10^{-4}$ m	119

6-7.	Effect of mesh size on the predicted concentration profile, with dispersion defined as $D = \alpha u$ for $\alpha = 5.0 \times 10^{-4}$ m	120
6-8.	Physical layouts and dimensions of uniform and non-uniform meshes defined near the wellbore for finite element analysis	121
6-9.	Comparison of simulation results with dispersion model: $D = \alpha u$ for $\alpha = 5.0 \times 10^{-4}$ m, using uniform and non-uniform mesh	122
6-10.	Comparisons showing the difference in concentration profiles obtained from the analytical solution (Chen, 1987) and numerical simulation near the wellbore for small injection time	124
6-11.	Comparison of breakthrough curves for dispersion with radial flow for core radii of (a) 4.75 mm, (b) 14.08 mm and (c) 44.2 mm	126
6-12.	Effect of boundary conditions at the exit on the predicted breakthrough curves at $r_e = 44.2$ mm. The Cauchy condition was used at the wellbore	129
6-13.	Effect of boundary conditions at the exit on the predicted breakthrough curves at $r_e = 442.0$ mm. The Cauchy condition was used at the wellbore	131
6-14.	Effect of injection flow rate on the experimental effluent profiles . . .	132
6-15.	Effect of injection flow rate on the predictions of a simulated effluent profile using $D = \alpha u$ for $\alpha = 5.0 \times 10^{-4}$ m	134
6-16.	Comparison of experimental data and numerical simulation using dispersion model: $D = \alpha u^m$ for $m = 0.8, 1$ and 1.2	136
6-17.	Effect of injection flow rate on the numerical solutions using $D = \alpha u^m$ for (a) $m = 0.8$ and (b) $m = 1.2$	137

6-18.	Numerical simulation of effluent curves assuming negligible mechanical dispersion for $D = D_0 = 2.5 \times 10^{-9} \text{ m}^2/\text{s}$	139
6-19.	Comparison of experimental data and numerical simulation using dispersion model: $D = D_0 + \alpha u^m$ for $m = 1.2$	140

Chapter 7

7-1.	Effluent profiles of tracer and surfactant. (a) A comparison of analytical and numerical solutions calculated using Henry's law, and (b) numerical solution fitted to experimental data	147
7-2.	Effluent profiles calculated using an equilibrium Langmuir adsorption model for surfactant slugs of different concentrations in 3 wt.% sodium chloride and injected at a flow rate of 20 mL/h	151
7-3.	Effluent profiles calculated using a kinetic Langmuir-type adsorption model for surfactant slugs of different concentrations in 3 wt.% sodium chloride and injected at a flow rate of 20 mL/h	153
7-4.	Effluent profiles calculated using a two-site model for surfactant slugs of different concentrations in 3 wt.% sodium chloride and injected at a flow rate of 20 mL/h	156
7-5.	Effluent profiles calculated using the two-site model for surfactant slugs of different concentrations in 3 wt.% sodium chloride and injected at 20 mL/h, $c \leq 0.1 \text{ wt.}\%$	160
7-6.	Effluent profiles calculated using the two-site model (common parameters) for different concentrations in 3 wt.% sodium chloride and injected at 20 mL/h, $c \leq 0.1 \text{ wt.}\%$	161
7-7.	Effluent profiles calculated using a bilayer model for surfactant slugs of different concentrations in 3 wt.% sodium chloride and injected at 20 mL/h, for $c \leq 0.1 \text{ wt.}\%$	164

7-8.	Effluent profiles calculated using the two-site model for different concentrations in 8 wt.% sodium chloride and injected at a flow rate of 20 mL/h, for $c \leq 0.1$ wt.%	167
7-9.	Illustration of regions on the effluent profile for surfactant adsorption under dynamic condition at a low flow rate of 5 mL/h . .	169
7-10.	Effluent profiles calculated using the two-site model for injection of 0.5 wt.% Neodol 25-3S and 8 wt.% sodium chloride, at 5, 20 and 120 mL/h, for $c \leq 0.1$ wt.%	170
7-11.	Effluent profiles calculated using the two-site model for injection of 0.5 wt.% Triton X-100 and 3 wt.% sodium chloride, at 20, 80 and 120 mL/h, for $c \leq 0.039$ wt.%	174
7-12.	Effluent profiles calculated using the two-site model for injection of 0.5 wt.% Triton X-100 and 3 wt.% sodium chloride, at 20, 80 and 120 mL/h, for $c \leq 0.39$ wt.%	175
7-13.	Effluent profiles calculated using the hemimicelle model for injection of 0.5 wt.% Triton X-100 and 3 wt.% sodium chloride, at 20, 80 and 120 mL/h, for $c \leq 0.039$ wt.%	178

Appendix A

A-1.	Apparent viscosity as a function of shear rate for 0.5 wt.% Neodol 25-3S solutions containing various sodium chloride concentrations	198
A-2.	Low-shear Newtonian viscosity of 0.5 wt.% Neodol 25-3S solutions as a function of sodium chloride concentration	199
A-3.	Effect of surfactant concentration on the flow curves of surfactant solution containing 12 wt.% sodium chloride	203

A-4.	Low-shear Newtonian viscosity of Neodol 25-3S solutions in 3, 8 and 12 wt.% sodium chloride brines as a function of surfactant concentration	204
-------------	---	------------

Appendix B

B-1.	Domain discretization in finite element	207
B-2.	(a) A typical quadratic triangular element and (b) its transformation to a reference triangle	212
B-3.	Quadratic points for a triangular element	215

List of Plates

Chapter 3

1. **Electron micrographs of Berea sandstone samples: (A) Low magnification of the whole rock sample, 100×; (B) Higher magnification of the same sample showing pore-lining and pore-filling cement minerals, 500× 47**

2. **Electron micrographs of Berea sandstone samples: (C) Low magnification SEM of the disaggregated sample, 100×; (D) Higher magnification of the sample showing a cluster of kaolinite booklets between grains, 500× 48**

Nomenclature

- a** = proportionality constant, Equation (6-2).
- A** = flow coefficient, m^2/s .
- c** = concentration in bulk fluid, mol/L.
- \tilde{c}** = concentration in bulk fluid in Laplace domain, mol/L.
- \tilde{c}** = effective concentration of surfactant monomers, mol/L.
- \tilde{c}** = trial value of concentration in bulk fluid used in finite element analysis, mol/L.
- c_s** = concentration at the solid surface, mol/L.
- C_b** = concentration in bulk solution, mol/L.
- C_{cmc}** = critical micelle concentration, mol/L.
- C_{hmc}** = critical hemimicelle concentration, mol/L.
- C_e** = equilibrium concentration in the bulk fluid, mol/L.
- C_c** = corrected concentration of second solution in Section 6.3, mol/L.
- C_i** = concentration in the injected solution, mol/L.
- C_p** = relative concentration of surfactant at equilibrium in Equation (2-12).
- $C_{w,e}$** = concentration of water at equilibrium in Equation (2-12), mol/L.
- C_a** = concentration within the annulus, mol/L.
- C_1** = concentration of the first injected solution in Section 6.3, mol/L.
- C_2** = concentration of the second injected solution in Section 6.3, mol/L.
- d** = characteristic length of unconsolidated porous media, m.
- d_c** = characteristic length of consolidated porous media, m.
- D** = dispersion coefficient, m^2/s .
- \underline{D}** = dispersion tensor, m^2/s .
- \underline{D}_b** = dispersion tensor in bulk fluid, m^2/s .
- D_m** = molecular diffusion coefficient in porous media, m^2/s .
- D_m^*** = molecular diffusion coefficient in bulk fluid, m^2/s .
- F** = formation resistivity.
- h** = core thickness, m.
- i** = complex variable, $(-1)^{1/2}$.
- k** = index, Equation (6-16).
- k_a** = adsorption rate constant, $L/mol \cdot s$.

$k_{a,hm}$	= adsorption rate constant for hemimicelle, $(L/mol)^{n-1} s^{-1}$.
$k_{a,m}$	= adsorption rate constant for monomer, $L/mol s$.
k_{a1}	= adsorption rate constant for first type of sites or first layer, $L/mol s$.
k_{a2}	= adsorption rate constant for second type of sites, $L/mol s$.
$k_{a2'}$	= adsorption rate constant for second layer, $L/mol s$.
k_d	= desorption rate constant, s^{-1} .
$k_{d,hm}$	= desorption rate constant for hemimicelle, s^{-1} .
$k_{d,m}$	= desorption rate constant for monomer, s^{-1} .
k_{d1}	= desorption rate constant for first type of sites or first layer, s^{-1} .
k_{d2}	= desorption rate constant for second type of sites, s^{-1} .
$k_{d2'}$	= desorption rate constant for second layer, s^{-1} .
$k_{f,mc}$	= forward rate constant for monomer-micelle kinetic expression, $L/mol s$.
$k_{b,mc}$	= backward rate constant for monomer-micelle kinetic expression, s^{-1} .
k_m	= mass transfer coefficient, s^{-1} .
K	= equilibrium ratio, $(mol/L)^{-1}$.
$K_{1/2}(\cdot)$	= modified Bessel function of the second kind.
K_{hm}	= equilibrium ratio for hemimicelle adsorption, $(mol/L)^{-n-1}$.
K_m	= equilibrium ratio for monomer adsorption, $(mol/L)^{-1}$.
K_m'	= equilibrium ratio for monomer adsorption in surface excess quantities, $(mol/L)^{-1}$.
m	= power constant, Equation (6-2).
n	= aggregation number.
\underline{n}	= normal vector on boundary S .
n^0	= total number of moles in the initial solution, mol.
n_1	= number of moles of solvent in the equilibrium solution, mol.
n_1^0	= number of moles of solvent in the initial solution, mol.
n_2	= number of moles of solute in the equilibrium solution, mol.
n_2^0	= number of moles of solute in the initial solution, mol.
n_1'	= number of moles of solvent adsorbed, mol/g_a .
n_2'	= number of moles of solute adsorbed, mol/g_a .
p	= complex variable defined in Equation (6-16).
Pe	= Péclet number.
Q	= volumetric flow rate, m^3/s or mL/h .
Q_s	= maximum adsorption capacity, mol/g_a .
Q_s^0	= maximum adsorption capacity, mol/m_0^3 .
Q_{s1}^0	= maximum adsorption capacity of first type of sites or first layer, mol/m_0^3 .
Q_{s2}^0	= maximum adsorption capacity of second type of sites, mol/m_0^3 .
$Q_{s2'}^0$	= maximum adsorption capacity of second layer, mol/m_0^3 .

Q_s^d	= maximum adsorption capacity under dynamic conditions, mol/m _s ³ .
Q_s^d	= maximum adsorption capacity under dynamic conditions, mol/g _a .
Q_s^M	= maximum adsorption capacity for monolayer saturation, mol/g _a .
r	= radial distance, m.
r_e	= radial distance at the exit, m.
r_w	= radial distance at the wellbore, m.
R	= retardation factor.
R_s	= fictitious radius of the simulated core, m.
s	= complex variable in Laplace domain.
S	= boundary.
t	= time, s.
t_R	= modified time, t/R , s.
t_{50}	= time at which $C/C_s = 0.5$, s.
T	= tortuosity.
u	= pore velocity, m/s.
\underline{u}	= pore velocity vector, m/s.
u_{inj}	= pore velocity at the injection wellbore, m/s.
V	= total volume of fluid collected, m ³ or mL.
V_s	= series defined in Equation (6-16).
V_p	= pore volume, m ³ or mL.
V_1	= volume of fluid collected at the end of first solution injection, m ³ or mL.
x_1	= mole fraction of solvent in equilibrium solution.
x_1^o	= mole fraction of solvent in initial solution.
x_2	= mole fraction of solute in equilibrium solution.
x_2^o	= mole fraction of solute in initial solution.
Y	= complex variable evaluated at r , defined in Equation (6-16).
Y_w	= complex variable evaluated at r_w , defined in Equation (6-16).

Greek Symbols

α	= dispersivity coefficient, m.
$\hat{\alpha}$	= equivalent dispersivity coefficient, $m^{(2-n_p)(1-n_p)}$
α_r	= dispersivity coefficient in r -direction, m.
α_θ	= dispersivity coefficient in θ -direction, m.
β	= ratio of molar volumes occupied by an adsorbed monomer molecules.
δ	= standard deviation, Equation (6-13).

γ	= real variable in complex plane, Equation (6-18).
$\gamma_{a,m}$	= activity coefficient of surfactant monomers in the adsorbed phase.
γ_m	= activity coefficient of surfactant monomers in the bulk phase.
Γ^*	= amount of surfactant adsorbed, mol/m _s ² .
Γ^*	= trial value of the amount of surfactant adsorbed, mol/m _s ² .
Γ_s	= total equilibrium adsorption, mol/g _R .
Γ_{hm}	= amount of surfactant hemimicelles adsorbed, mol/g _R .
Γ_{hm}^*	= amount of surfactant hemimicelles adsorbed, mol/m _s ² .
$\Gamma_{hm,e}$	= amount of surfactant hemimicelles adsorbed at equilibrium, mol/g _R .
Γ_m	= amount of surfactant monomers adsorbed, mol/g _R .
Γ_m^*	= amount of surfactant monomers adsorbed, mol/m _s ² .
$\Gamma_{m,e}$	= amount of surfactant monomers adsorbed at equilibrium, mol/g _R .
Γ_z	= amount of vacant sites, mol/g _R .
Γ_1^*	= amount of surfactant adsorbed on the first type of sites or first layer, mol/m _s ² .
Γ_2^*	= amount of surfactant adsorbed on the second type of sites, mol/m _s ² .
Γ_2^*	= amount of surfactant adsorbed on the second layer, mol/m _s ² .
ζ	= dimensionless variable defined in Equation (6-16).
θ	= angular position (in cylindrical coordinates).
κ	= Henry's law constant.
λ	= wavelength, nm.
μ_s	= low-shear Newtonian viscosity, mPa s.
ρ_s	= bulk density of solid, g _R /m _R ³ .
σ	= inhomogeneity factor.
σ_d	= sum of charge density in the diffuse layer.
σ_s	= surface charge density on the solid surface.
σ_p	= charge density at the inner Helmholtz plane.
τ	= dimensionless time.
u	= characteristic velocity, m/s.
ϕ	= porosity.
χ	= function defined for plotting on an arithmetic probability paper.
ψ	= Galertkin test function.
ω	= smallest angle of the tilted ethoxy chain made with the surface.
Ω	= global solution domain.
Ω^*	= element r : local solution domain.

Chapter 1

Introduction

Surfactants have applications in many areas, including cosmetics, detergents, pharmaceuticals, ore flotation and enhanced oil recovery. In enhanced oil recovery (EOR) methods, the role of surfactants varies from one process to another. In micellar flooding, surfactants are used to lower the interfacial tension between oil and water, thus mobilizing the trapped oil in the reservoir. In alkali/surfactant (AS) and alkali/surfactant/polymer (ASP) processes, the role of surfactants is to maintain low interfacial tension at the high salinity encountered in oil reservoirs. Surfactants are also employed in foam flooding to produce foam, which reduces the mobility of the gas phase, thus improving the sweep efficiency. For all of these surfactant-based flooding processes, loss of surfactant is a major factor in determining the oil recovery effectiveness and economic viability. Knowledge of surfactant propagation and adsorption is therefore very important in the continuing development and improvement of such processes.

The research described in this thesis is a collaborative venture with the Petroleum Recovery Institute (PRI) in Calgary, Alberta. The purpose of this study was to examine the sorption behaviour of two commercial surfactants, viz., Neodol® 25-3S (anionic) and Triton X-100® (non-ionic), on a representative sandstone under static and dynamic conditions. The ultimate goal is to apply these findings to the future assessment of the cost and technological efficiency of an ASP process (Nasr-El-Din and Hawkins, 1991).

Neodol 25-3S is commonly used in many secondary oil recovery processes. This surfactant is very soluble in high salinity brines with low concentration of multivalent

cations (Reisberg *et al.*, 1970) and is capable of remaining dissolved in aqueous alkaline solutions (Nelson, 1989). It has a high optimal salinity independent of the surfactant concentration (Glover *et al.*, 1979; Hirasaki, 1982; Nelson, 1983). For these reasons, it has been used as a cosurfactant to increase the optimal salinity in alkali/surfactant (Hill and Thigpen, 1976; Nelson *et al.*, 1984; Lawson and Thigpen, 1987), alkali/surfactant/gas (Reisberg *et al.*, 1985) and alkali/surfactant/polymer processes (Saleem and Faber, 1986; Naar-El-Din *et al.*, 1991, 1992).

The interest in employing non-ionic surfactants for EOR applications has increased recently. The traditional role in EOR of these surfactants has been somewhat limited because of the unacceptably high adsorption level compared with anionic surfactants (Lawson, 1978). Many reservoirs, however, contain harsh brines in which the inorganic multivalent cations tend to precipitate anionic surfactants such as petroleum sulphonates and sulphates. Non-ionic surfactants, on the other hand, are relatively insensitive to harsh brines, and thus highly desirable for use in these EOR applications. Recent research has suggested that the high adsorption levels can be reduced by modifying the molecular structure; and, subsequently, the optimal surfactant-oil-brine conditions can be tailored (Gracias *et al.*, 1981; Verkruyse and Salter, 1985; Lewis *et al.*, 1987). In the current study, a commercial non-ionic surfactant, Triton X-100, was chosen because it has potential for the production of foam as an EOR agent (Nutt *et al.*, 1981); it has been used successfully to maintain low interfacial tensions in alkali/surfactant processes, with a large optimal salinity region under high alkali conditions (Saleem *et al.*, 1986, 1987); and it can be mixed with other surfactants to enhance their properties (Huang and Gu, 1987; Ezumi *et al.*, 1990; Manohar and Kelkar, 1990). In addition to the EOR processes, this surfactant has also been employed in the areas of bio-technology for solubilizing membrane bound enzymes and for stabilizing enzymes in solution (Paradies, 1988). Such physical properties as size and shape of the micelles, critical micelle concentrations, and rheological behaviour have been well-documented in the literature (Mukerjee and Mysels, 1971; Ray and Némethy, 1971; Robson and Dennis, 1977; Paradies, 1988; Teh *et al.*, 1985; Pal, 1992). There have been several previous studies of adsorption of Triton X-100

on substrates such as quartz (or silica, sand, etc.) (Doren *et al.*, 1975; Nutt *et al.*, 1981; Levitz *et al.*, 1985; Travalloni-Louvisse and González, 1988; Denoyel and Rouquerol, 1991), silica gels (Huang and Gu, 1987; Zhu *et al.*, 1988), sandstone (Lawson, 1978), kaolin and alumina (Denoyel and Rouquerol, 1991), carbon black and sulphur (Douillard *et al.*, 1992). The present work extends from these previous studies on adsorption and investigates the adsorption dynamics of Triton X-100 on Berea sandstone.

The effect of surfactant adsorption on natural sandstone is difficult to evaluate due to the complexity of the rock formation and the aggregation properties of the surfactant species. Adsorption on the surfaces of clay minerals is governed by a combined interactive force at the solid-liquid interface, including the contributions of electrostatic attraction between charged surfaces and molecules, covalent and hydrogen bonding, hydrophobic bonding between surfactant molecules, and van der Waals forces (Somasundaran and Hanna, 1977). Consequently, hydrophobic interactions give rise to additional adsorption beyond the initial stage by forming surface aggregates. Structural models such as hemimicelles (Gaudin and Fuerstenau, 1955b) and admicelles (Harwell *et al.*, 1985) have been proposed to characterize the detailed adsorption mechanisms.

In addition to the mechanistic studies of surfactant adsorption, the effects of advection, dispersion and diffusion on the adsorbing surfactant components must also be considered when the various parameters governing the adsorption process are determined from a flow system. The physical phenomenon referred to as hydrodynamic dispersion is commonly characterized by an empirical relationship (Perkins and Johnston, 1963; Fried and Combarous, 1971), in which the dispersion mechanism is described by the combined contributions of diffusion and advection, and expressed as a function of the Péclet number. The earliest theory of dispersive transport was originated by Taylor (1953) based on an analogy between porous media and bundles of capillaries. Other authors, including Aris (1956, 1959), Brigham *et al.* (1961, 1974), Coats and Smith (1964), and Hoopes and Harleman (1967), have explored various aspects of dispersive behaviour in porous media, such as pore heterogeneity and core dimension. Detailed transport theories have been studied very extensively in such review articles as Saffman

(1959), Perkins and Johnston (1963), Fried and Combarous (1971), and Koch and Brady (1985). A novel approach has been proposed recently by Udey and Spanos (1993) using two immiscible flow equations with zero interfacial tension and negligible molecular diffusion. The dispersive transport expression obtained shows explicitly the dependence of concentration, concentration gradient and flow rate. In the areas of mathematical modelling, Genuchten and Alves (1982) have presented a comprehensive summary of over 40 models for the analytical solution of the one-dimensional advective-dispersive transport equation, accounting also for the effects of zero-order production, first-order decay and linear equilibrium adsorption.

Dispersion in consolidated sandstone with radial flow is of our interest in the current study. Previous studies of oil-displacement test (Krumrine *et al.*, 1982b) have suggested that more effective oil recovery can be obtained by using linear rather than radial flow geometry due to the higher sweep efficiency. Radial core floods are therefore recommended to provide better indications of oil recovery in reservoirs, especially with respect to the flow patterns around an injection wellbore (Nasr-El-Din and Hawkins, 1991). The governing transport equation for dispersion with radial flow can be derived from the general advection-dispersion equation. Numerous approximate analytical solutions obtained using zero initial concentration and the Dirichlet inlet boundary condition in a semi-infinite radial core, have been presented previously by Raimondi *et al.* (1959), Hoopes and Harleman (1967), Gelhar and Collins (1971), Tang and Babu (1979) and Hsieh (1986); and also using the Cauchy inlet condition by Chen (1987).

Because of adsorption, the active displacement front tends to advance more slowly than the advection frontal velocity of the injected fluid. In addition to the models summarized in Genuchten and Alves (1982), many analytical and numerical solutions have been derived for linear equilibrium and first- or second-order non-equilibrium sorption models with uniform and non-uniform flow, for example, Bear (1972), Gupta and Greenkorn (1974) and Ci-Quan and Jie (1990). Other mathematical models, such as an extension of the Coats and Smith's (1964) capacitance model describing the advection-dispersion-dynamic adsorption transport in porous media with stagnant volume by Bidner and Vampa (1989), have contributed significantly to the theoretical development of

adsorption in dynamic systems. The general models derived have been found suitable for producing different kinds of effluent concentration profile. Although interactions between surfactant and porous rock are complex, some simple kinetic models have successfully provided good approximations to the adsorption of surfactant systems (Trogus *et al.*, 1977). Satter *et al.* (1980) have examined the relationship between the advective-dispersive transport and rate-controlled adsorption, and simulated effluent concentration profiles of various kinds (eg., asymmetric tailing). Ramirez *et al.* (1980) suggested that both the mass transfer in the bulk solution by diffusion and surface kinetics of adsorption at the solid-liquid interface are important, and must be considered at all injection velocities. Several models of dynamic adsorption have been studied in Foulser *et al.* (1989). It appears that both the bilayer and two-site adsorption models provide equally good fits to the experimental data; however, the two-site model gives more consistent parameters between different sets of fitted data.

The objectives of this study are to examine the mass transport behaviour of surfactant solutions flowing through porous sandstone, and to develop a suitable mathematical model to describe this behaviour.

The work presented in the first half of this thesis aims to assess the mechanisms and dynamics of surfactant adsorption with the aid of laboratory-scale experiments. Chapter 2 provides a short summary of the factors influencing the adsorption systems and various mechanistic models proposed in the literature. Detailed experimental procedures and set-up are described in Chapter 3. In Chapters 4 and 5, experimental results are summarized and discussed. Isotherm equations are fitted to the static adsorption data in order to evaluate the maximum adsorption capacities under various conditions, and to assess the hypotheses proposed by different adsorption mechanisms. Flow experiments are performed using a unidimensional, axisymmetric geometry to simulate the radial flow pattern near an injection wellbore. The effects of sodium chloride, surfactant concentration, pH and flow rate on adsorption are examined. The propagation of solutions of an anionic surfactant having a liquid crystal phase is also investigated which, to the best of our knowledge, has not been considered before.

The second half of this thesis focuses on the modelling aspects of the transport phenomenon. Numerical solutions for the general advective-dispersive transport equation are obtained in Chapter 6 using the Galerkin finite element method. The variational problem is solved by domain discretization using straight-sided quadratic elements (in 1-D) and bi-quadratic triangular elements (in 2-D). The time derivative is approximated using the implicit second-order Gear scheme. For the purpose of ensuring adequate description of the dispersive transport of surfactant in the absence of adsorption, a two-step injection experiment is performed. The boundary conditions applied at the entrance and the exit are examined along the comparison with both the measured effluent history and the analytical solution. Experimental data of tracer injection obtained at different flow rates are simulated to discriminate the differences between various dispersion models reported in the literature, and to examine the model validity for evaluation of the radial flow problem.

In Chapter 7, numerical solutions of several linear equilibrium and second-order non-equilibrium adsorption models coupled with the advective-dispersive mass transport equation are presented. Compound models such as two-sites, bilayer and hemimicelle adsorption models are also investigated. The effects of monomeric-micellar equilibrium and surface aggregation are examined by limiting the concentration of surfactant monomers in the solution phase. Model validity based on the fitted parameters is evaluated by varying the surfactant concentration, flow rate and salinity condition.

Because of its limited coverage and exploratory nature, this study is not intended to provide direct applications to field conditions. It is hoped that it will encourage research into new aspects of the radial flow and dynamic adsorption problems.

Chapter 2

General Theories of Surfactant Adsorption on Mineral Surfaces

2.1 The Nature of Solid (Sandstone) Surfaces

To provide a clearer picture of the mechanisms of surfactant adsorption onto sandstones, it may be useful at this point to discuss some of the special aspects of the fundamental properties of sandstones.

The principal compositional elements of sandstone are mineral particles, called grains, which consist of quartz, feldspars and rock fragments, see Figure 2-1 (Berg, 1986). The finer mineral material between the grains is called the matrix and commonly consists of clay minerals and very fine particles of quartz and feldspar. After deposition and burial, the grains and matrix are altered by the physical effects of compaction and chemical changes. Cement (mineral particles commonly consist of silica and carbonate, introduced after deposition) precipitates to fill in the intergranular spaces and join the grains into a competent mass.

It has long been recognized that clay minerals in the matrix (as adsorbents) play an important role in the surfactant loss which occurs during a chemical flooding process. To visualize the unique adsorption characteristics at the clay-water interface, it is helpful to understand the surface chemistry and some physical properties of clays.

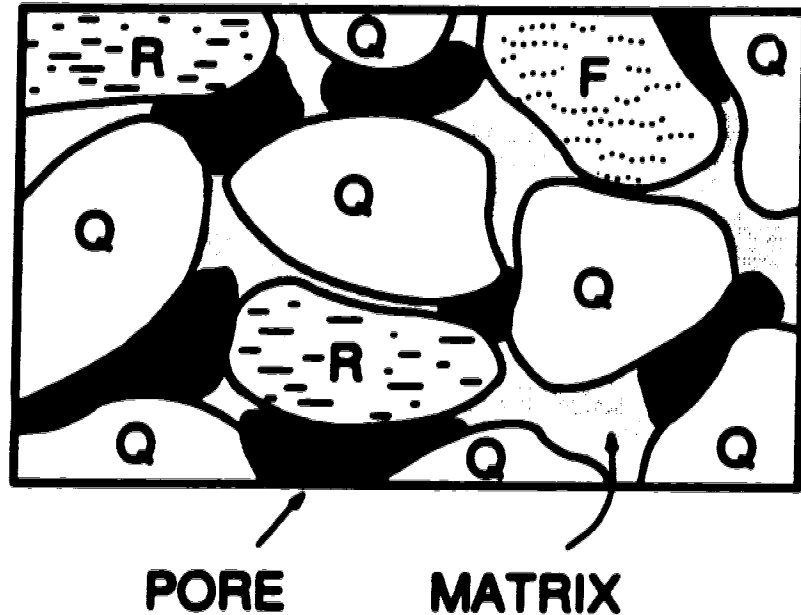


Figure 2-1. Schematic diagram showing the compositional elements of sandstone.
Q: Quartz, **F:** Feldspars, and **R:** Rock fragments.

2.1.1 Physical Properties of Clay Minerals

Three common types of clay minerals are known to be important for their sorptive properties: kaolinite, illite and montmorillonite. Kaolinite is often found in the form of a well-crystallized hexagonal grain. Illite and montmorillonite are of similar structure as kaolinite but contain poorer crystalline fabrics. Figure 2-2 shows the chemical structure of kaolinite: two-layer clay consisting of silicon in a tetrahedral layer with oxygen and aluminium in an octahedral layer with hydroxyl (Wayman, 1965). The structural formula is $Al_2Si_2O_5(OH)_2$.

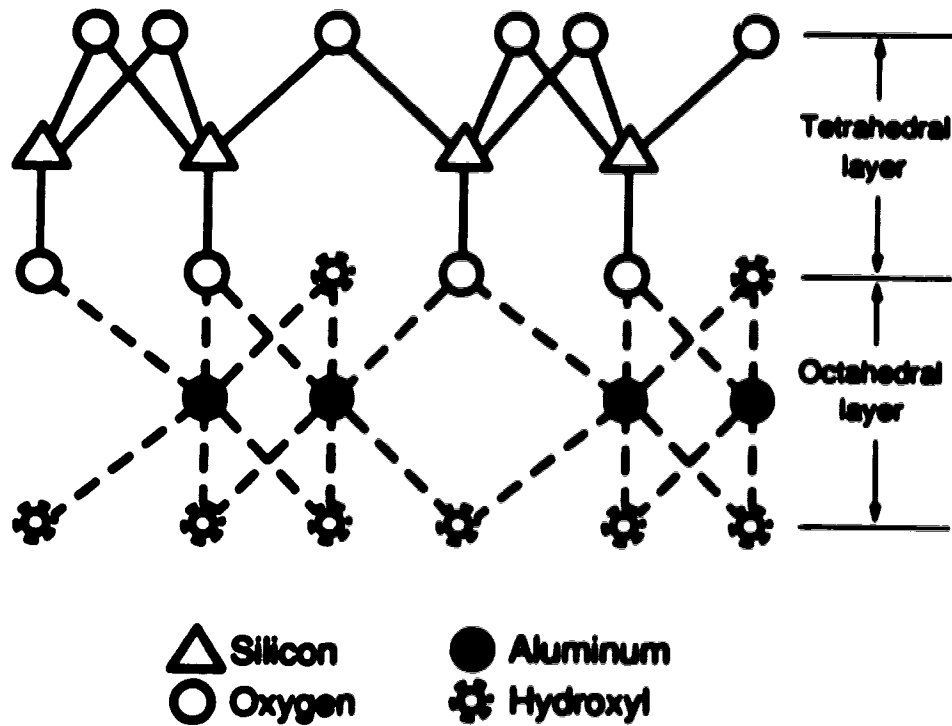


Figure 2-2. Schematic diagram of the unit cell of kaolinite.

2.1.2 Surface Forces

For all solids, there exists a field of forces around each ion, atom or molecule holding the solid together. At the surface of the solid this field of forces becomes discontinuous. Similarly, the field of forces holding a molecule in the adjacent gas, liquid or solid phase is also disrupted. The imbalance of forces at the interface can be described as an interaction between the field of forces of the solid surface and that of the particles (in the adjacent phase) being attracted. To attain a state of minimum free energy for the entire system, the surface units are subjected to a net inward attraction normal to the surface. In general, these forces of attraction can be classified as those associated with physical adsorption and chemisorption. Physical adsorption often refers to such forces as dispersion forces (or van der Waals attraction) and electrostatic forces. Dispersion

forces originate from the fluctuating electrical moment produced by the movement of electrons in their orbits (Gregg, 1961), which induces a corresponding moment in a neighbouring atom or ion and leads to attraction. For an ionic solid, its surface will develop an electrostatic field which will be superimposed on the field of forces produced by the dispersion forces. Chemical forces, on the other hand, arise when a transfer of electrons between the solid and the adsorbed molecule is involved. The adsorption of hydrogen on platinum or tungsten is an example of chemisorption in which each adsorbed hydrogen atom shares an electron with the metal.

2.1.3 Electrostatic Forces on Clay Surfaces

Many previous studies suggest that clay surfaces contain negative sites on the faces and positive sites along the edges of the particles, *see* Figure 2-3 (Wayman, 1965). The net charge carried is negative. Surface charge may be created by a number of mechanisms. In the case of mineral oxide surfaces, the three most common mechanisms are: *isomorphous replacement, lattice defects and broken bonds along crystalline edges.*

Isomorphous replacement represents the substitution of Al for Si in the tetrahedral layer or Mg for Al in the octahedral layer, which will produce a negatively charged surface. The charge created due to lattice defects corresponds to the presence of interstitial ions or vacancies in the lattice structure.

While the negative charge on the faces is not dependent on the surrounding environment, the edges of the clay, as shown in Figure 2-3, may exhibit *pH*-dependent characteristics due to hydroxylation and ionization of the broken bond of silicon or aluminium oxide, M-O, where M denotes Si or Al (Wayman, 1965; Hankins, 1989). The origin of charge can be represented by a two-step process (Gaudin and Fuerstenau, 1955a): (1) fracture of M-O bonds in the lattice crystal; followed by (2) adsorption and dissociation of H^+ and OH^- ions from solutions. In the first step, the broken bond hydrolyzes to form a weak acid, M-OH. The hydroxyl group then tends to adsorb or

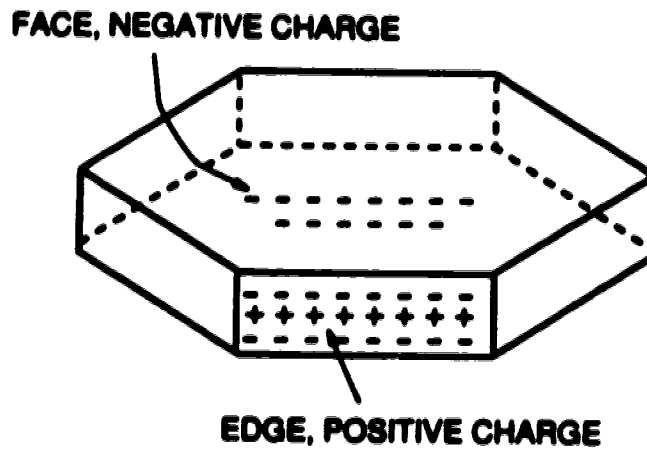


Figure 2-3. Dual charge on a kaolinite particle.

desorb a hydrogen ion forming $M-OH_2^+$ or $M-O^-$:



The charge on the surfaces is thus affected by the solution pH , where H^+ and OH^- are called the potential determining ions. It should be noted that the chemical potential of the solid remains unchanged and the bulk pH changes only the electrochemical equilibrium near the solid-liquid interface.

It is clear that any net charge on the solid surface, α_s , must be effectively neutralized by the opposite charge in the solution near the interface. Ions of opposite charge and like charge to that of the surface are redistributed due to the electrical potential developed at the interface, the forces introduced by attraction/repulsion, and the concentration gradients of ions. The diffused ionic atmosphere so formed is known as an electrical double layer. A simple representation of the model is illustrated in Figure 2-4 (Gandia and Fuerstenau, 1955a; Aveyard, 1984; Harwell *et al.*, 1985). The

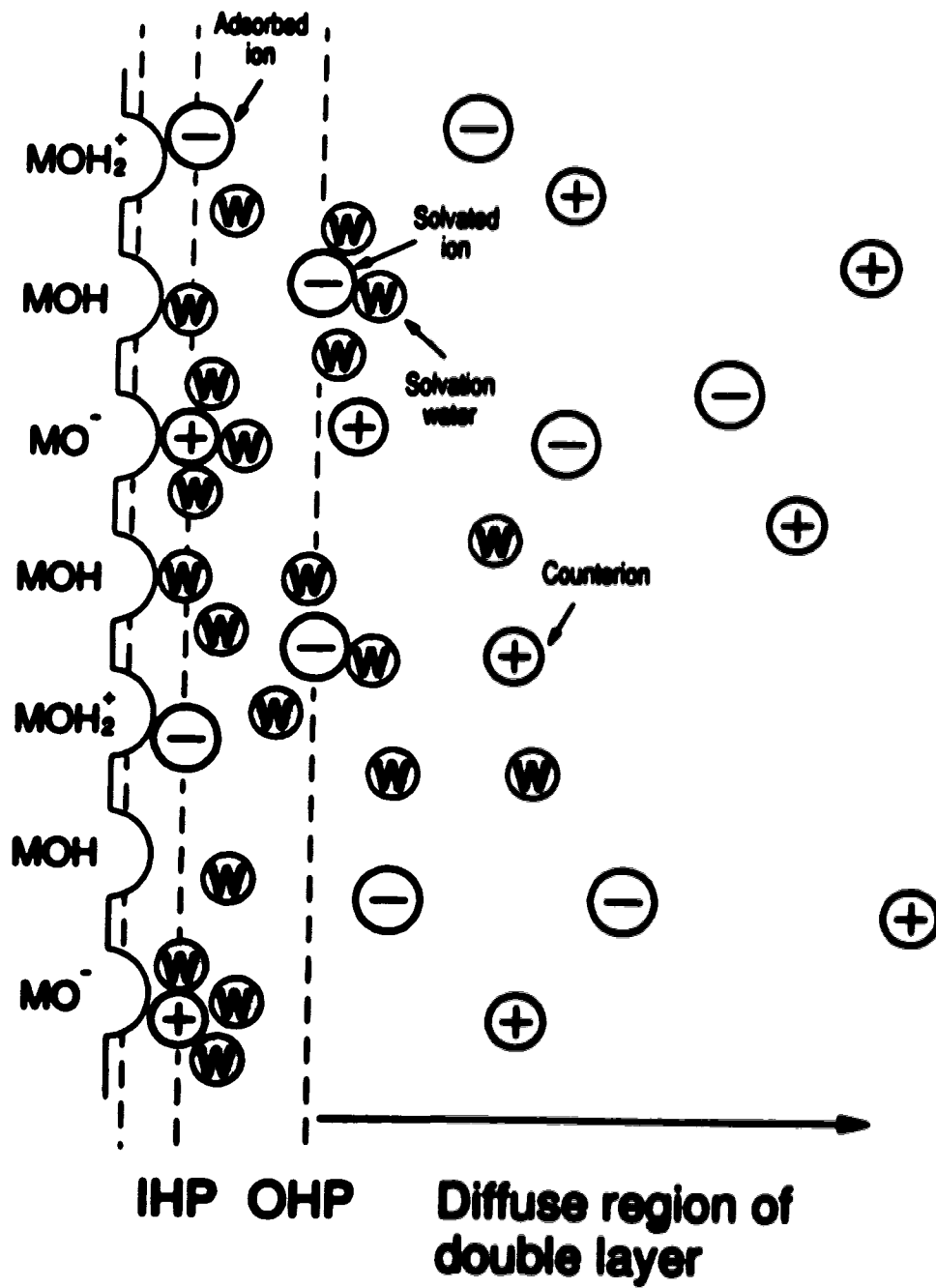


Figure 2-4. Structure of the electrical double layer near the clay-water interface.

potential determining ions may be considered as part of the solid lattice, which corresponds to the metal oxide hydration layer. The locus of centres of all adsorbed ions defines the inner Helmholtz plane (IHP), in which the charge density is given by σ_p . Centres of the solvated ions, on the other hand, define the outer Helmholtz plane (OHP) or Stern plane. The counterions which form an atmosphere extending infinitely out from the OHP is the diffuse or Guoy layer in which the total distributed charge density is σ_d . To obtain an electrically neutral system, $\sigma_s + \sigma_p + \sigma_d = 0$ must be satisfied at all times. The point of zero charge (p.z.c.) refers to the condition at which the net surface charge density is zero ($\sigma_s = 0$).

2.2 General Description of Adsorption Isotherm at the Solid-Liquid Interface

When a pure liquid is placed in contact with a solid, the forces acting on the liquid molecules at the solid-liquid interface will be different from those in the interior of the liquid phase. As a result, an increase in concentration of the liquid molecules near and at the interface will occur. This concentrated layer of molecules may be viewed as liquid molecules being "adsorbed" at the solid surface (Gregg, 1961); but the adsorption is often not obvious nor easily detectable for pure liquid because the concentration of liquid molecules is already high, even in free liquid.

The problem becomes quite different when the liquid phase contains two or more components. In general, all molecules will be adsorbed to different extents so that the concentrations of each component on the solid surface and in the bulk solution will vary accordingly. The classical method for determining this quantity is by the use of adsorption isotherms derived from the *surface excess method*.

Let us consider a solution which contains two components, viz., solute and solvent. Assuming the original solution contains n_1^0 moles of solute molecules and n_2^0 moles of solvent molecules, the total number of moles of molecules, n^0 , is given by

$$n^{\circ} = n_1^{\circ} + n_2^{\circ} \quad (2-2)$$

The quantity of each component adsorbed can then be evaluated from additional material balance, such that the total number of moles of solute (component 1) is equal to the sum of the amounts of free molecules in the bulk solution phase, n_1 , and the number of moles adsorbed *per unit mass of solid*, n_1° :

$$n_1^{\circ} = n_1 + m n_1^{\circ} \quad (2-3)$$

where m is the total mass of solid. Similarly, the mass balance of solvent (component 2) can be written as

$$n_2^{\circ} = n_2 + m n_2^{\circ} \quad (2-4)$$

where n_2 is the number of moles in the bulk solution phase after equilibrium has occurred, and n_2° is the number of moles adsorbed *per unit mass of solid*. Rearranging Equation (2-4), we obtain

$$\begin{aligned} m n_2^{\circ} &= n_2^{\circ} - n_1 \frac{n_2}{n_1} \\ &= n_2^{\circ} - n_1 \frac{x_2}{x_1} \end{aligned}$$

or

$$m n_2^{\circ} x_1 = n_2^{\circ} x_1 - n_1 x_2 \quad (2-5)$$

where x_1 and x_2 are the mole fractions in the bulk phase, for $x_1 = n_1 / (n_1 + n_2)$. We can then multiply Equation (2-3) by x_2 :

$$m n_1^{\circ} x_2 = n_1^{\circ} x_2 - n_1 x_2 \quad (2-6)$$

and subtract Equation (2-5) from the resulting equation. The final equation can be rearranged in the following form:

$$m(n_1^0 x_2 - n_2^0 x_1) = n^0(x_1^0 - x_1)$$

or

$$\frac{n^0 \Delta x_1}{m} = n_1^0 x_2 - n_2^0 x_1 \quad (2-7)$$

for $x_1^0 = n_1^0/n^0$; and similarly

$$\frac{n^0 \Delta x_2}{m} = n_2^0 x_1 - n_1^0 x_2 \quad (2-8)$$

for $x_2^0 = n_2^0/n^0$. The adsorption of individual components, n_1^0 and n_2^0 , can therefore be determined from the measured changes in the solute and solvent concentrations, or mole fractions in the bulk phase: $\Delta x_1 = x_1^0 - x_1$ and $\Delta x_2 = x_2^0 - x_2$, respectively. The adsorption curve obtained by plotting $n^0 \Delta x_1/m$ against x_1 is called a surface excess or composite isotherm. It is important to realize that the measured $n^0 \Delta x_1$ does not represent the "true" adsorption of solute as the values of Δx_1 will depend on the amount of solvent (component 2) being adsorbed. Consequently, this method is in fact a measure of the apparent adsorption of the solute and solvent components.

In dilute solutions, the variation in concentration of solvent is relatively insignificant when compared with that of the adsorbing solute. The mole fraction of the adsorbing solute in Equation (2-7) may be equated to zero ($x_1 \rightarrow 0$ and $x_2 \rightarrow 1$), so that the apparent adsorption of the solute may be considered as equivalent to the true adsorption:

$$n_1^0 = \frac{n^0 \Delta x_1}{m} \quad (2-9)$$

Adsorption isotherms of solute from dilute solution can often be represented by a plot of w/m against C_s , where w is the amount of solute adsorbed and C_s is the solute concentration at equilibrium. Under experimental conditions, the adsorbed amount can

be determined from the measured change in concentrations of the bulk solution before and after the solution contacts the solid:

$$n_1^0 \propto \Gamma_s = \frac{(VC_s) \Delta C}{m} \quad (2-10)$$

where Γ_s is the amount of solute adsorbed *per unit mass* of solid at equilibrium, ΔC is the change in concentration in the bulk fluid from the initial concentration to the final concentration at equilibrium ($C_i - C_f$), V is the volume of fluid in contact with the solid, and m is the *mass* of solid.

An early classification system for adsorption isotherms was given by Brunauer *et al.* (1940), who observed that most isotherms follow one of the five basic types, see Figure 2-5. An isotherm of Type I is obtained when the adsorbed solute forms a monolayer on the solid surface. Isotherms of all other types often indicate the development of multilayer adsorption. Another more general classification was derived by Giles and co-workers (1960) who suggested four basic isotherm shapes based on the initial slope of the curve at low concentrations: L for *Langmuirian*, S for *sigmoid*, H for *high affinity* or C for *constant partition*; the subgroups were then determined by their behaviour at the higher concentration: 1, 2, 3 and 4 depending on the number of inflection points. The subgroup of MAX was also considered to allow for the occurrence of a maximum on the curve (see Figure 2-6).

2.3 Properties of Surfactant in Aqueous Solutions

Surfactants are amphiphilic substances which commonly consist of two clearly distinguishable parts: a long hydrocarbon chain (hydrophobic) attached to a polar or ionic (hydrophilic) group. When these molecules are brought into contact with an aqueous medium, the molecules of surfactant will be hydrated by means of hydrogen bonding between the polar group and the water molecule. The hydrogen bond formed is represented by $B-X \cdots OH_2$, in which the molecules are held together via a weak non-

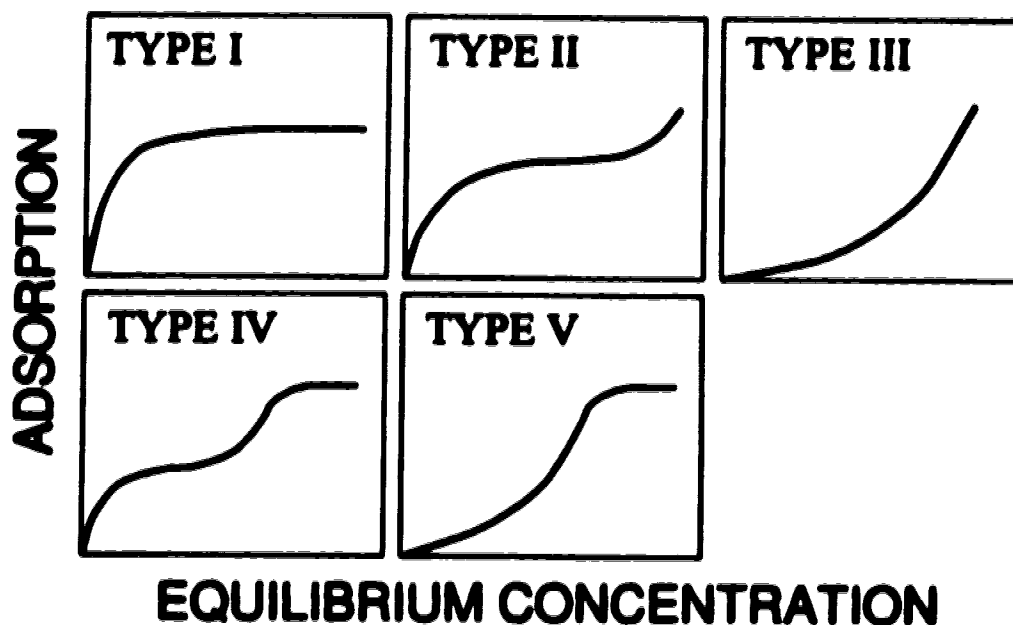


Figure 2-5. Types of adsorption isotherms according to Brunauer *et al.* (1940).

covalent bond of the unshared electron pair in the oxygen atom (of water) with the hydrogen atom in the hydrophilic group. The hydrocarbon tail, on the other hand, tends to escape from the aqueous environment because of the much higher affinity associated with water itself compared to that between water and hydrocarbons. This is commonly known as the hydrophobic effect (Tanford, 1980). In the bulk of a solution, surfactant molecules will migrate to the surface and result in a decrease in the surface tension. Here, the polar groups will anchor to the aqueous medium maintaining the solubility in water. The hydrocarbon chains closest to the polar groups will situate more or less perpendicular to the surface.

At very low concentrations of surfactant, the reduction in surface tension increases with the bulk concentration. As the bulk concentration reaches a certain value its reduction effect diminishes and the surface tension remains constant for higher concentrations. The change in behaviour is attributable to the sudden onset of molecular

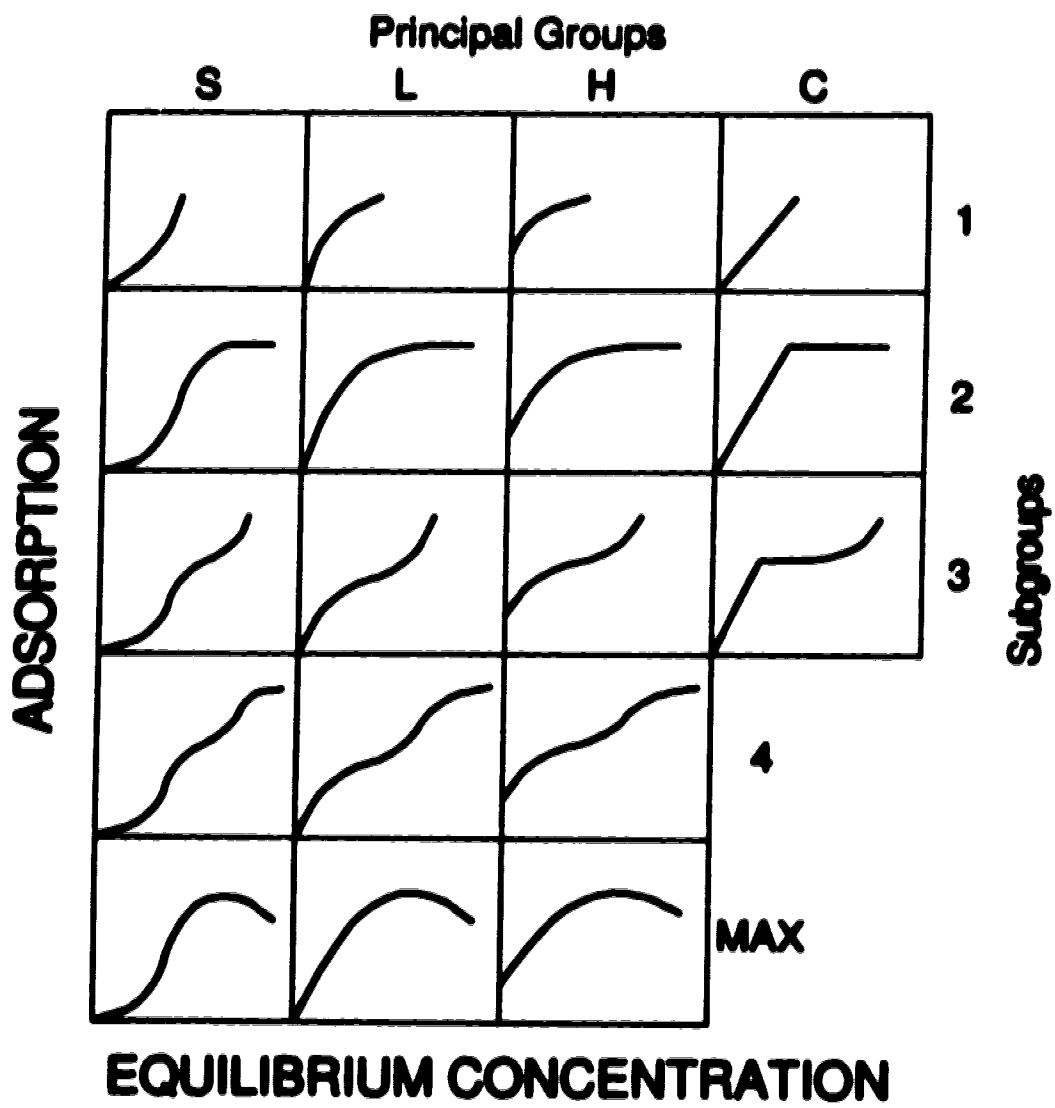


Figure 2-6. General classification of adsorption isotherms according to Giles *et al.* (1960).

aggregation or micellization. Surfactant molecules aggregate into micelles in which the hydrophobic portions of each molecule cluster together to form a hydrophobic (or hydrocarbon) core and the polar groups maintain the water affinity on the micelle surface. Since these surfaces are strongly hydrophilic, the micelles remain mostly in the bulk solution and thus do not influence the surface tension. The surfactant concentration marking the onset of such molecular aggregation is commonly known as the critical micelle concentration (c.m.c.).

Each surfactant at a given temperature and electrolyte concentration has a characteristic c.m.c. value. An extensive compilation of c.m.c. data for many surfactants over a wide variety of conditions has been published in the book by Mukerjee and Mysels (1971). Of considerable importance are the effects of molecular structure, nature of the charge group and properties of additives, since these factors determine the possibilities and limitations in the packing of surfactant molecules, intramicellar mobility, and micellar size and shape.

For ionic surfactants, the addition of electrolyte lowers the c.m.c., alters the size and shape of micelles, and increases the aggregation number (Aacker, 1979; Lindman, 1984). The decrease of c.m.c. depends mainly on the concentration of counterions, *i.e.*, the strength of counterion binding to the ionic micelle in bulk solution. Such binding provides a balance to the repulsion between ionic surfactant molecules by depressing the electrical double layer on the micellar surface, and thus promotes the aggregation of these molecules. Typically the micelles have a nearly spherical shape. As the aggregation number increases due to the addition of electrolyte, the shape of the micelles must be altered in order to allow for a stable geometrical configuration. For most ionic surfactants, micellar growth often leads to the formation of densely packed rod-like aggregates, which results in a dramatic increase in viscosity. According to Gray and Winsor (1974), "If these micelles are in sufficiently close proximity (*i.e.*, the amount of inter-micellar liquid is not sufficient to cause too great a separation of the micelles) and the temperature is not too high (*i.e.*, the disorganizing effect of thermal motion is not too great), the operation of inter-micellar forces causes the micelles to adopt a thermodynamically stable arrangement showing a minimum potential energy". Thus the

micelles appear to be fused together forming a stable mesomorphic phase, two "echelons" between a periodic arrangement of perfectly ordered crystal structure and perfectly disordered amorphous structure, commonly referred to as "liquid crystals". In the current study, viscosity measurements were used to characterize the surfactant aggregates of Neodol 25-3S in the presence of sodium chloride. The solution viscosity exhibited a strong dependence on the surfactant and salt concentrations, which may be associated with the formation of a liquid crystal phase (*see Appendix A*).

Electrolyte also lowers the c.m.c. values of non-ionic surfactants, but the effects are much smaller than for ionic surfactants. The phase behaviour of non-ionic surfactants is often characterized in terms of its cloud point, which denotes the temperature at which the separation of a micellar phase occurs. Maclay (1956) showed that the cloud point is a decreasing function of the concentration of various electrolytes. The increase in electrolyte affects the solution in the same direction as the cloud point by reducing the solubility of the non-ionic surfactant monomers and micelles. Docher *et al.* (1951) denoted this behaviour as the salting-out effect. On the other hand, in the presence of multivalent ions such as calcium ions in CaCl_2 , surfactant precipitates are formed by complexation, for example, with the ethylene oxide units of polyethoxylated molecules, $\text{CaCl}_2 \cdot 2\text{H}_2\text{O} \cdot \text{C}_2\text{H}_4\text{O}$. This is known as the salting-in or coagulating effect.

2.4 Mechanisms of Surfactant Adsorption

Adsorption of surfactant is a process of considerable complexity. The initial force driving the surfactant molecules to the solid-liquid interface is the same one that leads to the reduction of surface or interfacial tension, *i.e.*, the hydrophobic effect. Subsequently, the surfactant molecules near the interface are attracted to the solid surface due to a combination of adsorbate-adsorbate and adsorbate-adsorbent interactions. These latter interactions are highly dependent on the nature of the solid surface and the associated structured water, and also on whether the structure of water is disrupted by the hydrocarbon chains.

In addition to the hydrophobic effects, other interactions of considerable importance are the dispersion forces in the Stern plane originating from the van der Waals attraction, electrostatic effects induced by the unbalanced electrical charge distribution near the interface, dipolar effects induced by molecules consisting of electron-rich groups (such as aromatic and/or ionic groups), molecular interactions leading to the formation of hydrogen bonds between the adsorbed molecules and adsorbent, and interactions resulting from ion-exchange or ion-pairing (Myers, 1988).

The adsorption process is further complicated by the equilibrium between the monomeric and micellar surfactant in the bulk solution. Detailed mechanisms have been a subject of scientific interest for several decades. Most theories of surfactant adsorption fall into one of two categories to account for the hydrophobic interactions. One of these models is the hemimicelle model (Gaudin and Fuerstenau, 1955b) in which surfactant molecules are adsorbed vertically exposing the hydrocarbon tail to the solution. The resulting monolayer structure resembles a "half" micelle adsorbed on the surface. Subsequent adsorption forms a bilayer structure following the completion or partial completion of the adsorbed "half" micelle. Harwell *et al.* (1985), on the other hand, proposed a pseudophase model in which surfactant aggregation produces a bilayer structure, called an admicelle, which is formed in patches on a heterogeneous surface. A general description of the two adsorption isotherms are given below whereas the detailed mechanisms are to be discussed in later sections.

The mechanism of the hemimicelle adsorption process can be depicted by a sequence of five adsorption stages as illustrated in Figure 2-7 (Clunie and Ingram, 1983; Gao *et al.*, 1987). STAGE I represents the region of low surfactant concentration. Free hydrated surfactant monomer approaches the solid-liquid interface and is adsorbed as an individual molecule. As the concentration of surfactant increases, the adsorption isotherm gradually reaches a small plateau as shown in STAGE II which is denoted by the monolayer saturation of molecules adsorbed parallel to the surface, Q_m . After reaching this monolayer saturation, subsequent adsorption occurs by displacement of the weakly adsorbed alkyl chains (STAGE III); and tilting of the strongly adsorbed ethylene oxide segments by a small angle of θ (STAGE IV) as described by Klimenko *et al.* (1974). The

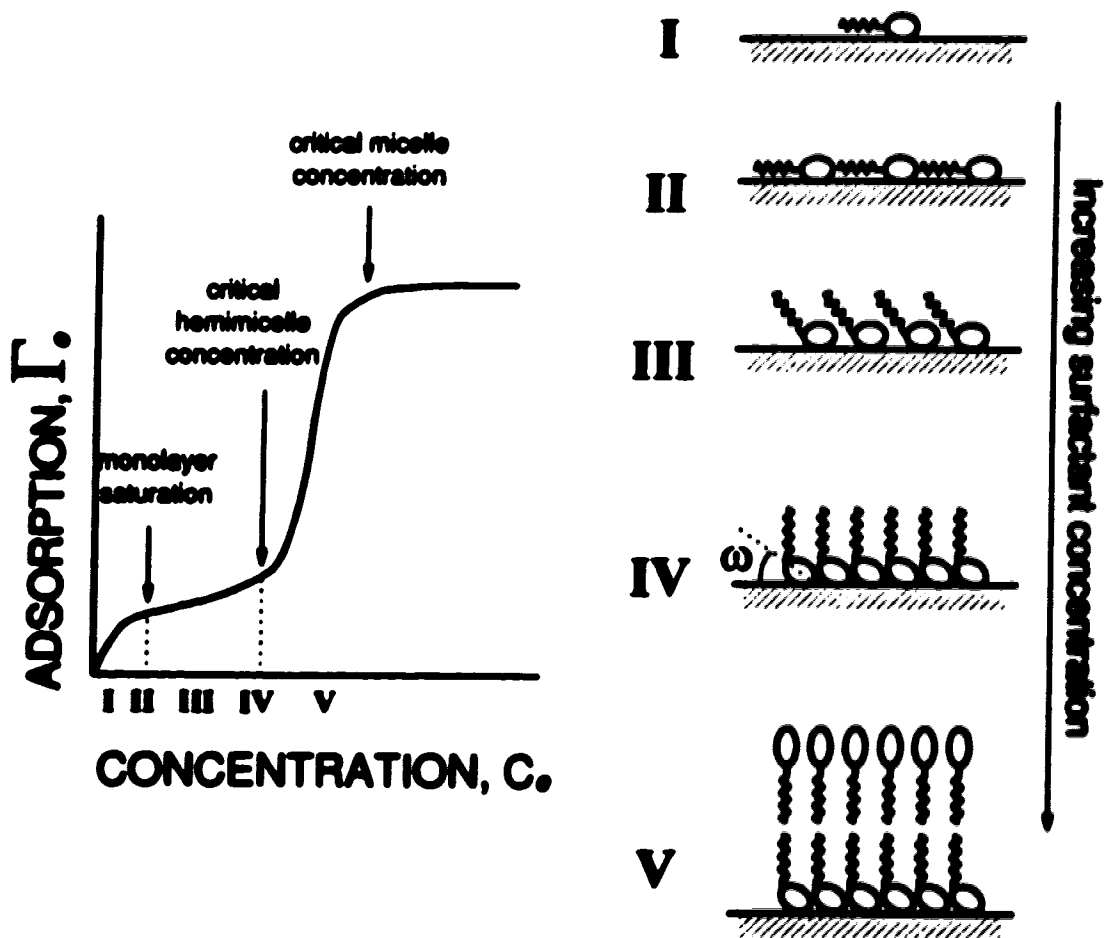


Figure 2-7. Stepped adsorption isotherm, showing the orientation of surfactant molecules and surface aggregates (hemimicelles).

upper concentration limit is defined as the critical hemimicelle concentration, C_{hm} , indicating the onset condition for surface aggregation. STAGE V of adsorption is denoted by the condensation of one or more surfactant monomers from the liquid phase onto an adsorbed monomer due primarily to hydrophobic bonding.

Figure 2-8 shows the schematic representation of the isotherm for the proposed pseudophase or admicelle model (Harwell *et al.*, 1985). REGION I is commonly referred to as the Henry region. For ionic surfactants, monomers are adsorbed due to the electrostatic attraction of the charged head groups for the charged surface in addition to the hydrophobic effect. The shape of the isotherm in REGION II indicates that the cooperative effect is important in the formation of surface aggregates. In Harwell's hypothesis it is stated that the first and second layers form simultaneously; that is, monolayers never form on any part of the surface. REGION III shows a decrease in slope of the isotherm due to repulsion of surfactant ions by the adsorbed charged molecules and also due to depletion of active adsorption sites available. The plateau shown in REGION IV occurs at the solution c.m.c. such that, according to the pseudophase model, all excess monomers will enter the micelles or micellar phase, leaving the solution monomer concentration constant (Trogus *et al.*, 1976; Scamhorn *et al.*, 1982). The REGION III/IV transition corresponds to the surface being completely covered by a bilayer.

2.4.1 Adsorption of Non-Associated Surfactant Molecules at Low Concentration

In the first stage of adsorption, the surfactant molecules adsorb on a solid surface independently of one another, as the result of one or more contributing forces arising from electrostatic attraction, chemisorption, hydrogen bonding and solvation effects (Somasekaran and Hanna, 1977). This is commonly referred to as the Henry region because surfactant adsorption isotherms generally are linear. Regardless of the detailed mechanism of adsorption, Avgal *et al.* (1964) have shown that most of the monomolecular and multimolecular adsorption isotherms on a uniform surface will reduce to the limiting Henry equation at low surface coverage.

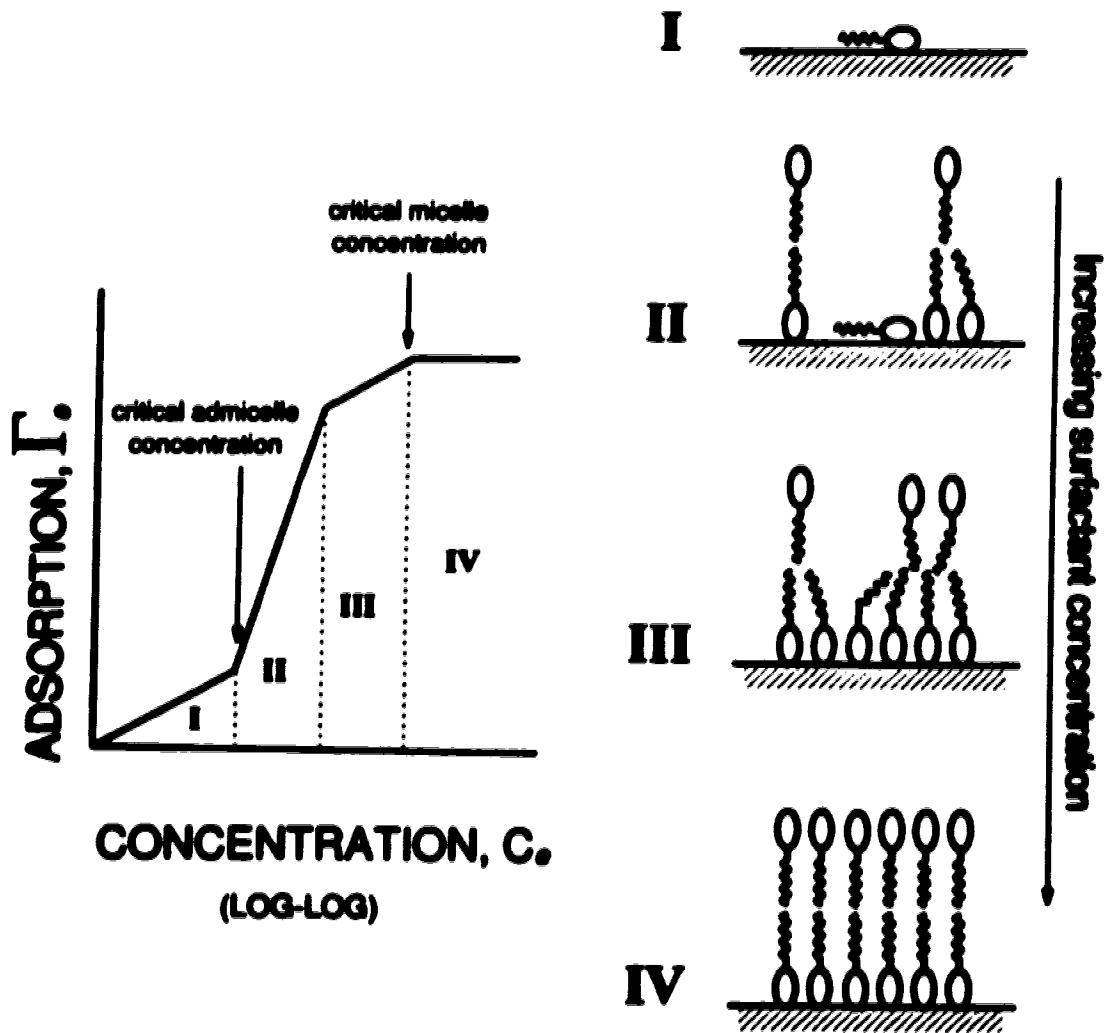
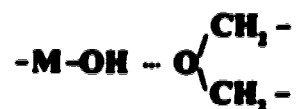


Figure 2-8. Adsorption isotherm and proposed mechanism for the formation of admicelle on solid surface.

For ionic surfactants, adsorption results mainly from electrostatic forces between the surfactant ions and charged surface. The adsorption process can be considered as a special case of specific adsorption of ions referred to in Grahame's treatment of the electrical double layer (Hough and Rendall, 1983). Surfactant ions adsorb at the inner Helmholtz plane (IHP), where head-head (Columbic) and tail-surface interactions are assumed to be of first order importance (Harwell *et al.*, 1985).

The mechanism of the adsorption of non-ionic surfactants is very different from that of the ionic ones. Because of the absence of ionic and chemisorbing components in the non-ionic surfactants, hydrogen bonding often provides the initial driving force for adsorption (Somasundaran *et al.*, 1991). A hydrogen bond is formed between the hydroxyl on the surface and the ethylene oxide group in the surfactant molecule (Furlong and Aston, 1982; Partyka *et al.*, 1984), *i.e.*,



This hydrogen bond is relatively stronger than that formed between the hydrated surfactant molecule and the water molecule. Thus adsorption may become more favourable, especially, for short ethylene oxide chain surfactants. A somewhat different type of hydrogen bonding, however, has been hinted for the conditions of dynamic adsorption. Trogus and co-workers (1977), by applying a kinetic Langmuir model, found that the rates of adsorption and desorption both increase substantially as the ethylene oxide chain is lengthened, and the rate of desorption increases more rapidly than the rate of adsorption. They argued that under dynamic conditions the ethylene oxide groups are not attached to the surface, but that surface linkage is caused by terminal OH-group hydrogen bonding.

In all cases, these surfactant molecules are believed to be adsorbed horizontally on the surface, with both the hydrophilic and hydrophobic portions adsorbed (Corkill *et al.*, 1967; Chmie and Ingram, 1983). This orientation was suggested because it

provides a minimal loss of entropy during adsorption and allows only a minimum distortion of the water structure near the surface.

Other investigators suggested that the first stage of adsorption must also account for the displacement of water molecules from the surface by the adsorbed surfactant molecules. A quantitative analysis for the adsorbed amount of surfactant molecules can be derived using the surface excess method as illustrated in the previous section. Some of the earliest work were presented by Koganovskii and co-workers (1976). They depicted the adsorption process as



Equilibrium adsorption for such a system was determined from the surface excess concentrations. The theory takes into account, in explicit terms, both the adsorbate-adsorbate and adsorbate-adsorbent interactions. The adsorption isotherm was given by

$$\gamma_m C_p K_m' = \frac{\theta \beta \gamma_{m,s}}{1 - \theta(1 - \beta)} \quad (2-12)$$

where $C_p = C_s / (C_s + C_{m,s})$ is the relative concentration of surfactant at equilibrium, $C_{m,s}$ is the concentration of water at equilibrium, K_m' is the equilibrium ratio expressed in the surface excess quantities, θ is the fractional coverage by the adsorbed monomer molecules, β is the ratio of molar volumes occupied by an adsorbed water molecule to an adsorbed monomer molecule, and $\gamma_{m,s}$ and γ_m are the activity coefficients of surfactant monomers in the adsorption phase and in the bulk phase, respectively.

Combining Equation (2-12) with the analogy of the Hill equation (Hill, 1946), Koganovskii *et al.* (1977) and Klimentko (1978a,b) demonstrated the effects of adsorbate-adsorbate and adsorbate-adsorbent interactions on the adsorption isotherms at low surfactant concentration for non-aggregated molecules. They showed that the adsorption of ethoxylated surfactants (below the c.m.c.) is a two-stage process. In the first stage, surfactant molecules are adsorbed by displacing the water molecules with molecules adsorbed flat on the surface. Beyond the saturation of a monolayer, a gradual re-

orientation of the adsorbed surfactant molecules may be involved to expose the active adsorption sites for subsequent adsorption.

Such changes in molecular orientation in an adsorption layer were first reported by Daniel (1951). He studied the adsorption process of several long-chain polar compounds on metal powders from hydrocarbon solutions, which resembles the use of additives in lubricating oils. All isotherms, obtained from the adsorption of octadecyl alcohol and ethyl stearate on silver, copper, nickel and iron, were found to consist of two distinguishable steps. By calculating the changes in areas occupied by the adsorbed molecules from one step to another, he suggested that these breaks in the isotherms corresponded to a transition of the molecular orientation from lying flat on the surface to being nearly perpendicular to the surface. This re-orientation phenomenon was later examined by Corkill and co-workers (1967) for the adsorption of alkylsulphinyl ethanols on graphon. During the initial stage of adsorption, they observed a linear increase of the integral heat of adsorption, ΔH , as a function of the surface coverage. This measured increase in ΔH is primarily due to the displacement of water molecules which leads to a breakdown of the water structure around the adsorbed layer; whereas, the enthalpy change resulting from the adsorption of individual surfactant molecules is considerably smaller. Upon the displacement of all water molecules from the surface (*i.e.*, saturation with an adsorbed monolayer), ΔH of the system decreased drastically, as reported by Corkill *et al.* (1967). Additional adsorption beyond this saturation (as indicated by the nearly constant ΔH) was therefore considered to be attributed to a change in the molecular orientation.

In addition to the re-orientation of surfactant molecules, Klimenko and co-workers (1974) suggested that, for the ethoxylated surfactants, the displacement of the alkyl chains from the surface may be accompanied by a small tilt of the strongly adsorbed ethylene oxide chains resulting in a densely packed structure. This minimum tilting angle of α was determined from the difference in the free energy of the adsorption of an alkyl chain and an ethylene oxide chain.

2.4.2 Formation of Surface Aggregates: Hemimicelles

As the surfactant concentration increases, there is a tendency for the hydrophobic moiety of the free and adsorbed molecules to aggregate on the surface. This concept was first proposed by Gaudin and Fuerstenau (1955b) in a study of quartz flotation. It was suggested that individual surfactant molecules are initially adsorbed as mentioned above, forming a monolayer of "half" micelles or hemimicelles. A hydrophilic surface is transformed to a hydrophobic surface having the molecules adsorbed vertically with the hydrocarbon tails exposed on the adsorbed surface. Rupprecht and Gu (1991) suggested that the first layer is mostly saturated within ± 20 percent of the maximum adsorbed amounts of non-aggregating species. Once the first layer is formed, a second adsorption layer with molecules of opposite orientation is then begun to complete the other layer of "half" micelles.

The onset concentration at which hemimicelles start forming at the solid-liquid interface is known as the critical hemimicelle concentration (h.m.c.). The h.m.c. can often be identified by an inflection point on the adsorption isotherm indicating the saturation of vertically oriented molecules on the surface (Corkill *et al.*, 1967). Beyond the h.m.c., adsorption occurs due to both the initial attraction forces and hemimicelle association, causing a sharp increase in the slope on the isotherm. When the adsorbed molecules in the first layer is equivalent to the number of surface sites, the contribution due to initial attraction forces disappears, and a further increase in adsorption will be due only to the association of hydrocarbons. A decrease in slope of the adsorption isotherm thus occurs (Somasundaran and Fuerstenau, 1966).

The surface aggregates, according to Gao *et al.* (1987) and Rupprecht and Gu (1991), are two- or three-dimensional, having an initially adsorbed surfactant molecule serving as an "anchor" or nucleus to attract free surfactant monomers from the bulk solution. These small, isolated aggregates consist of a number of monomers interacting with the adsorbed anchors, and are arranged in a spherical shape exhibiting minimum contact area between the aqueous medium and the hydrophobic parts (see Figure 2-9a). Counterions may also be attracted to the Stern layer formed by the surfactant head groups

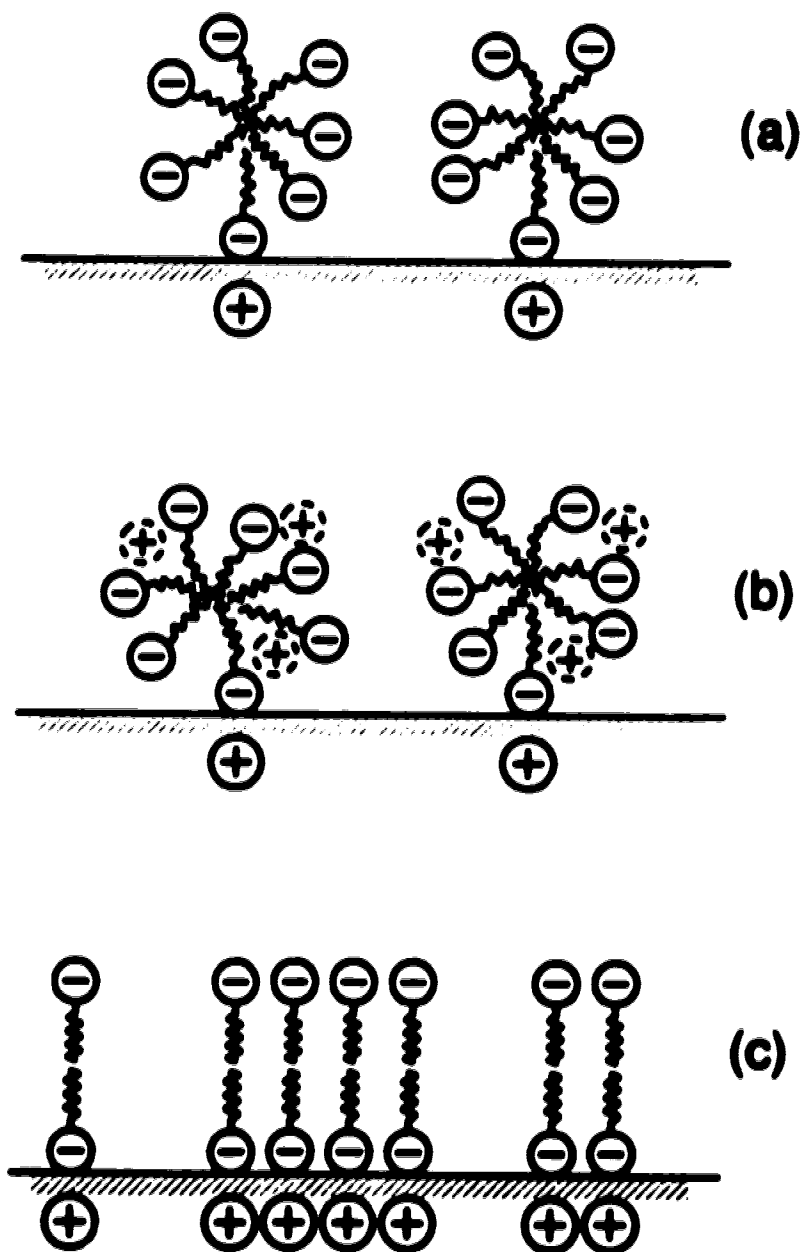


Figure 2-9. Structures of (a) surface aggregates, (b) aggregates incorporating counterions, and (c) bilayer.

of the surfactant aggregates (*see* Figure 2-9b), reducing the repulsion between the surfactant headgroups. The aggregation numbers are calculated from the ratio of the second adsorption plateau to the first plateau on the obtained adsorption isotherms. An increase in the total adsorption is accompanied by an equivalent increase in the aggregation number and an expansion of the volume of the surface aggregates. The surface aggregates become more closely packed and finally grow together forming a homogeneous bilayer on the surface (Rupprecht and Gu, 1991).

2.4.3 Formation of Surface Aggregates: Admicelles

The admicelle hypothesis maintains that surfactant aggregation producing a bilayer structure occurs on a given region of a heterogeneous surface at a critical solution concentration known as the critical admicelle concentration (c.a.c.), which is specified for an individual region (Harwell, 1983; Harwell *et al.*, 1985). The isotherms produced can be represented by discontinuous stepwise functions of the solution concentration or a continuous curve depending on the distribution of surface heterogeneities. For a homogeneous surface, an adsorption isotherm will consist of a low-concentration region in which the adsorption will increase slowly with concentration and a vertical step to complete bilayer coverage at the c.a.c., *see* Figure 2-10. The vertical steps are determined by the adsorption energy of the region on surface, and the horizontal portions represent the distribution of surface heterogeneities at a particular energy level.

The surface aggregates formed are two-dimensional and tend to be bilayered, like lipid membranes, as shown in Figure 2-9c (Scamhorn *et al.*, 1982). The admicelle structure is the upper limit of the adsorption values corresponding to densely packed double layers.

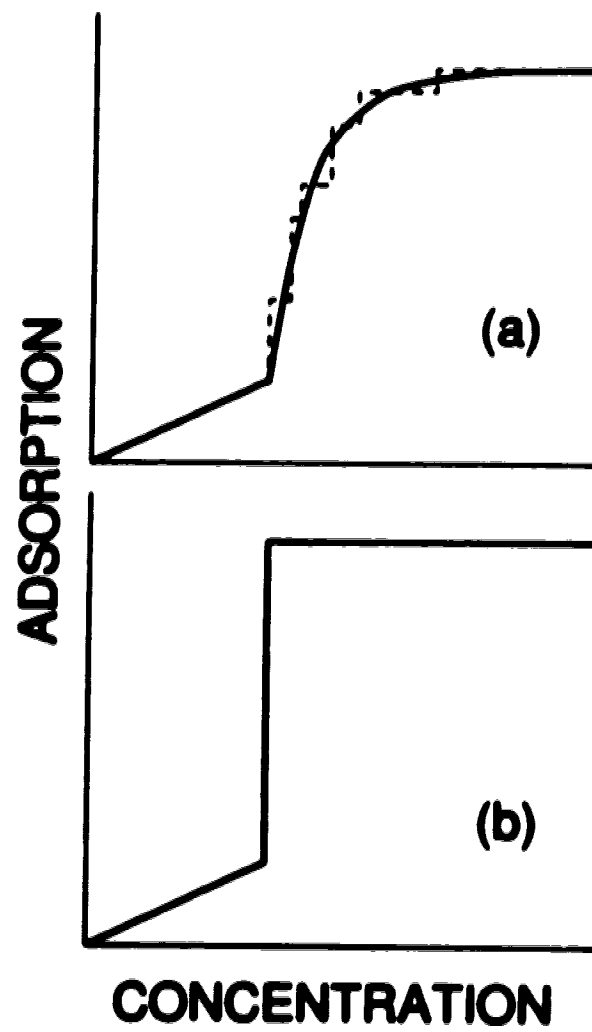
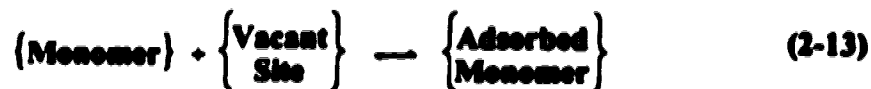


Figure 2-10. Adsorption isotherms with (a) heterogeneous and (b) homogeneous surfaces.

2.5 General Isotherm Equations of Two-Step Adsorption

A general isotherm equation for adsorption based on an empirical approach for the above two-step adsorption process has been derived by Zhu and Gu (1989, 1991). The stepped isotherm, in this case, is modelled as a Langmuir-sigmoid curve employing the concept of hemimicelle formation. The early stage describing the adsorption of individual surfactant monomers due to hydration of the surfactant molecules and surface attraction forces can be represented by an elementary and reversible mechanism:



The rate equation for the adsorption of surfactant monomers *per unit mass of solid* can then be expressed as

$$\frac{\partial \Gamma_m}{\partial t} = k_{a,m} C_b (Q_s^M - \Gamma_m) - k_{d,m} \Gamma_m \quad (2-14)$$

where $k_{a,m}$ and $k_{d,m}$ are the rate constants of adsorption and desorption for monomers, respectively, Γ_m is the amount of surfactant monomer adsorbed, C_b is the surfactant concentration in the bulk of the solution, Q_s^M is the maximum adsorption capacity for monolayer saturation on the solid surface such that the difference of $(Q_s^M - \Gamma_m)$ denotes the concentration of vacant adsorption sites. The adsorption isotherm (for adsorption not exceeding a monolayer and surfactant concentration of below the critical micelle concentration) can be represented by a plot of the amount of surfactant monomers adsorbed, $\Gamma_{m,e}$, against the bulk concentration, C_b , at equilibrium. The shape of the resulting isotherm can be described by

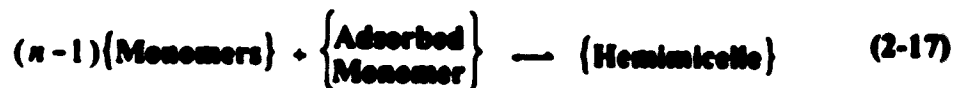
$$\frac{\Gamma_{m,e}}{Q_s^M} = \frac{K_m C_b}{1 + K_m C_b} \quad (2-15)$$

where K_m is the equilibrium ratio ($k_{a,m}/k_{d,m}$). From this expression, the amount of adsorption will initially increase with the bulk concentration; that is, for $C_b \rightarrow 0$, we have

$\Gamma_{m_1} \propto C_s$, which will then be followed by a gradual decrease and a plateau region as the concentration increases, that is, $\Gamma_{m_1} \rightarrow Q_s^M$ as $K_n C_s \gg 1$. The equilibrium ratio for the adsorption of monomer molecules, from Equations (2-15), may be rearranged to

$$K_n = \frac{\Gamma_{m_1}}{\Gamma_z C_s} \quad (2-16)$$

where Γ_z is the number of vacant sites. For the second stage, adsorption occurs as a result of surface aggregation forming hemimicelles (build-up of surfactant monomers on the monolayer due to sudden condensation from the bulk solution). Each adsorbed monomer acts as a nucleus of a hemimicelle with $(n-1)$ additional monomers where n is the aggregation number of the hemimicelle. This mechanism can be represented by



and the equilibrium ratio for hemimicellization becomes

$$K_{hm} = \frac{\Gamma_{hm_1}}{\Gamma_{m_1} C_s^{n-1}} \quad (2-18)$$

where Γ_{hm_1} is the amount of adsorbed hemimicelle. The total equilibrium adsorption, Γ_s , at a bulk concentration, C_s , and maximum adsorption capacity, Q_s , can be determined by material balance:

$$\begin{aligned} \Gamma_s &= \Gamma_{m_1} + n\Gamma_{hm_1} \\ Q_s &= n(\Gamma_z + \Gamma_{m_1} + \Gamma_{hm_1}) \\ \Gamma_z &= Q_s - \Gamma_s \end{aligned} \quad (2-19)$$

The general adsorption isotherm can be obtained upon combining Equations (2-16) through (2-19):

$$\frac{\Gamma_s}{Q_s} = \frac{K_n C_s / n + K_n K_{hm} C_s^n}{1 + K_n C_s + K_n K_{hm} C_s^n} \quad (2-20)$$

For $K_{hm} \rightarrow 0$ and $n \rightarrow 1$, Equation (2-20) reduces to Equation (2-16), the Langmuir isotherm (L2), such that $Q_s^M = Q_s/n$. If $K_n C_s \ll 1$ and $n > 1$, Equation (2-20) becomes

$$\frac{\Gamma_s}{Q_s} = \frac{K_n K_{hm} C_s^n}{1 + K_n K_{hm} C_s^n} \quad (2-21)$$

which is known as the one-step formation of hemimicelles (Zhu and Gu, 1989). In general, various shapes of the adsorption isotherms, such as Langmuir-type (L2), Sigmoid-type (S2) and two plateaux-type (L4), can be obtained in terms of the appropriate values of Q_s , K_n , K_{hm} and n . Accordingly, surface aggregation or hemimicelle formation occurs only if $n > 1$. The critical hemimicelle concentration, C_{hm} , can be determined using one of the following definitions (Zhu and Gu, 1989): (1) The h.m.c. is the concentration at which the straight line extended from the maximum $\partial\Gamma_s/\partial C_s$ on the isotherm intersects $\Gamma_s = 0$; and (2) the h.m.c. is the point at which $\partial^2\Gamma_s/\partial C_s^2 = 0$. An analytical expression derived from Equation (2-20), and based on definition (1), is given as

$$C_{hm} = \left(\frac{n-2}{n} \right)^{\frac{n}{n-1}} K_{hm}^{-\frac{1}{n-1}} \quad (2-22)$$

and based on definition (2), is given as

$$C_{hm} = \left[\frac{3(n-2) - \{3n(n-2)\}^{1/2}}{3n + \{3n(n-2)\}^{1/2}} \frac{1}{K_{hm}} \right]^{\frac{1}{n-1}} \quad (2-23)$$

Similarly, for the one-step formation of hemimicelles process, Equation (2-21), analytical expressions derived for definitions (1) and (2) are given by Equations (2-24) and (2-25), respectively, as follows:

$$C_{\text{ads}} = \left(\frac{n-1}{n+1} \right)^{\frac{n+1}{n}} (K_{\text{ads}} K_{\text{a}})^{-\frac{1}{n}} \quad (2-24)$$

and

$$C_{\text{ads}} = \left[\frac{3(n-1) - \{3(n^2-1)\}^{1/2}}{3(n+1) + \{3(n^2-1)\}^{1/2}} \frac{1}{K_{\text{ads}} K_{\text{a}}} \right]^{\frac{1}{n}} \quad (2-25)$$

2.6 Important Factors Affecting the Adsorption of Surfactants

Adsorption of surfactants at the solid-liquid interface is governed by a number of interactive forces, including electrostatic attraction, covalent bonding, hydrogen bonding between the surfactant molecules and interfacial species, van der Waals interactions among adsorbed species, and solvation or desolvation of adsorbate and adsorbent species (Somasundaran and Hanna, 1977). Depending on the specific surface area, mineralogical composition and surface charge density of the adsorbent, surfactant type and concentration, pH, temperature, and nature and concentration of the solvent, one or more interactive forces may play an important role in the adsorption process.

The effects of added electrolytes have been studied very extensively. The general trend reported is that adsorption increases linearly with increasing salinity (Hurd, 1976; Lawson, 1978; Somasundaran and Hanna, 1979; Friedmann, 1986), and such increases will continue up to a maximum value at which further increase in salinity results in the same maximum adsorption (Noll and Gell, 1991). Addition of electrolytes often results in an increase in adsorption because of a combined effect accounting for (1) the increase of surface acidity and the resultant ion-exchange capacity, and (2) decrease in the compression of the electrical double layer with increase in the ionic strength as well as salting out at higher ionic strengths (Somasundaran and Hanna, 1979; Figliore, 1982). While the effect of electrolytes on the adsorption of ionic surfactants is well documented,

very few similar studies have been conducted for the adsorption of non-ionic surfactants. Lawson (1978) found that the adsorption of non-ionic surfactants is relatively insensitive to the solution salinity.

Not all electrolyte additives affect the adsorption behaviour the same way as described above. In the presence of divalent and trivalent cations as well as certain univalent cations such as H^+ , anionic surfactant may be "salted in" by complexation (Figdore, 1982; Schott *et al.*, 1984). For example, an anionic surfactant such as RSO_3^- will form a cationic surfactant complex in the presence of the calcium ion, $Ca(RSO_3)^+$. Both of these species can adsorb on the surface of the clay, allowing the total adsorption to increase drastically. Similar complexation may also occur on the surface of Ca^{2+} clay (Glover *et al.*, 1979). Therefore, it is important to eliminate the effects of complexation or precipitation in order to conduct an accurate adsorption study.

Because of the pH-dependent nature of the clay surface as described in Equation (2-1), silicious rock and clays take on a negative charge as hydrogen atoms in the surface layer of the mineral react with the hydroxide ions in the solution. The negative charge repels the negatively charged (anionic) surfactants. Consequently, surfactant loss due to adsorption is reduced significantly under alkaline condition (Hill *et al.*, 1973; Hurd, 1976; Somasundaran and Hanna, 1979; Figdore, 1982; Nelson *et al.*, 1984; Labrid, 1989; Peru and Lorenz, 1990; French and Burchfield, 1990). The general trend is that adsorption of anionic surfactants will decrease as the surface charge becomes less positive due to increasing pH; and, above the p.z.c. of the surface the adsorption becomes immeasurably small. A similar effect has also been observed for systems of cationic surfactant on negatively charged surface with decreasing pH.

On the other hand, the pH of the solution will also critically influence the shape of the adsorption isotherm. Figdore (1982), in a study of the adsorption of anionic surfactants on kaolinite, noticed that even a small difference of pH in solutions at equilibrium (say from 4.2 to 5.2) for experiments conducted near the p.z.c. of the original surface (pH = 3-4) may result in an apparent adsorption maximum on the isotherm.

For the polyethoxylated surfactants, adsorption from aqueous solution is inversely dependent upon the extent of ethoxylation. Lawson (1978) examined the adsorption of a Triton series of surfactants on Berea sandstone, and reported a decrease in the adsorption plateau value as the number of ethylene oxide units increases. Trogus and co-workers (1976) suggested that such a decrease in the adsorption plateau is not due to an increase in molecular coverage for the lengthened ethylene oxide chain. Instead these results are interpreted as a result of increasing water solubility. Lawson (1978) also found an increase in the area of occupation per ethylene oxide group as the number of ethylene oxide units per molecule decreases; that is, a shorter chain of ethylene oxide gives rise to a closer packed monolayer. The interfacial characteristics of a polyethoxylated surfactant can therefore be controlled by varying its hydrophobic-hydrophilic balance; that is, producing various lengths of ethylene oxide chains on its hydrophobic portion.

The formation of surface aggregates also plays an important role in governing the adsorption characteristics. At high bulk concentrations, surfactant molecules are adsorbed by hydrophobic interactions. Surfactant molecules with longer hydrocarbon tails maintain a stronger tendency for aggregation, resulting in simultaneous adsorption of the first and second layers. On the other hand, a second adsorption layer formed by ionic surfactants gives rise to a charge reversal on the adsorbent surface. Thus, electrostatic repulsion forces are generated between the charged headgroups of adsorbed surfactant molecules and the surfactant ions in the solution. These repulsive forces oppose further adsorption. Eventually, the adsorption seems to be limited by the increasing repulsion between the charged headgroups.

Chapter 3

Experimental Procedures and Set-up for Static and Dynamic Adsorption Studies

3.1 Materials

Berea sandstone blocks with a nominal permeability of 400-500 mD were obtained from Cleveland Quarries, Ohio. Berea systems offer certain advantages in the study of adsorption mechanisms because of their relatively homogeneous mineral composition. The sandstone was not fired prior to use in order to preserve the natural state of the rock and to avoid chemical and mineral changes (Krumrine *et al.*, 1982; Ma and Narrow, 1991; Shaw *et al.*, 1991).

The anionic surfactant used was Neodol® 25-3S obtained from the Shell Chemical Company as a 58.3 wt.% active solution. This surfactant is the sodium salt of a C₁₂ - C₁₈ alcohol ethoxy sulphate with an average of three moles of ethylene oxide per mole of surfactant. Average molecular weight is approximately 440 g/mol (Hill and Thigpen, 1976; Pera and Lorenz, 1990). The critical micelle concentrations are 0.0005 and 0.0003 wt.% in 8 and 12 wt.% sodium chloride solutions, respectively, measured by A. Cameron of PRJ using the spinning drop method. The rheological properties of this surfactant were examined and are summarized in Appendix A.

Non-ionic surfactant, Triton X-100®, was purchased from J.T. Baker Inc., New Jersey. The surfactant was used as a 100% active agent as received. Triton X-100 is a polydisperse preparation of *p*-(1,1,3,3-tetramethylbutyl) phenoxy poly (oxyethylene glycol)

containing 8-10 ethylene oxide units per molecule (Robson and Dennis, 1977; Paradies, 1980). The surfactant has an average molecular weight of 680 g/mol with a narrow molecular distribution (Doscher *et al.*, 1951). The critical micelle concentration in water is 0.02 wt.% (Ray and Némethy, 1971; Nutt *et al.*, 1981) and that in 2.9 wt.% sodium chloride solution is 0.039 wt.% (Mukerjee and Mysels, 1971). The cloud points of this surfactant are 62 and 30 °C in water and 15 wt.% sodium chloride solution, respectively (Travalloni-Louvisse and González, 1988). In water, the solution viscosity is Newtonian and increases linearly with surfactant concentration up to about 5 mPa·s at 12 wt.%; a change in the shape of micelles from spherical to cylindrical occurs between 12 and 25.7 wt.%, which is followed by the formation of liquid crystals and exhibition of non-Newtonian behaviour at 38.2 wt.% (Pal, 1992).

A radioactive tracer, tritium in the form of tritiated water with an initial activity of 10 mci g⁻¹ or 2.29 × 10⁶ d.p.m., was obtained from Dupont Canada, Mississauga, Ontario.

The solution pH was adjusted using concentrated hydrochloric acid or sodium hydroxide pellets. All other chemicals were of reagent grade obtained from Fisher Scientific Company.

3.2 Analytical Methods

3.2.1 Analysis of Tracer Concentration

The tritium concentration was measured by liquid scintillation counting (LSC) on a Beckman LS-100C system with a ¹³⁷Cs external standard source. The instrument was initially calibrated with four quenched standards to determine the counting efficiencies with respect to different external source ratios (ESR). The counting time per sample was set at 20 minutes and the statistical precision was ± 0.2 % error. For a tritium concentration of 200 ppm, a standard deviation of less than 1.2 ppm (0.6 percent) can be obtained.

Tritium is an isotope of hydrogen ^3H containing one proton and two neutrons, and is available in forms of tritiated water, T_2O . This radionuclide releases its disintegration energy by emission of a beta particle (β -emitter). The amount of activity can be determined by detecting the number of disintegrations per minutes (d.p.m.) which is proportional to the tritium concentration in a sample. For the LSC method, the emitted beta particle excites the surrounding solvent molecules which subsequently collide with a fluor molecule contained in the liquid medium to produce a photon -- a light quantum. The total light quanta produced by a single beta particle emission is a scintillation.

In the current study, effluent samples from the core flood experiments were diluted by 1/50 times with a scintillation cocktail, INSTA-GEL[®] XF or HIONIC-FLUOR[™], prior to analysis. These cocktails were purchased from Packard Instrument Company, Downers Grove, Illinois. HIONIC-FLUOR was used for its high salinity and high alkalinity tolerance.

3.2.2 Analysis of Anionic Surfactant Concentration

The concentration of Neodol 25-3S was determined using the two-phase titration method (Reid *et al.*, 1967). This method utilizes the reaction between a cationic titrant, Hyamine, and a mixture of dimidium bromide (cationic) and disulphide blue VN (anionic) as an indicator in an aqueous-chloroform medium. Anions in the surfactant molecules were initially reacted with the cationic dye in the indicator forming a complex salt which is soluble in chloroform (pink in colour). During the titration, the surfactant-attached cationic dye was replaced by the added titrant (Hyamine). As a result, the chloroform layer was gradually discoloured. The end point of the titration was detected when an excess of Hyamine was added which reacts with the anionic dye in the indicator and forms blue-coloured salt in the chloroform.

Hyamine 1622 (0.004 M) titrant and dimidium bromide/disulphide blue indicator were purchased from BDH Chemicals Canada, Ltd. Hyamine was used as received. The

indicator was diluted to 1/25 with deionized water and acidified with 0.1 M sulphuric acid ($pH = 2$). Certified ACS grade chloroform was used.

3.2.3 Analysis of Non-ionic Surfactant Concentration

The concentration of Triton X-100 was determined by ultra-violet spectroscopy at 224 and 276 nm. Standard calibration curves at different sodium chloride concentrations (*i.e.*, different optical transmittance) were prepared according to Beer's law for surfactant concentrations in the range of 0.005 to 0.05 wt.%.

Analyses were performed on an HP 8452A Diode-Array Spectrophotometer using a Fisher Spectrosil cuvette (quartz, suitable for a range of wavelengths between 200-3500 nm with a path length of 10 mm). Figure 3-1 shows full spectral scans of 0.001-0.01 wt.% Triton X-100 in deionized water for wavelengths, $\lambda = 200-500$ nm. Two distinct absorbance peaks were observed such that $\lambda = 224$ nm can be used as an analytical wavelength for very low concentration (< 0.01 wt.%) and $\lambda = 276$ nm for moderate concentration (0.01-0.05 wt.%), *see* Figure 3-1. The relatively flat region of $\lambda = 320-500$ nm was selected as the reference absorbance to allow compensation for baseline shifts.

For solutions of higher surfactant concentrations (> 0.05 wt.%), a standard dilution procedure (with deionized water) was performed using a Hamilton MICROLAB[®] M Diluter/Dispenser unit prior to calibration and sample analysis.

The effects of added salt and solution pH on the analytical results were examined. Sample calibration curves are shown in Figures 3-2 and 3-3. Zero concentration for the calibrations was determined from a solution of the same sodium chloride concentration and pH , which was also used as a reference solution for subsequent analyses. From Figure 3-2, it was observed that the solution absorbance is less sensitive to the liquid medium using a lower wavelength of 224 nm for the measurements than using 276 nm. For the solutions of the same sodium chloride concentration as shown in Figure 3-3, the

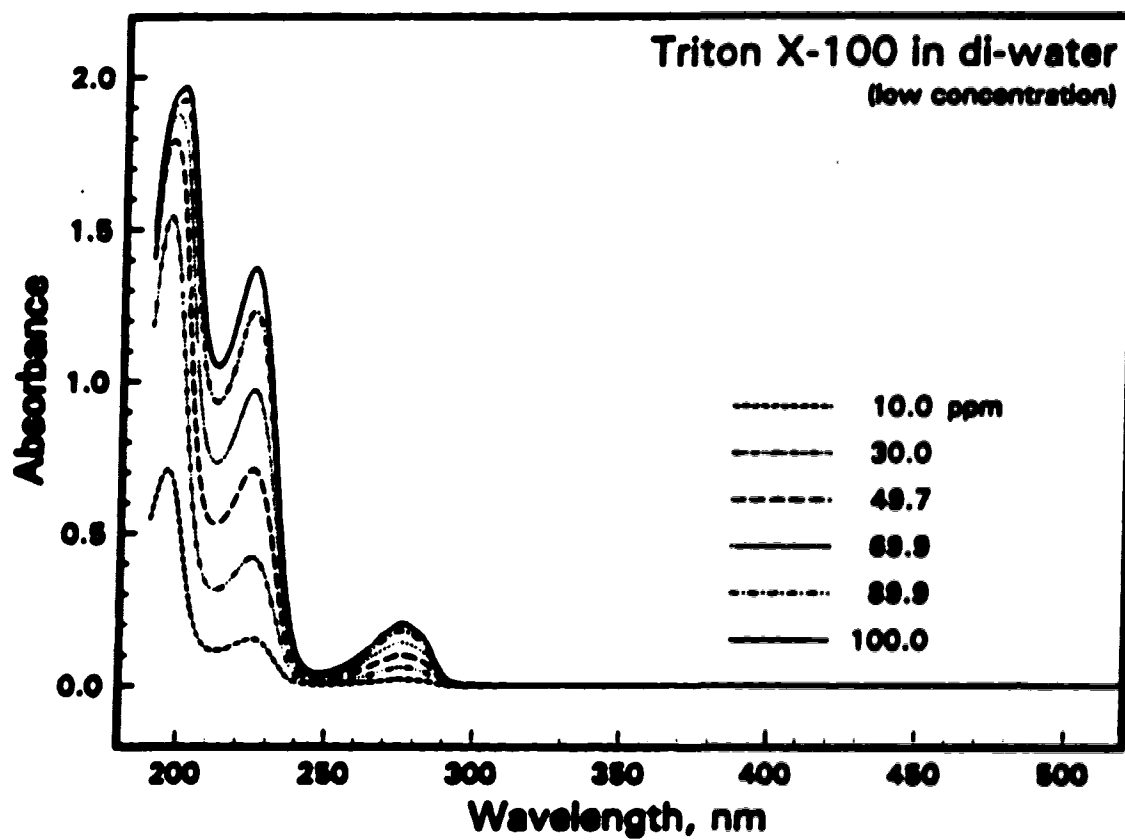


Figure 3-1. A full scan of the absorbance spectrum for dilute Triton X-100 solutions showing two absorbance peaks at $\lambda = 224$ and 276 nm.

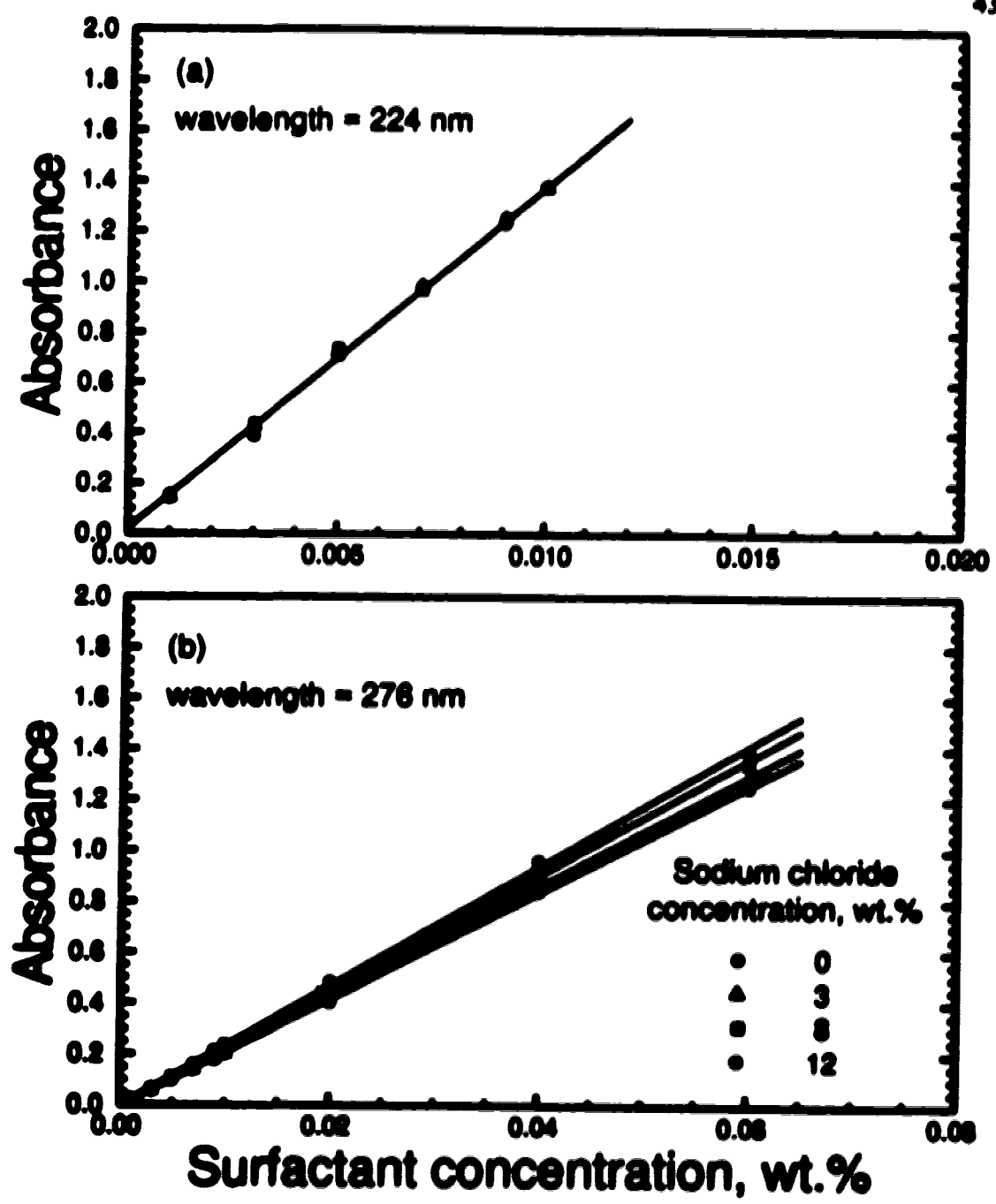


Figure 3-2. Effect of salt concentration on absorbance peak values at (a) 224 and (b) 276 nm.

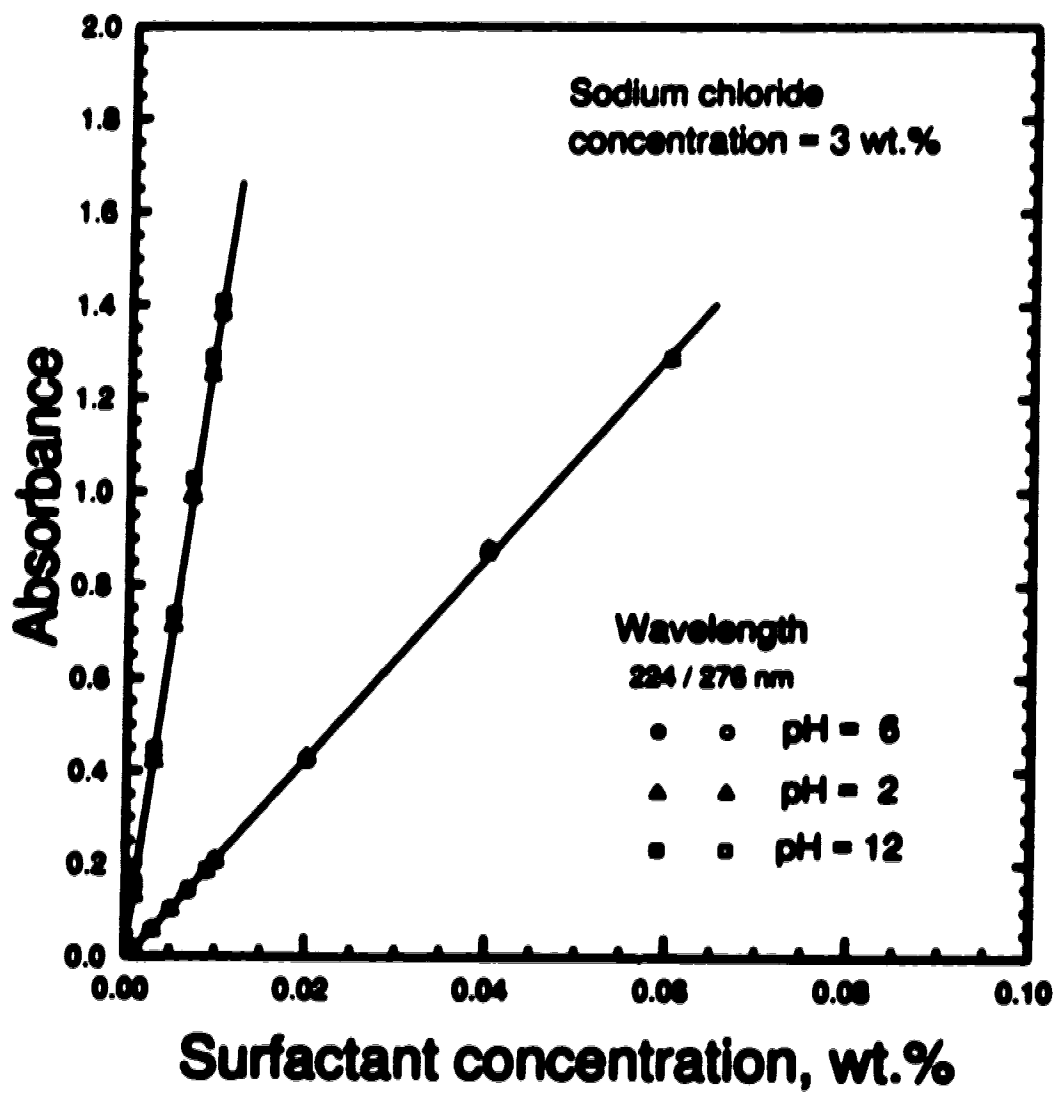


Figure 3-3. Effect of pH on absorbance peak values at 224 and 276 nm.

changes in solution pH show no effect on the measured absorbance at either wavelength. This is important to our analysis because a change in the solution pH is always observed after an aqueous solution was placed in contact with a sandstone sample (due to the dissolution of dolomite). Such insensitivity of the absorbance readings can ensure the solution pH is not a factor affecting the calculated changes in surfactant concentration.

3.3 Measurements of the Physical Properties in Solutions

Solution pH was measured on a Fisher Accumet® Selective Ion Analyzer Model 750 equipped with a combined electrode. The analyzer was calibrated for the pH range of interest to within 4 units using standard Fisher buffer solutions.

Density was measured on an Anton Paar DMA 46 densitometer with an oscillating glass tube at room temperature.

3.4 Geometric and Mineralogical Analyses of Berea Sandstone Samples

Table 3-1 summarizes the mineralogical composition as determined by X-ray diffraction (XRD) analyses. Compositions of the major clay minerals were 4 wt.% of kaolinite and 1 wt.% of illite. Fine particles of less than 2 μm in size were separated from the bulk of the solid samples, wet-mounted on a glass slide, and then dried before performing the XRD analysis.

The specific surface area of a consolidated, unfired Berea sandstone sample was 0.67 m^2/g and that of the disaggregated sample was in the range of 0.90 to 1.04 m^2/g measured by nitrogen adsorption using the BET method.

Scanning electron micrographic (SEM) analysis was performed on the whole and disaggregated sandstone samples, see Plates 1 and 2, to examine the cause for an increase in surface areas as a result of the disaggregation process. These SEM microphotographs

Table 3-1. Mineralogical analysis of Berea sandstone as determined by X-ray diffraction.

MINERAL	BULK (wt.%)	FINES, < 2 μm (wt.%)
Quartz	92	13
Kaolinite	4	43
Microcline	2	7
Illite	1	30
Dolomite	1	1
Chlorite	-	6

also show the typical geometric and mineralogical heterogeneity as well as the shapes and sizes of clay and mineral crystals. The microphotographs presented were made available to this study by R. French and S. Leggitt of the PRJ Geology group. For the whole rock sample, Plate 1 (A) at a low magnification shows the grains of quartz and feldspar (or microcline) cemented by quartz overgrowths, clays, and traces of dolomite. A higher magnification photomicrograph of these pore-lining and pore-filling cement minerals is shown in Plate 1 (B). An SEM photomicrograph of the disaggregated sample, Plate 2 (C), indicates that the quartz grains have not been sheared as a result of the disaggregation process. Several grains show the quartz overgrowth and cement minerals adhering to the detrital grain surface. Some of the cements, however, have been broken off from the grain surfaces and appear as a separate fraction of fine material. These broken cement minerals could result in a slightly increased specific surface area because the size and orientation of the material has changed. A cluster of kaolinite booklets between two grains is shown in Plate 2 (D) at a higher magnification. It is clear that this cluster is no longer a cement between the grains. Therefore, the crushing of kaolinite booklets during disaggregation could increase the surface area. Note that the measured increase in surface area in this study is less than that reported by Hurd (1976) and

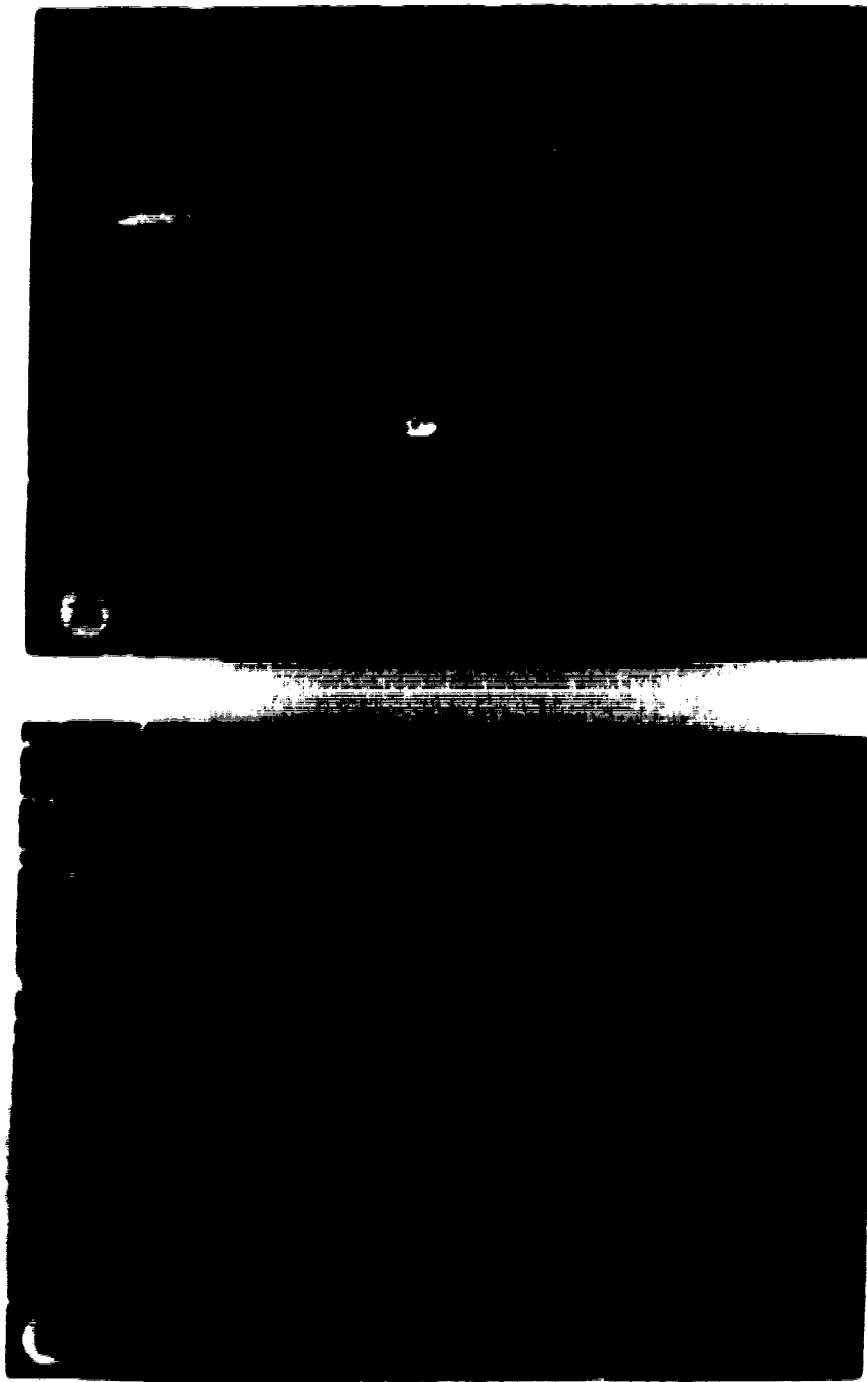


Plate 1.

Electron micrographs of Berea sandstone samples:
(A) Low magnification SEM of the whole rock
sample, 100 \times ; (B) Higher magnification of the same
sample showing pore-lining and pore-filling cement
minerals, 500 \times .



Plate 2.

Electron micrographs of Berea sandstone samples:
(C) Low magnification SEM of the disaggregated sample, 100 \times ; (D) Higher magnification of the sample showing a cluster of kaolinitic booklets between grains, 500 \times .

Lawson and Dilgren (1976). These authors observed a doubling in the specific surface area as a result of crushing or disaggregation of consolidated Berea sandstone samples.

3.5 Static Adsorption Experiments

Small pieces of sandstone were crushed or disaggregated gently using a mortar to break the cementation. Damage to the grain surface was insignificant as shown by SEM analysis. These disaggregated sandstone particles were rinsed with 12 wt.% sodium chloride solution to ion-exchange the multivalent ions such as calcium and magnesium with sodium ions. This is similar to the procedure followed in the dynamic tests (see 3.6). The particles were then washed thoroughly with 0.1 wt.% sodium chloride, and dried in an oven.

Predetermined amounts of disaggregated sandstone particles and a surfactant solution of known concentration were introduced into a vial. The solid and liquid mixture was allowed to equilibrate for a period of 7-10 days at room temperature with intermittent mixing. The supernatant was then extracted from the vial, and centrifuged to separate the fine suspended particles. Surfactant uptake due to adsorption was calculated using the surfactant concentrations measured before and after contact with the particles. Equilibrium isotherms were determined at sodium chloride concentrations of 0, 3, 8 and 12 wt.%.

3.6 Dynamic Tests

3.6.1 Experimental Set-up

A schematic diagram of the experimental set-up is shown in Figure 3-4. It consisted of a core holder, an Isco LC-500 syringe pump, chemical reservoirs, and a 0.5-micron in-line filter. A light mineral oil was used as a transferring fluid to prevent

corrosion of the pump. The pressure drop across the core was monitored to determine the permeability to brine, and to detect possible plugging due to fines migration in the core.

The cylindrical sandstone cores were 88.4 mm in diameter and 35.0 mm in height with an injection wellbore of approximately 3.5 mm in diameter drilled through the centre. An injection tube, 0.18 cm I.D. aluminum tube pierced on four sides, was inserted to provide uniform linear velocity along the injection wellbore. The sandstone core was mounted in the core holder as illustrated in Figure 3-5. The faces of the core were sealed with pressurized rubber gaskets. An overburden pressure of 3,000 kPa was applied to prevent channelling across the top and bottom of the core. Effluent fluid from the core was first collected in the annulus between the core and the core holder, and exited through the spigots. A new core was used for each run.

3.6.2 Procedure

Prior to commencing a run, the core was mounted and evacuated to 0.67 Pa ($\approx 5 \mu\text{m Hg}$ vacuum) for at least five hours. The pore volume was determined by imbibing brine to saturation. The calculated pore volume (PV) was $48.5 \pm 0.7 \text{ cm}^3$, which corresponds to an average porosity of 0.226. The core was then preflushed with brine of the same salinity as that of the surfactant solution. This was done to allow ion-exchange between sodium ions in solution and calcium and magnesium ions in the clay minerals and to ensure sodium form at most of the adsorption/exchange sites (Pers and Lorenz, 1990). Brine permeability was determined from the pressure drop measurements at a flow rate of 20 mL/h using Darcy's equation for radial geometry. The calculated brine permeability varied from 150 to 450 mD. No permeability damage due to fines migration was observed at injection flow rates up to 120 mL/h. However, significant permeability damage occurred at flow rates greater than 60 mL/h when the injected solutions were not thoroughly filtered.

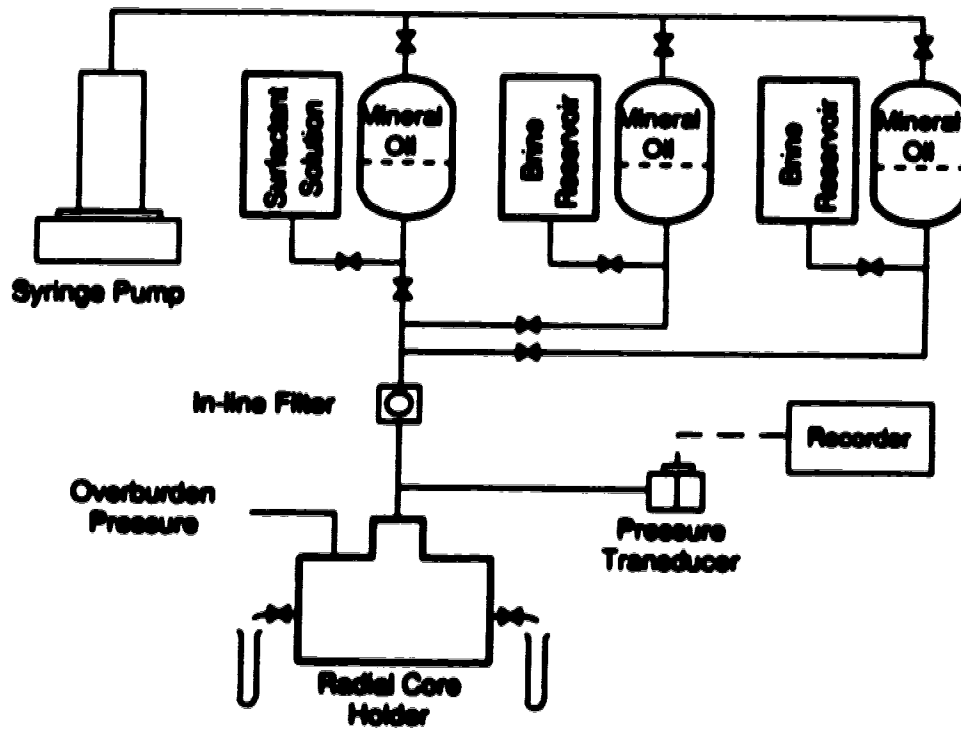


Figure 3-4. Experimental set-up.

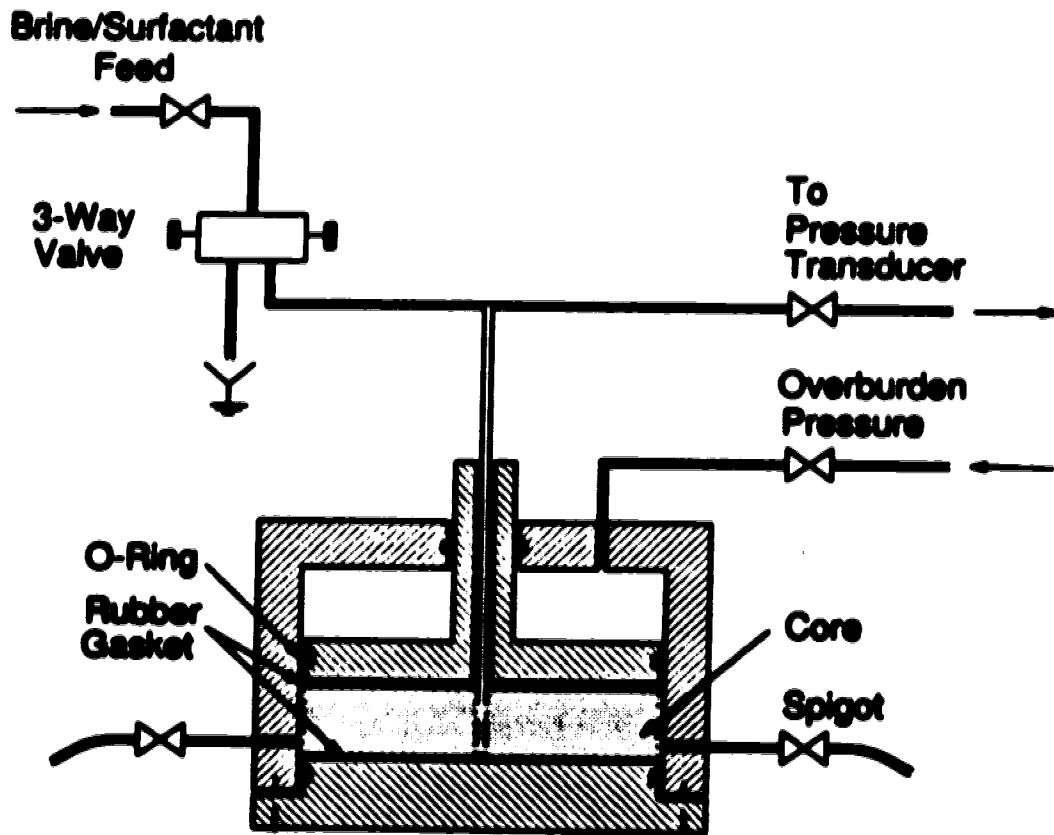


Figure 3-6. Schematic diagram of the radial core holder.

All sodium chloride solutions were prepared using boiled, deionized water, and filtered several times through 0.22 μm filter papers. A surfactant slug was then prepared by adding a pre-determined amount of surfactant and 0.02 wt.% tritium as a tracer. All fluids were injected at constant flow rates during each run. Effluent samples were collected in approximately 0.1 pore volume (PV) intervals. Experiment runs were conducted at room temperature.

Chapter 4

Propagation and Adsorption of NEODOL 25-3S (Anionic Surfactant) .

The adsorption of anionic surfactants on the surfaces of clay minerals is governed by "chemical" (*i.e.*, dispersive, hydrophobic) and electrical interactions (Hough and Rendall, 1983). The chemical forces correspond to the contributions of chain-chain interactions between the hydrophobic moieties of the adsorbed ions, chain-surface interactions due to hydrophobic bonding and van der Waals dispersive forces, and headgroup-surface interactions particularly due to the hydrogen bonding to the surface. Electrical forces can be subdivided into two major contributions: electrostatic and dipolar interactions. The dipole term accounts for the effects of desorption of water molecules occurring during the exchange of the surfactant ion from the bulk phase to the surface.

Somasundaran and Hanna (1977) show that higher adsorption of anionic surfactants occurs on sandstone with increasing salinity. This increase is caused by an increase in the surface acidity and the compression of the electrical double layer which reduces the electrostatic repulsion between the surfactant monomers and the surface of the clay minerals. Reduction of surfactant adsorption, on the other hand, can be attained in alkaline conditions due to an increase in repulsive forces between the surface and the ionic headgroup of the surfactant (Hill *et al.*, 1973; Hurd, 1976; Somasundaran and Hanna, 1979; Figdore, 1982; Nelson *et al.*, 1984; Labrid, 1989; Peru and Lorenz, 1990; French and Burchfield, 1990).

* A version of this chapter has been published. W. Eweh, E.A. Nass-El-Din and R.E. Mayes, 1993. *Journal of Canadian Petroleum Technology*, Vol.32, pp.39-48.

The mechanisms giving rise to the effects on adsorption as mentioned above have been discussed earlier. In this chapter, results from a detailed experimental study on the propagation and adsorption of an anionic surfactant in unfired Berea sandstone cores of radial geometry are presented. The primary objectives are (1) to study the effects of sodium chloride concentration, pH, surfactant concentration and flow rate on surfactant adsorption; and (2) to investigate the propagation of surfactant solutions having a liquid crystal phase in radial cores.

4.1 Static Adsorption Isotherms

4.1.1 Liquid-to-Solid Ratios

Previous static adsorption tests have been conducted over a wide range of liquid/solid weight ratios, e.g., 1.0 (Peru and Lorenz, 1990), 1.25 (Lawson, 1978), 10 (Figdore, 1982) and 50 (Somasundaran and Fuerstenau, 1966). It is of interest to examine the effect of this ratio on the static adsorption isotherms. Figure 4-1 shows the amount of surfactant adsorbed as a function of equilibrium surfactant concentration at a sodium chloride concentration of 3 wt.% using liquid/solid weight ratios of 0.5, 1.0, 2.1 and 4.0. Lower adsorbed surfactant values were obtained using liquid/solid weight ratios of 0.5 and 1.0. This is because at such low liquid/solid ratios, the particles were not fully wetted by the liquid. Higher adsorbed surfactant values were obtained at a liquid/solid weight ratio of 2.1 where all the particles were wetted by the surfactant solution. Increasing the liquid/solid ratio from 2.1 to 4.0 did not change the adsorbed surfactant values significantly. As a result, a liquid/solid ratio of nearly 2 was used in the present study.

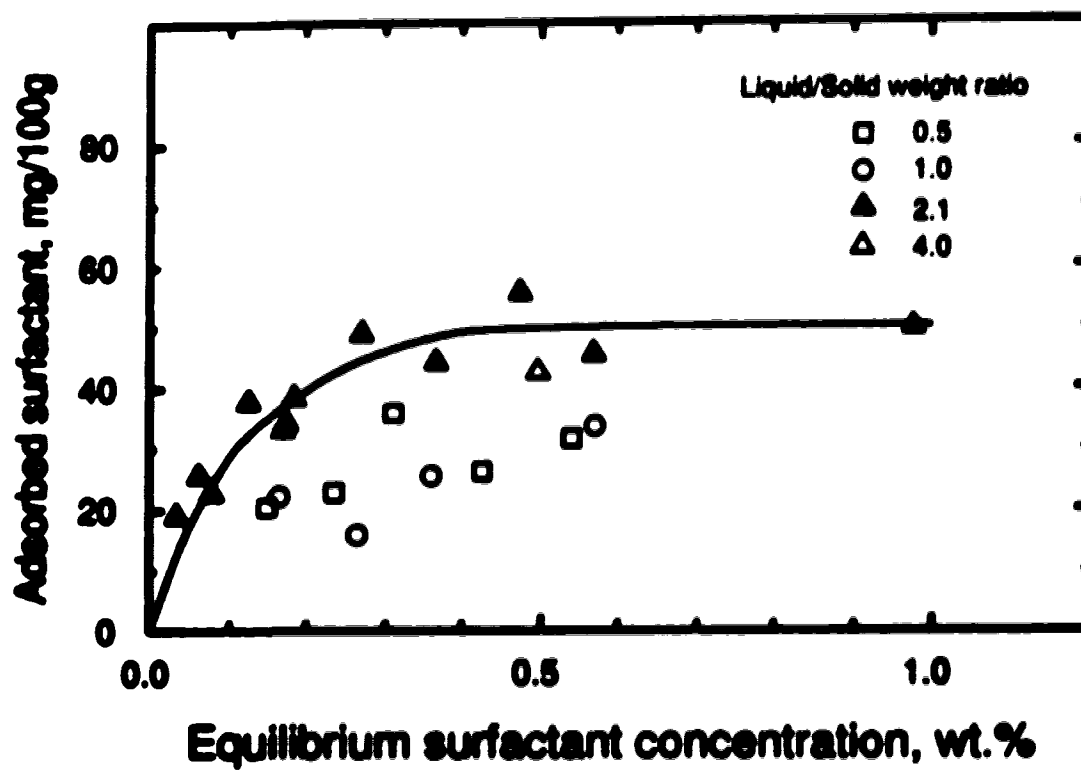


Figure 4-1. Static adsorption isotherm of Nocol 25-38 as a function of solid-to-liquid ratio at a sodium chloride concentration of 3 wt. %.

4.1.2 Effect of Salinity

The static adsorption isotherms of Neodol 25-3S at various sodium chloride concentrations are shown in Figure 4-2. At a given sodium chloride concentration, the amount of surfactant adsorbed increased with the surfactant concentration and gradually reached a constant or a plateau value. The solid lines shown in Figure 4-2 represent the fitted isotherms based on the Langmuir adsorption equation, defined as (Langmuir, 1918):

$$\Gamma_s = \frac{Q_s K C_s}{1 + K C_s} \quad (4-1)$$

where Q_s is the maximum adsorptive capacity of the system, K is the equilibrium ratio for adsorption, Γ_s is the amount of adsorbed surfactant and C_s is the equilibrium surfactant concentration in the bulk solution. Over the range of surfactant and sodium chloride concentrations examined, the experimental data can be fitted with the Langmuir adsorption isotherm. Table 4-1 summarizes the values of the two fitted constants as a function of sodium chloride concentration.

Very little, if any, adsorption of Neodol 25-3S from water onto the Berea sandstone was obtained. This surfactant has a relatively large water solubility and is expected to exhibit a small degree of adsorption in aqueous solution. There is however a tendency for this surfactant to precipitate and/or adsorb onto the surface in the presence of salt. This increase in the amount of surfactant adsorption with sodium chloride concentration is due to several factors. First, an increase in the sodium ion concentration reduces the repulsive forces between the anionic surfactant monomers and the negatively charged clay minerals, and compresses the electrical double layer near the charged surface. The solvation power for the surfactant is also reduced at high sodium chloride concentration which may drive the surfactant molecules to the solid-liquid interface. Another factor is that an increase in sodium chloride concentration may decrease headgroup-headgroup repulsion in the adsorbed layer, thereby increasing surfactant adsorption (Rupprecht and Gu, 1991).

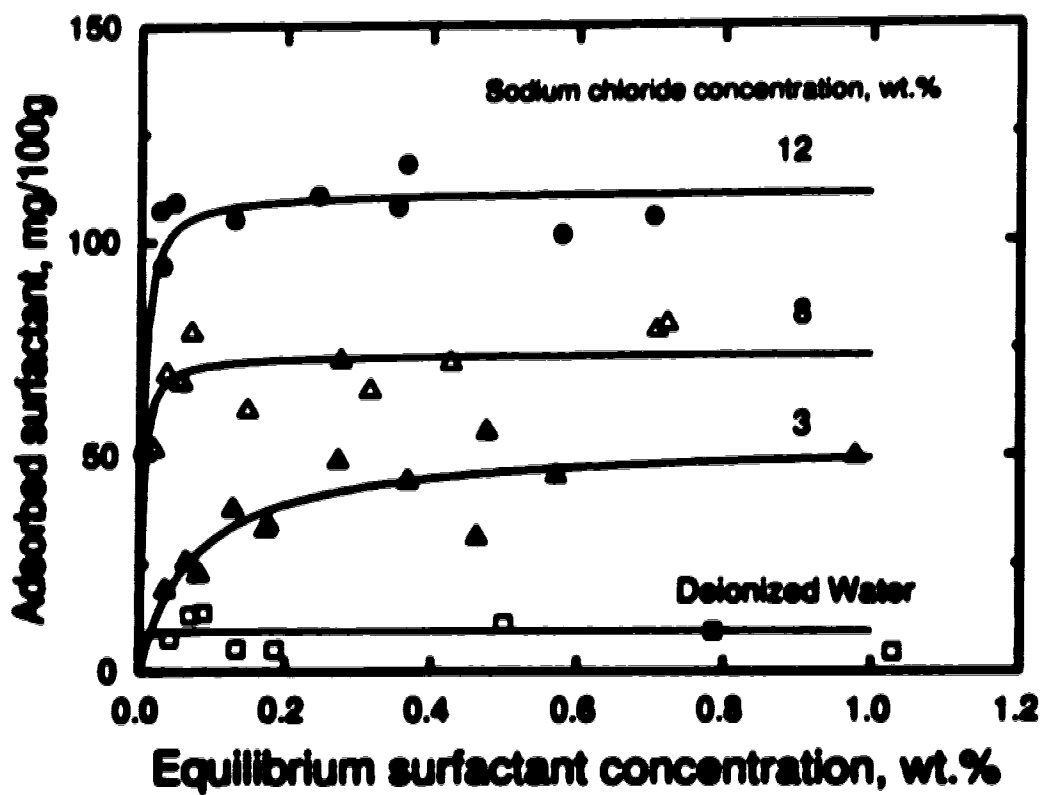


Figure 4-2. Static adsorption isotherm of Neodol 25-38 on disaggregated Berea sandstone as a function of sodium chloride concentration.

Table 4-1. Effect of sodium chloride concentration on Langmuir isotherm parameters.

Sodium Chloride Concentration (wt.%)	Equilibrium Ratio, K ⁽¹⁾ (g/g)	Maximum Adsorption Capacity, Q_0 ⁽²⁾ (mg/100g_a)
0	9.388×10^3	11.65
3	1.766×10^3	47.87
8	1.515×10^4	74.58
12	1.086×10^3	108.60

⁽¹⁾ unit = grams of solution per gram of surfactant adsorbed, g/g

⁽²⁾ unit = milligrams of surfactant adsorbed per 100 grams of rock, mg/100g_a

The surfactant concentration at which the transition to a constant adsorption value occurs shifted to a lower value with increasing sodium chloride concentration. This behaviour is typical for anionic surfactants and is due to the reduction in the critical micelle concentration with increasing sodium chloride concentration (*see for example, Walker et al., 1979*). The maximum adsorption increased linearly with increasing sodium chloride concentration. Good agreement was obtained between the maximum adsorption values obtained in the present study and those obtained by Lawson (1978).

4.2 Dynamic Tests

To avoid experimental complications from possible precipitation of the surfactant by divalent cations, sodium chloride brines were used throughout this study. Also, 5 PV of brine (sodium chloride) was injected prior to the injection of the surfactant slug. The experimental conditions and results are summarized in Table 4-2.

Table 4-2. Summary of dynamic tests. ⁽¹⁾

Sodium Chloride Concentration (wt.%)	Surfactant Concentration (wt.%)	Viscosity (mPa s)	Surfactant Injected (g)	Loss of Surfactant	
				End of Surfactant Injection (mg/100g)	End of Chase Brine Injection (mg/100g)
3	0.19	1.0	0.29	17.4	15.4
3	0.46	0.93	0.72	18.1	16.8
3	0.91	1.05	1.47	28.5	26.6
8	0.21	1.0	0.34	38.0	41.5
8	0.45	2.1	0.71	40.5	48.3
8	0.99	5.05	1.60	43.9	50.1
12	0.17	1.80	0.27	38.9	55.6
12	0.49	27.47	0.78	49.8	61.9
12	1.06	178.4	1.70	49.7	81.0
12	1.85	499.1	2.44	53.9	100.3
⁽²⁾ 8	0.49	1.15	0.74	39.7	37.0
⁽³⁾ 8	0.52	1.0	0.85	29.3	34.4
⁽⁴⁾ 8	0.47	1.08	0.73	35.4	32.6
⁽⁵⁾ 8	0.45	1.0	0.71	35.8	46.7

⁽¹⁾ All experiments (except notes 4 and 5) were conducted at a flow rate of 20 mL/h.

⁽²⁾ Solution pH of the injected surfactant slug, pH_i = 2.43.

⁽³⁾ Solution pH of the injected surfactant slug, pH_i = 12.53.

⁽⁴⁾ Injection flow rate, $Q = 5$ mL/h.

⁽⁵⁾ Injection flow rate, $Q = 120$ mL/h.

4.2.1 Effect of Salinity

The effect of sodium chloride concentration on the static adsorption isotherm of Neodol 25-3S was significant as shown in Figure 4-2. It is of interest to examine its effect on surfactant propagation and adsorption under dynamic conditions. Figure 4-3 shows the effluent concentration profiles of the tracer and surfactant expressed in a normalized form, C/C_0 , where C is the concentration of tracer or surfactant in the core effluent and C_0 is its concentration in the injected surfactant slug. The size of the surfactant slug was approximately 3 PV and contained 0.45 wt.% surfactant and 8 wt.% sodium chloride. The injection flow rate was 20 mL/h which corresponds to a linear Darcy velocity of 1.25 m/d at the core inlet ($r_i = 1.75$ mm) and 0.05 m/d at the core exit ($r_e = 44.2$ mm). The surfactant slug was displaced by 5 PV of a brine solution having the same sodium chloride concentration (constant salinity drive). Subsequently, this brine was displaced using brines of 5, 1 and 0.1 wt.% sodium chloride (negative salinity gradient drive). Two pore volumes of each sodium chloride solution were injected.

The concentration of the tracer in the effluent reached the injection level, that is, $C/C_0 = 1.0$, after nearly 1.7 PV of the surfactant slug was injected, then remained constant. Also, after the injection of 1 PV of the surfactant slug, the effluent C/C_0 of the tracer was nearly 0.5. This value is similar to that expected for the propagation of tracers in linear cores as a result of dispersion and advection. Comparing the tracer and surfactant profiles, a delay in surfactant breakthrough was observed. Throughout the injection of the surfactant slug, C/C_0 of the surfactant was lower than that of the tracer, indicating surfactant loss due to adsorption. Upon injection of the chase brine of the same sodium chloride concentration, the normalized surfactant and tracer profiles dropped significantly after the injection of nearly 0.7 PV and reached zero after the injection of 2 PV. At the end of the chase brine, 29 percent of the injected surfactant was retained in the core as determined from material balance. By decreasing the sodium chloride concentration in the injected brine to 5 wt.%, a surfactant bank indicating partial recovery of the adsorbed surfactant was obtained. A similar surfactant bank with a higher peak

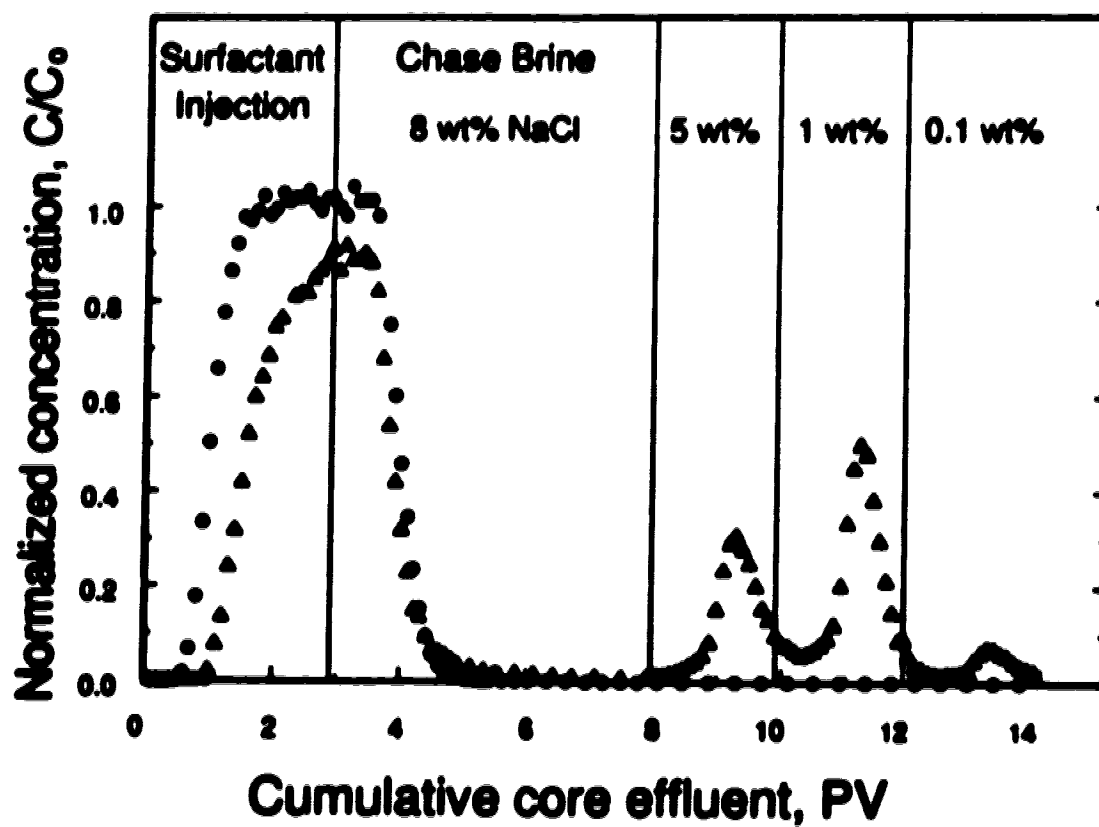


Figure 4-3. Propagation of surfactant slug containing 0.45 wt.% Nocol 25-38 and 8 wt.% sodium chloride at 20 mL/h followed by negative salinity gradient drives.

was observed when 1 wt.% sodium chloride brine was injected. A small but significant amount of surfactant was recovered when 0.1 wt.% sodium chloride was injected.

The most interesting observation in Figure 4-3 is that a negative salinity gradient recovers more surfactant than a constant salinity drive. If the surfactant slug is followed by a brine of constant salinity, the maximum concentration as measured would be 32 ppm. At this concentration, 130 PV of brine would be required to desorb all the surfactant. Hurd (1976) suggested that adsorbed surfactant can be effectively desorbed by a fresh water drive; this procedure, however, is not recommended. Severe damage to the sandstone cores causing an abrupt drop in permeability can result (Mungan, 1965).

In EOR, this negative salinity gradient has also been found beneficial when anionic surfactants are used as flooding agents, for example, in micellar/polymer (Friedmann, 1986), alkali/surfactant (Nelson *et al.*, 1984), or alkali/surfactant/polymer (Nasr-El-Din and Hawkins, 1991) flooding processes.

Figures 4-4a to 4-4c show the effluent profiles for surfactant solutions containing about 0.2 wt.% Neodol 25-3S and sodium chloride concentrations of 3, 8, and 12 wt.%, respectively. All surfactant slugs were injected at 20 mL/h for three pore volumes. The tracer profiles of the three runs were almost identical which indicated similar dispersion characteristics in the individual cores. Therefore, differences in the effluent surfactant profiles are due to changes in salinity only. The effect of sodium chloride concentration on the surfactant profile was dramatic. At a sodium chloride concentration of 3 wt.%, Figure 4-4a shows that the surfactant breakthrough occurred after the injection of 1.1 PV of the surfactant slug. The normalized surfactant concentration, C/C_0 , reached nearly 0.92 at the end of the surfactant slug. The normalized surfactant profile dropped significantly after the injection of nearly 0.7 PV of the chase brine and showed tailing. This tailing could be due to slow desorption of the adsorbed surfactant.

At a sodium chloride concentration of 8 wt.%, Figure 4-4b shows that surfactant breakthrough occurred after the tracer (1.65 PV after the injection of the surfactant slug). The surfactant normalized concentration reached 0.7 at the end of the surfactant slug and showed tailing during the chase brine flood.

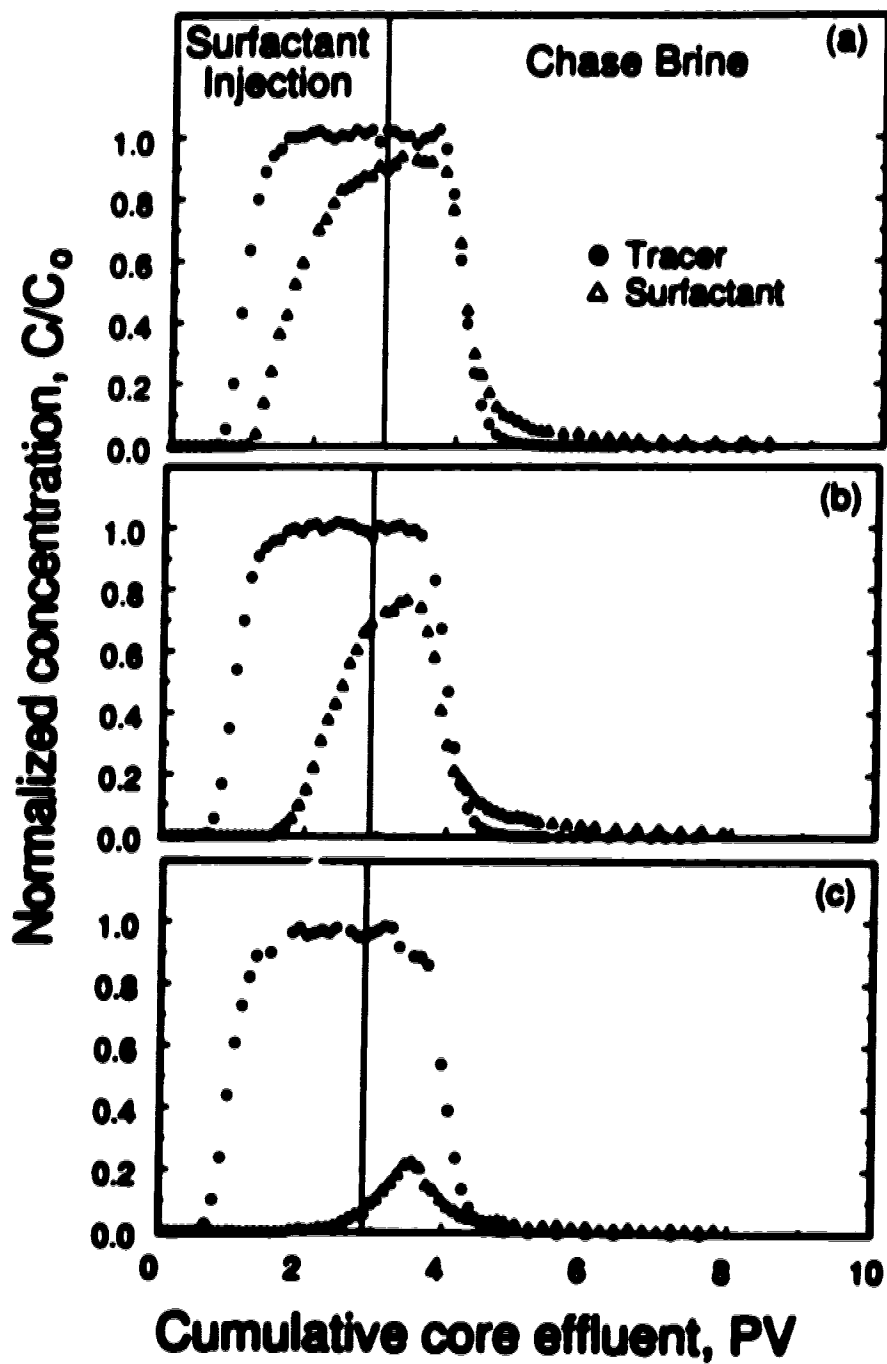


Figure 4-4. Propagation of surfactant slugs containing about 0.2 wt.% Nocol 25-35 and (a) 3, (b) 8 and (c) 12 wt.% sodium chloride at 20 mL/h.

At a sodium chloride concentration of 12 wt.%, Figure 4-4c shows that most of the injected surfactant was retained in the core. Surfactant breakthrough occurred after the injection of 2.4 PV of the surfactant slug. The value of C/C_0 of the surfactant at the end of the surfactant slug was 0.07 only, and it reached its maximum value during the chase brine flood. The effect of salinity shown in Figures 4-4a to 4-4c is similar to that obtained from the static adsorption tests (see Figure 4-2).

Viscosity measurements of surfactant solutions (in Appendix A) showed significant increase at higher surfactant concentrations over a narrow range of sodium chloride concentrations. It is of interest to examine the effect of such an increase in viscosity on surfactant propagation. Figures 4-5a and 4-5b depict the tracer and surfactant normalized profiles for two surfactant slugs containing nearly 1.0 wt.% Noodol 25-3S and sodium chloride concentrations of 3 and 12 wt.%, respectively. According to the results shown in Figure A-4, the low-shear Newtonian viscosity, μ_n , was 1.5 mPa·s for the former slug and 180 mPa·s for the latter. The viscosity of the surfactant slug was high at the higher sodium chloride concentration due to the formation of surfactant aggregates as explained in Appendix A. Increasing the sodium chloride concentration from 3 to 12 wt.% resulted in an increase in the area between the tracer and the surfactant profiles during the injection of the surfactant slug; that is, increasing surfactant loss. This trend is similar to that observed at the lower surfactant concentration as shown in Figures 4-4a to 4-4c. However, the increase in surfactant loss with sodium chloride concentration was less evident at the higher surfactant concentration. The effect of sodium chloride on surfactant propagation was more dramatic during the chase brine flood. First, C/C_0 for the tracer and surfactant sharply dropped upon the injection of the chase brine. Second, both profiles showed prolonged tailing. Third, the normalized surfactant concentration was lower than the tracer during most of the chase brine flood.

The effects of sodium chloride concentration on the tracer and surfactant profiles shown in Figures 4-5a and 4-5b will also affect the amount of surfactant retained in the core. At the lower sodium chloride concentration, where no viscosity changes occurred, surfactant loss at the end of injecting the surfactant slug was 28.5 mg/100 g_n and it dropped to 26.6 mg/100 g_n at the end of the chase brine flood. This slight drop was due

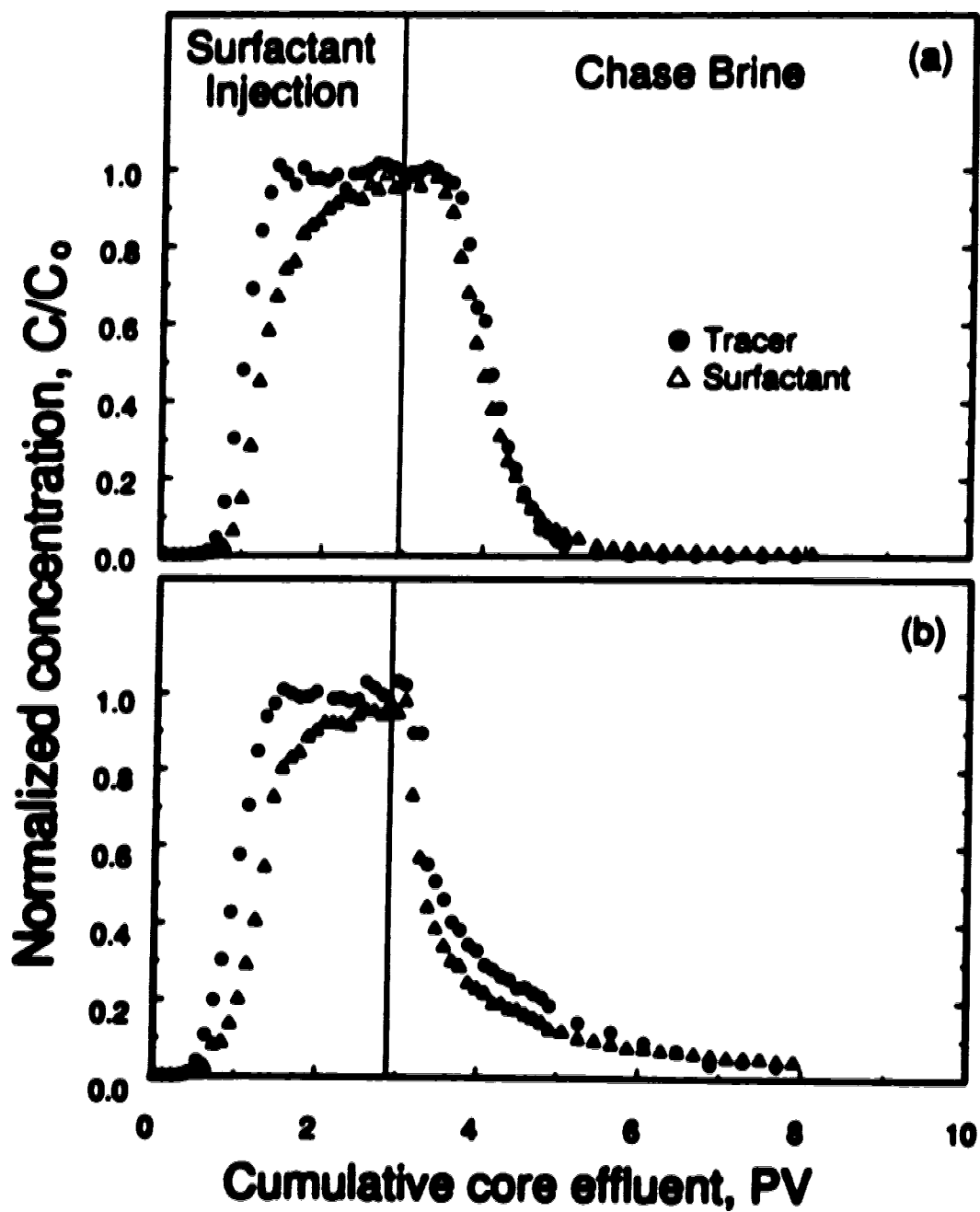


Figure 4-5. Propagation of surfactant slugs containing about 1 wt.% Neodol 25-3S and (a) 3 and (b) 12 wt.% sodium chloride at 20 mL/h.

to surfactant desorption during the chase brine flood. At the higher sodium chloride concentration, where significant viscosity changes occurred, surfactant retention at the end of injecting the surfactant slug was 49.7 mg/100 g_a. In this case, the adsorption process continued during the chase brine flood. The total surfactant loss increased dramatically to 81 mg/100 g_a at the end of the experiment.

The higher surfactant solution viscosity obtained at the higher sodium chloride concentration affected the tracer and surfactant profiles during the chase brine injection. Due to the unfavourable mobility ratio, the chase brine fingered through the surfactant solution and caused early breakthrough of the chase brine. Consequently, the tracer and surfactant profiles dropped earlier with the higher viscosity slug. The development of viscous fingers also caused a slower rate of change of the concentration of both chemical species in the effluent, that is, tailing. These changes in the surfactant profile were the reasons for the higher surfactant retention observed at the end of the chase brine flood for the surfactant slug having the higher sodium chloride concentration.

To confirm these findings, another experiment was conducted. The surfactant concentration in the slug was increased to 1.85 wt.% whereas the sodium chloride concentration was kept constant at 12 wt.%. The low-shear Newtonian viscosity of this slug was 500 mPa·s as shown in Figure A-4. Figure 4-6 shows the tracer and surfactant profiles for this experiment. The increasing portion of the tracer profile was similar to that observed for surfactant slugs having low viscosity (e.g., Figure 4-5a). However, the tracer and surfactant profiles showed distinct differences during the chase brine flood. The tracer and the surfactant profiles dropped almost instantaneously upon the injection of the chase brine. Both profiles showed tailing for a very long period of time. The surfactant profile was lower than the tracer except towards the end of the chase brine flood where the two profiles were identical. These trends confirm those observed in Figure 4-5b and are due to the interfacial instability (viscous fingering) between the surfactant slug (high viscosity) and the chase brine (low viscosity).

The viscosity of the surfactant solution will also affect the pressure drop across the core. Figure 4-7 shows the pressure drop across the core as a function of the cumulative core effluent for various floods conducted at 20 mL/h. Surfactant solutions

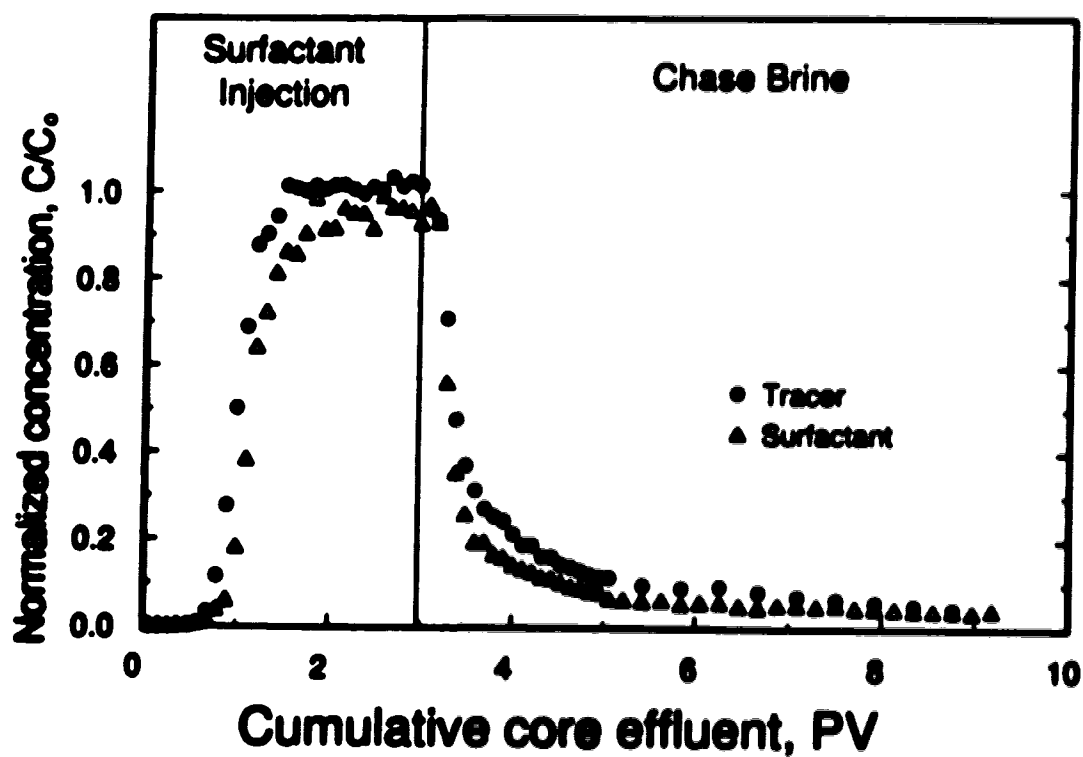


Figure 4-6. Propagation of surfactant slug containing 1.85 wt.% Neodol 25-38 and 12 wt.% sodium chloride at 20 mL/h.

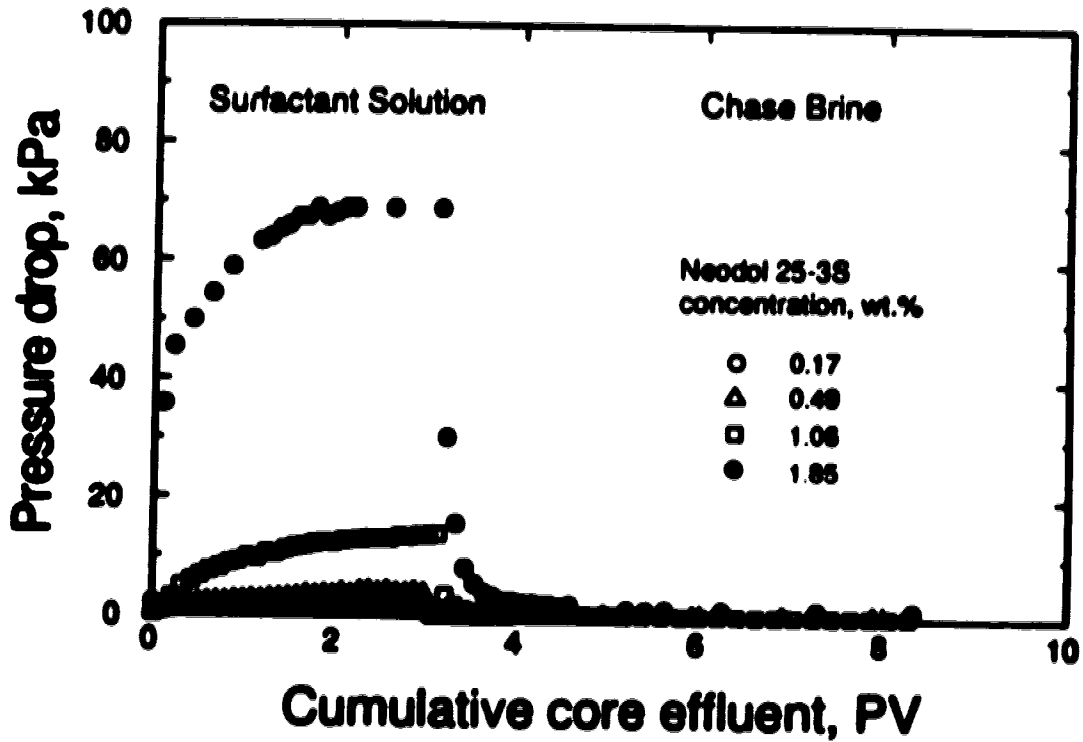


Figure 4-7. Pressure drop across the core as a function of core effluent volume for surfactant solutions containing 12 wt.% sodium chloride and various surfactant concentrations.

containing 12 wt.% sodium chloride and surfactant concentrations of 0.17, 0.5, 1.06 and 1.85 wt.% were used. At a surfactant concentration of 0.17 wt.% ($\mu_n = 1.8 \text{ mPa}\cdot\text{s}$), the pressure drop across the core remained low at nearly 1.6 kPa and did not change significantly during the run. However, at a surfactant concentration of 1.06 wt.% ($\mu_n = 180 \text{ mPa}\cdot\text{s}$), a significant increase in the pressure drop (up to 14 kPa) was observed. A dramatic increase in the pressure drop was observed with the surfactant slug having 1.85 wt.% surfactant ($\mu_n = 500 \text{ mPa}\cdot\text{s}$), where the maximum pressure drop obtained was 69 kPa. The pressure drop in all runs fell immediately once the chase brine was injected, and was reduced to the same value obtained during the initial brine flood.

4.2.2 Effect of pH

According to Equation (2-1), increasing the pH of the surfactant solution will change the surface charges of the clay minerals. Consequently, surfactant loss due to adsorption will be affected. To examine this effect, three core flood experiments were conducted with surfactant concentration keeping at about 0.5 wt.% in 8 wt.% sodium chloride. In each experiment, the core was initially flushed with a brine of the same pH and sodium chloride concentration as those of the surfactant slug. The chase brine also had the same composition as the brine used in the preflush.

Figures 4-8a to 4-8c depict the profiles of the tracer and the surfactant for surfactant slugs having pH_i of 2.4, 6.5 and 12.3, respectively. The term pH_i denotes the measured solution pH of the injected surfactant slug. The pH of the core effluent during the injection of the surfactant slug and the chase brine is also shown. The tracer profiles for the three runs were almost identical, which indicated that the dispersion characteristics of the three cores were the same. Increasing the pH_i of the surfactant slug from 2.4 (Figure 4-8a) to 6.5 (Figure 4-8b) had no significant effect on the amount of surfactant retained in the core. This unexpected result was due to the dissolution of dolomite present in the core at low pH conditions.

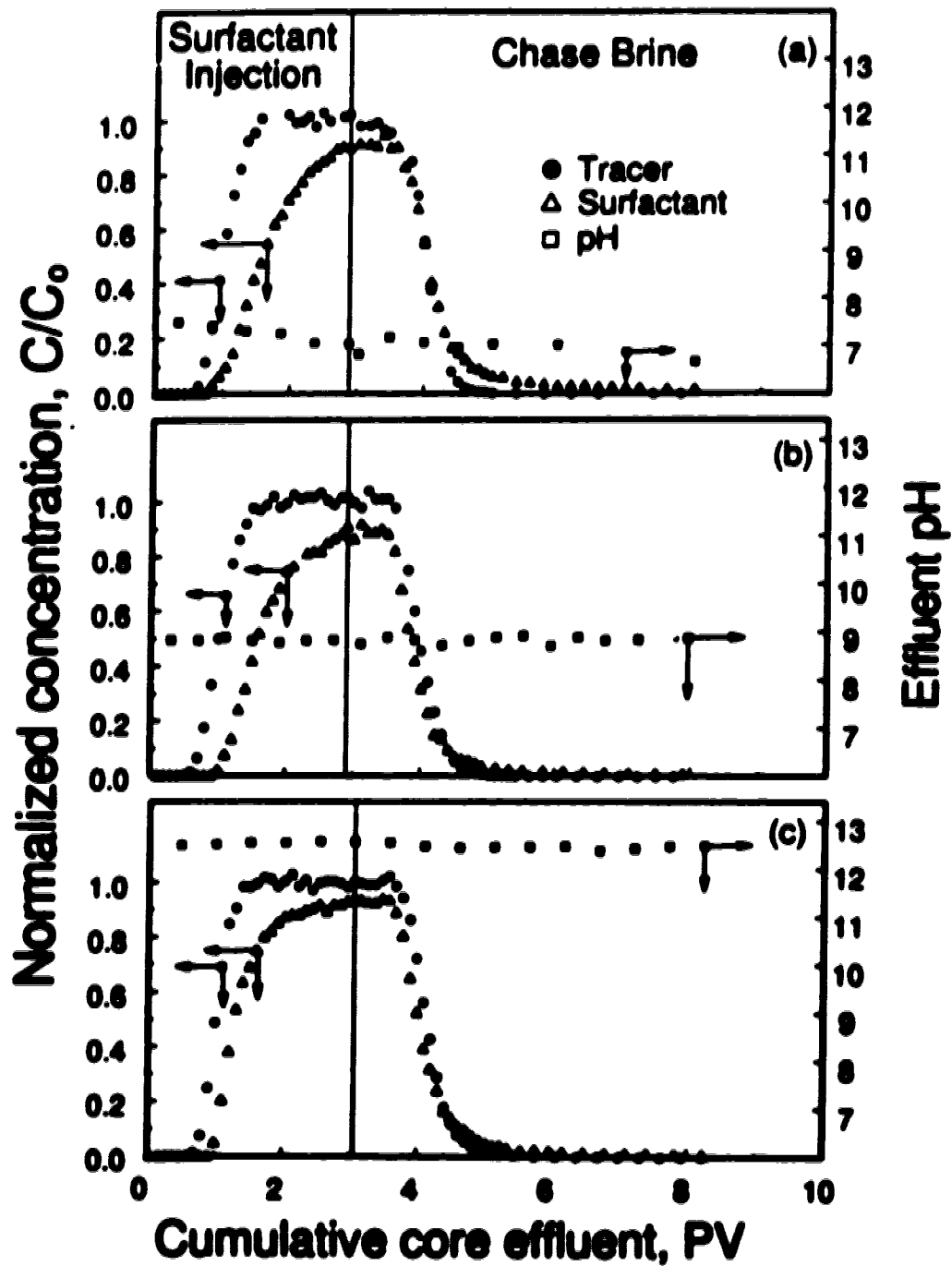


Figure 4-8.

Propagation of surfactant slugs having about 0.5 wt.% Neodol 25-35, 8 wt.% sodium chloride and pH_i of (a) 2.4, (b) 6.5 and (c) 12.3 at 20 mL/h.

As a result, the pH of the aqueous solution in contact with the sandstone was much higher than that of the injected solution as evident from the pH values measured in the core effluent. The resulting pH in the core effluent was not significantly different from that obtained in the core effluent at the injection pH of 6.5.

Increasing the pH of the injected solutions to 12.3 (Figure 4-8c) reduced the area between the tracer and the surfactant profiles. The surfactant loss as calculated from material balance on the surfactant indicated a drop in the surfactant loss from 48.3 mg/100 g_a at pH_i of 6.5 to 34.4 mg/100 g_a at pH_i of 12.3. At the higher pH values the surface of the clays particles becomes more negatively charged, see Equation (2-1). This will increase the electrostatic repulsion between the surface and the surfactant monomers, leading to lower adsorption.

The most important observation from Figures 4-8b and 4-8c is that increasing the pH of the injected surfactant slug from 6.5 to 12.3 resulted in a reduction in the amount of surfactant retained in the core by nearly 30 percent. This demonstrates the importance of adding an alkali to chemical EOR processes where an anionic surfactant is used in sandstone reservoirs.

4.2.3 Effect of Flow Rate

The injection flow rate can modify the propagation of surfactant in many ways. Increasing the injection flow rate reduces the mixing length, decreases the mass transfer resistance at the solid-liquid interface, and shortens the residence time of the surfactant solution in the core. To examine the effect of the injection flow rate in radial geometry, the experiment described in Figure 4-3 was repeated at flow rates of 5 and 120 mL/h. Surfactant propagation at flow rates greater than 120 mL/h was not studied because of possible mechanical fines migration and subsequent permeability damage.

Figures 4-9a to 4-9c show the normalized tracer and surfactant concentrations as a function of the cumulative core effluent at injection flow rates of 5, 20 and 120 mL/h.

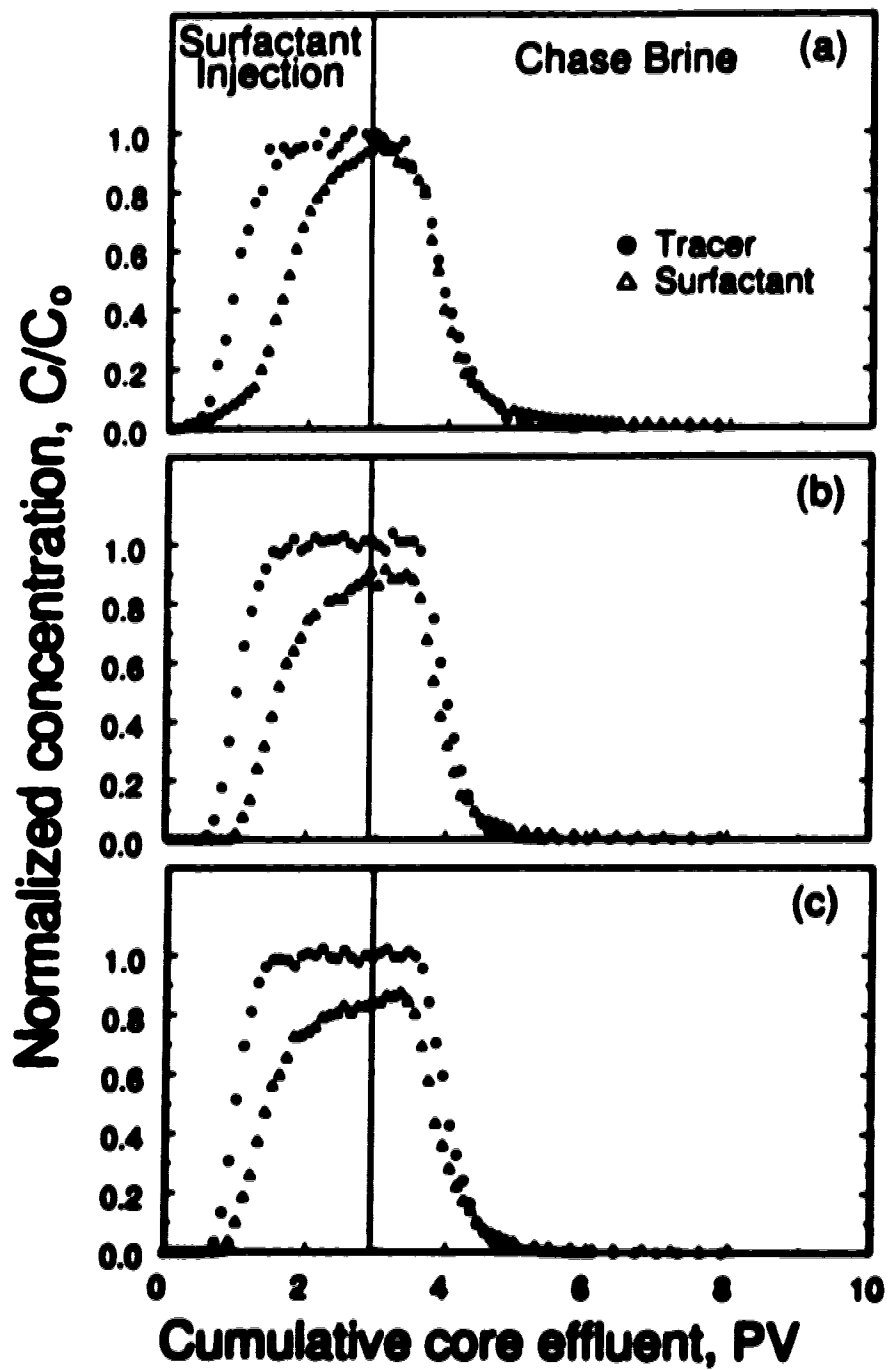


Figure 4-9.

Propagation of surfactant steps containing about 0.5 wt.% Neodol 25-38 and 8 wt.% sodium chloride at (a) 5, (b) 20 and (c) 120 mL/h.

At the lowest injection flow rate, the tracer breakthrough occurred after 0.5 PV and it did not reach unity even after the injection of two pore volumes. At the highest flow rate examined, the tracer breakthrough occurred after 0.7 PV and it reached unity after the injection of nearly 1.6 PV. These results indicate that increasing the injection flow rate in radial geometry resulted in a sharper tracer profile, that is, a shorter mixing length. This is similar to the results obtained with linear geometry.

Figure 4-9c shows the tracer and surfactant profiles obtained at an injection flow rate of 120 mL/h. Comparing the results obtained in Figures 4-9b and 4-9c, it can be seen that increasing the injection flow rate caused surfactant breakthrough to occur earlier. Increasing the injection flow rate reduced the residence time of the surfactant solution in the core. As a result, there was less time for surfactant adsorption at the higher flow rate and surfactant breakthrough occurred earlier. Increasing the flow also reduced the area between the tracer and surfactant profiles, that is, reduced surfactant loss due to adsorption. Calculating surfactant loss at the two flow rates indicated that surfactant loss at the end of injecting the surfactant slug had dropped by nearly 12 percent.

Chapter 5

Propagation and Adsorption of TRITON X-100 (Non-Ionic Surfactant) .

Adsorption of non-ionic surfactants on mineral oxide is a physical process which occurs via hydrogen bonding and van der Waals attraction forces. Polyethoxylated surfactants are the most common type of non-ionic surfactants employed in adsorption studies because they are available in a variety of forms differing in hydrocarbon chain length which can be tailored for a specific application (Doren *et al.*, 1975). Also, this type of surfactant is very stable in a broad range of pH and in the presence of divalent and multivalent ions. In the current study, a commercial surfactant, Triton X-100, was used. The physical and chemical properties of this surfactant are summarized in the Experimental Section, Chapter 3.

During the initial stage of adsorption, hydrogen bonds are formed between the hydrogen atom in the surface hydroxyl and the oxygen atom in the ethylene oxide units. As the surface coverage, as well as the bulk surfactant concentration, increases, a strong tendency for surface aggregation as a result of the hydrophobic effect leads to a significant increase in adsorption. A number of adsorption theories have been developed over the years. Because of the shape of the adsorption isotherms obtained in our experiments, the materials presented in this chapter focus mainly on the interpretation of

* A version of this chapter has been published. W. Eweh, H.A. Nasr-El-Din, R.E. Hayes and B. Sabi, 1992. *Colloids and Surfaces A: Physicochemical and Engineering Aspects*, Vol.78, pp.193-202.

hemimicelle formation proposed by Fuerstenau (1955b) and the general isotherm equation derived by Frier (1989, 1991).

By conducting static and dynamic tests, the effects of salinity, pH and flow rate on the adsorption and propagation of Triton X-100 in Berea sandstone were examined.

5.1 Equilibrium Static Adsorption Isotherms

Surfactant solutions of known concentration (between 0.04 and 1.2 wt.%) were added to the treated particles in a vial with a liquid-to-solid ratio of 2. As mentioned in Section 4.1.1, lower liquid-to-solid ratios resulted in lower surfactant adsorption values. Surfactant uptake (at equilibrium) due to adsorption was calculated using the surfactant concentrations measured before and after contact with the particles.

5.1.1 Discussion of Errors in Adsorption Isotherms

The sources of errors should be discussed briefly at this point. The measurements of non-ionic surfactant (Triton X-100) concentration with the least error were those in the range of 0.005 to 0.05 wt.% (linear relationship according Beer's law). Concentrations above this range must thus be diluted. In the current study, all samples of higher surfactant concentration were diluted using two or three different dilution ratios such that each of the reported concentrations was within an error of five percent or less.

However, adsorption values with the least error were obtained at low surfactant concentrations, since the difference between concentrations before and after contact is greater than that at high concentrations. This generally means that the best results were obtained at equilibrium Triton X-100 concentrations of less than 0.05 wt.%, and large errors in the calculated adsorption values can occur for high surfactant concentrations. For example, a small variation (say, $\pm 5\%$) in the measurement of surfactant concentrations

before and after adsorption results in a difference of 25-30 percent in the calculated adsorption values.

5.1.2 Effect of Salinity

Previous studies considering the adsorption of Triton X-100 on Berea sandstone are sparse. Lawson (1978) measured static adsorption isotherms of Triton X-100 and found them to be of the Langmuir type. Ramirez and co-workers (1980) conducted a similar study on fired Berea and arrived at a similar conclusion. The results obtained by these researchers disagree with those obtained in recent studies on the adsorption of non-ionic surfactants, especially those dealing with adsorption of Triton X-100 on silica gel (Huang and Gu, 1987). To investigate this discrepancy, static adsorption isotherms of Triton X-100 were measured at sodium chloride concentrations of 0, 3, 8 and 12 wt.%. Figure 5-1 shows the measured isotherms together with fitted curves based on the general isotherm equation for adsorption, Equation (2-20), by Zhu and Gu (1989).

The amount of surfactant adsorbed at equilibrium is expressed in terms of mg of surfactant per 100 g of rock (disaggregated Berea). The experimental data indicate that the static isotherms obtained at all salinities examined were of the L4-type, which suggests a two-step mechanism of adsorption. At lower surfactant concentrations, the surfactant was adsorbed onto the surface via the polyethylene oxide segment. However, at high surfactant concentrations, adsorption occurred due to the aggregation of surfactant monomers via hydrophobic interactions. The experimental data also show that the first plateau is much less than the second one. This indicates that most of the surfactant adsorption occurred due to the aggregation process.

For the Zhu and Gu model, see Figure 5-1 and Table 5-1, the least-square fit parameters of K_m , K_{m_2} , Q , and n in Equation (2-20) were determined by non-linear regression using a simplex search method. As the sodium chloride concentration was increased from 0 to 12 wt.%, the equilibrium ratio for monomer adsorption, K_m ,

decreased from 3.08×10^3 to 1.40×10^4 L/mol; whereas, for the equilibrium ratio of hemimicelles, K_{hm} , a very strong dependency was observed (reduced by as much as 10 orders of magnitude). The maximum adsorption capacity, Q_s , increased as a direct function of solution salinity. The aggregation number, n , however, decreased from 4 to 1.5 as sodium chloride concentration increased. The trends in Q_s and n suggest that the increase in salinity favoured and possibly accelerated the aggregation process of surfactant on the solid surface. Both mechanisms overlap and therefore were no longer clearly distinguished from the shapes of the isotherm. As a result, the second adsorption layer was formed simultaneously with the first layer, which is referred to as one-step formation of hemimicelle by Zhu and Gu (1989). The critical hemimicelle concentration, C_{hm} , was determined from the definitions given in Equations (2-22) to (2-25). By either definition, the calculated C_{hm} values were reduced as sodium chloride concentration was increased which is similar to the variation of the critical micelle concentration with salt concentration.

The increase in total adsorption, Q_s , as a function of salinity may be attributed to the possibility of surfactant desolvation. With the results from turbidmetric and viscometric measurements, Docher *et al.* (1951) showed that adding sodium chloride favours an increase in micellar size and causes the surfactant molecules to salt out of the aqueous phase. Although electrolytes such as sodium chloride do not adsorb on the micellar surface, they can influence the size of micelles and the extent of solvation at the micellar surfaces (Manohar and Kelkar, 1990). As a result, the addition of salts causes a considerable increase in the aggregation number and helps to promote the release of the hydrated surfactant molecules. These surfactant molecules, rejected by the micelles, thus are more likely to adsorb on the solid surfaces. This phenomenon is known as the salting-out effect (Docher *et al.*, 1951; Kuznetsova *et al.*, 1976; Imae *et al.*, 1988).

Similar observations of the effect of salinity on the adsorption of Triton X-100 have been reported elsewhere. Lawson (1978) reported that the plateau values for adsorption of Triton X-100 on Berea sandstone were 136 and 162 mg/100 g_s from 1.1 and 5.3 wt.% sodium chloride solutions, respectively. These results are considerably

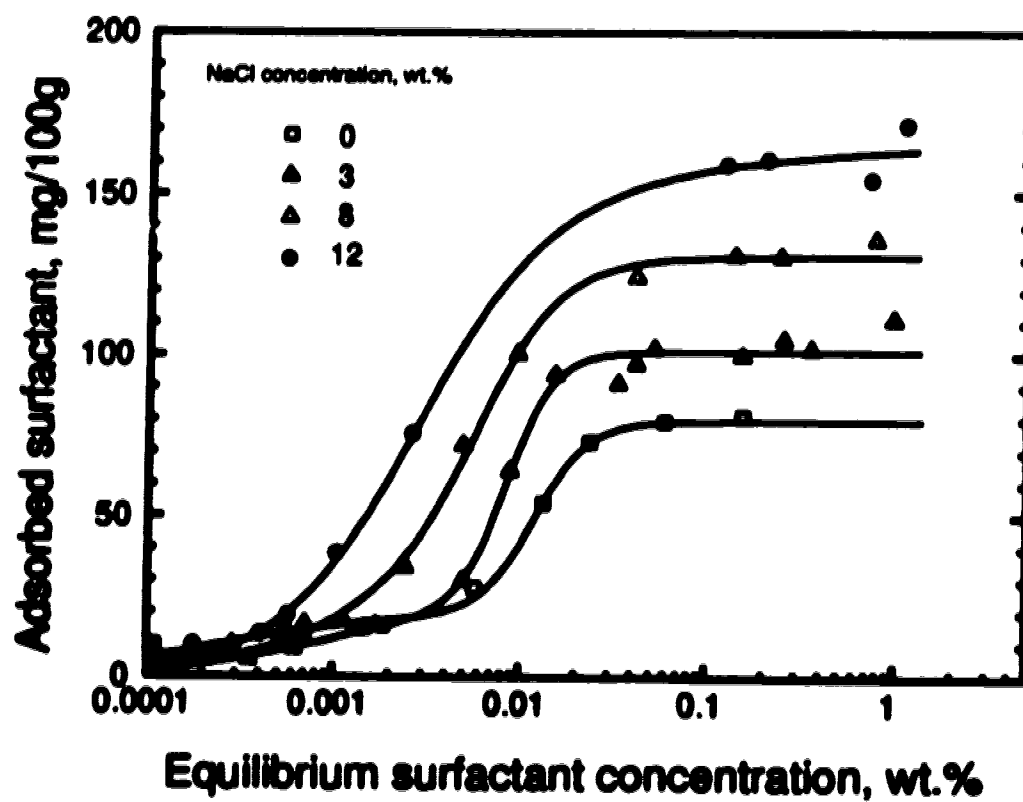


Figure 5-1. Effect of sodium chloride on the equilibrium static adsorption of Triton X-100 on disaggregated Berea sandstone.

higher than those obtained in this study because of the difference in specific surface area ($1.4 \text{ m}^2/\text{g}$) of the sandstone used. Lawson did not, however, examine the surfactant concentration range of below 0.05 wt.%, and as a result the adsorption isotherm obtained was of the Langmuir type. More recently, Denoyel and Rouquerol (1991) examined the adsorption of Triton X-100 on quartz (S-shaped isotherm) and kaolin (stepped isotherm) for 0 and 1 wt.% sodium chloride. For both surfaces, the observed critical hemimicelle concentrations were 0.01 and 0.014 wt.% for 0 and 1 wt.% sodium chloride, respectively.

5.1.3 Effect of pH

The adsorption isotherms of surfactant were measured and they are presented as a function of pH (initial and equilibrium) at a given sodium chloride concentration in Figure 5-2. Figure 5-2a shows the adsorption isotherm of Triton X-100 obtained at sodium chloride concentrations of 3 wt.%, where the initial pH values were 2.2, 6.0 and 11.9. The solid lines represent the predicted isotherms based on Equation (2-20). The fitted parameters are listed in Table 5-1. Note that the average equilibrium pH measured in both the lower and normal pH samples (initial pH values of 2.2 and 6.0) were increased to 8.0 and 8.4, respectively. The measured pH remained unchanged for the high pH samples. Similarly, the experimental and predicted adsorption isotherms of Triton X-100 from 8 wt.% sodium chloride for initial pH values of 2.1, 6.1 and 11.9 are shown in Figure 5-2b. The pH values of the equilibrium solution were 8.0, 8.4 and 11.8, respectively.

For the 3 wt.% sodium chloride solutions, a small decrease in maximum adsorption, Q_m , as a function of increasing pH was observed, as shown in Table 5-1. Such a decrease was, however, not observed for the 8 wt.% sodium chloride solutions. For either sodium chloride concentration, it appears that an increase in the initial pH from 2 to 6 suppressed adsorption by reducing the number of vacant sites for the monolayer adsorption, as suggested by Equations (2-1) and (2-13). The calculated monolayer

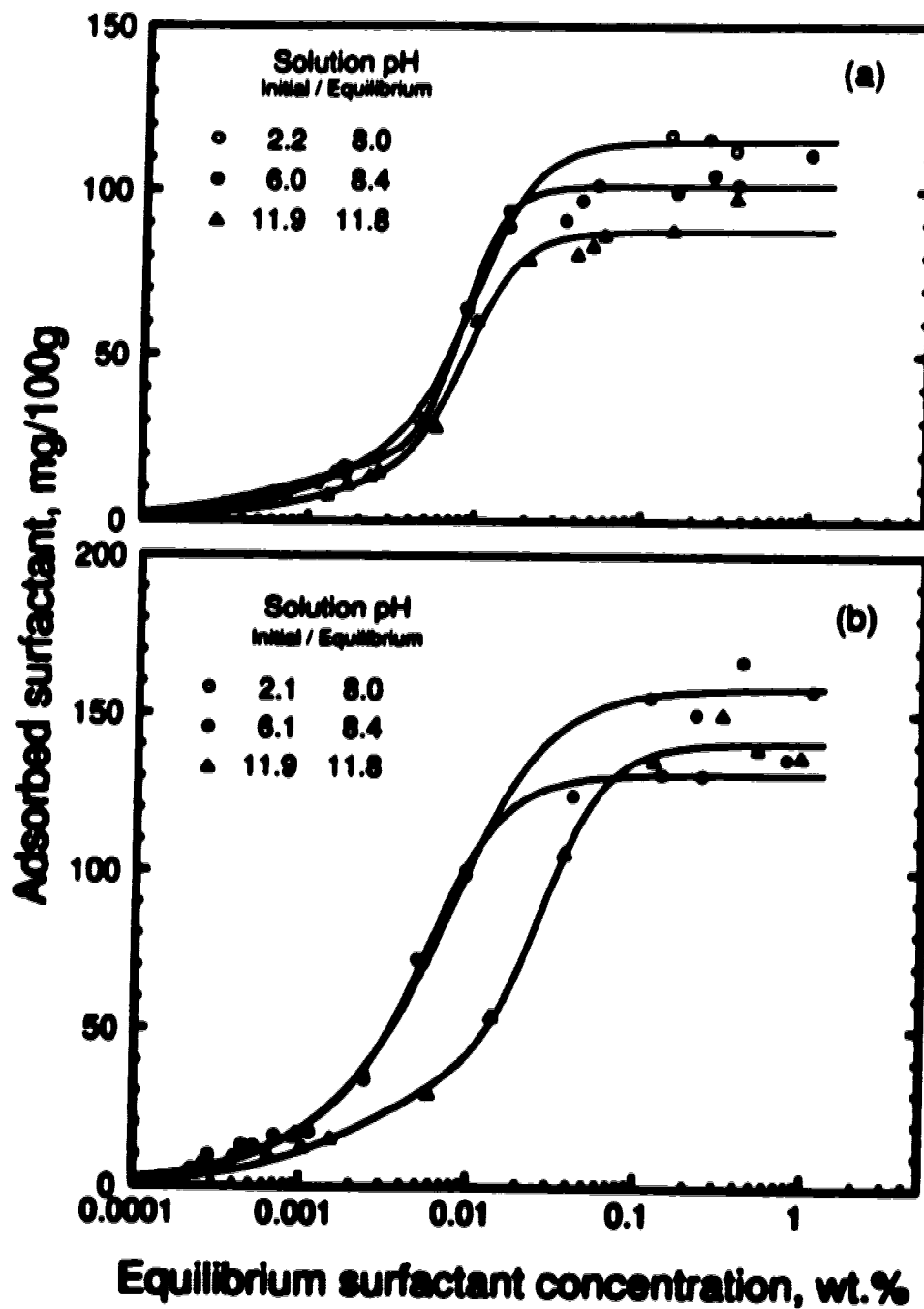


Figure 5-2. Effect of pH on the equilibrium static adsorption of Triton X-100 on disaggregated Berea sandstone from (a) 3 and (b) 8 wt.% sodium chloride solutions.

saturation, Q_s^M , decreased from 36.0 to 23.3 mg/100g_R (a decrease of 35 percent) for 3 wt.% sodium chloride, and from 65.5 to 46.5 mg/100g_R (a decrease of 29 percent) for 8 wt.% sodium chloride. An increase in pH from 6 to 12, however, seems to have no effect on the monomer adsorption as indicated by the constant values of monolayer saturation calculated. The differences in the measured maximum adsorption for increasing values of pH (especially, for alkaline) must thus be caused by the differences in the aggregation characteristics in the bulk solution (micellization) as well as at the solid/liquid interface (hemimicellization).

The effect of pH on the adsorption of Triton X-100 can be explained as follows. Adsorption of non-ionic surfactants occurs at the solid/liquid interface via hydrogen bonding between the hydrolyzed solid surface and ethylene oxide segments of the surfactant. When the pH of the surfactant solution is increased (by means of adding hydroxide ions), the number of hydroxyl groups (M-OH) at the surface available for hydrogen bonding is reduced. The surface of hydrated mineral oxides exhibits a strong negative charge (in forms of M-O⁻). As a result, the counterions (Na⁺) will accumulate near the surface and compete with the surfactant molecules (Boomgaard *et al.*, 1983). Both factors tend to decrease the amount of surfactant adsorbed. When the pH is decreased (by means of adding hydrogen ions), the hydroxyl groups at the solid surface may react and form a weak acidic group, M-OH₂⁺, which tends to repel the approaching counterions and apparently promotes the adsorption of the surfactant molecules at the interface. In addition, unreacted hydrogen ions in the bulk phase tend to dissolve the dolomite present in the sandstone, thus rising the pH of the equilibrium solution. Under the experimental conditions, the effect of pH appears to be more noticeable for low sodium chloride concentration because the competition between the counterions and surfactant molecules was relatively less important. No reasonable explanation, however, can be offered for the behaviour observed at the higher (8 wt.%) sodium chloride concentration at present.

Table S-1. Summary of model parameters for fixed adsorption isotherms. Equation (2-20), Ref. Zha and Gu (1989, 1990).

MeCl Conc. (wt.%)	Initial pH	Final pH	Saturation Adsorption, Q_s (mg/100g)	Equilibrium Coefficient, K_s (mol/L) ⁻¹	Equilibrium Coefficient, K_{eq} (mol/L) ⁻¹	Aggregation Number, n	Monolayer Saturation, Q_m (mg/100g)	⁽²⁾ Membrane Concentration	
								Definition (1) (wt.%)	Definition (2) (wt.%)
0	5.60	8.32	79.86	3.88×10^6	2.83×10^4	4.04	19.76	0.0047	0.0048
3	6.00	8.38	101.46	7.38×10^6	7.38×10^{11}	4.36	23.27	0.0022	0.0024
8	6.11	8.37	131.17	3.62×10^6	2.40×10^7	2.82	46.51	0.00004	-
12	6.00	8.36	166.09	1.40×10^6	164.1	1.50	110.73	0.00025 ^(a)	-
3	2.19	8.04	114.95	2.67×10^6	2.74×10^6	3.19	36.83	0.0022	0.0013
3	11.86	11.76	87.68	2.46×10^6	7.45×10^6	3.53	24.84	0.0026	0.0023
8	2.14	7.99	158.39	2.24×10^6	3.06×10^6	2.42	65.45	0.00045	-
8	11.90	11.80	141.00	2.19×10^6	2.42×10^6	3.11	45.34	0.0045	0.0022

^(a) $Q_m = Q_s$.
 on Pined as L1 isotherm, Equations (2-22) and (2-23).
 on Pined as S2 isotherm, Equations (2-24) and (2-25).

5.2 Dynamic Tests

Surfactant solution was continuously injected until the measured surfactant concentration in the core effluent reached the injection level. A chase brine of the same salinity was then injected to displace the surfactant slug remained in the bulk phase in order to calculate, by material balance, the saturation amount of adsorption during the injection period. The results are summarized in Table 5-2.

The range of sodium chloride concentration examined was 0 to 12 wt.% at a room temperature of about 23 °C. These conditions are in the region below the cloud point temperatures of Triton X-100 according to Travalloni-Louvisse and González (1988). Any instability during the injection as a result of phase separation is therefore not expected.

5.2.1 Effect of Salinity

Flow experiments were performed as described previously using sandstone cores. Typical effluent profiles are shown in Figure 5-3 for a continuous injection of 6 PV of a surfactant solution followed by 5 PV of a chase brine. The injected surfactant solution contained 0.50 wt.% Triton X-100, 3 wt.% sodium chloride and tritium as a tracer. The chase brine of 3 wt.% sodium chloride was then injected to displace the surfactant solution. A constant injection flow rate of 20 mL/h was used.

The normalized concentrations of tracer and surfactant in the core effluent C/C_0 were plotted against the cumulative core effluent, where C_0 is the concentration of the tracer or surfactant in the injected surfactant solution. The tracer profile showed an S-shaped distribution with $C/C_0 = 0.0$ (at 0.6 PV) increasing to 1.0 (at 1.4 PV). The advective front of the tracer was found at 1.0 PV as marked by $C/C_0 = 0.5$. This indicated that tracer propagation in this core was controlled by advection and dispersion only, and the effect of any dead-end pores, that is, capacitance effect (Coats and Smith, 1963) was not significant. The surfactant profile was significantly different from that of

Table 5-2. Summary of flow experiments on the propagation of Triton X-100.

Sodium Chloride Concentration (wt.%)	Flow Rate (mL/h)	Surfactant Concentration (wt.%)	Surfactant Loss, Q_s^d (mg/100g _s)
3	20	0.50	81.99
8	20	0.47	95.81
12	20	0.49	109.00
3	80	0.51	80.68
8	80	0.49	98.10
3	120	0.50	72.49
† 3	20	0.50	54.26
† 8	20	0.50	77.01

† These runs were conducted at pH = 12.0.

the tracer. The advective front was retarded due to adsorption. The distribution of effluent surfactant concentration curve was not symmetric at $C/C_0 = 0.5$. The effluent surfactant profile dropped at a rate slower than that of the tracer profile, signifying a small amount of surfactant desorption occurred during the injection of the chase brine. The total amount of surfactant adsorbed, Q_s^d , was evaluated from the difference between the integrated areas under the tracer and surfactant profiles upto the end of the surfactant solution injection, and was found to be 82 mg/100g_s (see Table 5-2). This value was significantly lower than that obtained at the same salinity under static condition (see Table 5-1). A comparison of surfactant adsorption under static (Q_s) and dynamic (Q_s^d) conditions will be discussed later.

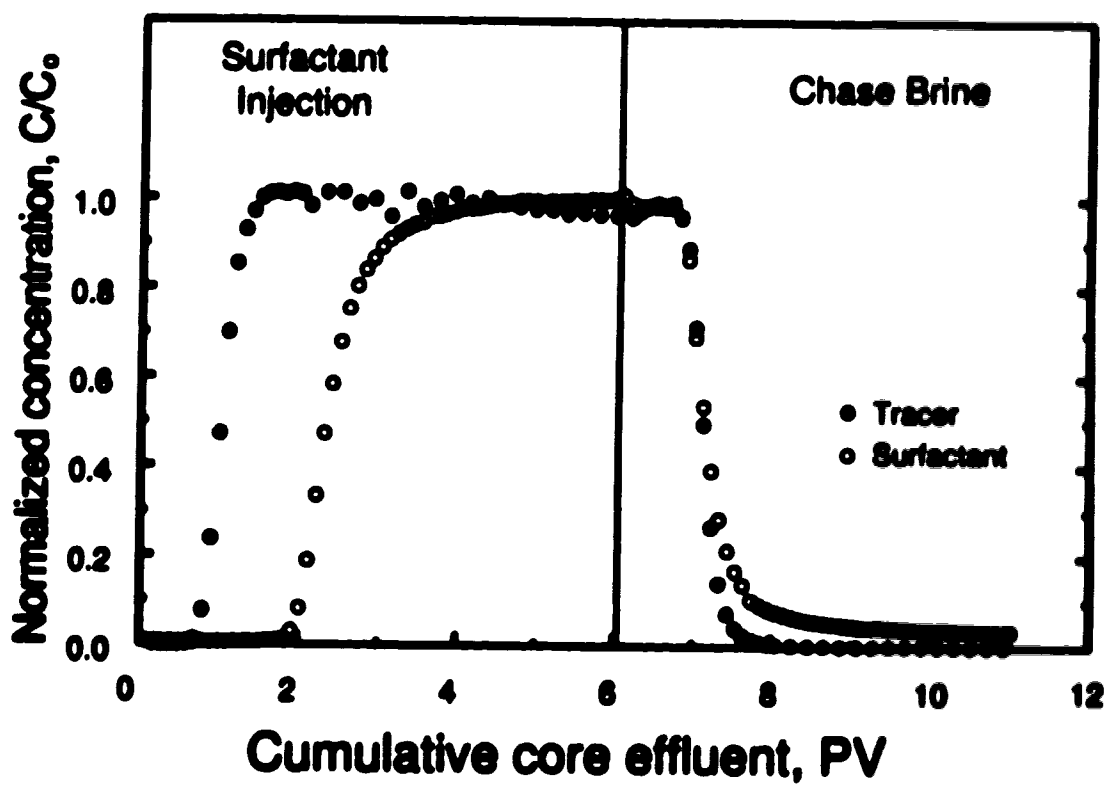


Figure S-3. Surfactant propagation of 0.50 wt.% Triton X-100 in 3 wt.% sodium chloride at 20 mL/h, followed by a chase brine of 3 wt.% sodium chloride.

Figure 5-4 shows the effluent profiles of about 0.5 wt.% Triton X-100 in 3, 8 and 12 wt.% sodium chloride during the injection of the first 6 PV of the surfactant solutions. The injection flow rate was kept constant at 20 mL/h during these runs. For the tracer, the three effluent profiles were almost identical, indicating that the dispersion characteristics in these cores were similar. The effect of salinity on the propagation of surfactant was significant. At a sodium chloride concentration of 3 wt.%, surfactant breakthrough occurred after 1.8 PV, whereas at 12 wt.% sodium chloride it occurred after 2.2 PV. This signifies more delay in surfactant breakthrough at the highest salinity examined. Also, loss of surfactant at the end of surfactant solution injection was found to be a function of sodium chloride concentration (Table 5-2). This result is consistent with the adsorption plateau values obtained in the static adsorption tests.

5.2.2 Effect of Flow Rate

The injection flow rate can modify the propagation of surfactant in many ways as discussed in Section 4.2.3. Firstly, increasing the flow rate reduces the spread of the tracer and surfactant profiles (*i.e.*, reduces the effect of the dispersion). Secondly, increasing in flow rate reduces the mass transfer resistance which hinders the transport of surfactant monomers from the bulk liquid phase to the solid surface (Ramirez *et al.*, 1980). Thirdly, increasing the flow rate at a given pore volume reduces the residence time of the surfactant solution in the core. Finally, increasing the flow rate increases the shear stress at the solid surface. This may affect the orientation of surfactant monomers on the surface and subsequently influences the maximum adsorptive capacity of the rock, as will be discussed later.

The effect of flow rate on the surfactant propagation was examined using surfactant solution containing about 0.5 wt.% Triton X-100 and 3 wt.% sodium chloride at injection rates of 20, 80 and 120 mL/h. Figure 5-5a shows the tracer profiles obtained at $Q = 20$ and 120 mL/h. Increasing flow rate slightly reduced the spread of the tracer

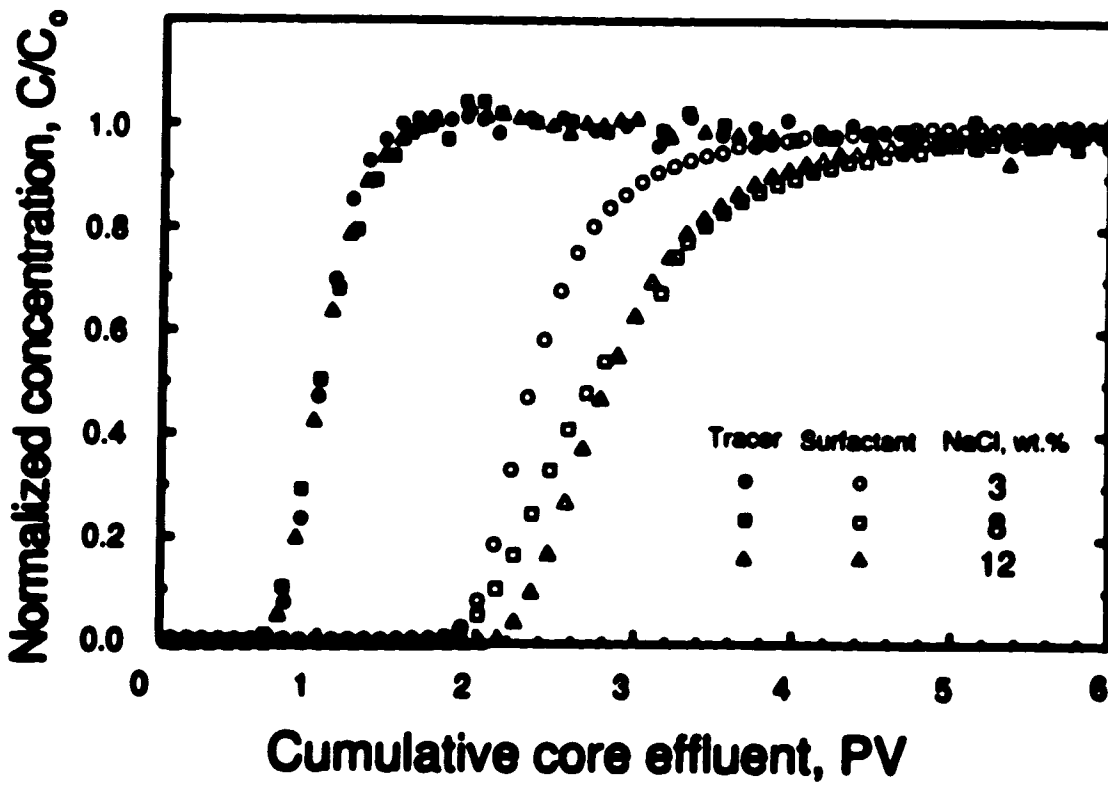


Figure 5-4. Effect of sodium chloride concentration on surfactant propagation with about 0.5 wt.% Triton X-100 in 3, 8 and 12 wt.% sodium chloride at 20 mL/h.

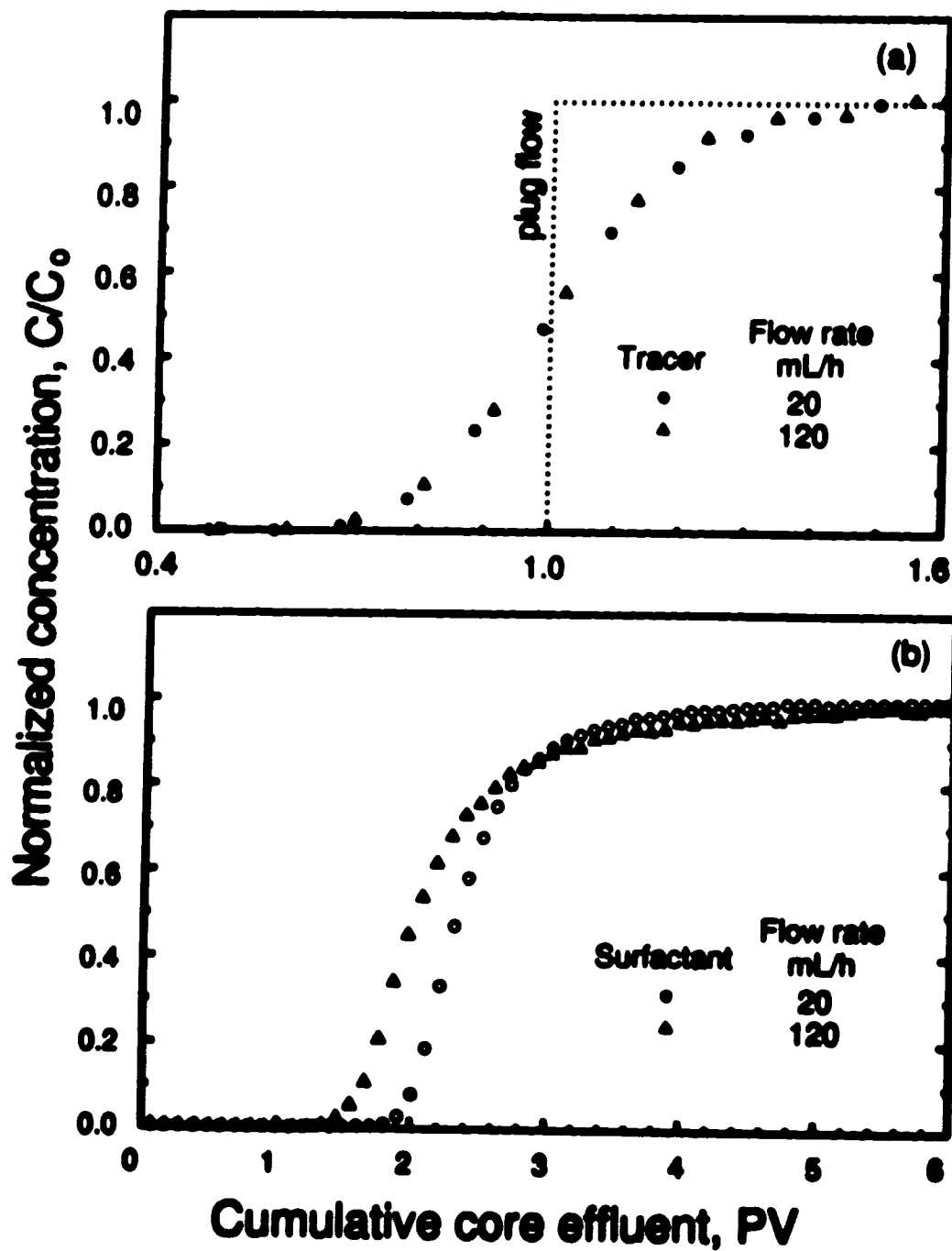


Figure 5-5. Propagation of surfactant solution of about 0.5 wt.% Triton X-100 in 3 wt.% sodium chloride at flow rates of 20 and 120 mL/h, (a) tracer and (b) surfactant.

flow as observed near the breakthrough point. No tailing was observed for either flow rates, indicating the absence of dead-end pore volume in the cores.

Figure 5-5b illustrates the effect of flow rate on surfactant propagation at the same conditions given in Figure 5-5a. Increasing flow rate to 120 mL/h resulted in early breakthrough in surfactant (1.5 PV compared with 1.8 PV at 20 mL/h), and a long tailing. Obviously, these trends cannot be explained in terms of dispersion shown in Figure 5-5a, or tailing. These trends (early breakthrough and tailing) indicate that surfactant adsorption is not instantaneous, but kinetically controlled; that is, there is a time required for surfactant to adsorb on the surface. The residence time was 2.4 hours, at the injection flow rate of 20 mL/h, and 0.4 hour at the higher flow rate of 120 mL/h. This means that at the lower flow rate, surfactant had more time to adsorb. As a result, the available adsorption sites were occupied at surfactant breakthrough and surfactant concentration rose very quickly to reach the injection level. At the higher flow rate, residence time was not sufficient to saturate all available adsorption sites. At surfactant breakthrough, there were more unoccupied sites available for adsorption and the surfactant concentration rose at a slower rate and showed long tailing to reach the injection level.

Figure 5-6 shows the effect of flow rate on the surfactant profiles obtained at salinities of 3 and 8 wt.% sodium chloride, respectively. At the low salinity, increasing the flow rate resulted in early breakthrough and long tailing in surfactant. However, difference between the two flow rates in 8 wt.% sodium chloride was not as significant as that in 3 wt.% sodium chloride. With the higher sodium chloride concentration, time required for adsorption is less; that is, more surfactant getting adsorbed before the breakthrough. Thus, the initial breakthrough curves for the two injection rates were very similar.

5.2.3 A Comparison between Static and Dynamic Adsorption

Figure 5-7 compares surfactant loss due to adsorption obtained from dynamic ($Q = 20$ mL/h) and static adsorption tests at sodium chloride concentrations from 3 to

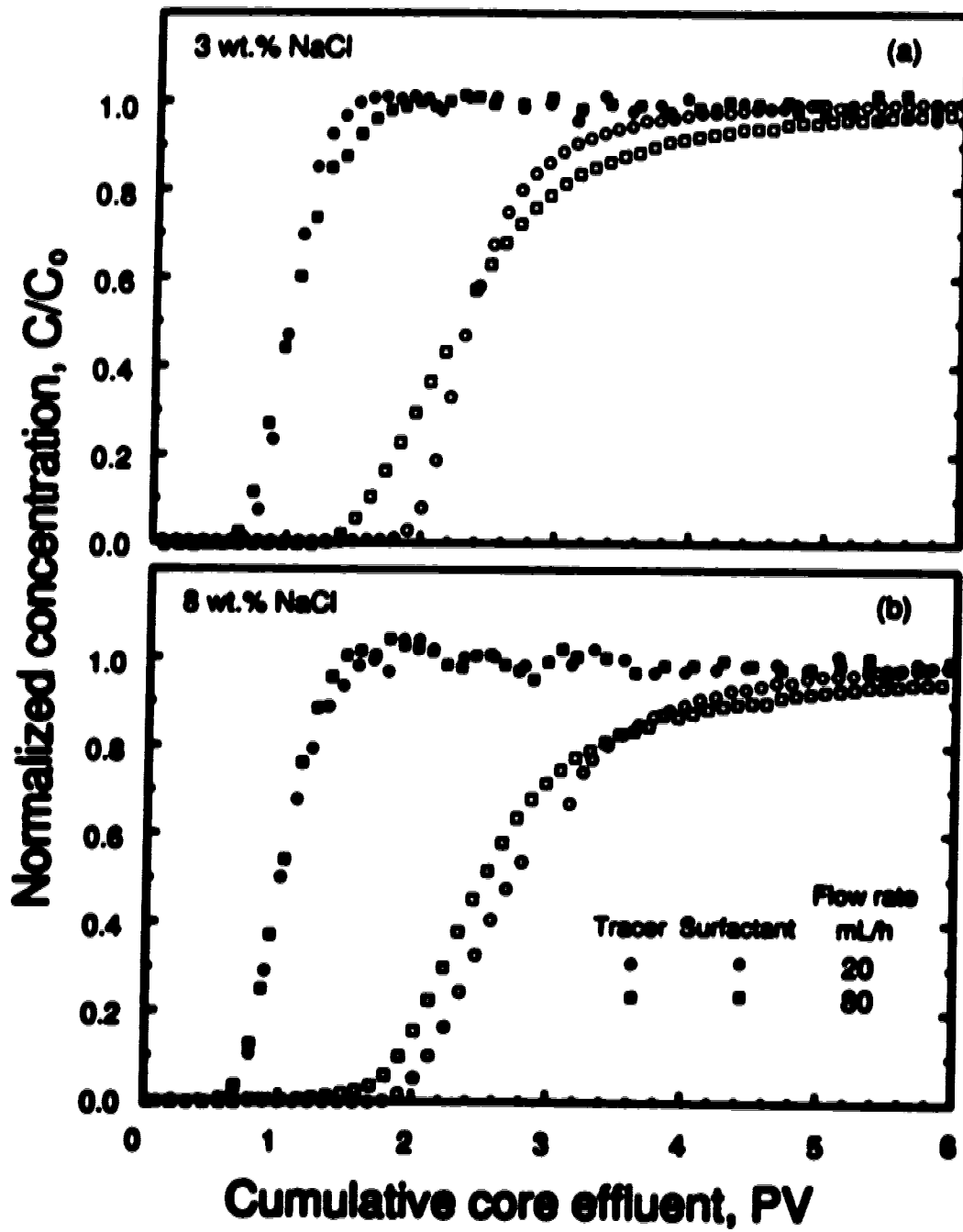


Figure 5-6. Propagation of surfactant solution of about 0.5 wt.% Triton X-100 in (a) 3 and (b) 8 wt.% sodium chloride at flow rates of 20 and 80 mL/h.

12 wt.%. A comparison between static and dynamic tests in water (no sodium chloride) was not possible. This is because of potential fines migration in the dynamic test upon the injection of water (Mungan, 1965; Khilar *et al.*, 1983). With 3 wt.% sodium chloride, surfactant loss due to adsorption obtained in dynamic test was 20 percent lower than that obtained in the static tests. The difference became more significant as the sodium chloride concentration was increased. Since the specific surface areas of consolidated and disaggregated Beres were very close, the difference in surfactant loss using dynamic and static tests may thus be caused by factors other than change in surface area.

Table 5-2 lists the surfactant loss due to adsorption for various dynamic tests. It is important to note that increasing flow rate from 20 to 120 mL/h caused more discrepancy between static and dynamic tests. Increasing flow rate increases the shear stress at the wall which may decrease the maximum adsorption capacity by one or more of the following mechanisms. Adsorbed surfactant monomer may be tilted towards the surface at an angle which increases with flow rate. As a result, the surface area available for adsorption decreases. A second mechanism is that the shear stress at the wall at a high flow rate may be stronger than hydrophobic binding forces between the adsorbed surfactant molecules and the second adsorption layer, which may also cause a decrease in adsorption.

At each flow rate, there is a dynamic equilibrium. The value of such dynamic equilibrium is less than that obtained with static tests. The difference increases as the flow rate is increased. These results should be considered when estimating surfactant loss for field applications.

To demonstrate that the maximum adsorption obtained under static and dynamic conditions are different, a surfactant solution of 0.49 wt.% Triton X-100 and 8 wt.% sodium chloride was injected at 80 mL/h (see Figure 5-8). After the effluent surfactant concentration reached the injection level, the flow was halted for two hours. Upon resuming the flow to displace the surfactant solution using the chase brine, a 10-percent drop in the effluent surfactant concentration was observed. This drop indicates surfactant adsorption beyond the dynamic saturation, while the bulk liquid was stationary. A similar experiment was conducted but at a low flow rate of 20 mL/h (see Figure 5-9). However,

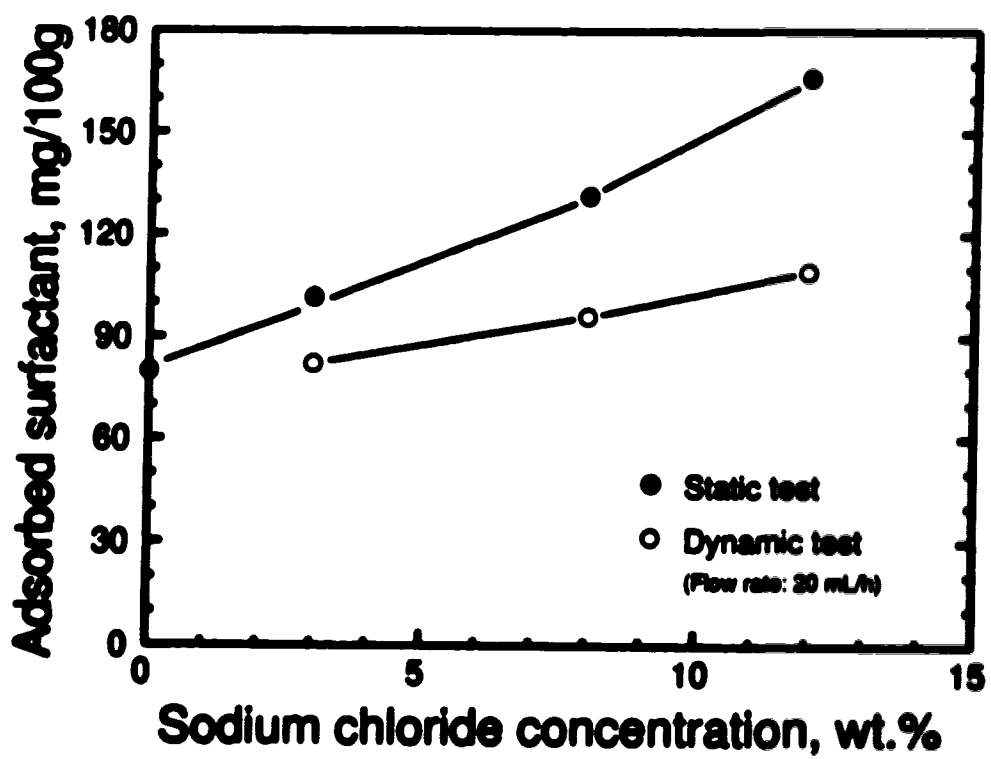


Figure S-7. Comparison of saturation adsorption of Triton X-100 under static and dynamic conditions.

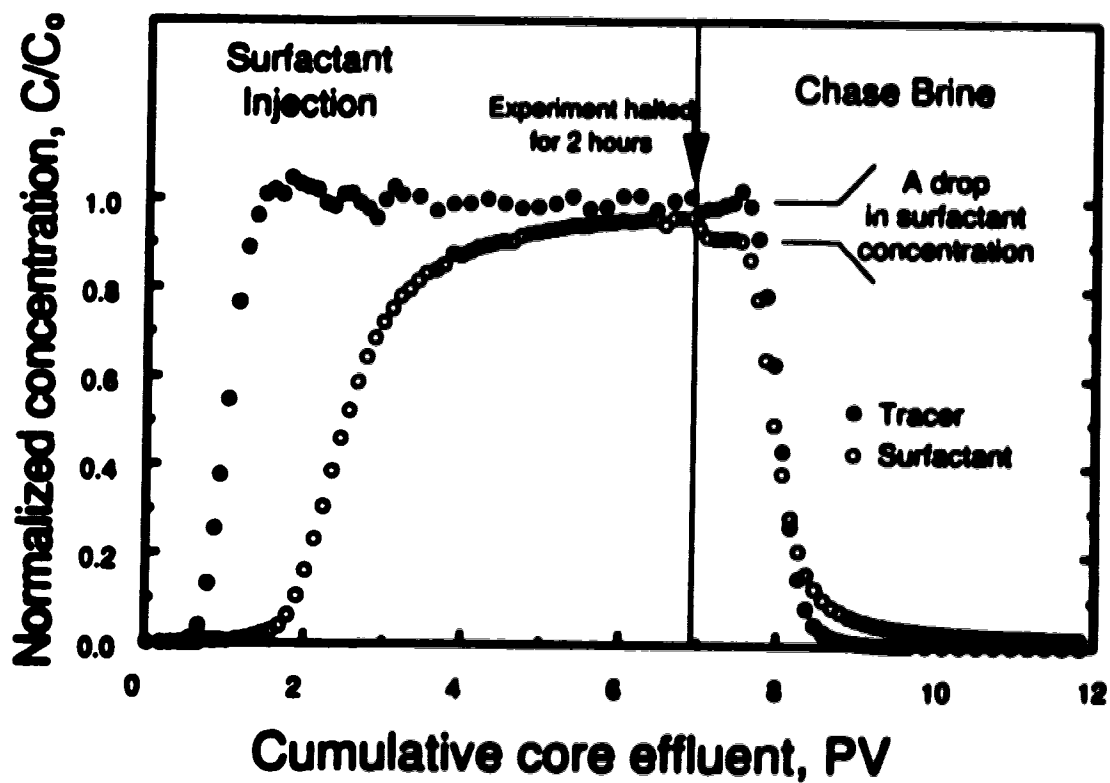


Figure 5-8. Surfactant propagation of 0.49 wt.% Triton X-100 in 8 wt.% sodium chloride at 80 mL/h, followed by a chase brine of 8 wt.% sodium chloride.

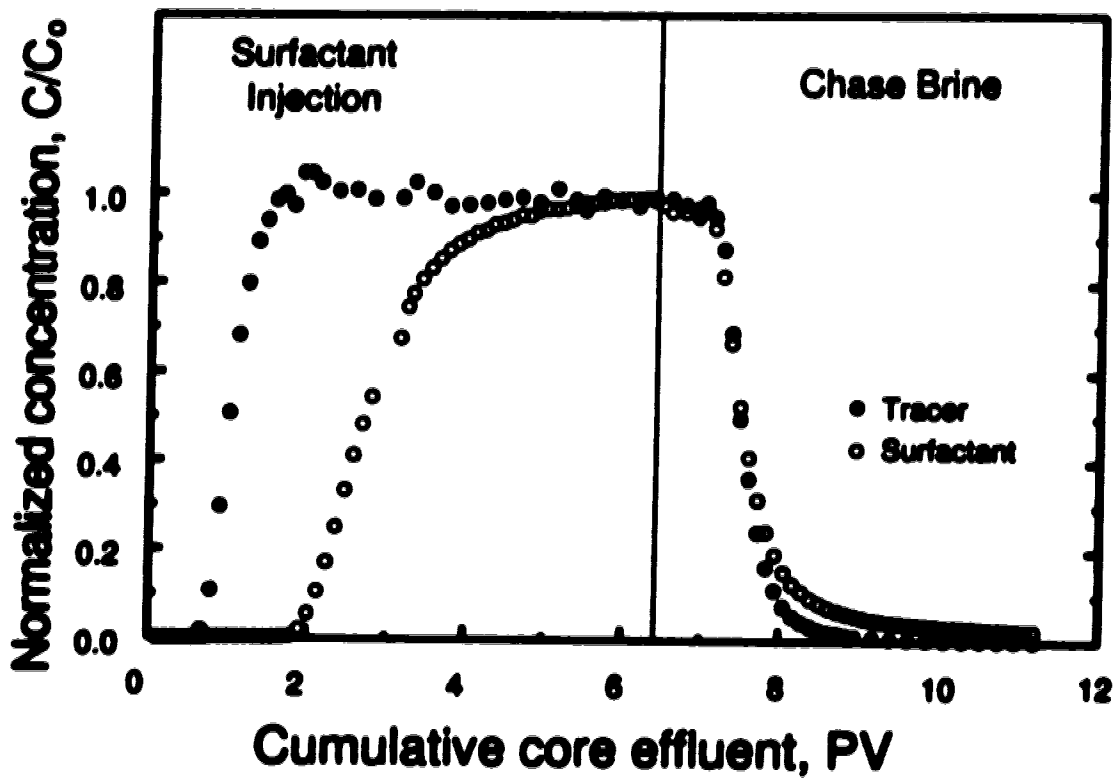


Figure 5-9. Surfactant propagation of 0.47 wt.% Triton X-100 in 8 wt.% sodium chloride at 20 mL/h, followed by a chase brine of 8 wt.% sodium chloride.

the drop in surfactant concentration upon resuming the flow was not as significant. This signifies that the difference between maximum adsorption obtained under static and dynamic conditions increases as the flow rate is increased.

5.2.4 Effect of pH

Four flow experiments, each at an injection rate of 20 mL/h, were conducted using about 0.5 wt.% Triton X-100 with salinities of 3 and 8 wt.% sodium chloride and injection pH of 7 and 12. From the retarded breakthrough curves of effluent surfactant (see Figure 5-10), a reduction of surfactant loss was obtained at the higher pH. This trend is similar to the results obtained from the static adsorption experiments. In this case, dynamic experiments seem to provide a better indication of how pH affects the adsorption values than static tests, especially, when non-ionic surfactant was examined (since relatively small variation was expected).

Interesting trends were observed when the combined effect of salt concentration and pH were examined. It was found that the total surfactant loss was more significant at the low salinity (*i.e.*, 3 wt.% sodium chloride) than that at the high salinity. In this case, the (dynamic) saturation adsorption values, Q_s^d , were reduced by 34 percent for low salinity (3 wt.% sodium chloride) but only 20 percent for high salinity (8 wt.% sodium chloride), see Table 5-1. As mentioned earlier, the tendency of surfactant molecules being hydrated and adsorbed is less probable at low salinity than at high salinity because of the smaller micellar size and aggregation number. High pH condition, in addition, reduces the number of adsorption sites. Therefore, the combined effect of high pH and low salinity resulted in a minimal adsorption loss.

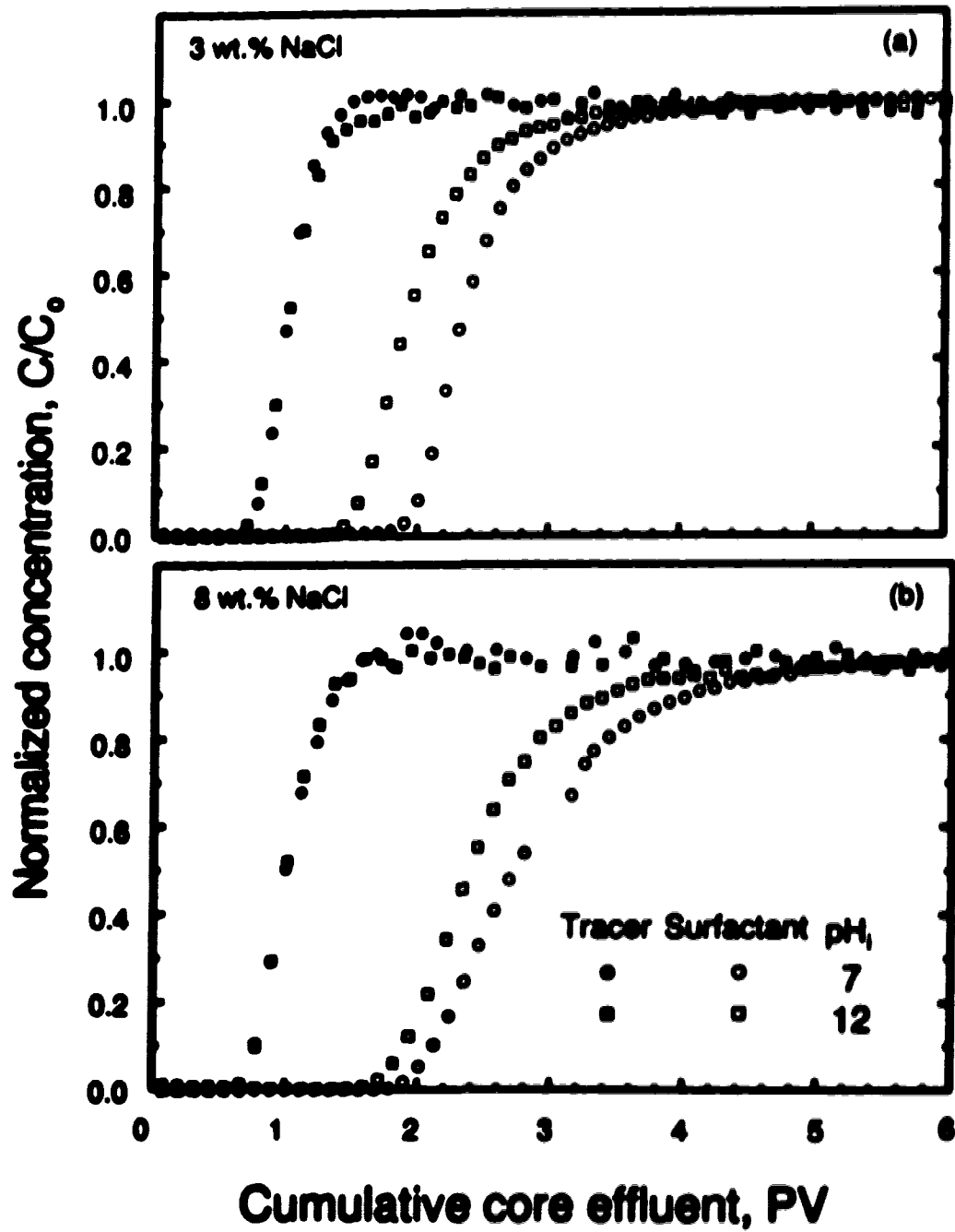


Figure 5-10. Effect of pH on surfactant propagation with 0.5 wt.% Triton X-100 in (a) 3 and (b) 8 wt.% sodium chloride at 20 mL/h, pH_i are 7 and 12.

Chapter 6

Dispersion in Consolidated Sandstone with Radial Flow

In designing a laboratory model for evaluation of the dynamic effects on the adsorption of surfactants, the essential displacement mechanisms must be thoroughly understood and accurately simulated. Since the dispersion mechanism in porous media can be influenced significantly by the spatially varying velocity field as a result of diverging or converging radial flow, velocity-dependence on dispersive transport must first be considered. Unfortunately, most of the previous (experimental) studies were performed in unconsolidated porous media with one-dimensional, linear flow. A precise description of the dispersion mechanisms, coupled with a radial flow field, is difficult and, thus, limits the accuracy of laboratory model predictions.

This chapter presents a brief review on the topics of hydrodynamic dispersion in radial geometry, and the use of the Galerkin finite element method to solve the mass transport in the radial flow equation. The objectives in this chapter are to evaluate the applicability and validity of various dispersion models discussed in the literature, to examine the dependence of the simulated solutions on the different boundary conditions used, and to derive a suitable dispersion model (or mechanism) for the experimental data obtained in this study. Subsequently, part of the numerical results will be employed in the following chapter to examine the effect of adsorption on the effluent surfactant breakthrough observed in the experiments.

6.1 Advection, Diffusion and Dispersion

When one fluid is miscibly displacing another in a homogeneous, isotropic porous medium, the overall transport and mixing of the incompressible fluid can be described by the general advection-dispersion equation, viz.:

$$\frac{\partial c}{\partial t} + \underline{u} \cdot \nabla c = \nabla \cdot (\underline{D} \cdot \nabla c) \quad (6-1)$$

where $c = c(\underline{x}, t)$ is the solute concentration in the bulk of the solution at position \underline{x} and time t , \underline{u} is the mean pore velocity of the fluid and \underline{D} is the dispersion tensor.

Advective transport is due primarily to bulk motions of the fluid. The dispersion term is commonly described by the combined effect of molecular diffusion and mechanical dispersion. Empirical correlations are often expressed in terms of the Péclet number, Pe (Perkins and Johnston, 1967; Fried and Combarous, 1971):

$$\frac{D}{D_m} = \frac{1}{F\phi} + aPe^m \quad (6-2)$$

where D is the effective longitudinal or transverse hydrodynamic dispersion coefficient, D_m is the molecular diffusion coefficient in porous media, F is the formation resistivity factor, ϕ is the porosity, a is a proportionality constant and m is a constant. Note that the definition of D_m should be distinguished from the molecular diffusion in bulk liquid, D_m^* , which is the result of Brownian motion only. The diffusion effect, in this case, is retarded due to the restriction of the pore walls and the lengthened tortuous path:

$$D_m = \frac{D_m^* \phi}{T} \quad (6-3)$$

where T is the tortuosity which is defined as a ratio of the length of a tortuous path to the length of a direct path.

The Péclet number is defined as the ratio of convective transport to diffusive transport:

$$Pe = \frac{ud}{D_m} \quad (6-4)$$

where u is a characteristic velocity and d is a characteristic length. For unconsolidated packs of uniform size sand or beads, the characteristic length d can be taken as the same as the particle diameter.

Fried and Combarous (1971) have summarized a large number of experimental data from the literature, and categorized the ratios of D/D_m into five dispersion regimes according to the Péclet number (see Figure 6-1):

- Regime a.** *Pure molecular diffusion* ($Pe \leq 0.6$): The limiting case of zero velocity (non-flow condition) or very high molecular diffusion coefficient, allows estimation of $1/F\phi$, which is commonly between 0.6 and 0.7.
- Regime b.** *Superimposition* ($0.6 < Pe \leq 6.5$): Both mechanical dispersion and molecular diffusion are important.
- Regime c.** *Predominantly mechanical dispersion* ($6.5 < Pe \leq 300$): Mechanical dispersion is predominant, but the contribution of molecular diffusion cannot be neglected. The dispersion coefficient can be described by Equation (6-2) with $a = 0.5$ and $m = 1.2$ for the longitudinal direction, and $a = 0.025$ and $m = 1.1$ for the transverse direction.
- Regime d.** *Pure mechanical dispersion* ($300 < Pe \leq 2.1 \times 10^3$): The effect of diffusion is negligible in this regime; dispersion can be expressed as a linear function of velocity; that is, $D = \alpha u$.

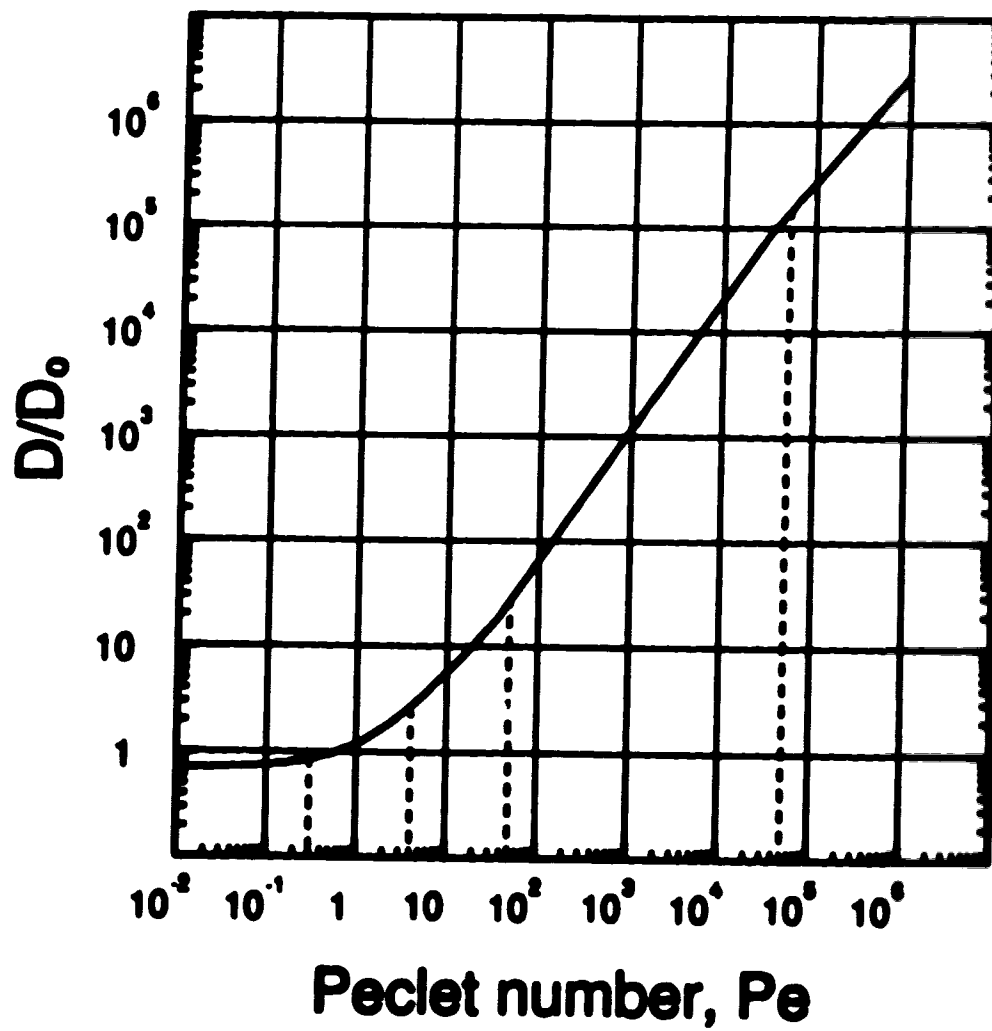


Figure 6-1. Dispersion regimes as a function of Peclet number (Fried and Combarous, 1971).

Regime a. Mechanical dispersion ($Pe > 2.1 \times 10^3$): The flow regime is out of the domain of Darcy's law.

For a consolidated porous medium such as cemented rocks, eg., sandstone, the Péclet number can be defined as

$$Pe = \frac{v\sigma d_p}{D_m} \quad (6-5)$$

where σ is the inhomogeneity factor, and d_p is a characteristic length (grain or pore size). Note that the inhomogeneity factor σ is a measure of the packing characteristics. The theoretical minimum value is unity representing a regularly packed porous medium made up of identical spherical beads. A value of ($\sigma = 3.5$) is typical for random packs. For consolidated porous media, the inhomogeneity factor has no physical meaning. Experimental data are often reported in terms of σd_p , to characterize the specific type of porous media, instead of σ alone. In the literature, values of σd_p are in the range of 0.39 to 0.46 cm for dispersion in consolidated Berea sandstone (Raimondi *et al.*, 1959; Brigham *et al.*, 1961; Perkins and Johnston, 1963; Legatski and Katz, 1967).

6.2 Dispersion in Porous Media with Radial Flow

6.2.1 Approximate and Analytical Solutions

In radial geometry, the first approximate solution was derived by Raimondi and co-workers (1959) in an unpublished manuscript. A comprehensive review of their work has been given by Hoopes and Harleman (1967) and by Tang and Bebe (1979). They considered the case of dispersion in plane, radial flow from a line source of thickness h , along the x -axis at $r = 0$. At a constant volume injection rate Q , the seepage velocity at any radial distance r is obtained from the continuity equation

$$u = \frac{Q}{2\pi hr\phi} = \frac{A}{r} \quad (6-6)$$

where ϕ is the porosity, and A is the flow coefficient which is directly proportional to Q . They then re-examined the dispersion term by introducing a velocity-dependent dispersion coefficient; that is,

$$D = D_e + \alpha u \quad (6-7)$$

where α is called the intrinsic dispersivity (a proportionality constant) and D_e is the effective or apparent diffusion coefficient (defined as the molecular diffusion coefficient D_m divided by the formation resistivity factor F and porosity ϕ , $D_e = D_m/F\phi$). The advection-dispersion equation, Equation (6-1), can be expressed in cylindrical coordinates:

$$\begin{aligned} \frac{\partial c}{\partial t} + \frac{A}{r} \frac{\partial c}{\partial r} &= \alpha_r \frac{A}{r} \frac{\partial^2 c}{\partial r^2} + \alpha_\theta \frac{A}{r} \frac{\partial^2 c}{r^2 \partial \theta^2} \\ &+ \frac{D_e}{r} \frac{\partial}{\partial r} \left(r \frac{\partial c}{\partial r} \right) + \frac{D_e}{r^2} \frac{\partial^2 c}{\partial \theta^2} \end{aligned} \quad (6-8)$$

where α_r and α_θ are the dispersivity coefficients in the r - and θ -directions, respectively. Assuming the concentration distribution is symmetrical with respect to the angular position θ , hence, $\alpha_\theta = 0$ and $\partial/\partial\theta = 0$, and letting $\alpha_r = \alpha$, Equation (6-8) can be reduced to

$$\frac{\partial c}{\partial t} + \frac{A}{r} \frac{\partial c}{\partial r} = \alpha \frac{A}{r} \frac{\partial^2 c}{\partial r^2} + \frac{D_e}{r} \frac{\partial}{\partial r} \left(r \frac{\partial c}{\partial r} \right) \quad (6-9)$$

At some distance away from the source, the influences of dispersion and diffusion on concentration are small in comparison to the total dispersion that has taken place up to that point. Thus, the right-hand side of Equation (6-9) can be neglected which allows a substitution of the spatial gradients by the temporal derivatives (Reimondi *et al.*, 1959; Hoopes and Harleman, 1967; Tang and Babu 1979); that is,

$$\frac{\partial}{\partial r} = -\frac{r}{A} \frac{\partial}{\partial t} \quad (6-10)$$

Introducing Equation (6-10) into the dispersion and diffusion terms of Equation (6-9) leads to the following expression

$$\frac{\partial c}{\partial t} + \frac{A}{r} \frac{\partial c}{\partial r} = \left(\alpha \frac{r}{A} + D_0 \frac{r^2}{A^2} \right) \frac{\partial^2 c}{\partial t^2} \quad (6-11)$$

For continuous injection at a steady rate with concentration C_0 at $r = 0$, the general solution is given by

$$\frac{c}{C_0} = \frac{1}{2} \operatorname{erfc} \left(\frac{A/r^2 - 1/2}{f(r)} \right) \quad (6-12)$$

where

$$f^2(r) = \frac{4}{3} \frac{\alpha}{r} + \frac{D_0}{A}$$

subject to the following conditions

$$\begin{aligned} c(r,t) &= 0 & \text{at } t &= 0 & \text{(initial),} \\ c(r,t) &= C_0 & \text{at } r &= 0 & \text{(line source)} \\ \text{and } c(r,t) &= 0 & \text{at } r &= \infty & \text{(exit)} \end{aligned}$$

Assuming the dispersion coefficient is much larger than the diffusion coefficient ($D \gg D_0$) the diffusion term, D_0 , in Equation (6-11) can be set equal to zero. Hoopes and Harleman (1967) showed that with suitable modifications the dispersivity coefficient defined in Equation (6-7) can be evaluated directly from a plot of C/C_0 versus $1-x$ on arithmetic probability paper such that

$$\alpha = \frac{3}{8} r \delta^2 \quad (6-13)$$

where δ is the standard deviation obtained. The new function χ is defined as $\chi = 2A(t - t_{50})/r^2$ and t_{50} is the time at which $C/C_0 = 0.5$. Note that C is defined as the measured or calculated solute concentration at the position denoted by r . In their experimental work, dispersivity data were obtained by injecting a sodium chloride solution into a recharge well of a sand pack model. The salt concentration was measured using conductivity probes located at different radial positions. Dispersivity coefficients, α , evaluated from Equations (6-12) and (6-13) were found to be constant, and independent of radial distance. A finite difference approximation (Shamir and Harleman, 1967) of Equation (6-9) was used to compare with the approximate solution. Less than 1 % error was resulted for large dimensionless time, $\tau = At/\alpha^2 > 1000$.

Bentsen and Nielsen (1965) also used the above approximate solution, Equation (6-12), to examine the effect of viscosity on dispersion. Core flood experiments were performed using fluids of having viscosities ranging from 0.4 to 3.4 mPa·s and injecting at different mobility ratios (0.25 - 1.02) in circular, consolidated Berea sandstone slabs. A very close agreement between experiment and theory was observed except near the entrance and exit. The dispersivity coefficient, α , was shown to be independent of velocity, and to be a linear function of favourable mobility ratio; that is, mobility ratios of less than one.

Gelhar and Collins (1971) extended Raimondi's approximate solution to generalize the cases of uniform, radial and spherical flows. They showed that the effects of flow configuration can be analyzed in terms of the growth of the dispersion zone since the estimated dispersion zones of radial and spherical flows were $3^{1/2}$ and $5^{1/2}$ times, respectively, thinner than that of linear flow. In the case of radial flow, they obtained a new solution that accounts for a finite injection radius; that is, the boundary conditions of

$$\begin{aligned}
 c(r,t) &= 0 & \text{at } t &= 0 & \text{(initial),} \\
 c(r,t) &= C_w & \text{at } r &= r_w & \text{(well bore)} \\
 \text{and } c(r,t) &= 0 & \text{at } r &= \infty & \text{(exit)}
 \end{aligned}$$

The results were also compared with numerical solutions. Good approximations can be obtained provided that the total distance travelled by the injection front is at least 100 times greater than the dispersivity coefficient.

An exact analytical solution for the radial dispersion problem was first derived by Tang and Babu (1979). They considered a simplified form of Equation (6-11):

$$\frac{\partial c}{\partial t} + \frac{A}{r} \frac{\partial c}{\partial r} = \alpha \frac{A}{r} \frac{\partial^2 c}{\partial r^2} \quad (6-14)$$

for $D \gg D_w$ and $D = \alpha u$. The problem is solved by applying the Laplace transformation (\mathcal{L}) in the t -variable; that is, multiply Equation (6-14) by e^{-st} and then integrate the resultant term with respect to t from 0 to ∞ :

$$rs\bar{c} + A \frac{\partial \bar{c}}{\partial r} = \alpha A \frac{\partial^2 \bar{c}}{\partial r^2} \quad (6-15)$$

where

$$\bar{c}(r,s) = \mathcal{L}\{c(r,t)\} = \int_0^{\infty} e^{-st} c(r,t) dt$$

and s is the Laplace complex variable. The general procedure for solving this equation can be found in standard advanced calculus text books, for example Hildebrand (1976):

$$\frac{\bar{c}}{C_0} = \frac{1}{s} \exp\left(\frac{r - r_w}{2\alpha}\right) \frac{\text{Ai}(Y)}{\text{Ai}(Y_w)} \quad (6-16)$$

where

$$Y = \frac{rp + \alpha/4}{\alpha p^{2/3}} \quad \text{for } p = \frac{\alpha^2}{A} s$$

and $\text{Ai}(Y)$ is the Airy function, which is defined as

$$\text{Ai}(Y) = \pi^{-1} \left(\frac{Y}{3}\right)^{3/2} K_{1/3}(\zeta) \quad (6-17)$$

where $\zeta = 2/3 Y^{3/2}$ and $K_{1/3}(\zeta)$ is the modified Bessel function of the second kind. The inverse Laplace transform (\mathcal{L}^{-1}) can be obtained by methods of complex variable theory. The inversion formula is

$$c(r,s) = \mathcal{L}^{-1}\{\bar{c}(r,s)\} = \frac{1}{2\pi i} \int_{\gamma-i\infty}^{\gamma+i\infty} e^{st} \bar{c}(r,s) ds \quad (6-18)$$

where $i = (-1)^{1/2}$ and γ is chosen so that all the singular points of $\bar{c}(r,s)$ lie to the left of the line $\text{Re}(s) = \gamma$ in the complex plane (s -plane). Tang and Babu derived the solution by direct evaluation of the integral along the (Bromwich) contour on the complex plane. They found very good agreement between this analytical solution and the finite-difference solution of Hoopes and Harleman (1967).

Hsieh (1986) later presented a simpler form of the exact analytical solution for Equations (6-14) to (6-16) by evaluating the Airy function in terms of an expansion equation given in the "Handbook of Mathematical Functions" (Abramowitz and Stegun, 1964):

$$Ai(Y) \cong \frac{1}{2\sqrt{\pi} Y^{1/4}} \exp(-\zeta) \sum_{k=0}^{\infty} (-1)^k V_k \zeta^k \quad (6-19)$$

where

$$V_k = \frac{(2k+1)(2k+3)\dots(6k-1)}{216^k k!} \quad \text{and} \quad \zeta = \frac{2}{3} Y^{3/2}$$

When compared with the Tang and Babu's method, Hsieh found that the new formula improves the accuracy of the results and reduces the effort of computation. Very good agreement was found between his solution and the finite-difference solution of Hoopes and Harleman (1967). For the case of finite injection radius, $r = r_w > 0$, Hsieh also showed an improvement over the approximate solution previously derived by Gelhar and Collins (1971), such that a usable estimate can be obtained when the total distance travelled by the injection front is 15 times (rather than 100 times) greater than the dispersivity coefficient, α .

On the other hand, Moench and Ogata (1981) studied a numerical Laplace inversion formula for Equation (6-18) developed by Stehfest (1970). Although the accuracy of the results is limited, the method is simple, requires little computation, and can be programmed on a hand-held calculator. For small dimensionless times, $\tau = At/\alpha^2 \leq 1800$, they showed that as low as 18 terms in the inversion formula is sufficient to give results in close agreement with Hoopes and Harleman's (1967) finite-difference solution.

Chen (1987) investigated the effect of the boundary condition at the wellbore of an aquifer. Consider the boundary condition at the exit, $C = 0$ at $r \rightarrow \infty$; this suggests that the physical system is a small portion of an infinitely large aquifer. If material balance is invoked, the fluid injected ($Q C_w$) must enter the aquifer through the well surface by advection and dispersion at the same rate as the rate of fluid flowing across any (cylindrical) plane; that is, continuity of flux. This situation can be represented by a Cauchy boundary condition:

$$\underline{u}c + \underline{D} \cdot \nabla c = \underline{u}C_s + \underline{D} \cdot \nabla C_s \quad (6-20)$$

for $\nabla C_s = 0$. Since the velocity is high near the wellbore, dispersion is assumed to be dominated by advection and mechanical dispersion: therefore, the Cauchy boundary condition can be expressed (using $D = \alpha u$) as

$$c - \alpha \frac{\partial c}{\partial r} = C_s \quad \text{at } r = r_w \quad (6-21)$$

A solution of Equations (6-14) and (6-21) was obtained using the Laplace transform and the inversion technique as applied in Hsieh (1986):

$$\frac{\bar{c}}{C_s} = \frac{1}{s} \exp\left(\frac{r - r_w}{2\alpha}\right) \frac{2 \text{Ai}(Y)}{\text{Ai}(Y_w) - 2s^{1/3} \text{Ai}'(Y_w)} \quad (6-22)$$

where Y and Y_w are defined same as in Equation (6-16). The Airy function $\text{Ai}(Y)$ is the bounded solution for the Airy equation and satisfies the relationship: $\text{Ai}''(Y) = Y \text{Ai}(Y)$, for $\text{Ai}'(Y)$ and $\text{Ai}''(Y)$ denoting the first and second derivatives of $\text{Ai}(Y)$, respectively. Disagreement between the two solutions was observed, especially for short injection periods. For example, at the dimensionless time of $\tau = 0.01$ ($= At/\alpha^2$) with $r_w = \alpha$, the Dirichlet condition ($C = C_s$ at $r = r_w$) predicts the concentration front at a distance 1.4α away from the injection well, whereas, the Cauchy condition predicts the front at about 1.23α . It was suggested that the sharp concentration gradient forces more solute into the aquifer contradicting the conservation of mass. As the local concentration gradient decreases at large τ , the solution for both the Dirichlet and the Cauchy boundary conditions become practically identical. Similar observations have been reported and discussed previously by Brigham (1974) for linear dispersion problems.

At this point, several available analytical solutions for the transport equation in porous media with radial flow has been reviewed. For the simplest case (as in Raimondi's solution), dispersion coefficients can be approximated easily from a probability plot; whereas, an exact solution must be obtained using the integral transform

techniques. As the physical system becomes more complicated, for example, the Cauchy boundary condition at the entrance, or the presence of reaction or adsorption, analytical solutions are complicated by the added parameters and variables. In addition to the drawbacks and limitations of the boundary condition and the evaluation of complicated integrals, the analytical solutions found are only available for the simplest dispersion models, *viz.*, a linear relationship between the dispersion coefficient and velocity, $D = \alpha u$. Development of numerical methods is therefore essential for describing more complicated physical systems.

6.3 Dispersion Characteristics of Tracer and Surfactant

In core flood experiments, loss of surfactant due to adsorption was estimated from the difference in the integrated areas between the surfactant and tracer profiles (normalized effluent concentration versus cumulative volume). This method, however, is valid only if the following assumptions are satisfied: (1) both tracer and surfactant propagate through the porous medium at the same rate in the absence of adsorption, and (2) the molecular size and structure of the two components are very similar such that the magnitudes of dispersion and diffusion in the liquid phase are comparable. It is obvious that the second condition can never be satisfied since surfactant molecules are made up of long-chain hydrocarbons and tend to aggregate as concentration increases (known as micellization) and tracer molecules, tritium which is an isotope of hydrogen, occupy much smaller volumes. The following experiment is thus performed to examine the consequence of such discrepancies.

Two surfactant solutions were prepared in 3.0 wt.% sodium chloride solution. The first solution contained 0.52 wt.% Triton X-100 and 0.02 wt.% tracer. The second solution was prepared by diluting the first solution to about half of its concentration using a sodium chloride solution of the same salinity. The exact surfactant and tracer concentrations were determined as described in Chapter 3. The lower concentration surfactant solution was first injected until the measured effluent concentration reached the

injection level of 0.26 wt.% (assuming maximum adsorptive capacity achieved). The higher concentration solution was then injected. Propagation of surfactant in this step is presumed due to the effects of dispersion and diffusion only in the absence of adsorption. Injection was continued for about three pore volumes until the effluent profile approaches a plateau, and then followed by the lower concentration solution and chase brine in order to verify material balances.

Figure 6-2 shows the complete profile (two-step injection) of tracer and surfactant as a function of cumulative effluent pore volume. In Figure 6-3, the upper portion of the profiles in Figure 6-2 is replicated in terms of the normalized concentration, C_2/C_0 , versus the corrected effluent volume, V_2/V_p , for

$$\frac{C_2}{C_0} = \frac{C - C_1}{C_2 - C_1} \quad \text{and} \quad \frac{V_2}{V_p} = \frac{V - V_1}{V_p}$$

where C is the measured concentration of tracer or surfactant in the effluent, C_0 is the reference concentration which is equal to the difference in injection concentrations between the first and second solutions, $C_2 - C_1$, and V is the volume of liquid collected, V_1 is the total liquid volume collected at the end of the first solution injection, and V_p is the measured pore volume. Both components began breakthrough after 0.6 pore volumes of injection and levelled at $C_2/C_0 = 1.0$ after 1.4 pore volumes. Almost identical breakthrough curves were observed indicating that these two components are very similar in their dispersion characteristics under the flow conditions considered in this investigation; that is, the assumption of similar rates of propagation for both components may be valid, at least for the range of flow rates used. Adsorptive losses estimated from the integrated areas should provide a good approximation.

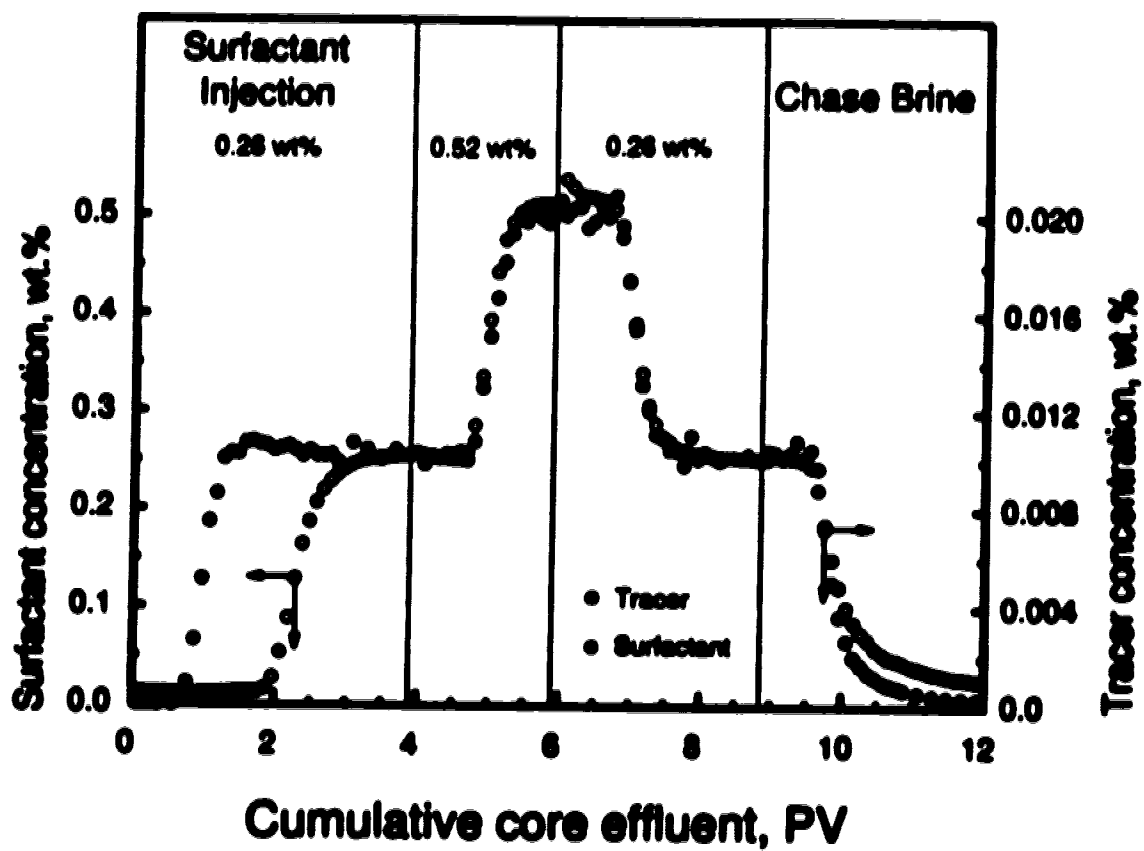


Figure 6-2. Surfactant propagation in Berea sandstone core of 0.26/0.52 wt.% Tricon X-100 (two-step injection) with 3 wt.% sodium chloride at 20 mL/h.

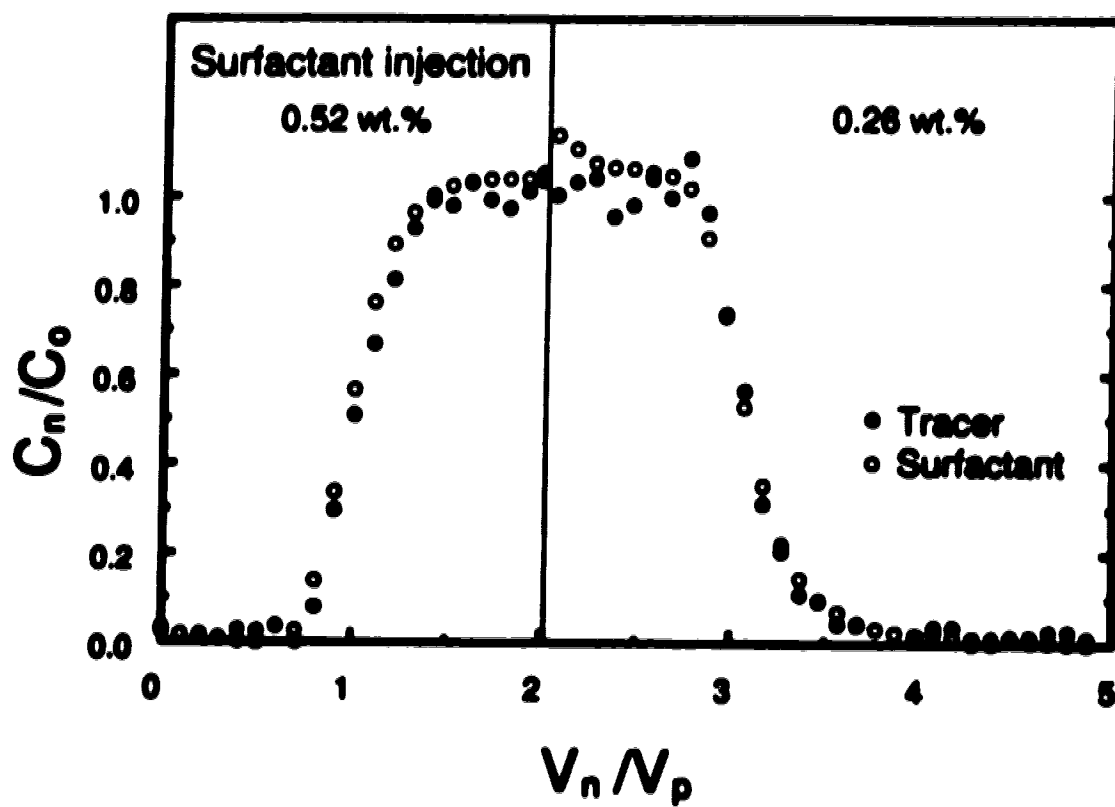


Figure 6-3. Dispersion of tracer and surfactant in Berea sandstone in the absence of adsorption.

6.4 Mathematical Description of the Experimental Data

Assuming that the flow field is symmetric with respect to the angular position, the velocity distribution along the radial distance is one-dimensional and can be obtained directly from the continuity equation, $\nabla \cdot \mathbf{u} = 0$, as in Equation (6-6); that is, velocity varies inversely with the radius, $u = A/r$.

For the experiment described in Figures 6-2 and 6-3, the measured core dimension was 88.38 mm in diameter and 35.10 mm in height with a wellbore diameter of 3.50 mm. The pore volume and porosity were 49.47 cm³ and 0.23, respectively. Using Equation (6-6), $A = 1.095 \times 10^{-7}$ m²/s for the injection rate of 20 mL/h, and the calculated seepage velocities at the entrance and exit were 6.082×10^{-5} and 2.478×10^{-6} m/s, respectively.

Figure 6-4 shows the relationship of the seepage velocity of the displacing fluid (normalized by the injection velocity at the entrance, u_{inj}) as a function of pore volume and radial distance. The fluid velocity is inversely proportional to the radial distance as described by the mathematical equation. This plot suggests that, after the first 0.1 PV of injection, the front of the displacing fluid would have advanced for about 14 mm away from the wellbore (~32 percent of the core radius) and the velocity would have been reduced by about 88 percent. The velocity then decreases slowly for the next 0.9 pore volumes of travel. Using an estimated value of the molecular diffusion coefficient for tritium in water of $D_m = 6.25 \times 10^{-9}$ m²/s, the calculated Péclet numbers were about 38.0 at the entrance and 1.55 at the exit with $cd_p = 0.39$ cm (Brigham *et al.*, 1961). The reduction in the seepage velocity represents a transition of dispersion characteristics from *Regime c* to *Regime b* as defined by Fried and Combarous (1971).

6.5 Numerical Simulations of Dispersion with Radial Flow

The solution of the general advection-dispersion equation, Equation (6-1), can be approximated by applying the Galerkin finite element method. The governing equation

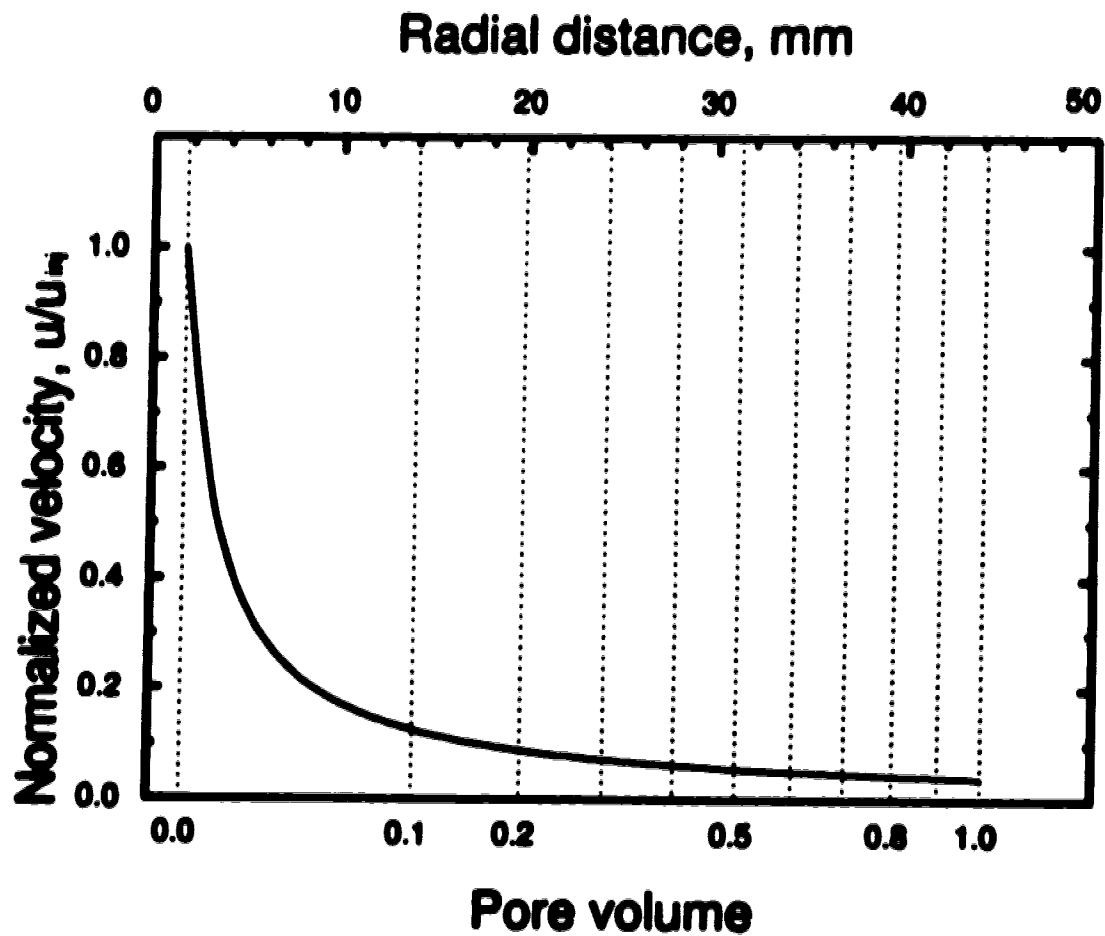


Figure 6-4. Variation of pore velocity as a function of radial distance and fraction of pore volume.

in the form of a weighted variational equation:

$$\int_{\Omega} \left[\psi \frac{\partial c}{\partial t} + \psi \underline{u} \cdot \nabla c - \psi \nabla \cdot (\underline{D} \cdot \nabla c) \right] d\Omega = 0 \quad (6-23)$$

where ψ is the Galerkin test function and Ω denotes the entire solution domain. The unknown concentration C can be estimated using a trial value \hat{C} as a linear combination with ψ over the domain Ω :

$$c \cong \hat{c}(\underline{x}, t) = \sum_{i=1}^n \psi_i(\underline{x}) c_i(t) \quad (6-24)$$

in which C_i are the unknown nodal values to be determined at position \underline{x} and time t , and n is the total number of nodes in the finite element network.

The variational problem was solved by first discretizing the domain Ω into m finite elements where the subregion of any element e is denoted by a local domain Ω^e . In the current study, a bi-quadratic triangular element with six nodes was used. The solution for the time derivative was evaluated using the implicit second-order Gear scheme. Details of the mathematical formulation and treatment are summarized in Appendix B.

6.5.1 Numerical Approximations and Errors

Assuming the effect of molecular diffusion is negligible compared to mechanical dispersion $D \gg D_m$, Equation (6-1) can be re-written as Equation (6-14) with $D = \alpha u = \alpha A/r$ (Hoopes and Harleman, 1967; Tang and Babu, 1979):

$$\frac{\partial c}{\partial t} + \frac{A}{r} \frac{\partial c}{\partial r} = \alpha \frac{A}{r} \frac{\partial^2 c}{\partial r^2}$$

... (6-14)

A numerical solution was determined using the following initial and boundary conditions:

$$c(r,t) = 0 \quad \text{at } t = 0 \quad (\text{initial}),$$

$$c(r,t) - \alpha \frac{\partial c(r,t)}{\partial r} = C_0 \quad \text{at } r = r_w \quad (\text{well bore})$$

and

$$c(r,t) = 0 \quad \text{at } r \rightarrow \infty \quad (\text{exit})$$

Very good agreement between the experimental data and the numerical simulation was observed as shown in Figure 6-5 with the solid line representing the results obtained from the simulation using $\alpha = 5.0 \times 10^{-4}$ m.

Possible truncation errors resulting from numerical discretization were examined by varying the time step Δt and the mesh size h (approximate length of a side in the triangular elements). The results are shown in Figures 6-6 and 6-7 using the same parameters as in Figure 6-5. At a flow rate of 20 mL/h, a time step of 20 seconds is sufficient to provide a reliable approximation. On the other hand, a mesh size of at most 1.77 mm width is required, which corresponds to 50 triangular elements uniformly spaced from the wellbore to the core exit for the core radius of 44.2 mm.

Based on the analysis in Figure 6-4, it is recognized that sharp velocity (and concentration) gradients occurred across the first 1/10 pore volumes. It is therefore of interest to examine the use of non-uniform mesh near the wellbore. As illustrated in Figure 6-8, a non-uniform mesh was constructed from a "base mesh" with ($h = 0.884$ mm) such that the smallest triangles are approximately one tenth the size of the base elements. Figure 6-9 shows the breakthrough curves, predicted by using the uniform and non-uniform meshes, at a distance 3 mm away from the wellbore (or $r = 4.75$ mm, corresponding to 1/100 of the total pore volume). No significant difference was observed.

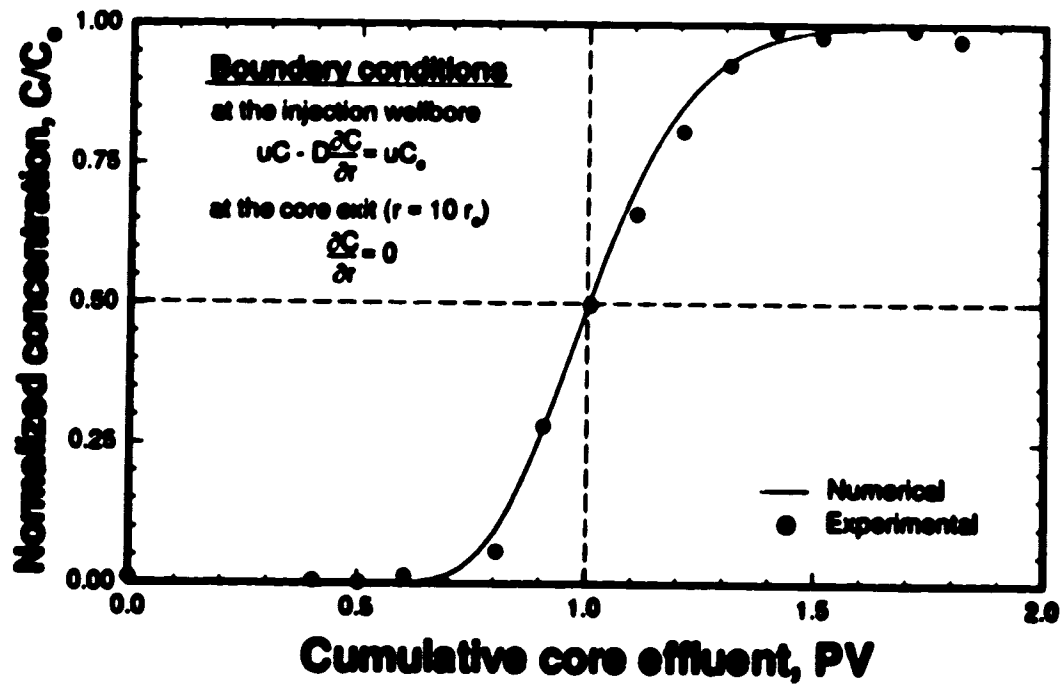


Figure 6-5. Comparison of experimental data and numerical simulation with dispersion model: $D = \alpha u$ for $\alpha = 5.0 \times 10^{-4}$ m.

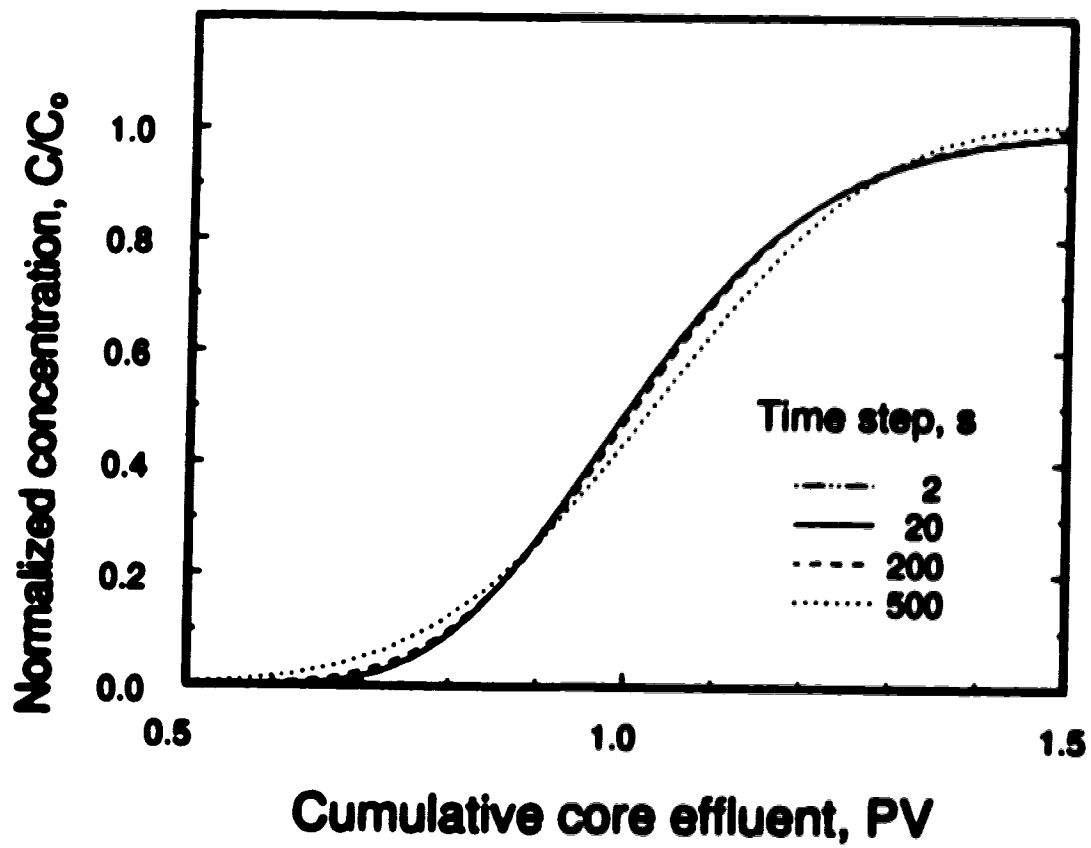


Figure 6-6. Effect of time step on the predicted concentration profile, with dispersion defined as $D = \alpha u$ for $\alpha = 5.0 \times 10^{-4}$ m.

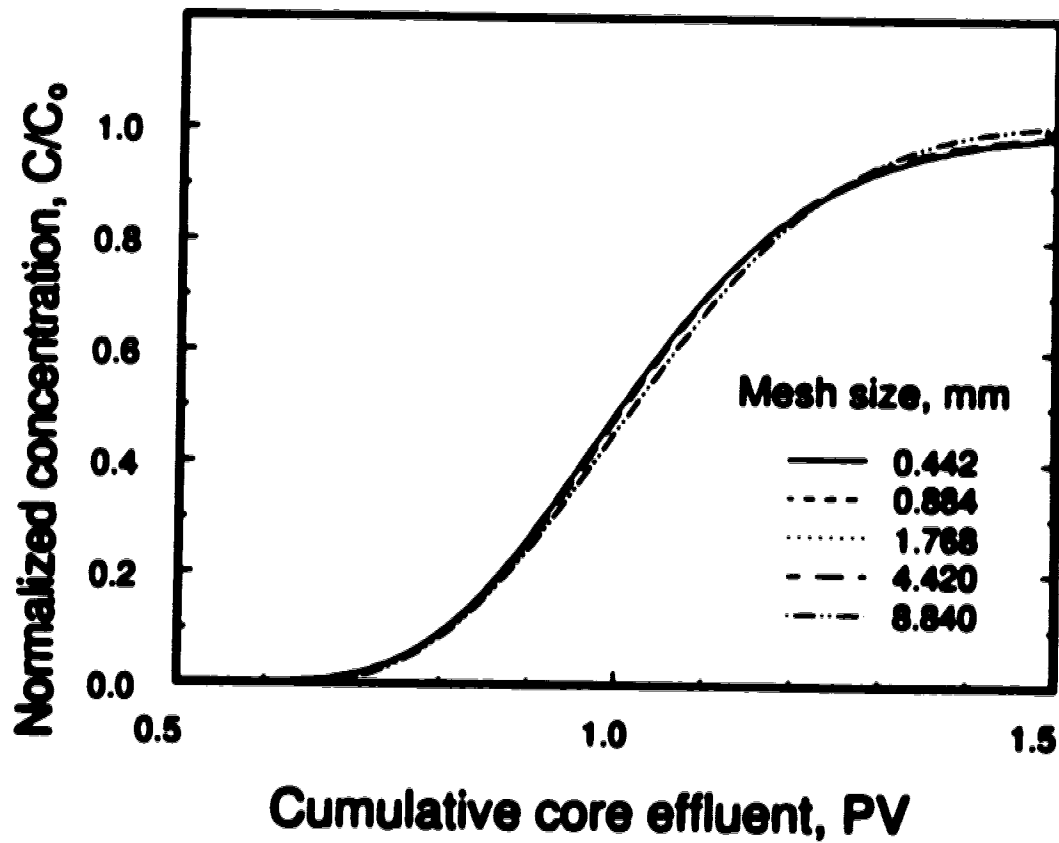


Figure 6-7. Effect of mesh size on the predicted concentration profile, with dispersion defined as $D = \alpha u$ for $\alpha = 5.0 \times 10^{-4}$ m.

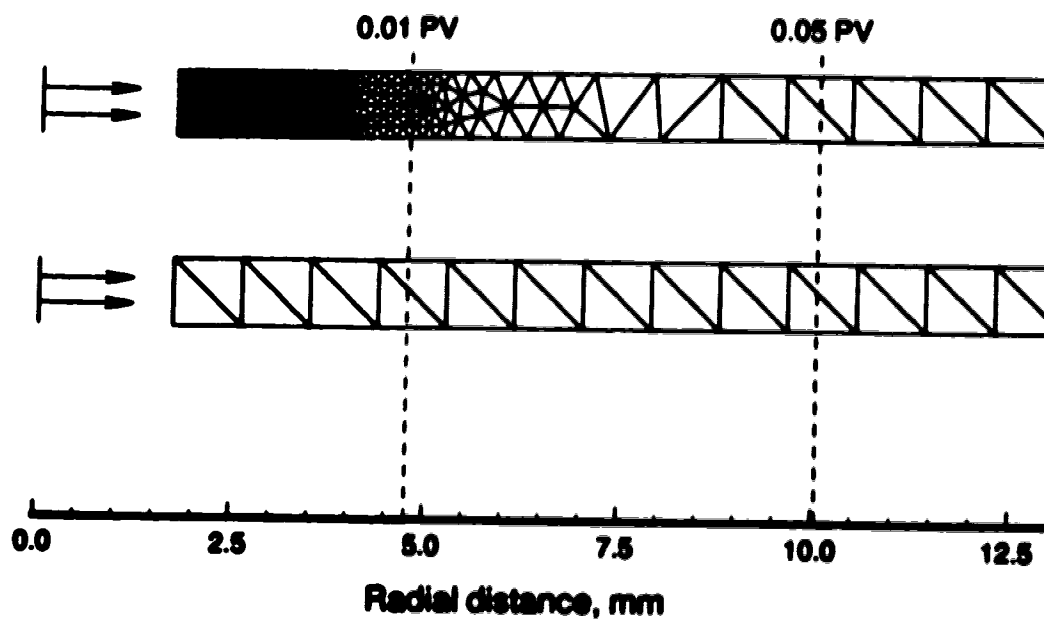


Figure 6-8. Physical layouts and dimensions of uniform and non-uniform meshes defined near the wellbore for finite element analysis.

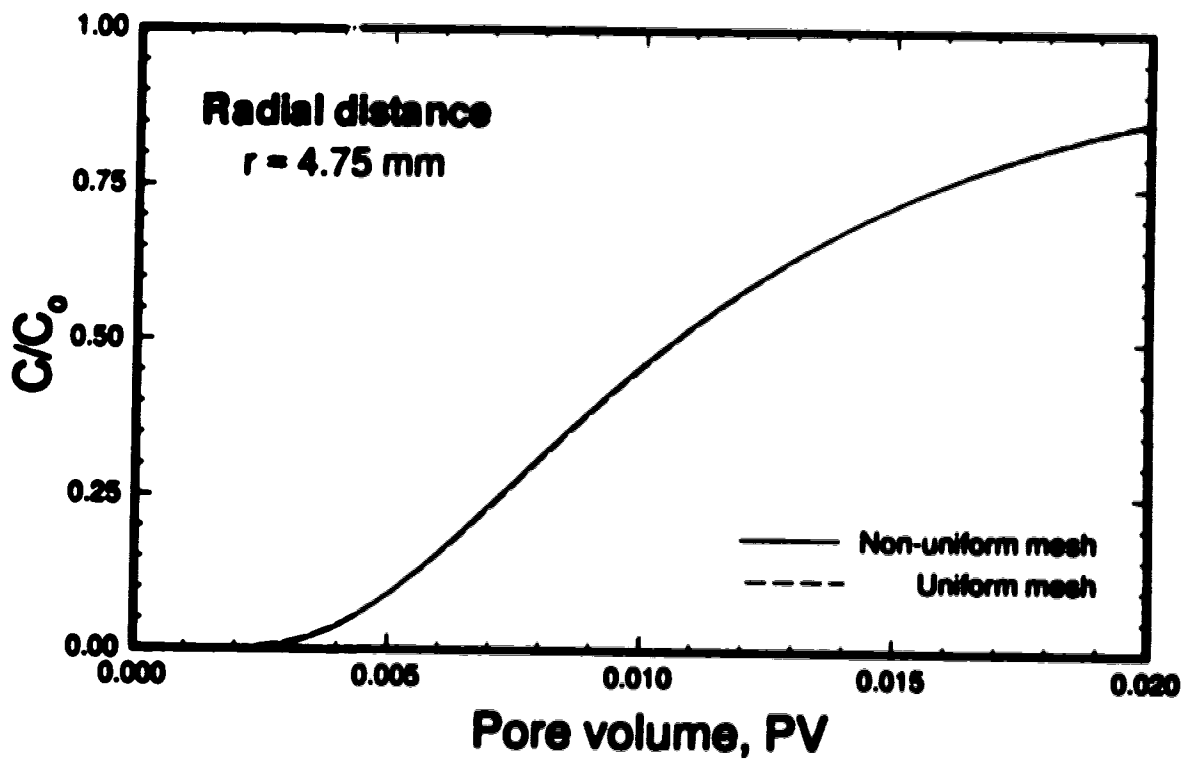


Figure 6-9. Comparison of simulation results with dispersion model: $D = \alpha u$ for $\alpha = 5.0 \times 10^{-4}$ m, using uniform and non-uniform mesh.

6.5.2 Comparison of Numerical Solution with Analytical Solutions

The validity of the numerical model is established by comparing the numerical solution with Chen's (1987) solution. The complete solution for Equations (6-14) subject to the Cauchy condition at the wellbore is given by Equation (6-22). For small dimensionless time, $\tau = At/\alpha^2 \ll 1$, the Airy function and its first derivative can be approximated by

$$\begin{aligned} \text{Ai}(Y) &\cong \frac{1}{2\sqrt{\pi}} Y^{-1/4} \exp(-\zeta) \\ \text{Ai}'(Y) &\cong \frac{-1}{2\sqrt{\pi}} Y^{1/4} \exp(-\zeta) \end{aligned} \quad (6-25)$$

The inverted form of Equation (6-22) can then be expressed as

$$\begin{aligned} \frac{c}{C_s} &= 2 \exp\left(\frac{r-r_w}{2\alpha}\right) \left(\frac{r_w}{r}\right)^{1/4} \times \left[\text{erfc}\left(\frac{m}{2} \sqrt{\frac{\alpha^2}{At}}\right) \right. \\ &\quad \left. - \exp\left(\frac{m}{2} \sqrt{\frac{\alpha}{r_w}} + \frac{1}{4} \frac{At \alpha}{\alpha^2 r_w}\right) \text{erfc}\left(\frac{m}{2} \sqrt{\frac{\alpha^2}{At}} + \frac{1}{2} \sqrt{\frac{At \alpha}{\alpha^2 r_w}}\right) \right] \end{aligned} \quad (6-26)$$

where $m = 2/3(\rho^{2/3} - \rho_w^{2/3})$ for $\rho = r/\alpha$ and $\rho_w = r_w/\alpha$. On the other hand, the solution for the Dirichlet boundary condition is (Tang and Babu, 1979)

$$\frac{c}{C_s} = \exp\left(\frac{r-r_w}{2}\right) \left(\frac{r_w}{r}\right)^{1/4} \text{erfc}\left(\frac{m}{2} \sqrt{\frac{\alpha^2}{At}}\right) \quad (6-27)$$

which is always equal to unity at $\rho = \rho_w$. Comparisons of Equations (6-26) and (6-27) with the numerical solutions, for $\rho_w = 1$ (i.e., $r_w = \alpha$) and $\tau = 0.01, 0.05$ and 0.2 shown in Figure 6-10, clearly indicate the agreement between the analytical and the numerical solutions.

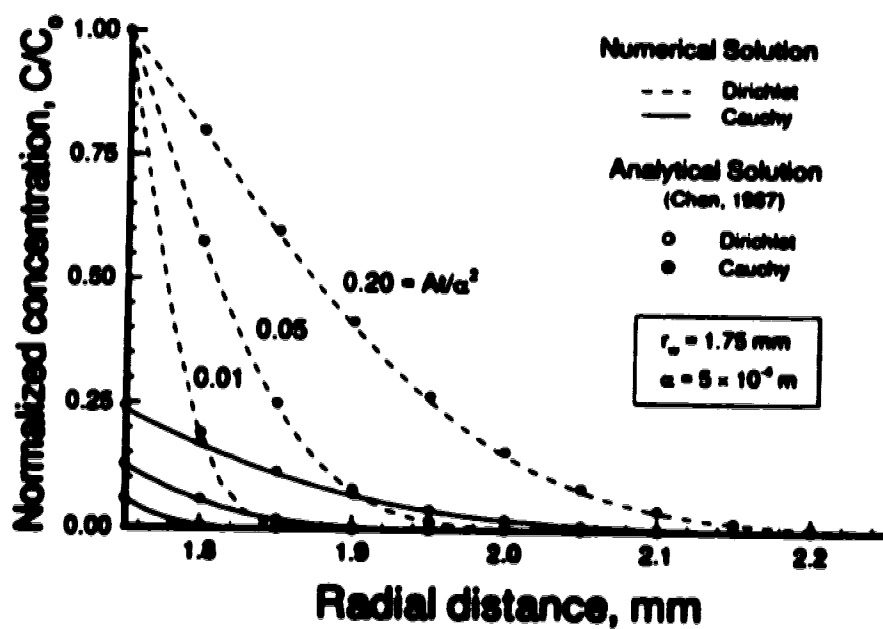


Figure 6-10. Comparisons showing the difference in concentration profiles obtained from analytical the solution (Chen, 1987) and numerical simulation near the wellbore for small injection times.

6.5.3 Boundary Condition at the Injection Wellbore

As illustrated by the results obtained in Section 6.5.2, which are based on Chen (1987), the boundary condition at the injection well appears to play an important role in determining the flow characteristics and concentration distribution across the porous core. For linear dispersion problems, it has long been recognized that the entrance boundary condition is a significant factor, especially, for injection into a "short" core (Brigham, 1974). There have been, however, very few studies on the effect of the boundary condition at the wellbore for dispersion with radial flow. Chen (1987) compared the two (analytical) solutions for large τ (dimensionless time) in a semi-infinite core. The two solutions converged to the same profile as time and radial distance increased. No generalized or conclusive correlation was offered. Gelhar and Collins (1971) found a decrease in mixing length for dispersion in radial flows as compared to uniform or linear flow problems. Such a shortened dispersion zone may suppress the effect of a sharply dropping seepage velocity near the wellbore on dispersion. In this section, several simulations were performed to examine and explain the importance of the entrance boundary condition under the current experimental set-up.

Figures 6-11a through 6-11c show the breakthrough curves of the simulation results for various radial distances, $r = 4.75, 14.08$ and 44.2 mm, with a wellbore radius r_w of 1.75 mm and a flow coefficient A of $1.095 \times 10^{-7} \text{ m}^2/\text{s}$ (for $Q = 20 \text{ mL/h}$). The results clearly indicated that the entrance boundary condition becomes important as the core radius is reduced. Further studies, by varying the core and the wellbore dimensions, provide an estimate of a limiting ratio, $r/r_w \geq 10$, for the entrance boundary effect becoming negligible. It may be concluded that either the Dirichlet or the Cauchy condition applied at the entrance may result in an equally valid solution under the current experimental condition, where the actual core radius, r_c , was 44.2 mm.

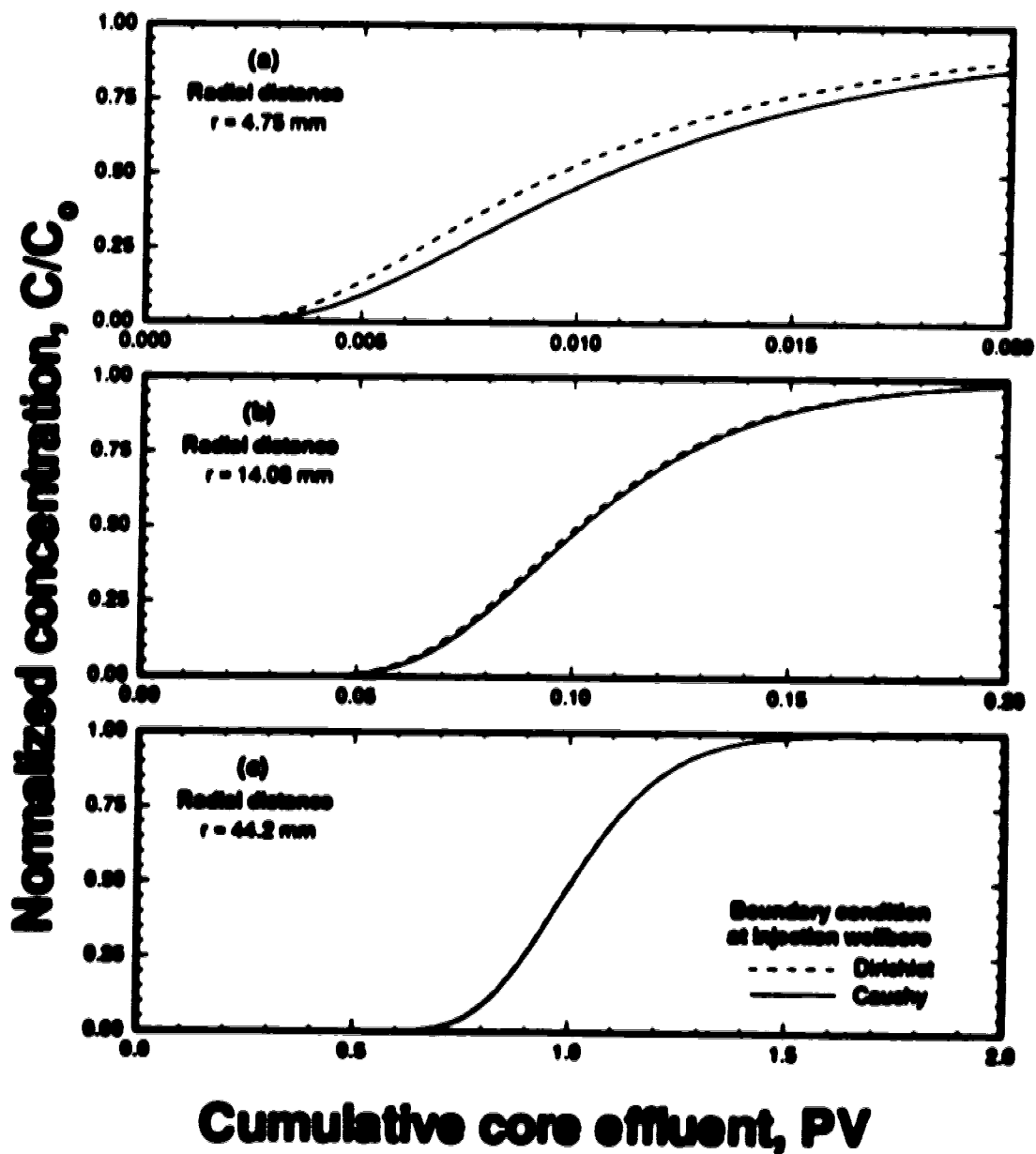


Figure 6-11. Comparison of breakthrough curves for dispersion with radial flow for core radii of (a) 4.75 mm, (b) 14.08 mm and (c) 44.2 mm.

6.5.4 Boundary Condition at the Core Exit

In the experiment, the effluent solution was first collected in the annulus between the sandstone core and the core holder (thickness < 0.5 mm), and then transferred to a sampling tube for analysis. The condition across the core-annulus boundary defined in mathematical modelling is therefore important for proper interpretation of the measured (effluent) concentrations.

In early displacement studies, an assumption of continuous concentration distribution at the exit boundary is frequently applied; that is, a zero flux (or concentration gradient) condition is imposed at the exit:

$$\frac{\partial c}{\partial t} = \frac{\partial c}{\partial r} = 0 \quad \text{at } r = r_c \quad (6-28)$$

where r_c is the (exit) radius of the sandstone core. This condition is however not necessary to provide a good description of the physical system. As illustrated in Figure 6-10, for the Cauchy condition, the requirement of mass conservation across the boundary leads to a discontinuous concentration distribution at the wellbore, which seems to contradict the necessity of having a continuous concentration distribution at the exit boundary. On the other hand, for a physical system using cores of small radius (especially, applicable to physically well-defined finite cores used in laboratory studies), the above imposed zero flux condition may force mass out at the exit; that is, mass will not be conserved. In this case, solutions of the mathematical approximation may be improved by using a semi-infinite core. Instead of imposing a zero concentration gradient at $r = r_c$, we apply

$$\frac{\partial c}{\partial t} = \frac{\partial c}{\partial r} = 0 \quad \text{at } r \rightarrow \infty \quad (6-29)$$

The calculated concentration at r_c is in fact equivalent to the concentration evaluated at a point in a continuum, without the knowledge of having a discontinuous solid phase.

In the literature, because of the relatively small influence of the imposed boundary conditions, analytical and numerical solutions are often derived from one of the above boundary conditions. It is, however, clear that if the requirement for the continuity of flux across the exit boundary is considered, the boundary condition may be written as

$$\underline{u}c + \underline{D} \cdot \nabla c = \underline{g}C_o + \underline{D}_o \cdot \nabla C_o \quad (6-30)$$

where C_o is the concentration within the annulus, \underline{g} is the velocity vector of liquid in annulus ($= Q/\pi r_o^2 h = \phi \underline{u}$, discharge per unit cross-sectional area normal to the direction of flow), and \underline{D}_o is the dispersion tensor (in the absence of a porous medium or open vessel). Previous investigations of this boundary condition have been sparse mainly due to the introduction of errors and uncertainties as such factors as flow in an open vessel, geometry and dimensions near the discharging area are being considered.

In the current study, only solutions obtained using the boundary conditions of Equations (6-28) and (6-29) are considered. For the condition described in Equation (6-28), the applied method of solution is straight forward which is discussed in detail in Appendix B. The situation of $R_c \rightarrow \infty$ for applying Equation (6-29) can be incorporated into the simulation model by defining a fictitious radius for the "simulated" core denoted as R_s . This value should be much larger than the radius of the "physical" core, r_c , such that the approximate solutions obtained at ($r = r_c$) in the simulated core should be relatively insensitive to the conditions at the fictitious boundary, R_s .

Figure 6-12 shows the effect of the boundary conditions at the exit on the effluent concentration profiles estimated at $r = r_c$. Solid and dashed lines represent the resulting effluent profiles for the boundary conditions described by Equations (6-28) and (6-29), respectively. It is clearly demonstrated that, by defining $R_s = r_c$, solute mass was forced out of the core as indicated by an early breakthrough curve. The material balance can be confirmed by comparing the integrated areas, for $0 \rightarrow 1$ PV and $1 \rightarrow \infty$ PV, on the breakthrough curve. Brigham (1974) suggested these two integrated areas should be equal but they are not as the area to the left ($0 \rightarrow 1$ PV) is larger. The material balance is not

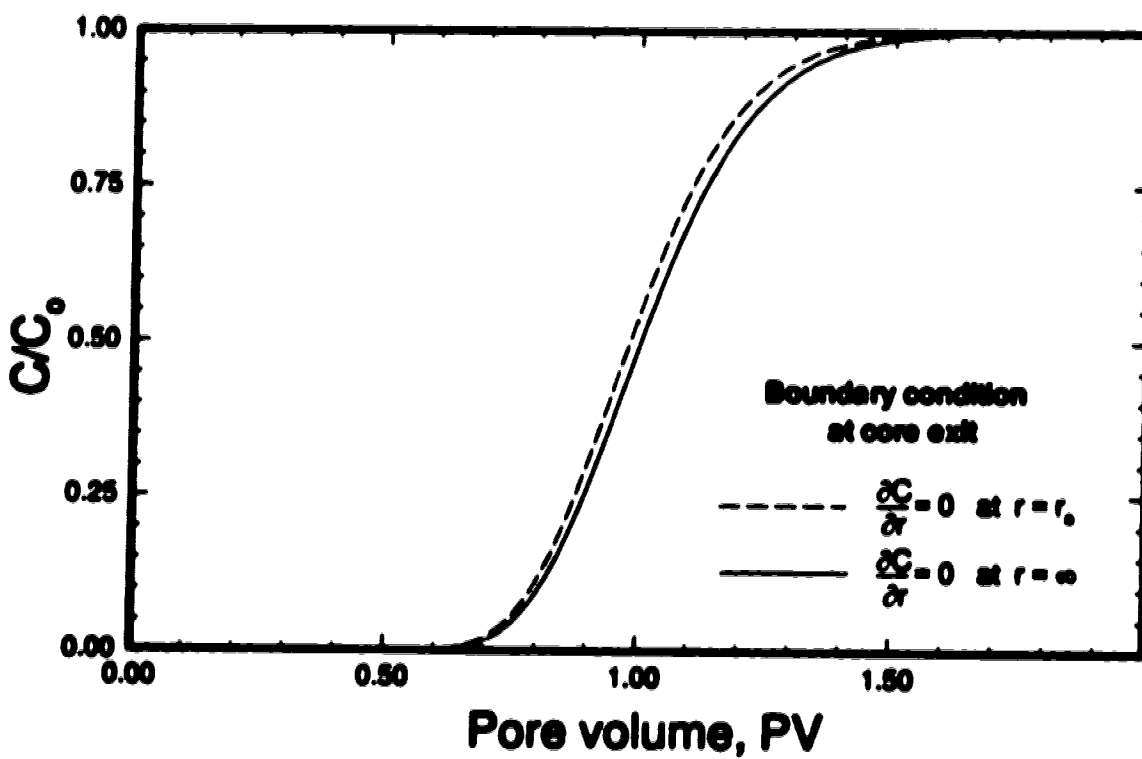


Figure 6-12. Effect of boundary conditions at the exit on the predicted breakthrough curves at $r_e = 44.2$ mm. The Cauchy condition was used at the wellbore.

preserved. In the case of $R_c \rightarrow \infty$, the resultant effluent profile was found to be symmetric about $C/C_o = 0.5$ at 1 PV; that is, mass was conserved.

In addition, as the core dimension (or radius, r_c) increased, the resulting solutions from using these two boundary conditions will eventually converge to a single solution (see Figure 6-13).

6.6 Models of Dispersion Coefficient

To evaluate the most suitable mathematical formulation for the dispersion coefficient under the experimental conditions employed in this study, the effect of flow rate on dispersion was studied by examining the effluent tracer profiles obtained in the previous chapters, Chapters 4 and 5. Figure 6-14 shows the measured profiles obtained from the injection slugs of 0.02 wt.% tritium in 8 wt.% sodium chloride at volumetric flow rates of 5, 20 and 120 mL/h. At an injection rate of 5 mL/h, the tracer breakthrough occurred after 0.5 PV and it did not reach unity even after the injection of two pore volumes. At the highest flow rate examined (120 mL/h), the tracer breakthrough occurred after 0.7 PV and it reached unity after the injection of nearly 1.6 PV. These results indicate that increasing the injection flow rate resulted in a sharper tracer profile; that is, a shorter mixing length.

6.6.1 Dispersion with Negligible Diffusion Effect

In the literature, the problem of solute transport from an injection well into a confined porous medium is often described by advection and longitudinal dispersion in a steady diverging flow field. Many investigators considered a dispersion model having the same form as Equation (6-9) as suggested by Hoopes and Harleman (1967). Application of the Fried and Combarous' (1971) generalized dispersion model in this region, on the other hand, can be ambiguous. By expanding Equation (6-2), it can be

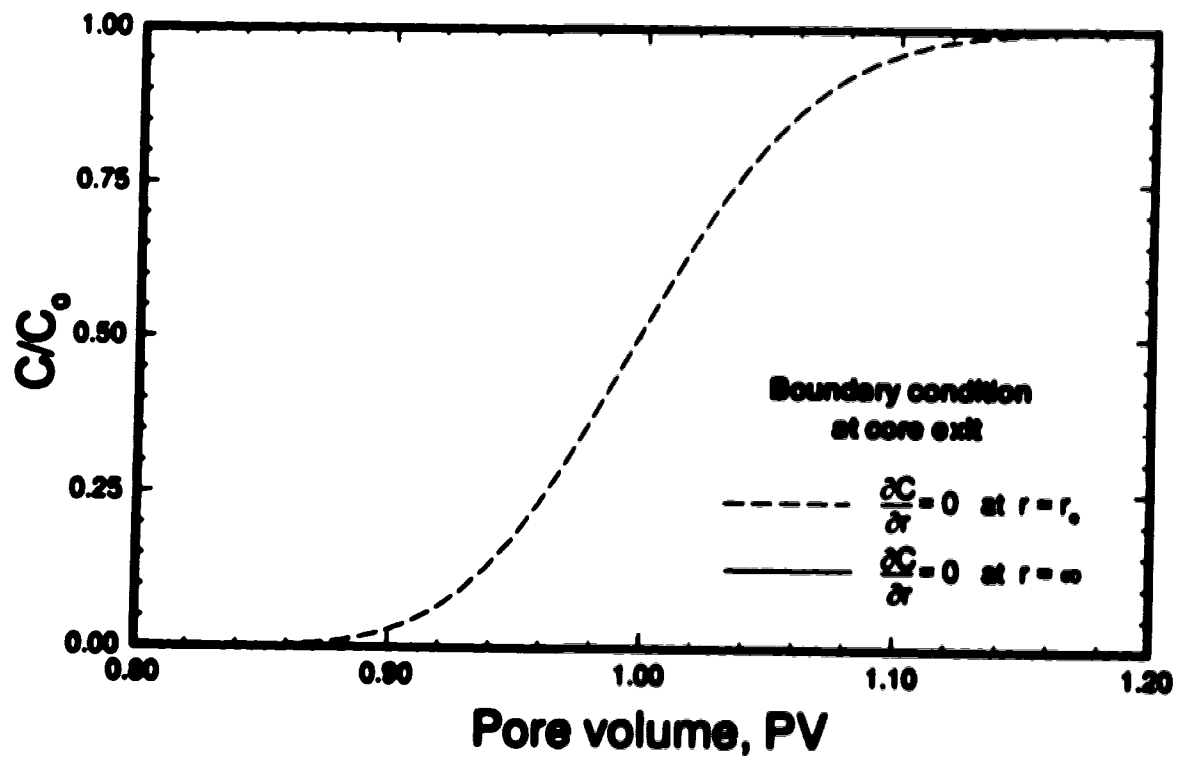


Figure 6-13. Effect of boundary conditions at the exit on the predicted breakthrough curves at $r_e = 442.0$ mm. The Cauchy condition was used at the wellbore.

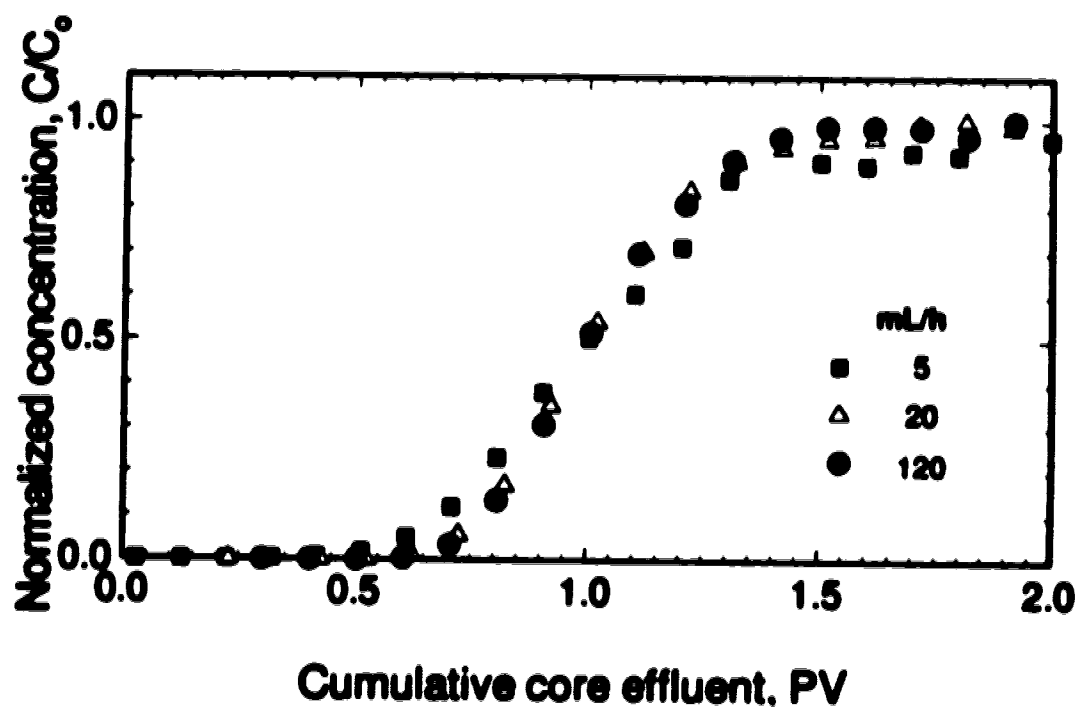


Figure 6-14. Effect of injection flow rate on the experimental effluent profiles.

seen that the dispersion coefficient is in fact a non-linear function of the diffusion coefficient where $D \propto D_m^{1-m}$. For the case of $m > 1$, the resulting equation implies that a minimum may occur at certain critical value of D_m . Beyond this minimum point, decreasing D_m (small or negligible molecular diffusion) may result in an increase in the calculated dispersion coefficient. In the current study, only a unity power constant, m , will be considered in detail; otherwise, the dispersion model will be slightly modified to avoid any ambiguous interpretation.

First, by assuming the effect of molecular diffusion is negligible as compared to the mechanical dispersion $D \gg D_m$, Equation (6-1) can be re-written as Equation (6-14) with $D = \alpha u$

$$\frac{\partial c}{\partial t} + \frac{A}{r} \frac{\partial c}{\partial r} = \alpha \frac{A}{r} \frac{\partial^2 c}{\partial r^2}$$

... (6-14)

As shown in Figure 6-5, a value of $\alpha = 5.0 \times 10^{-4}$ m for the dispersivity coefficient provides a good numerical approximation to the dispersion process at 20 mL/h. It was however found that an increase or a decrease in the injection flow rate Q (as in Section 6.6), while keeping the value of α unchanged, causes no variation in the simulated effluent profiles (see Figure 6-15 plotted in terms of the normalized concentration versus cumulative pore volume). With a close examination of Equation (6-14), the estimated concentration at any r is, in fact, a function of the dispersivity coefficient α only and independent of the flow coefficient A (\propto injection rate, Q). This may explain the discrepancies observed in this study as compared with the literature for the same system of unfired consolidated Berea sandstone with radial flow ($\alpha = 0.12$ cm by Bentsen and Nielsen, 1965; and $\alpha = 0.0081$ cm by McCoy and Kelkar, 1990). It appears that a linear relationship between longitudinal dispersion and flow velocity, $D = \alpha u$, may not be a valid model for radial geometry.

With the absence of the diffusion effect, it is of interest to examine the direct dispersion-velocity relationship. In this case, rather than expressing the dispersion

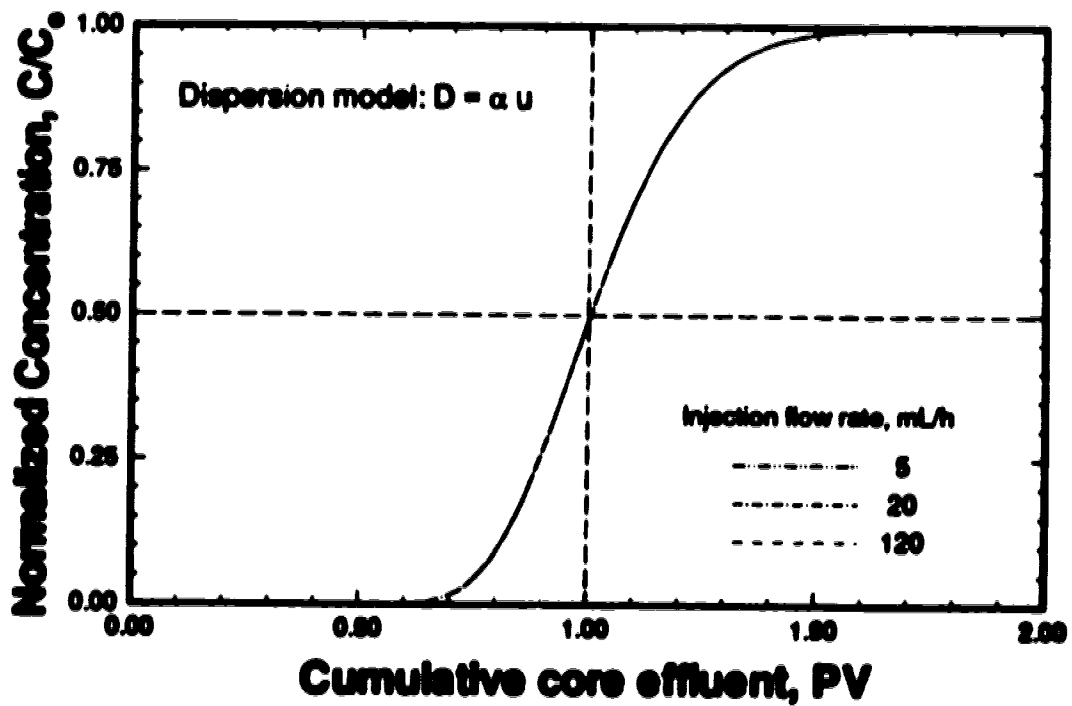


Figure 6-15. Effect of injection flow rate on the predictions of a simulated effluent profile using $D = \alpha u$ for $\alpha = 5.0 \times 10^{-6}$ m.

coefficient in terms of the Péclet number, a generalized power function for dispersion as

$$D = \hat{\alpha} u^m \quad (6-31)$$

where m is a constant, was used. A linear relation of $D = \alpha u$, as above, is a special case of $\hat{\alpha} = \alpha$ and $m = 1$. It is thus possible to perform a parallel study on the parametric sensitivity for the power constant in Equation (6-2) without interference from the diffusion effect.

Figure 6-16 shows the results of the least-square fit numerical solutions to the experimental data for $m = 0.8, 1$ and 1.2 with $\hat{\alpha} = 3.7 \times 10^{-5} \text{ m}^{1.2} \text{ s}^{-0.2}$, $5.0 \times 10^{-4} \text{ m}$, and $6.0 \times 10^{-3} \text{ m}^{0.8} \text{ s}^{0.2}$, respectively. All three power constants were able to provide a reasonably good approximation to the experimental data. The effect of injection flow rate on the dispersion profiles is shown in Figures 6-17a and 6-17b for $m = 0.8$ and 1.2 , respectively. For $m = 0.8$, an increase in the injection rate reduced the dispersive front as a result of lesser dispersive mixing. The opposite behaviour was observed as $m = 1.2$ was used. Comparing to the experimental data obtained in this study, Figure 6-14, the simulation results seem to suggest that the dispersion coefficient must be expressed in forms of $D \propto u^m$ for $m < 1$. This behaviour however has not been reported previously by other researchers. Nevertheless, neither of these models alone was able to predict correctly the breakthrough data without further adjusting the value of $\hat{\alpha}$.

6.6.2 Dispersion Dominated by Diffusion

As indicated in the previous section, a simple form of velocity-dependent dispersion models, such as $D \propto u$ or $D \propto u^m$, was unable to predict the experimental breakthrough data. It appears that neglecting the diffusion effect might have hindered the "true" dispersion characteristics. In this section, the effect of molecular diffusion is considered assuming mechanical dispersion is negligible (*Regime a* as defined by Fried and Combarous, 1971); that is, dispersion coefficient D is constant, $D_e = D_e / P\phi$.

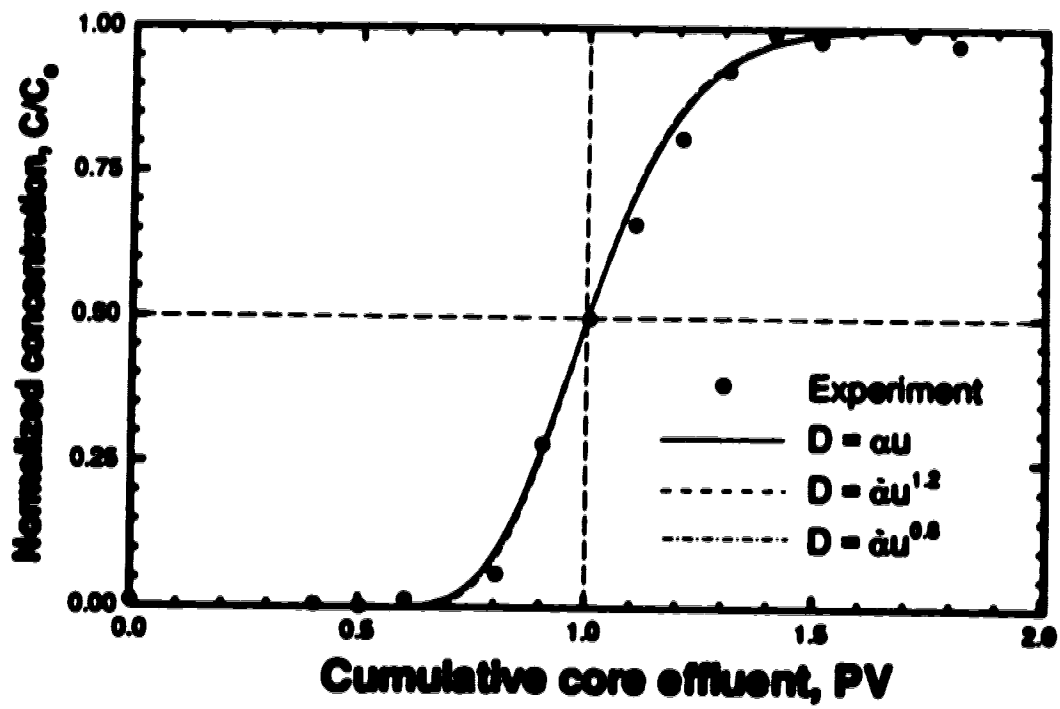


Figure 6-16. Comparison of experimental data and numerical simulation using dispersion model: $D = \alpha u^n$ for $n = 0.8, 1$ and 1.2 .

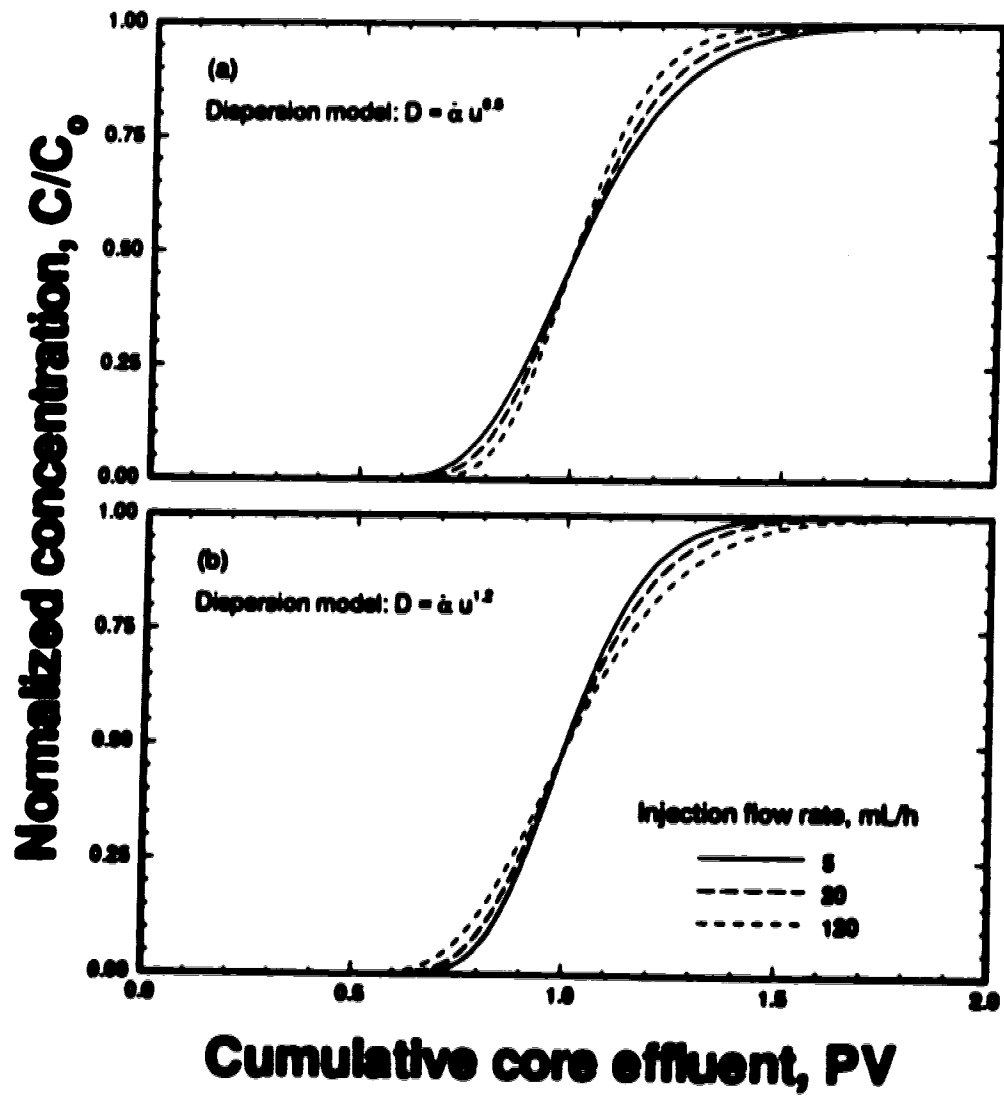


Figure 6-17. Effect of injection flow rate on the numerical solutions using $D = \alpha u^m$ for (a) $m = 0.8$ and (b) $m = 1.2$.

Figure 6-18 shows the predicted effluent profile simulated using $D_e = 2.0 \times 10^{-9} \text{ m}^2/\text{s}$, and its comparison with the experimental data. An increase in the injection flow rate results in a decrease in the length of mixing zone, which is consistent with the data presented in Figure 6-14.

6.7 Dispersion with Mechanical Mixing and Diffusion

At this point, analytical approximation methods for solving the hydrodynamic dispersion problems with radial flow have been reviewed. It was found that use of the simplified linear dispersion model, $D = \alpha u$, was not suitable, despite the wide acceptance of such a model in many published results. The dispersion term, on the other hand, was analyzed using a different prototype of the generalized dispersion model mentioned in Perkins and Johnston (1963), and Fried and Combarous (1971), in an attempt to examine the relative importance of individual parameters.

Under the current experimental conditions, it was found that a dispersion model combining the effects of both mechanical dispersion and diffusion (*Regime b*) is required. The most suitable form of dispersion model is

$$D = D_e + \alpha u^m \quad (6-32)$$

of which the effects of diffusion and advection can be treated separately. This model is similar to the general dispersion model as in Equation (6-2) (Fried and Combarous, 1971), replacing the Péclet number by the pore velocity. Figure 6-19 shows the simulated profiles for the three injection flow rates studied using $D_e = 1 \times 10^{-9} \text{ m}^2/\text{s}$, $\alpha = 6 \times 10^{-3} \text{ m}^{0.2} \text{ s}^{0.2}$ and $m = 1.2$. Very good agreement for all flow rates examined was obtained. These results will thus be used in the next chapter to predict the dispersion characteristics of all runs.

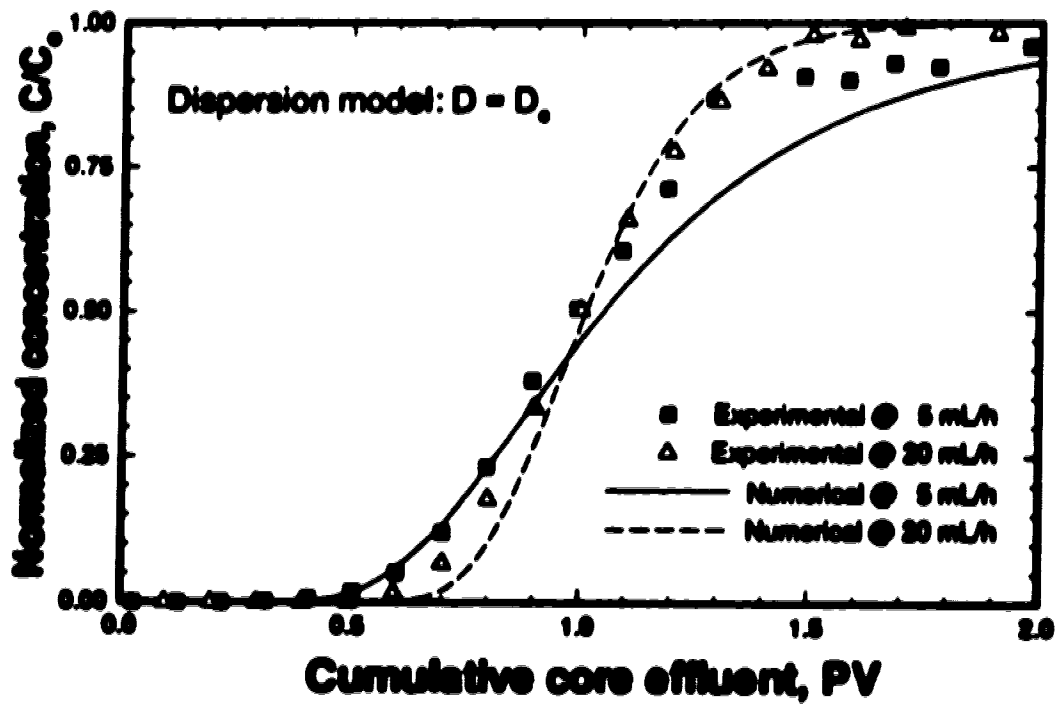


Figure 6-12.

Comparison of experimental data and numerical simulation assuming negligible mechanical dispersion for $D = D_0 = 2.5 \times 10^9 \text{ m}^2/\text{a}$.

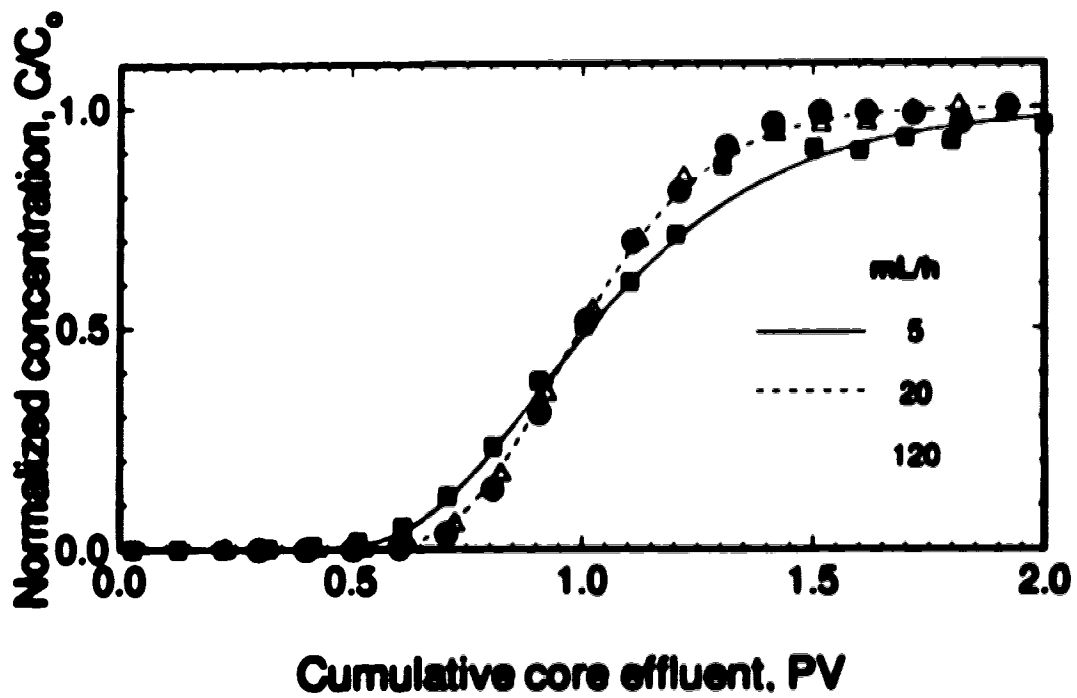


Figure 6-19. Comparison of experimental data and numerical simulation using dispersion model: $D = D_0 + \alpha u^n$ for $n = 1.2$.

Chapter 7

Dynamic Adsorption of Surfactants

When an adsorbing species is injected into a porous medium, the active displacement front tends to advance more slowly, due to adsorption, than the advection frontal velocity of the injected fluid. A classical approach in describing such a delay in the displacement is to assume that the adsorption process is represented by a first-order reversible, equilibrium mechanism (Lapidus and Amundson, 1952; Bear, 1972). An extension of the advection-dispersion equation was employed and the adsorption process was incorporated in the model as a retardation in the solute breakthrough curve. Over the years, this approach has gained wide acceptance in the areas of hydrogeological simulation, primarily for solute transport at very low concentrations and surface coverage, for example, contamination by organic compounds in ground water flows. Methods of solution for various equilibrium or non-equilibrium effects in terms of first- or second-order formulae and Freundlich or Langmuir isotherms, have been derived by many investigators, for example, in Bear (1972), Gupta and Greenkorn (1974) and, more recently, Valocchi (1985, 1989). Of specific interest is a recent publication by Ci-Quin and Jie (1990). They extended the solution of Chen (1987) for the radial advection-dispersion equation and derived the first analytical solution for chemical transport with dispersion and first-order non-equilibrium adsorption in a *radial flow* geometry.

For surfactant systems, many efforts have been devoted to perfect an understanding of the adsorption dynamics of surfactant under reservoir conditions. Static analyses have been a major contribution in this area with a variety of studies.

Researchers have focused on representations of the adsorption equilibrium isotherm, and its implications on the mechanisms underlying adsorption. Several publications, such as Scamehorn *et al.* (1982), Clunie and Ingram (1983), Hough and Rendall (1983), and Zhu and Gu (1991), have provided a comprehensive survey of the detailed adsorption mechanisms for surfactants on various adsorbent surfaces. They focused on the initial forces leading to the adsorption of individual surfactant molecules on the solid surface, and the interactions of adsorbed surfactant molecules with one another which give rise to surface aggregates. Considering the large number of adsorption and transport models that have been formulated, it is surprising that there have been so few investigations into the dynamic nature of these surface aggregates.

Dynamic adsorption of surfactants from dilute solution was commonly examined using the advection-dispersion equation coupled with either instantaneous equilibrium or a rate-controlled mechanism. Troguis *et al.* (1977) showed that the mechanism of adsorption of surfactants can be represented by a Langmuir-type kinetic model for concentrations below the critical micelle concentration. The rate constant for adsorption was then evaluated by solving numerically the coupled transport equation and rate expression. The rate constant of desorption was expressed in terms of the equilibrium ratio of the sorption process obtained through static experiments.

The combined effect of mass transfer to the solid-liquid interface and the kinetics of surface adsorption was first considered by Ramirez *et al.* (1980). They suggested that the dynamic effects of adsorption can be evaluated by comparing the relative importance of adsorption and dispersion which allows speculation about whether the mechanism is kinetic-controlled, mass-transfer controlled, or a combination of both. Six dimensionless groups were defined to characterize the process by relating the advection, dispersion, adsorption, desorption, adsorptive capacity and mass-transfer characteristics. Over the range of injection velocities examined, they found that neither mass transfer at low velocities nor adsorption kinetics at high velocities dominates the adsorption dynamics. Thus a new dynamic model was developed showing the importance of both kinetic adsorption and mass-transfer rate mechanisms.

Foulser *et al.* (1989) examined the dynamics of surfactant adsorption in displacement experiments. They demonstrated the application of equilibrium, kinetic and truncated Langmuir models, two-site model and bilayer model for surfactant concentration up to the critical micelle concentration. Above the c.m.c., the surfactant monomer concentration must remain constant. Various Langmuir-type models were found to be insufficient for matching such dynamic behaviour. The two-site model, on the other hand, provided a better fit to the experimental data and more consistent rate parameters between runs than other models.

In this chapter, several previously proposed adsorption models are examined in an attempt to match the experimental effluent concentration profiles obtained in Chapters 4 and 5. The trends of which model parameters vary in relation to the injected surfactant concentration, salt concentration and flow rate are studied. The effects of molecular aggregation in the bulk solution and at the solid-liquid interface are also examined.

7.1 General Transport Equation for Dynamic Adsorption

The governing transport equation for an adsorbing species in a porous medium is an extension of the advection-dispersion equation, Equation (6-1). The resulting transport equation is (Bear, 1972):

$$\frac{\partial c}{\partial t} + \underline{u} \cdot \nabla c - \nabla \cdot (\underline{D} \cdot \nabla c) + \frac{1-\phi}{\phi} \frac{\partial \Gamma}{\partial t} = 0 \quad (7-1)$$

where $c = c(\underline{x}, t)$ is the concentration of surfactant in the bulk solution at position \underline{x} and time t , $\Gamma = \Gamma(\underline{x}, t)$ is the amount of adsorption per unit volume of fluid, and ϕ is the porosity.

The units of Γ are defined as below. The unit for the rate of change in the bulk concentration, $\partial c / \partial t$, is expressed in terms of the number of moles of surfactant per unit volume of fluid per unit time, for example, $\text{mol}/\text{m}_L^3 \cdot \text{s}$. The unit for the multiplication factor of $(1-\phi)/\phi$ is expressed in $(\text{m}_L^3 - \text{m}_L^3) / \text{m}_L^3$ since ϕ is defined in terms of $\text{m}_L^3 / \text{m}_L^3$.

Note that the subscripts of L and R denote the quantities of the fluid phase and of the solid phase (or rock), respectively. When the amount of adsorption, Γ , is reported in terms of the number of moles of surfactant adsorbed *per unit mass* of solid or mol/g_R, an equivalent quantity for Γ^* in mol/(m_R³-m_L³) can be evaluated as follow:

$$\Gamma^* = \frac{\rho_s}{1-\phi} \Gamma$$

where ρ_s is the bulk density of solid in the mass per unit volume of solid or g_R/m_R³, and $1/(1-\phi)$ is expressed in m_R³/(m_R³-m_L³). Similarly, the amount of maximum adsorption, Q_s^* , can be expressed in the units of mol/(m_R³-m_L³). For the sake of convenience, the unit of m_R³-m_L³ was abbreviated to m_s³.

7.2 Approximate Solution of Adsorption in an Advective-Dispersive System

For a dilute surfactant solution (where $c \rightarrow 0$), the extent of adsorption can be approximated using Henry's law:

$$\Gamma_s^* = \kappa C_s \quad (7-2)$$

where κ is a proportionality constant and the subscript *s* denotes the equilibrium status. When the adsorption is instantaneous such that $\Gamma^* = \Gamma_s^*$ and $c = C_s$. The rate of adsorption can be re-written as $\partial\Gamma^*/\partial t = \kappa \partial c/\partial t$, and Equation (7-1) thus becomes

$$\frac{\partial c}{\partial t} + \underline{u} \cdot \nabla c - \nabla \cdot (\underline{D} \nabla c) + \frac{1-\phi}{\phi} \kappa \frac{\partial c}{\partial t} = 0 \quad (7-3a)$$

or

$$R \frac{\partial c}{\partial t} + \underline{u} \cdot \nabla c - \nabla \cdot (\underline{D} \cdot \nabla c) = 0 \quad (7-3b)$$

where $R = 1 + \kappa(1-\phi)/\phi$ is called the retardation factor, since it retards the appearance of the breakthrough curve (Bear, 1972). Analytical solutions for several one-dimensional linear flow problems have been presented by Lapidus and Amundson (1952), and Bear (1972). For the case of one-dimensional radial flow problems, an analytical solution can be derived following the analogy of Raimondi *et al.* (1959). Equation (7-3b) can be written in cylindrical coordinates for $D = D_e + \alpha u$ and $u = A/r$, where D_e is the effective diffusion coefficient, α is the intrinsic dispersivity and A is the flow coefficient as defined in the previous chapter:

$$R \frac{\partial c}{\partial t} + \frac{A}{r} \frac{\partial c}{\partial r} = \alpha \frac{A}{r} \frac{\partial^2 c}{\partial r^2} + \frac{D_e}{r} \frac{\partial}{\partial r} \left(r \frac{\partial c}{\partial r} \right) \quad (7-4)$$

The time variable can be modified by $t_R = t/R$. Thus, the spatial gradients can then be approximated by (Ogata, 1958), similar to Equation (6-10),

$$\frac{\partial}{\partial r} = -\frac{r}{A} \frac{\partial}{\partial t_R}$$

Upon substitution into Equation (7-4), we have

$$\frac{\partial c}{\partial t_R} + \frac{A}{r} \frac{\partial c}{\partial r} = \left(\alpha \frac{r}{A} + D_e \frac{r^2}{A^2} \right) \frac{\partial^2 c}{\partial t_R^2} \quad (7-5)$$

Using the Laplace transformation, an analytical solution can be derived and is given by

$$\frac{c}{C_0} = \frac{1}{2} \operatorname{erfc} \left(\frac{A \sqrt{t_R} - R/2}{R \sqrt{t_R}} \right) \quad (7-6)$$

subject to the initial and boundary conditions of

$$\begin{aligned}
 c(r,t) &= 0 & \text{at } t &= 0 & \text{(initial),} \\
 c(r,t) &= C_0 & \text{at } r &= 0 & \text{(line source)} \\
 \text{and } c(r,t) &= 0 & \text{at } r &= \infty & \text{(exit)}
 \end{aligned}$$

The term $f(r)$ is expressed as

$$f^2(r) = \frac{4}{3} \frac{\alpha}{r} + \frac{D_0}{A}$$

In this case, the retardation factor can be determined directly by tracking the retarded advective front; that is, the value of R is equal to $PV_{0.5}$, which is the cumulative effluent pore volume at $C/C_0 = 0.5$. The concentration, C , is defined as the measured solute concentration at the exit of the core, $r = r_0$, and $C = c(r_0, t)$. Equation (7-6) is known as the Ogata-Banks equation.

Figure 7-1a shows a comparison of the analytical approximation using Equation (7-6), and the numerical solution. The parameters for dispersion and adsorption used were $D_0 = 1 \times 10^{-9} \text{ m}^2/\text{s}$, $\alpha = 5 \times 10^{-4} \text{ m}$, $A = 1.095 \times 10^{-7} \text{ m}^2/\text{s}$, $\kappa = 0.198 \text{ m}_L^3/\text{m}_s^3$ and $r = r_0 = 44.2 \text{ mm}$. The numerical solution was obtained by the finite element method for a retarded advection-dispersion equation, discussed in Appendix B. The effluent profiles were plotted in terms of normalized concentration of tracer or surfactant against cumulative effluent volume in pore volumes. It is believed that the discrepancy observed between the two solutions is caused by the assumption of line source injection, $c(r,t) = C_0$, at $r = 0$, in the analytical approximation.

Figure 7-1b shows the effluent profiles simulated using the above parameters and matched with experimental data from 0 to 7 PV. The surfactant slug consisted of 0.19 wt.% Neodol 25-3S, 0.02 wt.% of tritium (tracer) and 3 wt.% sodium chloride and was injected at a constant flow rate of 20 mL/h.

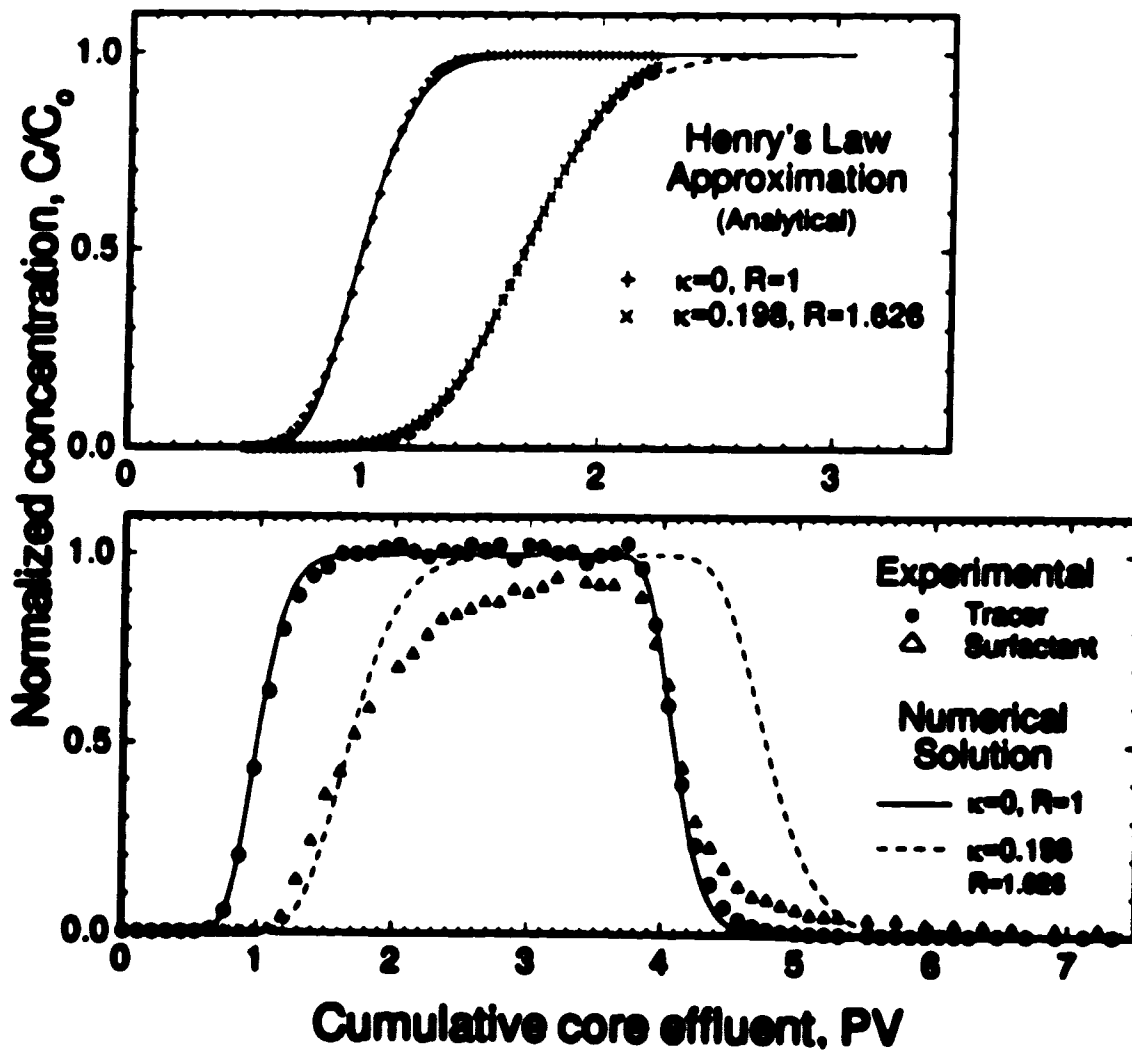


Figure 7-1. Effluent profiles of tracer and surfactant. (a) A comparison of analytical and numerical solutions calculated using Henry's law, and (b) numerical solution fitted to experimental data.

Very good agreement between the experimental and simulated tracer profiles during both the injection and displacement of the slug was observed. A detailed discussion on the dispersion of tracer with radial flow has been presented in the previous chapter. For the effluent surfactant profile, experimental data showed a "sharp" breakthrough near 1.1 PV (increased linearly and instantaneously from $C/C_0 = 0.0$ to 0.65 between 1.1 to 1.8 PV), which cannot be described by the retarded advective front (that is, the simulated curve). After the initial breakthrough of surfactant, continuous injection appears to increase the rate of adsorption, leading to a sudden drop in slope on the effluent profile. Upon injection of the chase brine, the measured concentration of surfactant dropped simultaneously with the effluent tracer concentration; that is, little or no desorption occurred. Since Henry's law maintains that the adsorption process is linear and reversible, a step decrease in the injected concentration will result in simultaneous desorption of the adsorbed species. Thus, the effluent profile simulated according to the Henry's law assumption can, in fact, be viewed as a shifted dispersion breakthrough curve with a delay specified by the retardation factor.

7.3 Dynamic Effects on the Overall Adsorption

The overall adsorption process in a flow system can be considered as a two-step process: (1) mass transfer by diffusion of the adsorbing species from the bulk solution to the adsorbent surface across a stagnant boundary layer, and (2) adsorption of the species on the surface.

In a system in which the adsorption process is mass-transfer controlled, the rate of change in adsorption, Γ' , can be determined by

$$\frac{\partial \Gamma'}{\partial t} = k_m(c - c_s) \quad (7-7)$$

where k_m is the mass transfer coefficient and c_s is the concentration adjacent to the surface in the fluid phase. Adsorption is assumed to be intrinsically fast relative to the rate of

mass transfer. The amount of solute adsorbed on the surface can thus be evaluated using an equilibrium Langmuir-type relation:

$$\Gamma^* = \frac{Q_s^* K c_s}{1 + K c_s} \quad (7-8)$$

where Q_s^* is the maximum adsorption capacity and K is the equilibrium ratio.

If, on the other hand, the rate of adsorption at the surface is slow compared to the rate of mass transfer, the concentration gradient across the stagnant boundary layer may appear to be insignificant or virtually negligible. The rate of the overall adsorption, $\partial\Gamma^*/\partial t$, can be approximated using a reversible second-order rate expression (Ramirez *et al.*, 1980), assuming $c = c_s$:

$$\frac{\partial\Gamma^*}{\partial t} = k_s c (Q_s^* - \Gamma^*) - k_d \Gamma^* \quad (7-9)$$

where k_s and k_d are the rate constants for adsorption and desorption, respectively.

In the case when the rates of both mass transfer and kinetic adsorption are fast, the concentration of the adsorbing species in the bulk solution may be considered as the same as that near the surface; that is, $c = c_s$. The rate of adsorption can be determined using the time derivative of the equilibrium expression of Equation (7-8) (Gupta and Greenkorn, 1974; Ramirez *et al.*, 1980; Satter *et al.*, 1980; Badakhshan and Bakes, 1991). In the current study, this sorption process is the equilibrium Langmuir adsorption:

$$\frac{\partial\Gamma^*}{\partial t} = \frac{d\Gamma^*}{dc} \frac{\partial c}{\partial t} = \frac{Q_s^* K}{(1 + Kc)^2} \frac{\partial c}{\partial t} \quad (7-10)$$

Note that the above expression of $\partial\Gamma^*/\partial t$ can be directly substituted into Equation (7-1) to obtain the same equation form as Equation (7-3b). In this case, the retardation factor becomes a function of the bulk concentration, and is expressed as

$$R = 1 + \frac{1-\phi}{\phi} \frac{Q_s^* K}{(1+Kc)^2} \quad (7-11)$$

Figure 7-2 shows the experimental data and the best possible matches of the surfactant breakthrough curves using Equation (7-10). For the experiments, the injected solutions consisted of 0.19, 0.46 and 0.91 wt.% of Neodol 25-3S prepared in 3 wt.% sodium chloride. All surfactant solutions were injected at a flow rate of 20 mL/h for about three pore volumes and then displaced by five pore volumes of chase brine (of the same salinity). At a low surfactant concentration (0.19 wt.% Neodol 25-3S), the surfactant breakthrough occurred after the injection of 1.1 PV of the surfactant slug. The normalized surfactant concentration reached nearly 0.92 at the end of the surfactant slug injection. The effluent surfactant concentration then dropped significantly after the injection of 0.7 PV of the chase brine.

As the injected concentration increases, it was observed that the breakthrough of the surfactant profile occurred more rapidly. The total adsorption of surfactant in the core tends to reach its saturation as the measured C/C_0 approaches unity. For all three surfactant concentrations, the adsorption process appears to be slow and irreversible as indicated by the flat tailing of the effluent profile during the injection of chase brine.

The dashed lines in Figure 7-2 represent the simulated results obtained from the equilibrium Langmuir adsorption model, Equation (7-10). The maximum adsorption value of Q_s^* for Neodol 25-3S in 3 wt.% sodium chloride solution is 2.84×10^{-4} mol/m³ as calculated from static adsorption measurements. The fitted values of the equilibrium ratio are summarized in Table 7-1. In common with all three simulated curves, the calculated effluent concentration increases gradually to saturation and is followed by a decrease to zero concentration, similar to the delayed or shifted breakthrough curve (of surfactant) obtained using Henry's law. It was apparent that the discrepancy between the simulated curve and the experimental data during the injection of a surfactant slug becomes less obvious as the injected concentration increases (see Figure 7-2). At a high concentration, the measured difference in experimental data was less sensitive, especially expressed in

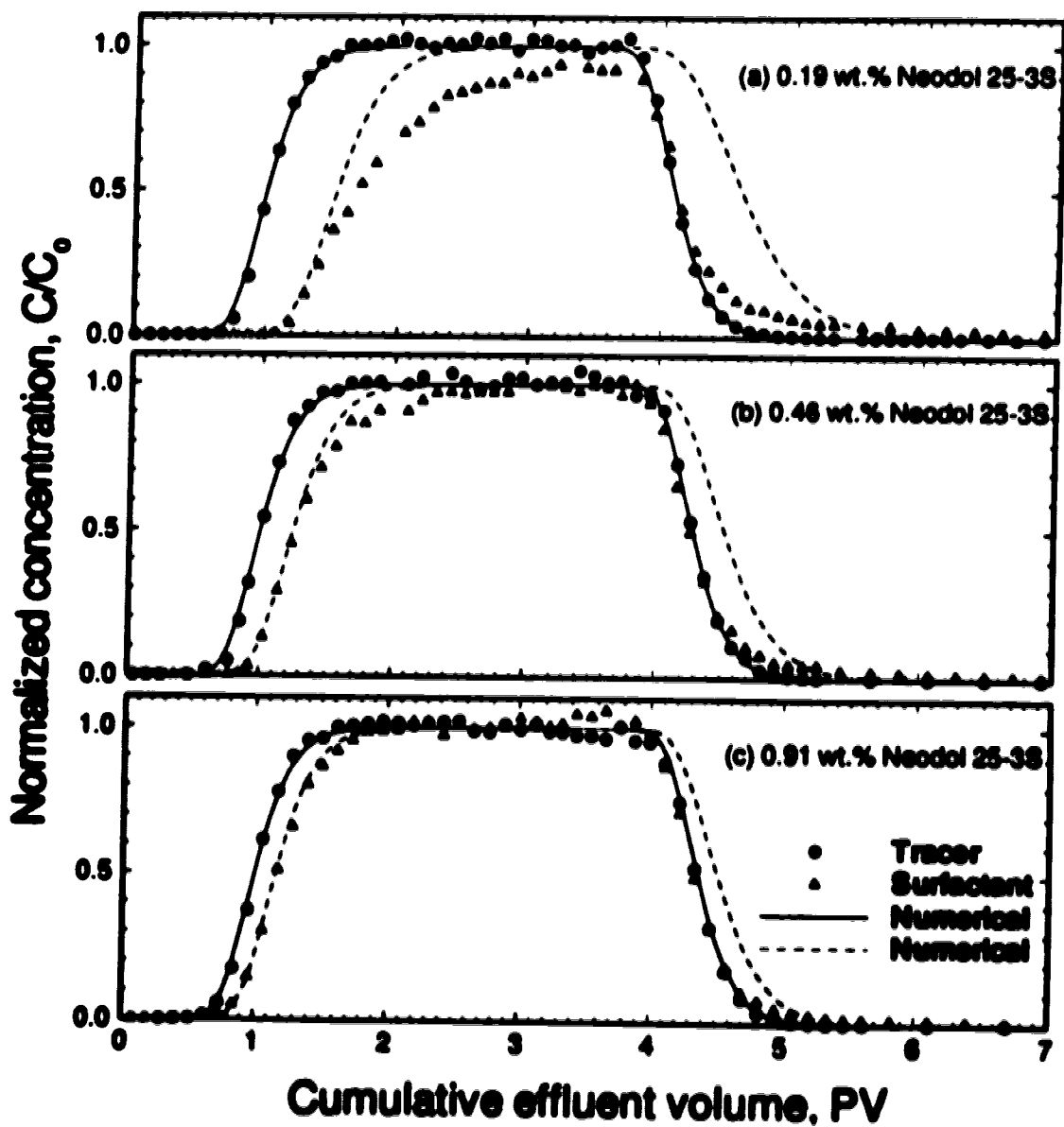


Figure 7-2.

Effluent profiles calculated using an equilibrium Langmuir adsorption model for surfactant slugs of different concentrations in 3 wt.% sodium chloride and injected at a flow rate of 20 mL/h.

terms of C/C_0 ; therefore, the detailed features of the adsorption process were less apparent. Hence, in order to provide an unambiguous interpretation for the dynamics of adsorption in a flow system, it is necessary to examine both the slug injection and displacement profiles (to characterize the desorption kinetics), and to use a lower concentration for injection.

Table 7-1. Summary of model parameters obtained using the equilibrium Langmuir adsorption model.

Surfactant Concentration (wt.%)	K (L mol ⁻¹)
0.19	70.0
0.46	35.0
0.91	25.0

For the use of the kinetic Langmuir model, Equation (7-9), a slight improvement for the brine chasing portion on the fitted curves was observed (see Figure 7-3). Since the accuracy of this model was still low, the values for the rate constants were therefore estimated only to the nearest order of magnitude. The desorption rate constants for all three runs were arbitrarily set to $1 \times 10^{-5} \text{ s}^{-1}$ (see Table 7-2) to show the extent of desorption as compared to the rate of adsorption. The ratios of k_d/k_a obtained were of the order of 10^4 , which are much higher than the equilibrium ratios estimated by the equilibrium Langmuir model. Thus, instantaneous adsorption/desorption on the surface is not likely to occur for the time scale and rate of injection examined here.

Another important aspect for the application of this model is the estimated change in the adsorptive capacity. In order to provide a close approximation to the actual process, it was necessary to limit the amount of adsorption for the entire system. Equation (7-9) was re-written as follows:

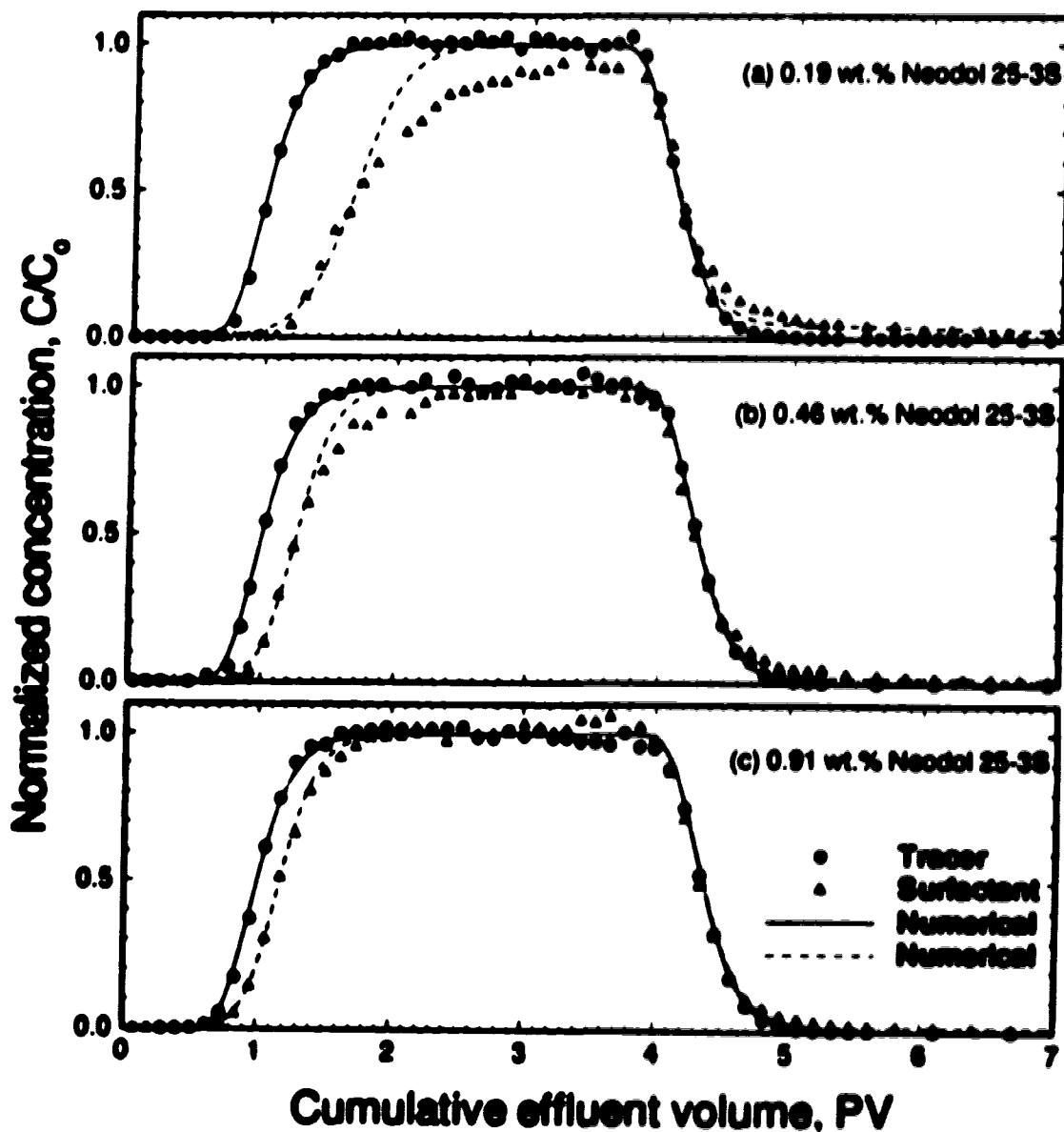


Figure 7-3.

Effluent profiles calculated using a kinetic Langmuir-type adsorption model for surfactant slugs of different concentrations in 3 wt.% sodium chloride and injected at a flow rate of 20 mL/h.

Table 7-2. Summary of model parameters obtained using the kinetic Langmuir model.

Surfactant Concentration (wt.%)	k_a (L mol ⁻¹ s ⁻¹)	$k_d = 10^6$ (s ⁻¹)	Q_s^{**}/Q_s^*
0.19	0.180	10	0.30
0.46	0.150	10	0.28
0.91	0.080	10	0.36

$$\frac{\partial \Gamma^*}{\partial t} = k_a c (Q_s^{**} - \Gamma^*) - k_d \Gamma^* \quad (7-12)$$

such that Q_s^{**} is used in place of Q_s^* to denote the difference in adsorptive capacity under dynamic conditions. The estimated values (see Table 7-2) in terms of Q_s^{**}/Q_s^* are in the range of 0.28 - 0.36 indicating that only a portion of the available adsorptive sites were being occupied.

7.4 Compound Adsorption Model

From the results in Figures 7-1 to 7-3, it is obvious that neither an equilibrium model nor a simple Langmuir kinetic model can provide an acceptable fit to the experimental data. For the injection of surfactant slug of low concentration (see Figure 7-3a), the simulation obtained using Equation (7-9) shows a major discrepancy between the experimental data and the simulated results near the end of slug injection as well as during chase-brine injection. Also, it appears that a change in the overall adsorption rate may have occurred as the bulk and/or adsorbed concentration across the core increases, perhaps due to a change in surface charge as surfactant ions adsorb or the formation of surface aggregates.

In this case, the sorption can be considered to be governed by two independent types of adsorption kinetics occurring on a heterogenous surface, where the overall adsorption rate expressed is replaced by a two-site non-equilibrium model:

$$\begin{aligned}\frac{\partial \Gamma_1^*}{\partial t} &= k_{a1}c(Q_{a1}^* - \Gamma_1^*) - k_{d1}\Gamma_1^* \\ \frac{\partial \Gamma_2^*}{\partial t} &= k_{a2}c(Q_{a2}^* - \Gamma_2^*) - k_{d2}\Gamma_2^*\end{aligned}\tag{7-13}$$

where Q_{a1}^* and Q_{a2}^* are the adsorption capacities of each type of adsorption site such that the maximum adsorption of the system and the total rate of change in adsorption are given by

$$Q_s^* = Q_{a1}^* + Q_{a2}^* \quad \text{and} \quad \frac{\partial \Gamma^*}{\partial t} = \frac{\partial \Gamma_1^*}{\partial t} + \frac{\partial \Gamma_2^*}{\partial t} ,$$

respectively.

Figure 7-4 shows the numerical simulation result obtained by solving the transport equation coupled with the kinetic adsorption model, Equation (7-13). The resultant curves were fitted to the same set of experimental runs as above by error minimization. The model parameters obtained are summarized in Table 7-3. Significant improvement over the simple Langmuir models was observed. The rate constants for both types of adsorption decreased as the injected concentration increases, which is due to an increase in the driving concentration (that is, increasing C_s), knowing that the rates of adsorption in each run were calculated as $k_{a1}c(Q_{a1}^* - \Gamma_1^*)$ and $k_{a2}c(Q_{a2}^* - \Gamma_2^*)$. By comparing the magnitude of all the rate constants (k_{a1} , k_{a2} , k_{d1} and k_{d2}), it appears that the first type of is more rapid and irreversible than the second type. Also, the ratios of Q_{a1}^*/Q_s^* indicated that about 30 percent of the injected surfactant was adsorbed irreversibly in the first type of adsorptive sites.

From the results obtained using the two-site model as in Table 7-3, it is surprising to note that the rate constants for adsorption vary as a function of the injected

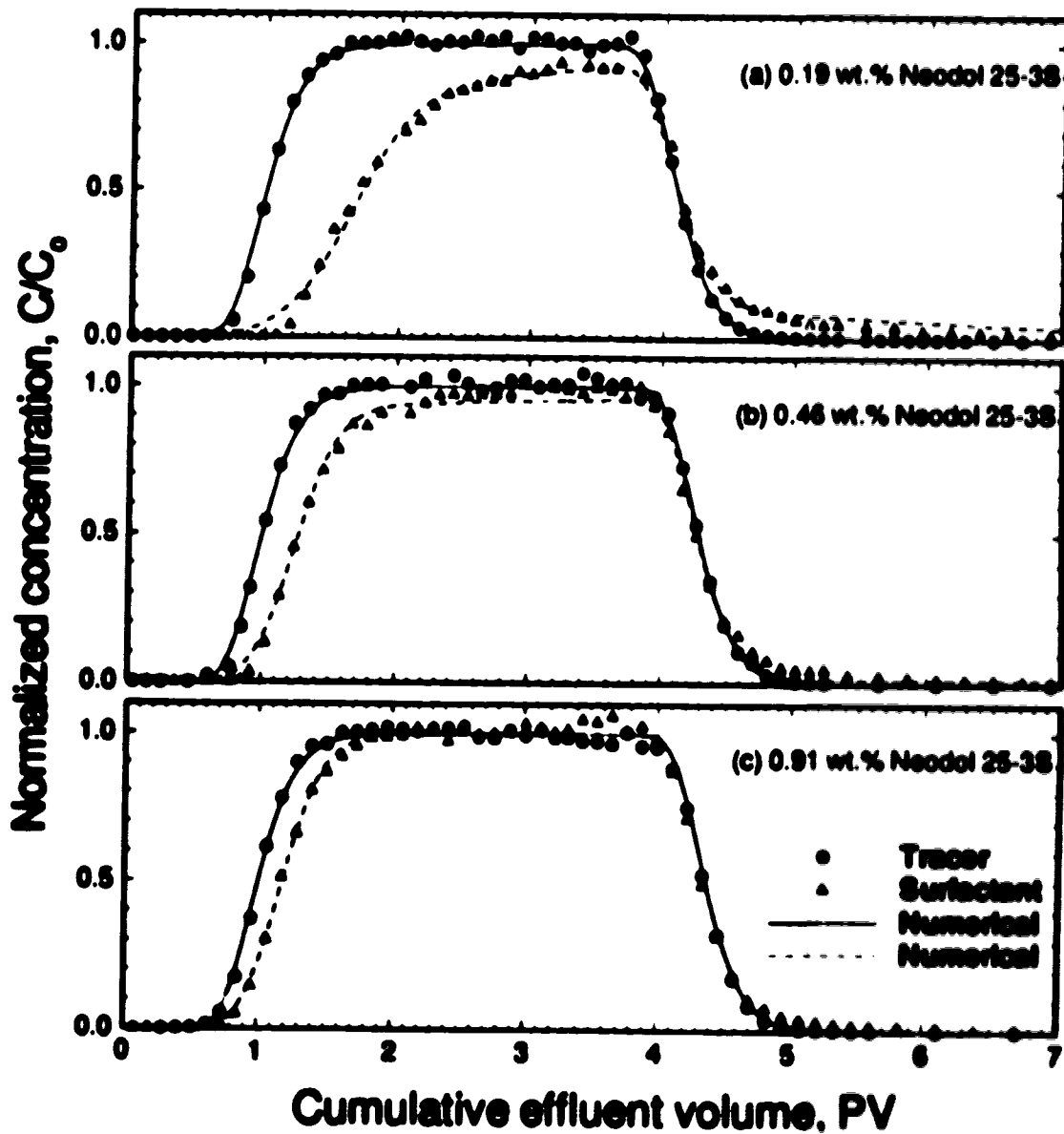


Figure 7-4. Effluent profiles calculated using the two-site model for surfactant slugs of different concentrations in 3 wt.% sodium chloride and injected at a flow rate of 20 mL/h.

Table 7-3. Summary of model parameters obtained using the two-site model.

Surfactant Concentration (wt.%)	k_{a1} (L mol ⁻¹ s ⁻¹)	$k_{d1} = 10^6$ (s ⁻¹)	$k_{a2} = 10^3$ (L mol ⁻¹ s ⁻¹)	$k_{d2} = 10^6$ (s ⁻¹)	Q_{a1}/Q_{a2}
0.19	0.147	13.57	3.340	41.08	0.263
0.46	0.114	14.21	1.028	10.00	0.262
0.91	0.062	6.85	0.029	0.28	0.374

concentration. In our experiments, all three sandstone cores used were subjected to the same environment in terms of salinity, pH and flow rate. The distribution of adsorption sites and attractive forces on the surface; that is, the adsorption kinetics, as well as the mass transfer characteristics should therefore be very similar for all core samples. The model parameters obtained, however, are inconsistent with this theory. If the proposed model is valid, a common set of parameters that satisfies all injected concentrations (within experimental error) should be resulted.

7.5 Effects of the Solution Characteristics on Surfactant Adsorption

As discussed earlier in Chapter 2, the mechanisms of surfactant adsorption can be varied as the concentration of surfactant approaches the critical micelle concentration (c.m.c.). Above the c.m.c., it is believed that the surfactant monomers tend to be released from the solution to form micelles in the bulk or surface aggregates at the interface. The monomer concentration will remain constant, whereas the concentration of micelles will increase linearly with the total concentration (Scamehorn *et al.*, 1982). The total amount of surfactant adsorbed should therefore be governed by both the surface adsorption capacity and the c.m.c. of the surfactant solution. In other words, the effective surfactant concentration in the bulk solution, \bar{c} , is limited to only the concentration of monomers

available and bound by the solution c.m.c. (Trogu *et al.*, 1977, 1979; Foulser *et al.*, 1989)

$$c = \begin{cases} c & \text{for } c < C_{cmc} \\ C_{cmc} & \text{for } c \geq C_{cmc} \end{cases}$$

assuming the monomer and micelle equilibration is very rapid compared to the rate of adsorption.

Foulser and co-workers (1989) presented a modified form of the two-site model in terms of effective concentration, which is suitable for surfactant concentrations both above and below the c.m.c.:

$$\begin{aligned} \frac{\partial \Gamma_1^*}{\partial t} &= k_{a1} c (Q_{a1}^* - \Gamma_1^*) \\ \frac{\partial \Gamma_2^*}{\partial t} &= k_{a2} c (Q_{a2}^* - \Gamma_2^*) - k_{d2} \Gamma_2^* \end{aligned} \quad (7-14)$$

The assumption of an irreversible adsorption process was adopted to minimize the number of parameters involved and to reflect the fact that a slow desorption process would have little effect on the overall adsorption. They examined a dynamic adsorption system of an anionic surfactant (sodium dodecylbenzene sulphonate, SDS) on Clashach sandstone. A linear core was used with an injection flow rate of 60 mL/h (or a constant superficial velocity of 1.048×10^{-3} m/s). The values of Q_{a1}^* and Q_{a2}^* were determined from the overall mass balance in the effluent profiles (where $Q_{a1}^*/Q_{a2}^* \sim 0.18$). The experimental results were fitted to the numerical simulation by error minimization, with k_{a1} , k_{a2} , k_{d2} and C_{cmc} as the model parameters. By increasing the injected concentration from 1 to 10 times its nominal c.m.c., they observed that the values of k_{a1} remain nearly constant, k_{a2} reduces by about one-third, k_{d2} changes insignificantly and C_{cmc} becomes six times higher than the nominal c.m.c. No physical explanation of the differences in model parameters was, however, given. Rather than limiting the monomer concentration by the nominal c.m.c. which is prescribed by equilibrium or static measurements, the increase in the

overall concentration of monomers observed may be associated with a decrease in micelle concentration in the moving fluid.

In the current study, the experimental data were fitted using Equation (7-14) by varying the rate constants of k_{a1} , k_{a2} and k_d , and the ratio of Q_{a1}^*/Q_a^* . The limiting concentration for c was fixed at 0.1 wt.% (or 2.274×10^{-3} mol/L) which is about two orders of magnitude higher than the solution c.m.c. of 0.00075 wt.% (extrapolated from the values measured by A. Cameron of PRI using the spinning drop method). The solution c.m.c. was not used as the upper limit of the effective concentration because the c.m.c. of Neodol 25-3S is very low as compared to the injected concentration. In this case, the second-order adsorption equation becomes first order at all time as $c = C_{max}$: that is,

$$\begin{aligned} \frac{\partial \Gamma_1^*}{\partial t} &= k_{a1} C_{max} (Q_{a1}^* - \Gamma_1^*) \\ \frac{\partial \Gamma_2^*}{\partial t} &= k_{a2} C_{max} (Q_{a2}^* - \Gamma_2^*) - k_d \Gamma_2^* \end{aligned} \quad (7-15)$$

where $k_{a1} C_{max}$ and $k_{a2} C_{max}$ are of constant value. The rate constants estimated for the adsorption component, k_{a1} and k_{a2} , became an increasing function of surfactant concentration, which is also inconsistent with the adsorption kinetics and mass-transfer characteristics for a system of similar solid-liquid interfacial properties as discussed in the previous section.

Figure 7-5 shows the least-squares fitted curves obtained by using the model parameters listed in Table 7-4a. Although the results obtained from the previously mentioned models were as accurate a match to the experimental data as the results of applying this model, it should be noted that the parameters utilized to generate the fitted curves were much closer in magnitude than those used in the simple two-site model. Recalling the discussion on model validity at the end of the previous section, it is physically more realistic to have a single set of parameters fitted to all the experimental data obtained from the different injected concentrations.

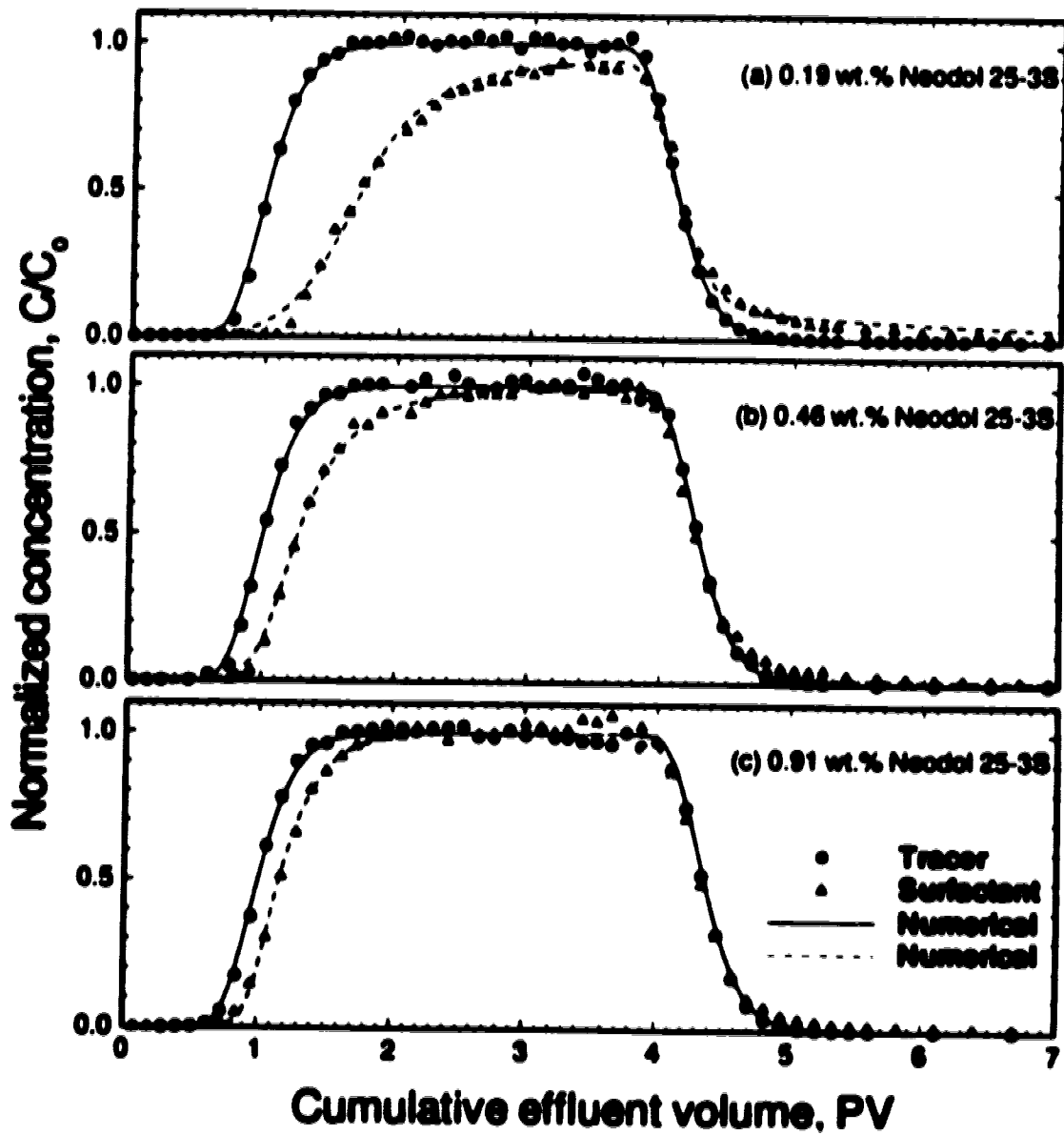


Figure 7-5. Effluent profiles calculated using the two-site model for surfactant slugs of different concentrations in 3 wt.% sodium chloride and injected at 20 mL/h, $\epsilon \leq 0.1$ wt.%.

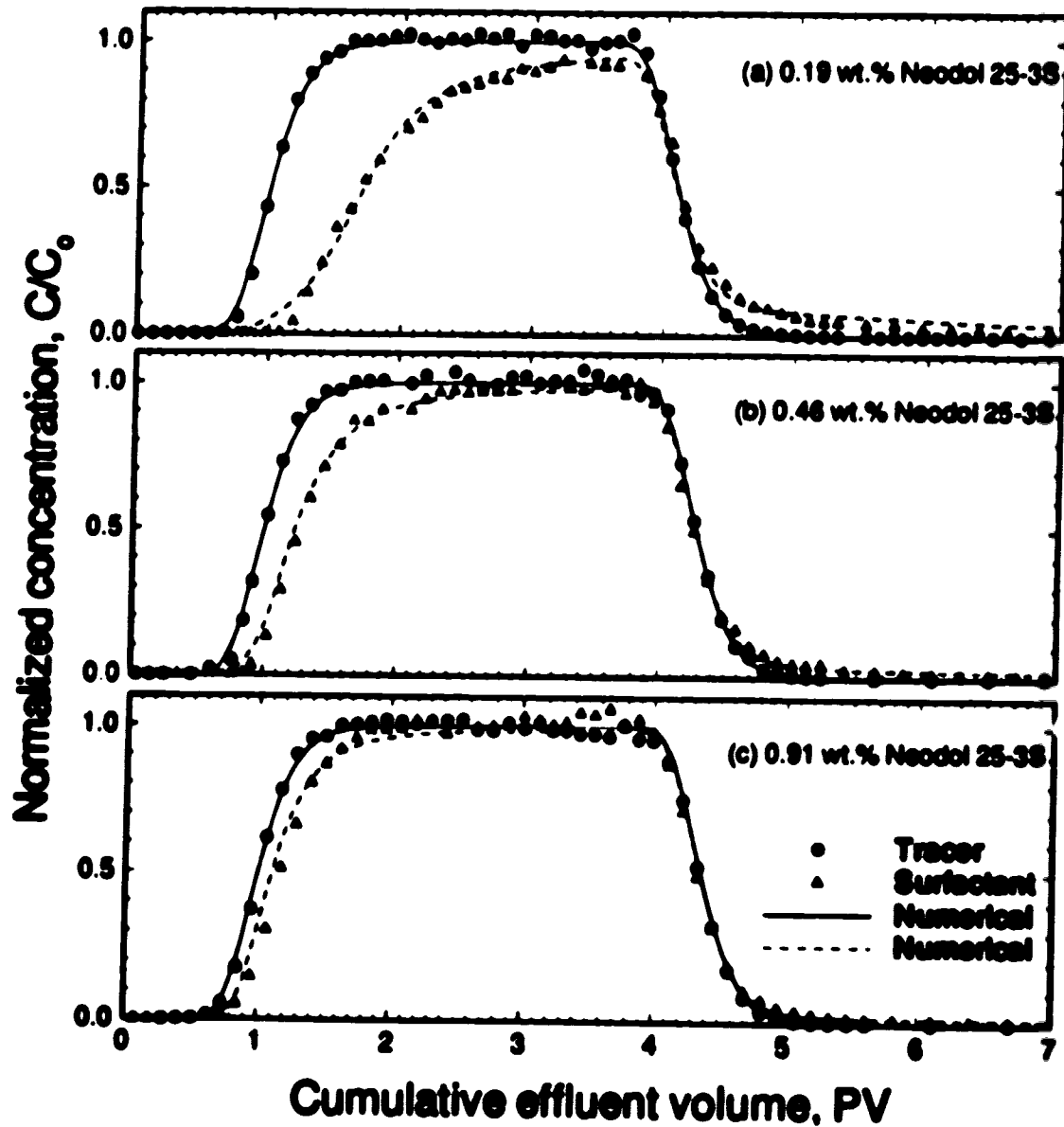


Figure 7-6. Effluent profiles calculated using the two-site model (common parameters) for different concentrations in 3 wt.% sodium chloride and injected at 20 mL/h, $\epsilon \leq 0.1$ wt.%.

Table 7-4. Summary of (a) individually fitted and (b) a common set of model parameters obtained using the two-site model, for $c \leq 0.1$ wt.%.

	Surfactant Concentration	k_{a1}	$k_{a2} = 10^3$	$k_{a2} = 10^4$	Q_{a1}/Q_a	Sum of Error Square
	(wt.%)	(L mol ⁻¹ s ⁻¹)	(L mol ⁻¹ s ⁻¹)	(s ⁻¹)		
(a)	0.19	0.154	5.965	45.90	0.260	0.04034
	0.46	0.140	3.040	79.97	0.337	0.02608
	0.91	0.213	0.240	161.8	0.412	0.03127
(b)	0.19	0.154	5.965	45.90	0.260	0.04034
	0.46	0.154	5.965	45.90	0.260	0.03295
	0.91	0.154	5.965	45.90	0.260	0.07228

As a simple illustration, the model parameters obtained from the experiment with the lowest injected concentration (0.19 wt.% Neodol 25-3S) were applied to generate new simulation profiles, as shown in Figure 7-6, for the runs of higher injected concentrations (0.46 and 0.91 wt.% Neodol 25-3S). Although, by comparing the calculated sums of error squared (see Table 7-4b), the curves obtained with a common set of model parameters were obviously less satisfactory in fitting the experimental data than those obtained from individually fitted profiles, the simulated profiles provide a good match to the trend of increasing injected concentration.

7.6 Bilayer Adsorption Model

Many studies have suggested that hydrophobic or tail-tail attractions between the adsorbed and free surfactant monomers are responsible for the sharp increase in adsorption due to the formation of surface aggregates. The proposed adsorption layer is often of a bilayer structure. By assuming strong and irreversible adsorption in the first layer followed by the adsorption of additional molecules on the previously adsorbed molecules, the overall rate of adsorption can be determined from (Foulsler *et al.*, 1989)

$$\begin{aligned}\frac{\partial \Gamma_1^*}{\partial t} &= k_{a1} c (Q_{a1}^* - \Gamma_1^*) \\ \frac{\partial \Gamma_2^*}{\partial t} &= k_{a2} c \left(Q_{a2}^* \frac{\Gamma_1^*}{Q_{a1}^*} - \Gamma_2^* \right) - k_{d2} \Gamma_2^*\end{aligned}\tag{7-16}$$

These equations are very similar to the two-site model discussed in the previous section. The amount of the second adsorbing layer is determined by the extent of saturation of the first layer. The rates of adsorption were again limited by the concentration of monomers in the bulk phase of the solution. Figure 7-7 shows the least-squares fitted profiles obtained using the bilayer model. As before, the limiting concentration used was 0.1 wt.%. The model parameters are listed in Table 7-5.

By comparing the rate constants of adsorption, it appears that the first layer forms at a much higher rate than does the second layer. The degree of first-layer saturation; that is, the ratio of Γ_1^*/Q_{a1}^* , will therefore reach unity very rapidly on all active sites. The mathematical formula for bilayer adsorption is thus reduced to a form to that identical to that of the two-site model. As a result, both the simulated curves and fitted model parameters are almost indistinguishable with those obtained using the two-site model.

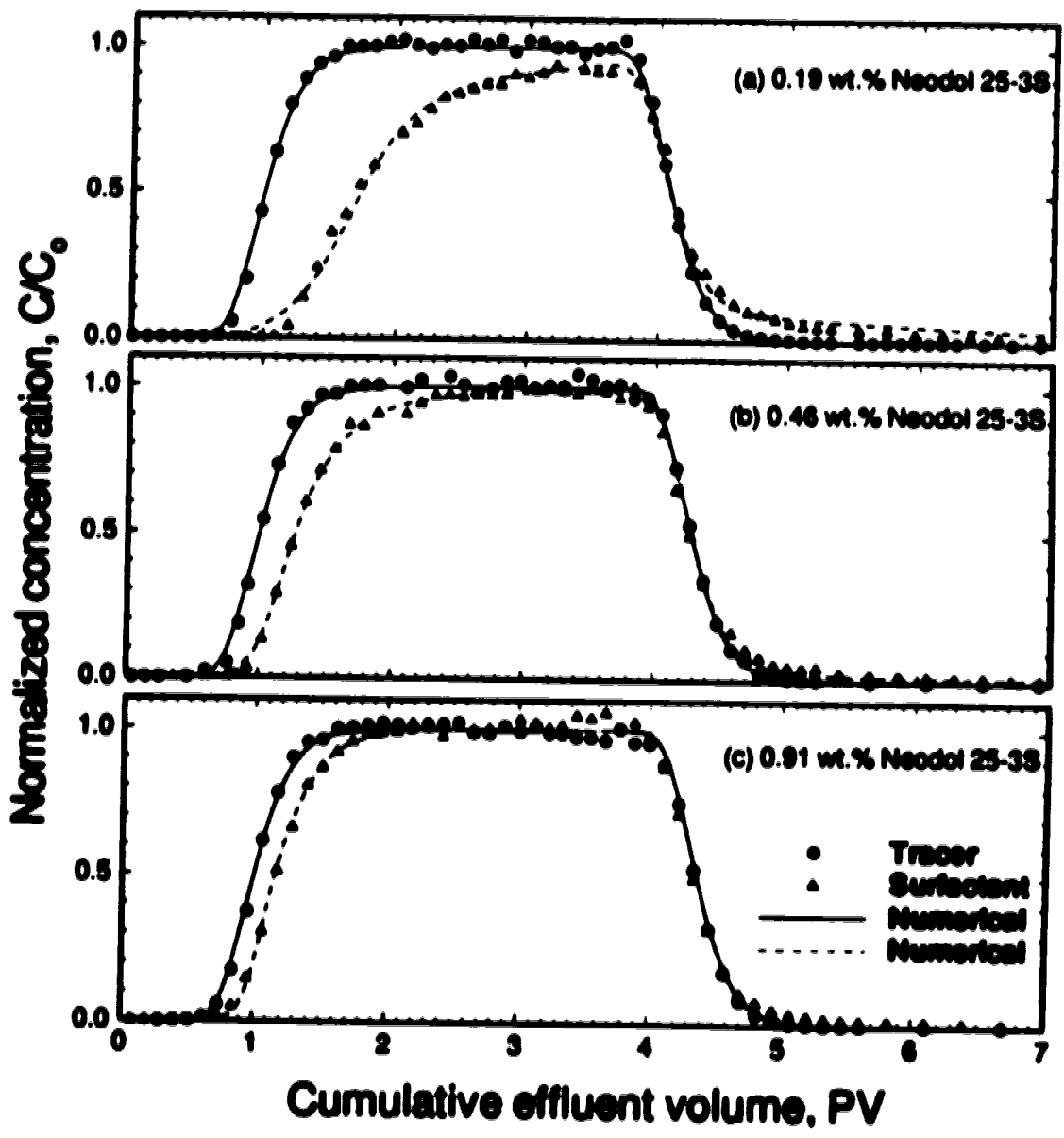


Figure 7-7. Effluent profiles calculated using a bilayer model for surfactant slugs of different concentrations in 3 wt.% sodium chloride and injected at 20 mL/h, for $\epsilon \leq 0.1$ wt.%.

Table 7-5. Summary of model parameters obtained using the bilayer model, for $c \leq 0.1$ wt.%.

Surfactant Concentration (wt.%)	k_{a1} (L mol ⁻¹ s ⁻¹)	$k_{a2} \times 10^4$ (L mol ⁻¹ s ⁻¹)	$k_{d2} \times 10^4$ (s ⁻¹)	Q_{a1}/Q_{a2}
0.19	0.166	6.474	53.92	0.283
0.46	0.163	3.948	65.20	0.333
0.91	0.215	0.438	47.32	0.414

7.7 Dynamic Adsorption at Higher Salinity

In this section, a different set of experiments was examined. The injected slugs consisted of 0.21, 0.45 and 0.99 wt.% Neodol 25-3S and 8 wt.% sodium chloride, injected at a constant flow rate of 20 mL/h. As before, all the surfactant solutions were injected for three pore volumes and then displaced by five pore volumes of 8 wt.% sodium chloride as chase brine. For the same reasons as discussed previously, the adsorption kinetics and mass-transfer characteristics are expected to be identical for all core samples. The difference in the amounts of adsorption should only be a function of the extent of saturation and independent of the driving force for adsorption; that is, the injected concentration, C_i .

Figure 7-8 shows the fitted curves using the modified two-site adsorption model. The limiting concentration for c was arbitrarily fixed at 0.1 wt.%, as before, which is 200 times higher than the measured c.m.c. of 0.0005 wt.%. Very good fits were obtained for all three injection concentrations examined. The fitted model parameters were all of the same order of magnitude, which is consistent with the conditions (for model validity) as discussed earlier. The simulated curves for the chase brine displacement did not provide as good an estimate as those simulated for the runs in 3 wt.% sodium chloride. This is possibly due to the changes in viscosity of the injected solutions (see Table 4-2). Chase

Table 7-6. Summary of model parameters obtained using the two-site model, for $c \leq 0.1$ wt.%. Surfactant slugs were prepared in 8 wt.% sodium chloride.

Surfactant Concentration (wt.%)	k_{a1} (L mol ⁻¹ s ⁻¹)	$k_{a2} = 10^3$ (L mol ⁻¹ s ⁻¹)	$k_{a2} = 10^6$ (s ⁻¹)	Q_{a1}/Q_{a2}
0.21	0.128	7.370	13.82	0.341
0.45	0.115	8.818	7.16	0.327
0.99	0.118	4.107	3.44	0.417

brine of slightly lower viscosity may have channelled through the sandstone core, displacing a lesser amount of the remaining surfactant solution in the bulk phase. This phenomenon is known as viscous fingering.

At the low surfactant concentration (0.21 wt.% Neodol 25-3S), this fingering effect was relatively insignificant as shown by the comparison of the experimental and simulated tracer profile. The viscosity measured for this surfactant solution was very close to that of the solutions of 8 wt.% sodium chloride alone (see Figure A-2). Fingering may have occurred near the injection wellbore because of a very small difference in viscosity (which was however not notable from our experimental measurements), but such an effect would have dissipated quickly due to diffusion or mechanical mixing in the porous rock. The lower effluent surfactant concentration measured may perhaps be caused by this "fingering" during initial injection, resulting in an increase in the residence time for a small portion of the surfactant solution. At higher surfactant concentrations, the effect of fingering was intensified as indicated by the discrepancy observed between the experimental and simulated tracer profiles. Although the irreversible adsorption mechanism may still be simulated because the displacement for the injection of a viscous slug is stable, the flow dynamics, adsorption-desorption mechanisms and mass-transfer characteristics cannot be accurately represented. The model employed in the current

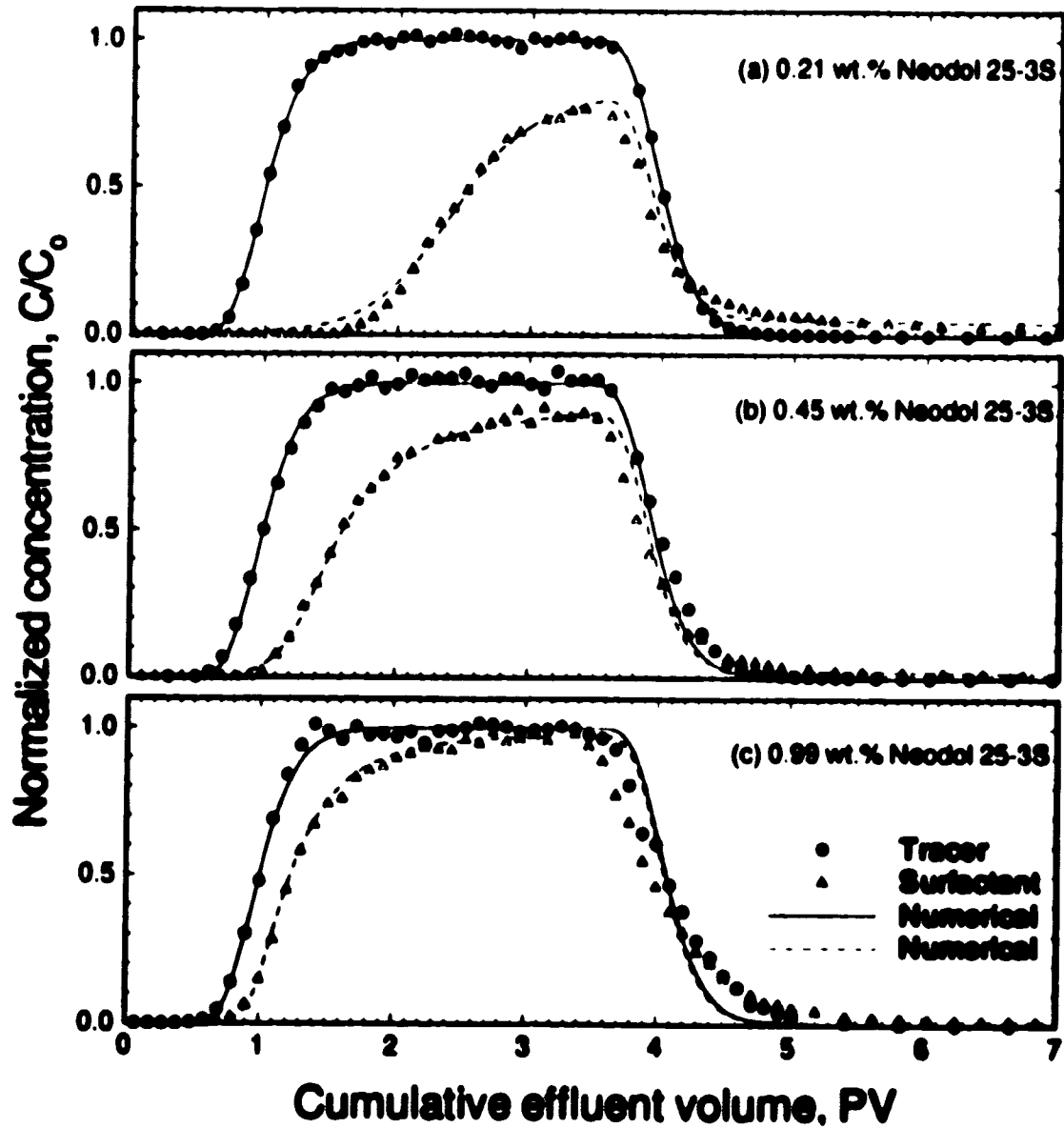


Figure 7-8. Effluent profiles calculated using the two-site model for different concentrations in 8 wt.% sodium chloride and injected at a flow rate of 20 mL/h, for $c \leq 0.1$ wt.%.

study, assuming transport of soluble mass in miscible flows, is therefore no longer valid in describing the displacement of a viscous surfactant slug by chase brine.

Consequently, investigations into the effect of surfactant concentration at higher salinity (12 wt.% sodium chloride) is not possible at this stage. The presence of a liquid crystal phase in the solution is expected to affect both the adsorption kinetics at the solid-liquid interface and the mass-transfer characteristics in the bulk phase. As observed in the experiments, this liquid crystal phase causes problems of fingering during the injection of chase brine as discussed above, which may further complicate the mechanism associated with desorption. Rather than representing the transport process as a miscible displacement problem, the mathematical formulation for a multiphase, immiscible flow model is required, which is beyond the scope of the current study.

7.8 Effect of Flow Rate

The surfactant slugs injected were prepared with approximately 0.5 wt.% Neodol 25-3S and 8 wt.% sodium chloride. The injection flow rates were 5, 20 and 120 mL/h. Detailed experimental conditions are summarized in Table 4-2.

At the lowest injection rate of 5 mL/h, the breakthrough curve appears to consist of three regions as illustrated in Figure 7-9. The initial region shows a linear increase of effluent concentration with surfactant breakthrough beginning at 0.3 PV and gradually increasing until 1.2 PV. The second region, from 1.2 - 2.0 PV, seems to approximate a portion of a retarded advection-dispersion curve. The end region shows a sudden drop in slope of the surfactant profile, possibly due to an increase in adsorption rate. In a previous study, Bae and Petrick (1977) suggested that the shape of such a breakthrough curve is a result of chromatographic separation of the surfactant components resulting from a distributed molecular weight.

Figure 7-10 shows the fitted curves of the experimental data at the three injection flow rates using Equation (7-13) with a limiting concentration of 0.1 wt.%. Model parameters are summarized in Table 7-7. As the injection flow rate increases, the initial

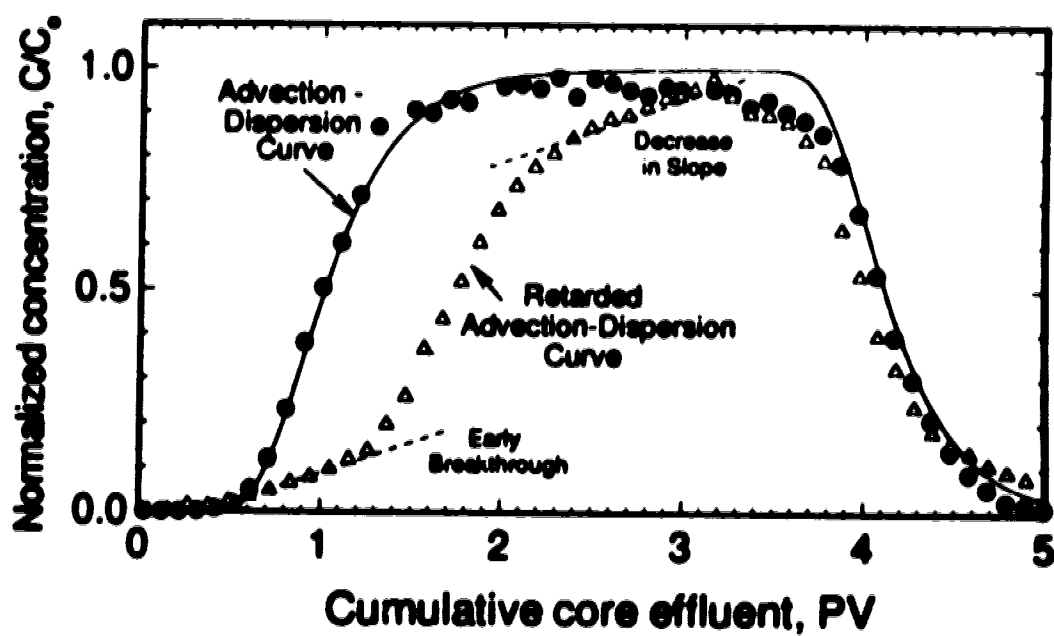


Figure 7-9. Illustration of regions on the effluent profile for surfactant adsorption under dynamic condition at a low flow rate of 5 mL/h.

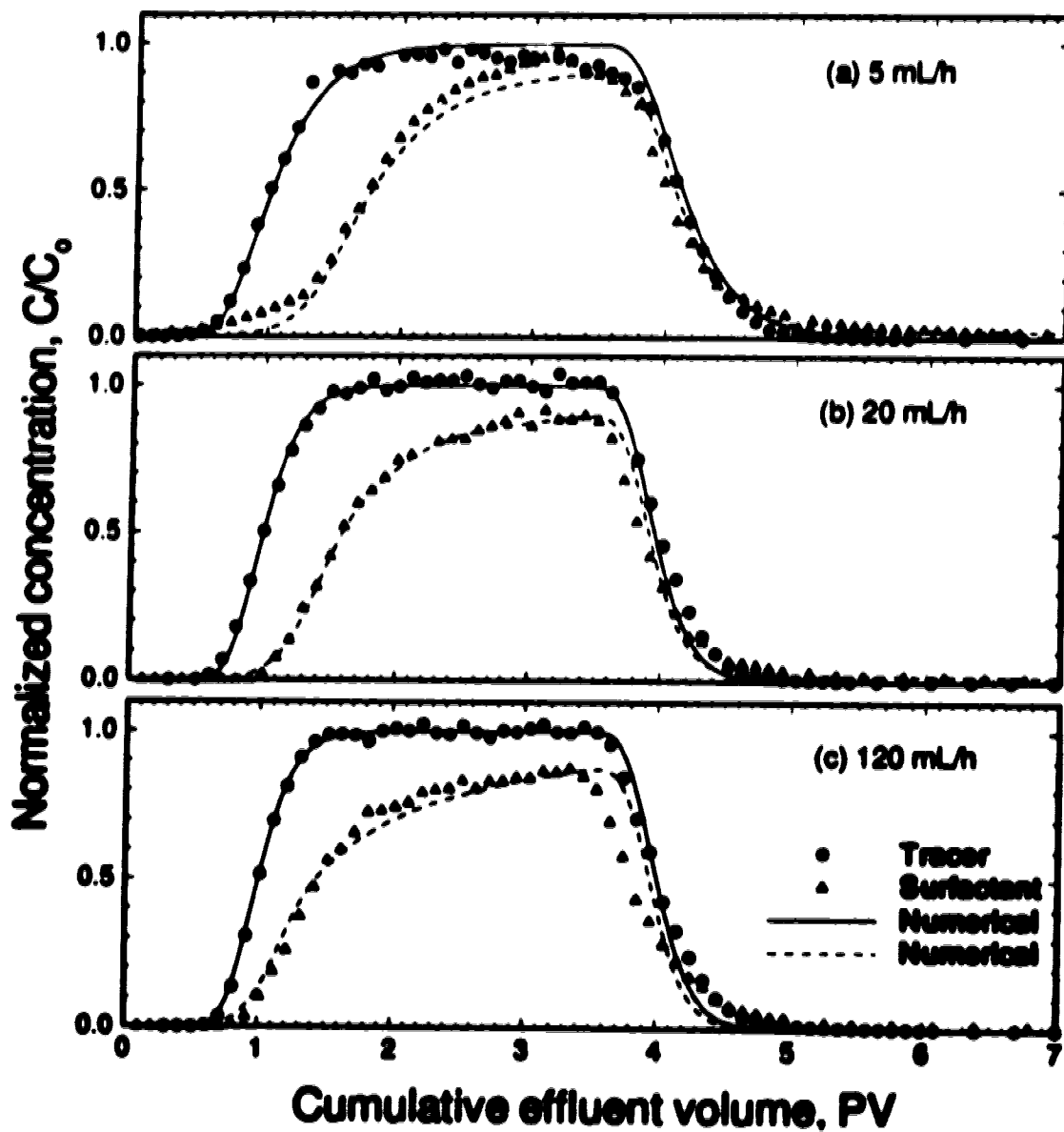


Figure 7-10. Effluent profiles calculated using the two-site model for injection of 0.5 wt.% Neodol 25-3S and 8 wt.% sodium chloride, at 5, 20 and 120 mL/h, for $\epsilon \leq 0.1$ wt.%.

region seems to disappear accompanied by a decrease in time (or pore volume) required for the breakthrough of surfactant to occur. The decreasing final or maximum values of C/C_0 in the effluent surfactant as a function of increasing flow rate indicated an increase in the extent of adsorptive saturation, even though the measured amount of adsorption varied insignificantly. An increase in flow rate also results in higher rate constants for both the first and second types of adsorption kinetics; that is, higher rates of adsorption for surfactant slugs having the same injected concentration. This observation is important since it indicates a higher rate of adsorption must have occurred near the injection wellbore. This sharp drop in surfactant concentration near the injection point has been a major concern in EOR applications as whether the effectiveness of surfactant maintains at a distance far away from the wellbore (Chung, 1991). This may explain the lower oil recovery efficiency resulting from using radial corefloods compared to that obtained using linear corefloods (Krumrine, 1982b).

Table 7-7. Summary of model parameters obtained using the two-site model, for $c \leq 0.1$ wt.%, showing the effect of flow rate on dynamic adsorption.

Flow Rate (mL/h)	k_{s1} (L mol ⁻¹ s ⁻¹)	$k_{s2} = 10^3$ (L mol ⁻¹ s ⁻¹)	$k_{d2} = 10^6$ (s ⁻¹)	Q_{s1}/Q_s
5	0.038	2.33	2.642	0.395
20	0.115	8.82	7.156	0.327
120	0.323	41.08	0.326	0.347

Recalling our early discussion of kinetic adsorption, Equation (7-9) states that the rate of adsorption depends on the maximum adsorption capacity of the adsorbent and the solute concentration (more specifically, the concentration at the surface, c_s). As the flow rate increases, convection of the stagnant boundary layer reduces the mass-transfer resistance from the bulk solution to the surface, and eventually the solute concentration

at the surface becomes the same as that in the bulk solution at high enough flow rates. In contrast, the surface and bulk concentrations may be significantly different at low injection flow rates. Although this may explain the increase in the adsorption rate constant observed in the fitted model parameters, the increase in adsorption rate constants seems to be too drastic for mass transfer by molecular diffusion to be the only explanation.

Let us consider the "effective" concentration employed in the kinetic equations. Both Troguis *et al.* (1977) and Foulser *et al.* (1989) have considered the effective concentration of monomers in solution as limited by the c.m.c. of the solution, assuming the monomer-micelle equilibration is relatively rapid. The kinetics and dynamics of micelle formation however were not mentioned. When the solution was subjected to high shearing due to the increasing flow velocity against the pore wall, micelles may be distorted and the monomers tend to escape from the micelles to the solution. This may coincide with the shear-thinning behaviour of the surfactant solutions as in Figures A-1 and A-3. The concentration of monomers in the bulk solution may therefore be higher than that calculated using instantaneous monomer-micelle equilibrium. As indicated in Foulser *et al.* (1989), a higher value for the "limiting" c.m.c. was required in order to obtain a good fit to the experimental data.

In order to provide a good estimate for effective monomer concentrations in the dynamic adsorption system, kinetics of the micellization process may also be incorporated. The rate of change in the monomer concentration can be expressed as (Hall and Tiddy, 1981):

$$\frac{\partial c}{\partial t} = -k_{f,mic}c(c-c) + k_{d,mic}(c-c) \quad (7-17)$$

The first term signifies the rate of incorporation of monomer into micelles and the second term denotes the rate of release of surfactant monomers by micelles, where $(c - c)$ is the amount of surfactant in micellar form. It should be noted that more elaborate models as mentioned here would no doubt fit equally well, but would require additional parameters ($k_{f,mic}$ and $k_{d,mic}$) that could not be evaluated unambiguously from the available data.

Detailed experimentation on the dynamic characteristics of micelles is essential; that is, in order to confirm our hypothesis of the effect of monomer concentration as a result of the increase in velocity of a bulk fluid, and to evaluate independently the rate constants of $k_{f,mic}$ and $k_{b,mic}$ as a function of flow rate.

7.9 Dynamic Adsorption of Non-fast Surfactant

As an illustration, the effect of flow rate on the adsorption of Triton X-100 in 3 wt.% sodium chloride was studied. The surfactant slugs consisted of approximately 0.5 wt.% Triton X-100 and 3 wt.% sodium chloride injected at flow rates of 20, 80 and 120 mL/h. Details of the experimental conditions are summarized Table 5-2. Figure 7-11 shows the fitted effluent profiles calculated using the two-site model with the effective concentration bound by the c.m.c. of 0.039 wt.% (see Table 7-8a). All three simulated profiles fitted well with the experimental measurements. A distinguishable change in the slope of the effluent profiles was observed, which may represent the sudden condensation of monomers on the adsorbed layer forming a bilayer or hemimicelles.

Table 7-8 summarizes the fitted model parameters obtained using the two-site model with the effective concentration defined by (a) $c \leq C_{cmc}$, and (b) $c \leq 10 \times C_{cmc}$. As the limit of the effective concentration of monomers rises, the accuracy of the fits was reduced, especially for the initial and desorption portions on the effluent profiles (see Figure 7-12).

7.10 Kinetic Adsorption of the Hemimicelle Model

In Chapter 5, the static adsorption behaviour of Triton X-100 on Berea sandstone was examined. It was observed that the adsorption isotherms were of the L4-type

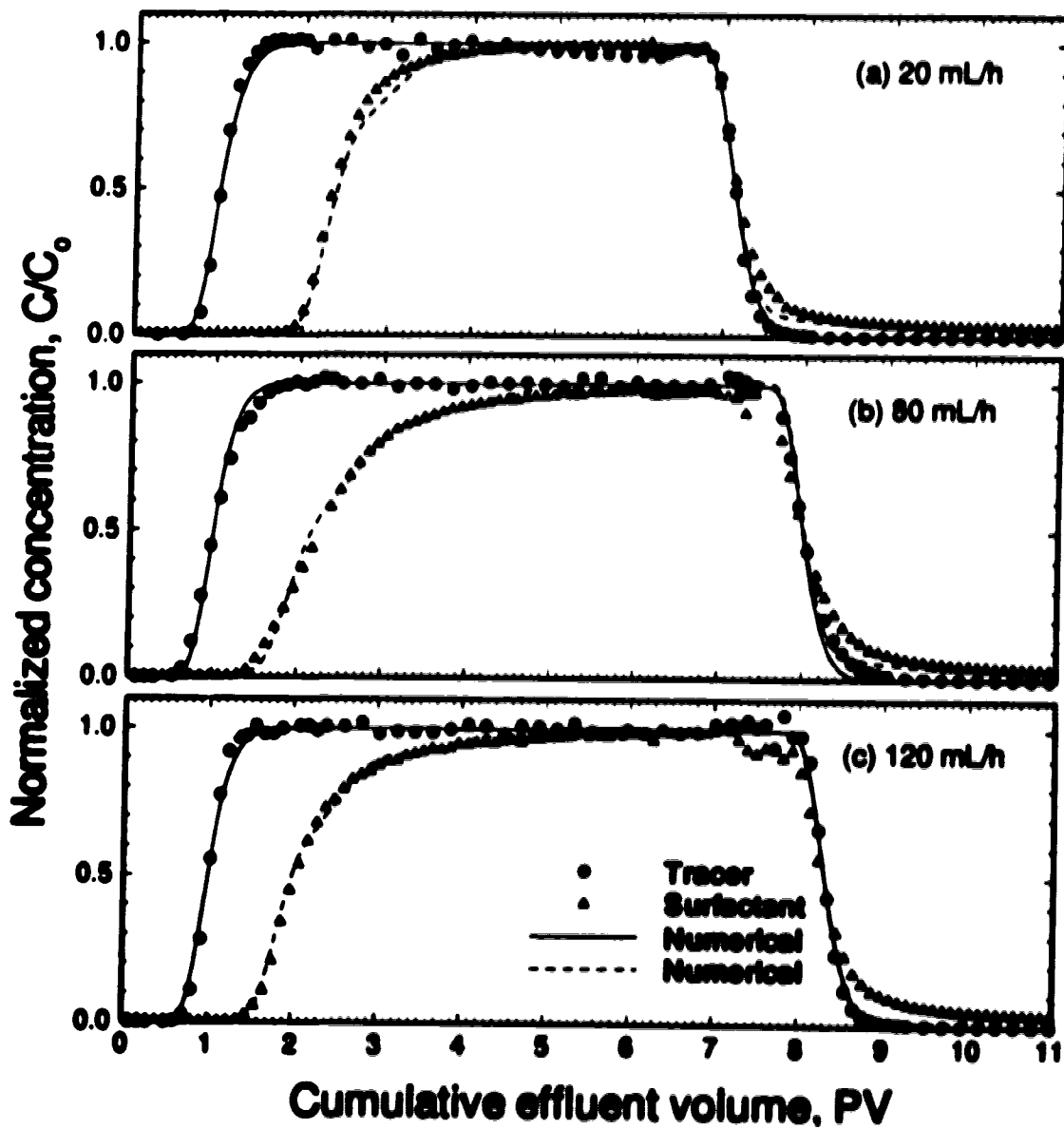


Figure 7-11. Effluent profiles calculated using the two-site model for injection of 0.5 wt.% Triton X-100 and 3 wt.% sodium chloride, injected at 20, 80 and 120 mL/h, $\epsilon \leq 0.039$ wt.%.

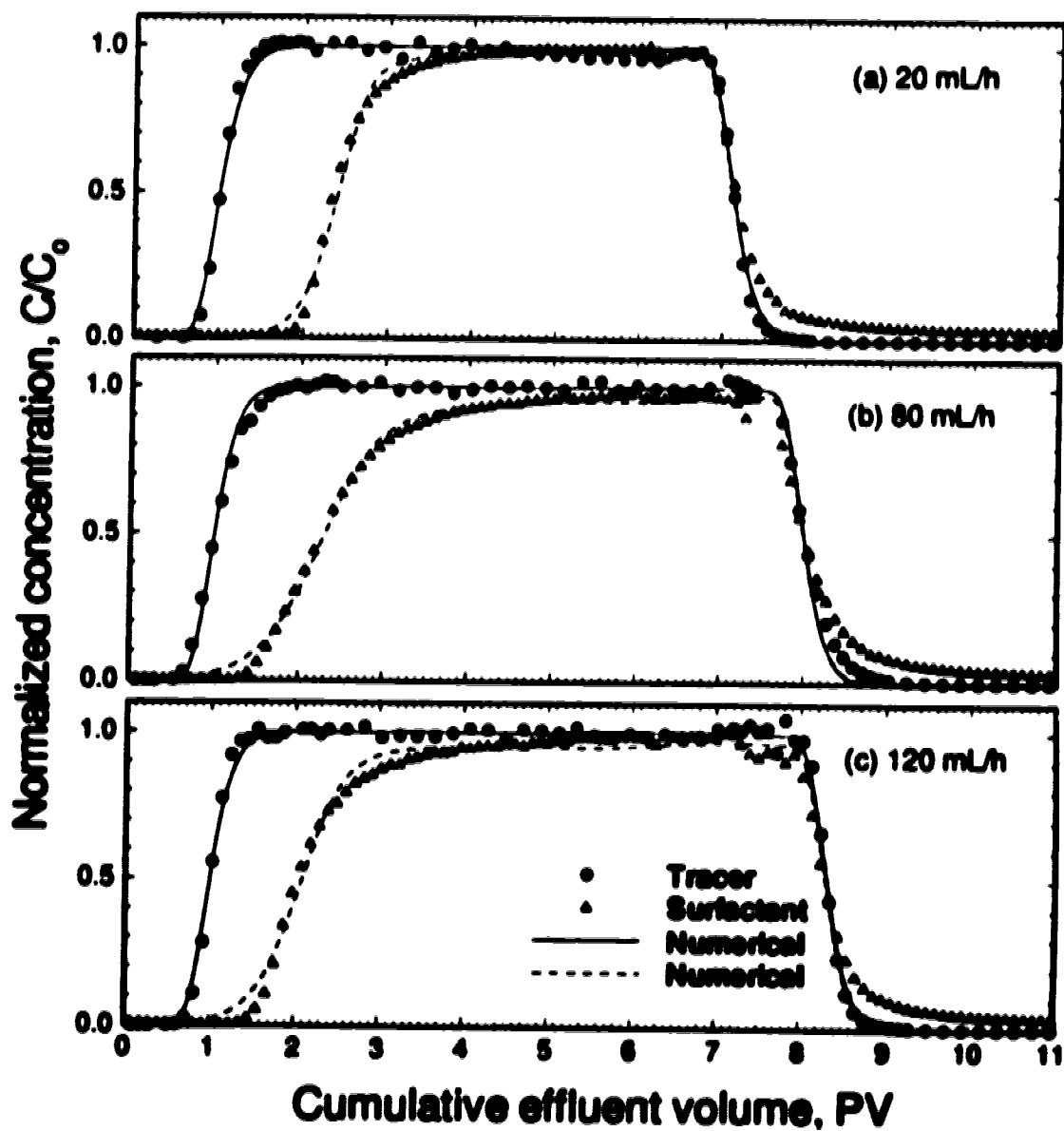


Figure 7-12. Effluent profiles calculated using the two-site model for injection of 0.5 wt.% Triton X-100 and 3 wt.% sodium chloride, injected at 20, 80 and 120 mL/h, $\epsilon \leq 0.39$ wt.%.

Table 7-8. Summary of model parameters obtained using the two-site model, for (a) $c \leq 0.039$ wt.%, and (b) $c \leq 0.39$ wt.%.

	Flow Rate (mL/h)	k_{a1} (L mol ⁻¹ s ⁻¹)	k_{a2} (L mol ⁻¹ s ⁻¹)	k_{d2} (s ⁻¹)	Q_{a1}/Q_{a2}
(a)	20	0.359	1.36×10^{-1}	1.07×10^{-4}	0.798
	80	0.999	4.88×10^{-1}	9.66×10^{-5}	0.476
	120	1.852	1.24×10^{-1}	1.28×10^{-4}	0.629
(b)	20	0.099	1.29×10^{-3}	1.29×10^{-9}	0.785
	80	0.198	1.42×10^{-2}	1.23×10^{-7}	0.687
	120	0.409	9.36×10^{-3}	3.40×10^{-7}	0.584

(Langmuir-type with two plateaux, according to Giles *et al.*, 1960) in the ranges of salinity and pH studied. From the static experiments, the maximum adsorption capacity was 3.881×10^{-4} mol/m², the equilibrium ratios for monomer and hemimicelle adsorption were 7.38×10^4 L/mol and 7.38×10^{13} (L/mol)⁻¹, respectively, and the aggregation number n was 4.36. The measured adsorption isotherms were fitted with the general isotherm equation, Equation (2-20), and the fitted model parameters were summarized in Table 5-1. It is of interest to examine further this two-step adsorption model under dynamic conditions, and to compare the results with those obtained using the two-site adsorption model.

As discussed in Zhu and Gu (1989), the L4-type isotherm as in Figure 2-7 can be represented by a two-step or hemimicelle adsorption process: (1) adsorption of monomers on the surface, serving as an "anchor", and (2) subsequent adsorption due to hydrophobic interactions forming small, isolated aggregates on the adsorbed "anchor" monomers. The rates of adsorption of monomers and hemimicelles can be expressed as

$$\frac{\partial \Gamma_m^*}{\partial t} = k_{a,m} \bar{c} (Q_s^* - \Gamma_m^* - n \Gamma_{hm}^*) - k_{d,m} \Gamma_m^* \quad (7-18)$$

$$\frac{\partial \Gamma_{hm}^*}{\partial t} = k_{a,hm} \bar{c}^{n-1} \Gamma_m^* - k_{d,hm} \Gamma_{hm}^*$$

where $k_{a,m}$ and $k_{d,m}$ are the rate constants for adsorption and desorption for the adsorbed monomers, respectively, $k_{a,hm}$ and $k_{d,hm}$ are the rate constants for hemimicelles, and n is the aggregation number. Figure 2-9 shows the detailed structure of the surface aggregates as proposed by Gao *et al.* (1987) and Harwell *et al.* (1985).

Figure 7-13 shows the fitted effluent profiles obtained using the hemimicelle adsorption model, Equation (7-18), for injection flow rates of 20, 80 and 120 mL/h. The simulated profiles were obtained using the solution c.m.c. (0.039 wt.%) as a limiting concentration for \bar{c} . At the injection rate of 20 mL/h, effluent surfactant breakthrough began at about 2 PV with a very sharp increase in slope, and gradually increased to saturation after surfactant slug was injected for 6 PV. Very good agreement between the experimental data and the fitted simulation was achieved. From Table 7-9a, it was found that the estimated number of aggregation for all three flow rates were much smaller than that calculated from the static adsorption isotherms, for which $n = 4.36$. That is, for $1 \leq n \leq 2$, adsorption beyond the initial monolayer was unsaturated (less than a bilayer). Unlike the spherical surface aggregates as suggested in Figure 2-9a (Gao *et al.*, 1987), surfactant molecules adsorbing as hemimicelles were shared by more than one molecule from the adsorbed monolayer.

The simulation for the hemimicelle model was repeated by neglecting the limit for \bar{c} ; that is, \bar{c} is equal to the total concentration of surfactant in the bulk solution. The fitted model parameters are summarized in Table 7-9b. Similar to the simulation results calculated using the two-site model, a better fit to the experimental data was obtained when \bar{c} was bound by the c.m.c. By limiting the maximum rates of adsorption, the model was able to produce a good fit to the sharp increase in the initial slope on the effluent profile.

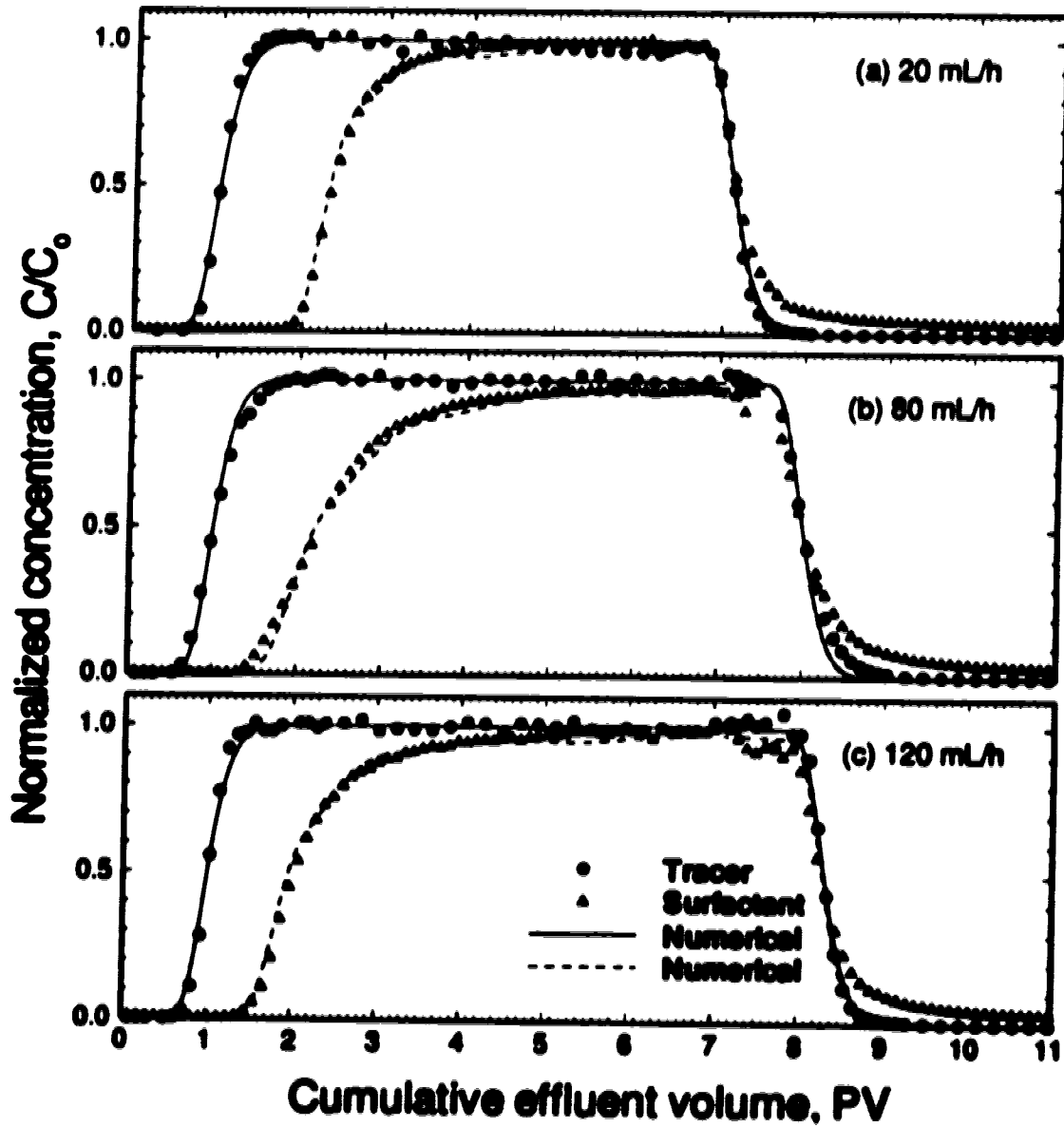


Figure 7-13. Effluent profiles calculated using the hemimicelle model for injection of 0.5 wt.% Triton X-100 and 3 wt.% sodium chloride, at 20, 80 and 120 mL/h, for $\epsilon \leq 0.039$ wt.%.

Table 7-9. Summary of model parameters obtained using the kinetic adsorption model for hemimicelle formation. (a) $c \leq 0.039$ wt.%, and (b) $c = c$.

	Flow Rate (mL/h)	$k_{a,m}$ (L mol ⁻¹ s ⁻¹)	$k_{a,hm} = 10^1$ (L ² mol ⁻² s ⁻¹)	$k_{d,hm} = 10^0$ (s ⁻¹)	n
(a)	20	0.517	2.489	0.213	1.362
	80	1.014	4.777	0.128	1.516
	120	2.070	7.628	0.337	1.667
(b)	20	0.106	0.703	16.67	1.533
	80	0.209	0.788	0.048	1.475
	120	0.470	3.423	0.169	1.771

Chapter 8

Conclusions and Recommendations

8.1 Propagation and Adsorption of Neodol 25-3S

An experimental study was conducted to examine the propagation and adsorption of the anionic surfactant, Neodol 25-3S, in unfired Berea sandstone cores. This investigation has found that many parameters, *i.e.*, sodium chloride concentration, pH, flow rate, surfactant concentration and the presence of a liquid crystal phase, affect the rate of surfactant propagation in the following ways:

- i*** At low surfactant concentrations, the effect of sodium chloride concentration on surfactant propagation and adsorption was significant, giving higher adsorption at higher salinity. Both the static and dynamic adsorption tests showed that surfactant adsorption is a direct function of sodium chloride concentration.

- ii*** No significant change in the amount of surfactant adsorption was observed as the pH was decreased from 6 to 2. Increasing the pH of the surfactant slug from 6 to 12, on the other hand, reduced surfactant loss by nearly 30 percent. This demonstrates the importance of adding an alkali to chemical EOR processes where an anionic surfactant is used in sandstone reservoirs.

- iii** At a given sodium chloride concentration and surfactant concentration, surfactant loss was found to decrease as the injection flow rate was increased.
- iv** At high surfactant concentrations and over a narrow range of sodium chloride concentrations, a liquid crystal phase was formed. The presence of this phase resulted in a higher apparent viscosity, a dramatic increase in the pressure drop across the core and significant retention in the core. The latter was due to the formation of viscous fingers at the tail of the surfactant slug.

8.2 Propagation and Adsorption of Triton X-100

Similarly, an experimental study was performed to study the propagation and adsorption of the non-ionic surfactant, Triton X-100, on consolidated Berea sandstone. Static tests were also conducted to study the adsorption mechanism. The effects of sodium chloride, pH and injection flow rate were examined. The results are summarized as below:

- i** Static adsorption isotherms were of the stepped Langmuir type (L4), with the value of second plateau significantly higher than the first. The adsorption mechanism could be described by the hemimicelle model.
- ii** An increase in adsorption for increasing sodium chloride concentration was observed, which is due to the "salting-out" effect.
- iii** A reduction in adsorption for increasing pH (from 6 to 12) and increasing flow rate (from 20 to 120 mL/h) was observed. More significant variation

or pronounced trend was reported at low sodium chloride concentration (3 wt.%) than that at high sodium chloride concentration (8 wt.%).

- iv* The maximum adsorption obtained from dynamic tests was consistently lower than that obtained from static tests. This discrepancy increased as the flow rate was increased. Increasing the pH from 7 to 12 reduced the adsorption. This effect was also more significant under dynamic conditions than under static conditions.

8.3 Dispersion in Berea Sandstone Cores with Radial Flow

A numerical model was derived to describe the dispersion processes occurring in consolidated porous media (sandstone cores) with axisymmetric radial flow. The Galerkin finite element method was applied to solve the unidimensional advection-dispersion equation. Several dispersion models, which were previously applied in the literature, have been re-examined in the current study for the evaluations of model validity and applicability on the radial flow problems. The following conclusions have been made:

- i* The boundary condition employed at the injection wellbore, viz., Dirichlet and Cauchy conditions, was not important for the core dimensions and the range of flow rates tested.
- ii* The simulated results showed that a semi-infinite core, by defining a fictitious radius for the simulated core, is required in order to provide a good approximation of the effluent profiles, for the core size used.
- iii* An empirical form of $D = D_0 + \alpha v^n$ was the most suitable dispersion model in characterizing the dispersive transport of soluble mass in the flow

pattern and regime examined (for *Regime b*, both the effects of mechanical dispersion and diffusion are important).

8.4 Dynamic Adsorption

The mathematical modelling of the propagation of the anionic and non-ionic surfactants, determined experimentally in Chapters 4 and 5, is presented. Numerical solutions of the coupled advective-dispersive transport and adsorption equations were obtained. Several commonly applied adsorption models, such as equilibrium and kinetic Langmuir, two-site, bilayer and hemimicelle models, were examined. The following results have been observed:

- i* Linear (Henry's law) and non-linear (Langmuir-type) equilibrium adsorption models were not suitable for matching effluent profiles of surfactant propagation under the experimental conditions employed.
- ii* For the dynamic adsorption of Neodol 25-3S on Berea sandstone cores, a kinetic Langmuir model, which assumes a homogeneous surface for adsorption of all surfactant components, overestimated the amount of surfactant adsorbed.
- iii* Two-site and bilayer adsorption models provided a good approximation to the observed effluent profiles for the anionic surfactant, Neodol 25-3S.
- iv* For the bilayer model, the rate of first-layer adsorption was found to be more rapid than that of the second-layer formation. As a result, the mathematical formula for bilayer adsorption reduces to an identical form as the two-site model. For the adsorption processes examined in this

study, the simulated curves (and the fitted model parameters) obtained by the bilayer and two-site models were virtually indistinguishable.

- v The simulated rate of adsorption increases with increasing injection flow rate, which may be attributed to an increase in the monomer concentration in the bulk solution. This observation is important since it indicates a higher rate of adsorption would have occurred near the injection wellbore; thus, the effectiveness of surfactant would not be maintained at a distance far away from the wellbore. As a result, the oil recovery efficiency in radial corefloods is lower as compared with that in linear corefloods. Hence, a better indication to the actual adsorption process in the oil reservoirs is obtained by using the radial geometry.

- w The kinetic hemimicelle model appears to provide a better description for the effluent profiles than two-site model for the injection of non-ionic surfactant, Triton X-100. The motivation for this hemimicelle formation approach is based upon the experimentally observed two-plateaux adsorption isotherms from Chapter 5.

- vi The effects of monomeric-micellar equilibrium and/or kinetics play an important role in surfactant adsorption in a dynamic system. It is possible that the concentration of surfactant monomers in solutions is a function of the injection flow rate, such that distortion of micellar shape and reduction in the number of aggregating molecules (both in micelles and surface aggregates) becomes more pronounced at higher flow rates.

8.5 Recommendations

In summary, future studies must fully address the numerical simulation of the detailed mass transport characteristics in the flow regime where both mechanical dispersion and molecular diffusion are important. A wide range of injection flow rates and various core dimensions should be examined.

Future experimental work should employ sandstone cores of various radii to provide better characterizations of the dispersive transport with non-uniform flow patterns and the dynamics of adsorption closer to the injection wellbore. The sandstone samples after each run should be sectioned and analyzed for the adsorbed chemical contents in order to determine the distribution of adsorption across the core (*i.e.*, as a function of fluid velocity). It may be then possible to establish useful relationships between the rate parameters of mass transfer and kinetic adsorption.

The effects of monomer-micelle kinetics should be studied more carefully. In the current work, the amount of monomers is assumed to be bound by a constant limiting concentration, similar to the critical micelle concentration, which determines the driving potential for adsorption. Detailed and complicated experimentation into the kinetics of micelle formation or monomer-micelle equilibration in a flow system is necessary in order to provide an unambiguous interpretation. Nevertheless, additional flow experiments using the existing procedure and set-up may be helpful but they should include only the use of low surfactant concentrations for injection, for example, in the monomer-micelle transition region near the critical micelle concentration.

The mathematical model for miscible displacement of an adsorbing species developed in this work is relatively simple in form. A general flow model can be obtained by applying Darcy's law for the approximation of the bulk motion in fluid, which can be extended to describe multiphase flow problems and to model the flow patterns in unstable displacement due to viscous fingering.

References

- Abramowitz, M., and I.A. Stegun (Eds.), "Handbook of Mathematical Functions", Applied Mathematics Series 55, National Bureau of Standards, Washington, D.C. (1964).
- Anacker, E.W., *Electrolyte Effect on Micellization*, in "Solution Chemistry of Surfactants, Volume 1", K.L. Mittal (Ed.), Plenum Press, New York (1979) 247-265.
- Aris, R., *On the Dispersion of a Solute in a Fluid Flowing through a Tube*, Proc. Roy. Soc., Ser. A, 235 (1956) 67-77.
- Aris, R., *The Longitudinal Diffusion Coefficient in Flow Through a Tube with Stagnant Pockets*, Chem. Eng. Sci., 11 (1959) 194-198.
- Aveyard, R., *Adsorption at the Air/Liquid, Liquid/Liquid and Solid/Liquid Interfaces*, in "Surfactants", Th.F. Tadros (Ed.), Academic Press, London (1984) 153-173.
- Avgal, N.N., A.V. Kiselev and L.A. Lygina, *Standard Thermodynamic Functions for Adsorption on a Uniform Surface and Activity Coefficients of the Adsorbate in the Adsorbed Layer*, Zh. Fiz. Khim. (Russian J. Phys. Chem.), 38 (1964) 2055-2059.
- Bedekhehan, A., and P. Bakes, *Experimental Investigation and Numerical Modelling of Surfactant Adsorption in Dilute Surfactant Flooding in Carbonate Rock*, in "Enhanced Oil Recovery", A. Chakma, M.R. Islam and F. Berruti (Eds.), AIChE Symposium Series, Number 280, Volume 87 (1991) 98-104.
- Bee, J.H., and C.B. Patrick, *Adsorption/Retention of Petroleum Sulfonates in Berea Cores*, SPE J., 17 (1977) 353-357.
- Bear, J., "Dynamics of Fluids in Porous Media", Dover Pub., Inc., New York (1972).
- Bouton, R.G., and R.F. Nielsen, *A Study of Plane, Radial Miscible Displacement in a Consolidated Porous Medium*, SPE J., 5 (1965) 1-5.
- Berg, R.R., "Reservoir Sandstones", Prentice-Hall, Inc., Englewood Cliffs, New Jersey (1986).
- Bidner, M.S., and V.C. Vampa, *A General Model for Convection-Dispersion-Dynamic Adsorption in Porous Media with Stagnant Volume*, J. Pet. Sci. Eng., 3 (1989) 267-281.

- Boomgaard, Th. van den, Sh.M. Zourab and J. Lyklema, *On the Influence of Concentrated Electrolytes on the Association Behaviour of a Non-Ionic Surfactant*, *Prog. Colloid Polym. Sci.*, 68 (1983) 25-32.
- Brigham, W.E., *Mixing Equations in Various Geometries*, *SPE Res. Eng.*, 1 (1986) 203-208.
- Brigham, W.E., and P.W. Reed, *Experiments on Mixing During Miscible Displacement in Porous Media*, *SPE J.*, 1 (1961) 1-8.
- Brunauer, S., L.S. Deming, W.E. Deming and E. Teller, *Theory of the Van der Waals Adsorption of Gases*, *J. Am. Chem. Soc.*, 62 (1940) 1723-1732.
- Chen, C.S., *Analytical Solutions for Radial Dispersion with Cauchy Boundary at Injection Well*, *Water Resources Res.*, 27 (1987) 1217-1224.
- Chung, F.T.H., "Modeling of Surfactant Transport and Adsorption in Porous Media", Topical Report submitted to U.S. Department of Energy, Assistant Secretary for Fossil Energy, prepared by IIT Research Institute, National Institute for Petroleum and Energy Research, Bartlesville, Oklahoma, April (1991).
- Ci-Qun, L., and Y. Jia, *Radial Transport in Porous Media with Dispersion and Adsorption*, *J. Hydrodynamics, Ser. B*, 4 (1990) 87-90.
- Clunis, J.S., and B.T. Ingram, *Adsorption of Nonionic Surfactants*, in "Adsorption from Solution at the Solid/Liquid Interface", G.D. Parfitt and C.H. Rochester (Eds.), Academic Press, New York (1983) 105-152.
- Coats, K.H., and B.D. Smith, *Dead-End Pore Volume and Dispersion in Porous Media*, *SPE J.*, 4 (1964) 73-84.
- Corkill, J.M., J.F. Goodman and J.R. Tate, *Adsorption of Alkylsulphonylalkanol on Graphon*, *Trans. Faraday Soc.*, 63 (1967) 2264-2269.
- Daniel, S.G., *The Adsorption on Metal Surfaces of Long Chain Polar Compounds from Hydrocarbon Solutions*, *Trans. Faraday Soc.*, 47 (1951) 1345-1359.
- Denoyel, R., and J. Rouquerol, *Thermodynamic (including Microcalorimetry) Study of the Adsorption of Nonionic and Anionic Surfactants onto Silica, Kaolin, and Alumina*, *J. Colloid Interface Sci.*, 143 (1991) 555-572.
- Doran, A., D. Vargas and J. Goldfarb, *Non-ionic Surfactants as Flotation Collectors*, *Trans. Instn. Min. Metall., Sec. C.*, 84 (1975) C34-37.
- Doehar, T.M., G.E. Myers and D.C. Atkins, Jr., *The Behavior of Nonionic Surface Active Agents in Salt Solutions*, *J. Colloid Sci.*, 6 (1951) 223-235.

- Douillard, J.M., S. Pougnet, B. Faucompre and S. Partyka, *The Adsorption of Polyoxyethylenated Octyl and Nonylphenol Surfactants on Carbon Black and Sulfur from Aqueous Solutions*, *J. Colloid Interface Sci.*, 154 (1992) 113-121.
- Esami, K., Y. Sakamoto and K. Meguro, *Mixed Bilayers of Anionic and Nonionic Surfactants on Alumina*, *J. Colloid Interface Sci.*, 134 (1990) 283-288.
- Figdore, P.E., *Adsorption of Surfactants on Kaolinite: NaCl versus CaCl₂, Salt Effects*, *J. Colloid Interface Sci.*, 87 (1982) 500-517.
- Foulsler, R.W.S., S.G. Goodyear and R.J. Sims, *Dynamic Adsorption of an Anionic Surfactant on Sandstone*, Proceedings of the 5th European Symposium on Improved Oil Recovery held in Budapest, Hungary, April 25-27 (1989).
- French, T.R., and T.E. Burchfield, *Design and Optimization of Alkaline Flooding Formulations*, SPE Paper 20238 presented at the SPE/DOE 7th Symposium on Enhanced Oil Recovery held in Tulsa, Oklahoma, April 22-25 (1990).
- Fried, J.J., and M.A. Combarous, *Dispersion in Porous Media*, *Adv. Hydro. Sci.*, 1 (1971) 169-282.
- Friedmann, F., *Surfactant and Polymer Losses During Flow Through Porous Media*, *SPE Res. Eng.*, 1 (1986) 261-271.
- Furlong, D.N., and J.R. Aston, *Adsorption of Polyoxyethylated Nonyl Phenols at Silica/Aqueous Solution Interfaces*, *Colloids Surfaces*, 4 (1982) 121-129.
- Geo, Y., J. Du and T. Gu, *Hemimicelle Formation of Cationic Surfactants at the Silica Gel-Water Interface*, *J. Chem. Soc., Faraday Trans. 1.*, 83 (1987) 2671-2679.
- Gaudin, A.M., and D.W. Fuerstenau, *Quartz Flotation with Anionic Collectors*, *Trans. AIME, Mining Eng.*, 202 (1955a) 65-72.
- Gaudin, A.M., and D.W. Fuerstenau, *Quartz Flotation with Cationic Collectors*, *Trans. AIME, Mining Eng.*, 202 (1955b) 958-962.
- Gethar, L.W., and M.A. Collins, *General Analysis of Longitudinal Dispersion in Nonuniform Flow*, *Water Resources Res.*, 7 (1971) 1411-1521.
- Genuchten, M.Th. van, and W.J. Alves, "Analytical Solutions of the One-Dimensional Convective-Dispersive Solute Transport Equation", U.S. Department of Agriculture, Technical Bulletin No. 1661 (1982) 151p.

- Giles, C.H., T.H. MacEwan, S.N. Nakhwa and D. Smith, *Adsorption. XI. A System of Classification of Solution Adsorption Isotherms, and its Use in Diagnosis of Adsorption Mechanisms and in Measurement of Specific Surface Areas of Solids*, *J. Chem. Soc.*, (1960) 3973-3993.
- Glover, C.J., M.C. Puerto, J.M. Maerker and E.L. Sandvik, *Surfactant Phase Behavior and Retention in Porous Media*, *SPE J.*, 12 (1979) 183-193.
- Gracias, A., L.N. Fortney, R.S. Schechter, W.H. Wade and S. Yiv, *Criteria for Structuring Surfactants to Maximize Solubilization of Oil and Water. I. Commercial Non-Ionics*, SPE Paper 9815 presented at the SPE/ODE 2nd Joint Symposium on Enhanced Oil Recovery of the Society of Petroleum Engineers of AIME held in Tulsa, Oklahoma, April 5-8 (1981).
- Gray, G.W., and P.A. Winsor (Eds.) , "Liquid Crystals & Plastic Crystals. Volume I. Physico-Chemical Properties and Methods of Investigation", Ellis Horwood Limited, Chichester (1974).
- Gregg, S.J., "The Surface Chemistry of Solids", 2nd Ed., Reinhold Pub. Corp., New York (1961).
- Gupta, S.P., and R.A. Greenkorn, *Determination of Dispersion and Nonlinear Adsorption Parameter for Flow in Porous Media*, *Water Resources Res.*, 10 (1974) 839-846.
- Hall, D.G., and G.J.T. Tiddy, *Surfactant Solutions: Dilute and Concentrated*, in "Anionic Surfactants. Physical Chemistry of Surfactant Action", E.H. Lucassen-Reynders (Ed.), Marcel Dekker, Inc., New York (1981) 55-108.
- Hankins, N.P., "A Study of Surfactant Adsorption with Applications in Surfactant Assisted Enhanced Oil Recovery Processes", Ph.D. Dissertation, University of Oklahoma, Norman, Oklahoma (1989).
- Harwell, J.H., "Surfactant Adsorption and Chromatographic Movement with Application in Enhanced Oil Recovery", Ph.D. Dissertation, University of Texas at Austin, Texas (1983).
- Harwell, J.H., J.C. Hoskins, R.S. Schechter and W.H. Wade, *Pseudophase Separation Model for Surfactant Adsorption: Isomerically Pure Surfactants*, *Langmuir*, 1 (1985) 251-262.
- Hildebrand, F.B., "Advanced Calculus for Applications", 2nd Ed., Prentice-Hall, Englewood Cliffs, New Jersey (1976).
- Hill, H.J., J. Reisberg and G.L. Stegemeier, *Aqueous Surfactant Systems for Oil Recovery*, *J. Pet. Techn.*, 25 (1973) 186-194.
- Hill, H.J., and D.R. Thigpen, *Waterflood Oil Recovery with Chromatographically Balanced Surfactant and Thickenor*, Canadian Patent No.994,094, August 3 (1976).

- Hill, T.L., *Statistical Mechanics of Multimolecular Adsorption. I & II.*, J. Chem. Phys., 14 (1946) 263-267, 441-453.
- Hirasaki, G.J., *Interpretation of the Change in Optimal Salinity with Overall Surfactant Concentration*, SPE J., 22 (1982) 971-982.
- Hoopes, J.A., and D.R.F. Harleman, *Dispersion in Radial Flow from a Recharge Well*, J. Geophys. Res., 72 (1967) 3595-3607.
- Hough, D.B., and H.M. Rendall, *Adsorption of Ionic Surfactants*, in "Adsorption from Solution at the Solid/Liquid Interface", G.D. Parfitt and C.H. Rochester (Eds.), Academic Press, New York (1983) 247-319.
- Hsieh, P.A., *A New Formula for the Analytical Solution of the Radial Dispersion Problem*, Water Resource Res., 22 (1986) 1597-1605.
- Huang, Z., and T. Gu, *Mixed Adsorption of Nonionic and Cationic Surfactants on Silica Gel and Methylated Silica Gel*, Colloids Surfaces, 28 (1987) 159-168.
- Hurd, B.G., *Adsorption and Transport of Chemical Species in Laboratory Surfactant Water-flooding Experiments*, SPE Paper 5818 presented at the Improved Oil Recovery Symposium of the Society of Petroleum Engineers of AIME held in Tulsa, Oklahoma, March 22-24 (1976).
- Khilar, K.C., H.S. Fogler and J.S. Ahluwalia, *Sandstone Water Sensitivity: Existence of a Critical Rate of Salinity Decrease for Particle Capture*, Chem. Eng. Sci., 38 (1983) 789-800.
- Klimenko, N.A., and A.M. Koganovskii, *Adsorption of Nonionic Surfactants in the Associated State from Aqueous Solutions on Polar Sorbents*, Kolloid. Zh., 36 (1974) 151-154.
- Klimenko, N.A., *Activity Coefficient of Adsorbed Anions of Surfactants at the Interface Between an Aqueous Solution and a Carbon Sorbent*, Kolloid. Zh., 40 (1978a) 994-997.
- Klimenko, N.A., *Calculation of Isotherms for Adsorption of Nonionic Surfactants from Aqueous Solutions on a Carbon Sorbent Below the Critical Micellization Concentration*, Kolloid. Zh., 40 (1978b) 1105-1109.
- Koch, D.L., and J.F. Brady, *Dispersion in Fixed Beds*, J. Fluid Mech., 154 (1985) 399-427.
- Koganovskii, A.M., N.A. Klimenko and M.M. Chobana, *Adsorption of Alkylsulfates and Alkylsulfonates on Acetylene Black from Aqueous Solutions up to Critical Micelle Concentration*, Kolloid. Zh., 39 (1977) 358-361.
- Koganovskii, A.M., T.M. Levchenko and V.A. Kirichenko, *The Adsorption of Mixtures of Organic Substances from Aqueous Solutions on Carbonaceous Adsorbents. I, II & III.*, Zh. Fiz. Khim. (Russian J. Phys. Chem.), 50 (1976) 1239-1240, 1255-1257, 1241-1243.

- Krumrine, P.H., J.S. Falcone, Jr. and T.C. Campbell, *Surfactant Flooding 1: The Effects of Alkaline Additives on IFT, Surfactant Adsorption, and Recovery Efficiency*, SPE J., **22** (1982a) 503-513.
- Krumrine, P.H., J.S. Falcone, Jr. and T.C. Campbell, *Surfactant Flooding 2: The Effects of Alkaline Additives on Permeability and Sweep Efficiency*, SPE J., **22** (1982b) 983-992.
- Kuznetsova, A.M., V.A. Volkov and E.M. Aleksandrova, *Effect of Electrolytes on the Hydration of Nonionic Surfactants in Aqueous Solutions and in Adsorption Layers*, Kolloid. Zh., **38** (1976) 172-175.
- Labrid, J., *Flow Modelling of Alkaline Dissolution by a Thermodynamic or By a Kinetic Approach*, SPE Res. Eng., **8** (1993) 151-159.
- Lapidus, L., and N.R. Amundson, *Mathematics of Adsorption in beds. VI. The Effects of Longitudinal Diffusion in Ion Exchange and Chromatographic Columns*, J. Phys. Chem., **56** (1952) 984-988.
- Lawson, J.B., *The Adsorption of Non-ionic and Anionic Surfactants on Sandstone and Carbonate*, SPE Paper 7052 presented at the 5th Symposium on Improved Methods for Oil Recovery of the Society of Petroleum Engineers of AIME held in Tulsa, Oklahoma, April 16-19 (1978).
- Lawson, J.B., and R.E. Dilgrea, *Adsorption of Sodium Alkyl Aryl Sulfonates on Sandstone*, SPE Paper 6121 presented at the 51st Annual Fall Conference and Exhibition of the Society of Petroleum Engineers of AIME held in New Orleans, Louisiana, October 3-6 (1976).
- Lawson, J.B., and D.R. Thigpen, *Staged Performed-Surfactant-Optimized Aqueous Alkaline Flood*, Canadian Patent No.1,221,621, May 12 (1987).
- Legatski, M.W., and D.L. Katz, *Dispersion Coefficients for Gases Flowing in Consolidated Porous Media*, SPE J., **7** (1967) 43-53.
- Levitz, P., H.V. Damms and D. Kernis, *Fluorescence Decay Study of the Adsorption of Nonionic Surfactants at the Solid-Liquid Interface. I. Structure of the Adsorption Layer on a Hydrophilic Solid*, J. Phys. Chem., **88** (1984) 2228-2235.
- Lewis, S.J., L.A. Verkruyse and S.J. Salter, *Selection of Nonionic Surfactants for Minimized Adsorption and Maximized Solubilization*, SPE Paper 14910 presented at the SPE/DOE 5th Symposium on Enhanced Oil Recovery of the Society of Petroleum Engineers and the Department of Energy held in Tulsa, Oklahoma, April 20-23 (1986).
- Lindman, B., *Structural Aspects of Surfactant Micellar Systems*, in "Surfactants", Th.F. Tadros (Ed.), Academic Press, London (1984) 83-109.

- Ma, S., and N.R. Morrow, *Effect of Firing on Petrophysical Properties of Berea Sandstone*, SPE Paper 21045 presented at the International Symposium on Oilfield and Geothermal Chemistry held in Anaheim, California, February 20-22 (1991).
- Maclay, W.N., *Factors Affecting the Solubility of Nonionic Emulsifiers*, J. Colloid Sci., 11 (1956) 272-285.
- Manohar, C., and V.K. Kelkar, *Model for the Cloud Point of Mixed Surfactant Systems*, J. Colloid Interface Sci., 137 (1990) 604-606.
- McCoy, T.F., and B.G. Kelkar, *Investigation of Radial Dispersion-Capitance System in Porous Media*, Water Resources Res., 26 (1990) 87-98.
- Moench, A.F., and A. Ogata, *A Numerical Inversion of the Laplace Transform Solution to Radial Dispersion in a Porous Medium*, Water Resources Res., 17 (1981) 250-252.
- Mukerjee, P., and K.J. Mysels, "Critical Micelle Concentrations of Aqueous Surfactant Systems", NSRDS-NBS 36, National Bureau of Standards, Washington, D.C. (1971) 227p.
- Mungan, N., *Permeability Reduction Through Changes in pH and Salinity*, J. Pet. Techn., 17 (1965) 1449-1460.
- Myers, D., "Surfactant Science and Technology", VCH Publishers, Inc., New York (1988).
- Nasr-EI-Din, H.A., and B.F. Hawkins, *Recovery of Waterflood Residual Oil using Alkali, Surfactant and Polymer Slugs in Radial Cores*, Revue de L'institut Français du Pétrole, 46 (1991) 199-219.
- Nasr-EI-Din, H.A., B.F. Hawkins and K.A. Green, *Recovery of Waterflood Residual Oil Using Alkali Concentration*, J. Pet. Sci. Eng., 6 (1992) 381-401.
- Nelson, R.C., *The Effect of Live Crude on Phase Behavior and Oil-Recovery Efficiency of Surfactant Flooding Systems*, SPE J., 23 (1983) 501-510.
- Nelson, R.C., *Chemically Enhanced Oil Recovery: The State of the Art*, Chem. Eng. Prog., (1989) 50-57.
- Nelson, R.C., J.B. Lawson, D.R. Thigpen and G.L. Stagemeyer, *Co-surfactant-Enhanced Alkaline Flooding*, SPE Paper 12672 presented at the SPE/DOE 4th Symposium on Enhanced Oil Recovery held in Tulsa, Oklahoma, April 15-18 (1984).
- Noll, L.A., and B.L. Gell, *Flow Adsorption Calorimetry of Surfactants as a Function of Temperature, Salinity, and Wettability*, Colloids Surfaces, 54 (1991) 41-60.
- Nutt, C.W., M.G.H. Bayet and R. Burley, *Sorption Behavior of Triton X-100 Surfactant by Sand*, Chem. Eng. Sci., 36 (1981) 609-619.

- Ogata, A., "Dispersion in Porous Media", Ph.D. Dissertation, Northwestern University, Evanston, Illinois (1958).
- Pal, R., *Rheological Behaviour of Concentrated Surfactant Solutions and Emulsions*, *Colloids Surfaces*, **64** (1992) 207-215.
- Paradies, H.H., *Shape and Size of a Nonionic Surfactant Micelle. Triton X-100 in Aqueous Solution*, *J. Phys. Chem.*, **84** (1980) 599-607.
- Partyka, S., S. Zaini, M. Lindheimer and B. Brun, *The Adsorption of Non-Ionic Surfactants on a Silica Gel*, *Colloids Surfaces*, **12** (1984) 255-270.
- Perkins, T.K., and O.C. Johnston, *A Review of Diffusion and Dispersion in Porous Media*, *SPE J.*, **3** (1963) 70-84.
- Peru, D.A., and P.B. Lorenz, *Surfactant-Enhanced Low-pH Alkaline Flooding*, *SPE Res. Eng.*, **2** (1990) 327-332.
- Raimondi, P., G.H.F. Gardner and C.B. Petrick, *Effect of Pore Structure and Molecular Diffusion on the Mixing of Miscible Liquids Flowing in Porous Media*, Preprint Paper No. 43 presented at AIChE and SPE Joint Symposium on Oil Recovery Methods held in San Francisco, California, December 6-9 (1959).
- Ramirez, W.F., P.J. Shuler and F. Friedman, *Convection, Dispersion, and Adsorption of Surfactants in Porous Media*, *SPE J.*, **20** (1980) 430-438.
- Ray, A., and G. Némethy, *Micelle Formation by Nonionic Detergents in Water-Ethylene Glycol Mixtures*, *J. Phys. Chem.*, **75** (1971) 809-815.
- Reid, V.W., G.F. Longman and E. Heinrich, *Determination of Anionic Active Detergents by Two-Phase Titration*, *CIA Report, Tenside*, **4** (1967) 292-304.
- Reisberg, J., L.J. Bielamowicz and D.R. Thigpen, *Recovering Oil by Injecting Aqueous Alkali, Cosurfactant and Gas*, U.S. Patent No.4,493,371, January 15 (1985).
- Reisberg, J., J.B. Lawson and G. Smith, *Waterflood Oil Recovery using Calcium Compatible Mixture of Anionic Surfactants*, U.S. Patent No.3,508,612, April 28 (1970).
- Robson, R.J., and E.A. Dennis, *The Size, Shape, and Hydration of Nonionic Surfactant Micelles. Triton X-100*, *J. Phys. Chem.*, **81** (1977) 1075-1078.
- Rupprecht, H., and T. Gu, *Structure of Adsorption Layers of Ionic Surfactants at the Solid/Liquid Interface*, *Colloid Polym. Sci.*, **269** (1991) 506-522.
- Saffman, P.G., *A Theory of Dispersion in a Porous Medium*, *J. Fluid Mech.*, **6** (1959) 321-349.

- Saleem, S.M., and M.J. Faber, *Studies on the Optimum Caustic-Cosurfactant Flooding Formulations for a Medium Viscosity Crude Oil*, *Revista Técnica Intevep*, 6 (1986) 133-142.
- Saleem, S.M., and A. Hernandez, *Enhanced Oil Recovery of Acidic Crudes by Caustic Cosurfactant-Polymer Flooding*, *J. Surf. Sci. Tech.*, 1 (1987) 1-10.
- Satter, A., Y.M. Shun, W.T. Adams and L.A. Davis, *Chemical Transport in Porous Media with Dispersion and Rate-Controlled Adsorption*, *SPE J.*, 20 (1980) 129-138.
- Scamhorn, J.F., R.S. Schechter and W.H. Wade, *Adsorption of Surfactants on Mineral Oxide Surfaces from Aqueous Solutions. Parts I, II & III.*, *J. Colloid Interface Sci.*, 85 (1982) 463-478, 479-493, 494-501.
- Schott, H., A.E. Royce and S.K. Han, *Effect of Inorganic Additives on Solutions of Nonionic Surfactants. VII. Cloud Point Shift Values of Individual Ions*, *J. Colloid Interface Sci.*, 92 (1984) 196-201.
- Shamir, U.Y., and D.R.F. Harleman, *Numerical Solutions for Dispersion in Porous Mediums*, *Water Resources Res.*, 1 (1967) 557-581.
- Shaw, J.C., P.L. Churcher and B.F. Hawkins, *The Effect of Firing on Berea Sandstone*, *SPE Formation Evaluation*, 6 (1991) 72-78.
- Somasundaran, P., and H.S. Hanna, *Physico-Chemical Aspects of Adsorption at Solid/Liquid Interfaces. I. Basic Principles*, in "Improved Oil Recovery by Surfactant and Polymer Flooding", D.O. Shah and R.S. Schechter (Eds.), Academic Press, New York (1977) 205-251.
- Somasundaran, P., and H.S. Hanna, *Adsorption of Sulfonates on Reservoir Rocks*, *SPE J.*, 24 (1979) 221-232.
- Somasundaran, P., E.D. Snell and Q. Xu, *Adsorption Behaviour of Alkylarylethoxylated Alcohols on Silica*, *J. Colloid Interface Sci.*, 144 (1991) 165-173.
- Stahfest, H., *Numerical Inversion of Laplace Transforms*, Algorithm 368, *Commun. ACM*, 11 (1970) 47-49.
- Tanford, C., "The Hydrophobic Effect: Formation of Micelles and Biological Membranes", 2nd Ed., John Wiley & Sons, New York (1980).
- Tang, L. H., and D.K. Baba, *Analytical Solution of a Velocity Dependent Dispersion Problem*, *Water Resources Res.*, 15 (1979) 1471-1478.
- Taylor, Sir Geoffrey, *Dispersion of Soluble Matter in Solvent Flowing Slowly Through a Tube*, *Proc. Roy. Soc., Ser. A*, 212 (1953) 186-203.

- Teh, H.C., G.H. Ong, S.C. Ng and L.M. Gan, *The Dependence of the Hydrodynamics Size of Triton X-100 Micelles on Temperature and Isopropanol Concentration in Aqueous Media*, *J. Disp. Sci. Techn.*, 6 (1985) 255-262.
- Travalloni-Louvière, A.M., and G. González, *Adsorption of Nonionic Surfactants on Quartz in the Presence of Ethanol, HCl, or CaCl₂, Its Effect on Wettability*, in "Surfactant-Based Mobility Control. Progress in Miscible-Flood Enhanced Oil Recovery", Ch. 11, D.H. Smith (Ed.), ACS Symposium Series 373, Washington, D.C. (1988).
- Trogus, F.J., T. Sophany, R.S. Schechter and W.H. Wade, *Static and Dynamic Adsorption of Anionic and Nonionic Surfactants*, *SPE J.*, 17 (1977) 337-344.
- Udey, N., and T.J.T. Spanos, *The Equations of Miscible Flow with Negligible Molecular Diffusion*, *Transport in Porous Media*, 10 (1993) 1-41.
- Valocchi, A.J., *Validity of the Local Equilibrium Assumption for Modeling Sorbing Solute Transport Through Homogeneous Soils*, *Water Resources Res.*, 21 (1985) 808-820.
- Valocchi, A.J., *Spatial Moment Analysis of the Transport of Kinetically Adsorbing Solutes Through Stratified Aquifers*, *Water Resources Res.*, 25 (1989) 273-279.
- Verkruyse, L.A., and S.J. Salter, *Potential Use of Nonionic Surfactants in Micellar Flooding*, SPE Paper 13574 presented at the International Symposium on Oilfield and Geothermal Chemistry held in Phoenix, Arizona, April 9-11 (1985).
- Walker, R.D., Jr., W.E. Ray, M.K. Tham and M.C. Lee, *Cation Exchange, Surfactant Precipitation, and Adsorption in Micellar Flooding*, in "Chemistry of Oil Recovery", ACS Symposium Series 91 (1979) 1-16.
- Wayman, C.H., *Adsorption on Clay Mineral Surfaces*, Principles and Applications of Water Chemistry, Proceedings of the 4th Rudolf's Research Conference, Rutgers, State Univ. (1965) 127-167.
- Zhu, B-Y., and T. Gu, *General Isotherm Equation for Adsorption of Surfactants at Solid/Liquid Interfaces. Part I. Theoretical*, *J. Chem. Soc., Faraday Trans. I*, 85 (1989) 3813-3817.
- Zhu, B-Y., and T. Gu, *Surfactant Adsorption at Solid-Liquid Interfaces*, *Adv. Colloid Interface Sci.*, 37 (1991) 1-32.
- Zhu, B-Y., X. Zhao and T. Gu, *Surface Solubilization*, *J. Chem. Soc., Faraday Trans. I*, 84 (1988) 3951-3960.

Appendix A

Investigation of the Electrolyte Effect on Surfactant Aggregation.

In this appendix, the viscosity of Neodol 25-3S solutions is examined at different salinities (sodium chloride concentration). The objective is to provide a better understanding of the aggregation phenomenon of the anionic surfactants and, subsequently in Chapter 4, to examine the propagation of surfactant solutions having a liquid crystal phase in porous media.

A.1 Viscosity Measurements

The viscosity of surfactant solutions was measured using a co-axial rotational rheometer (Contraves AG Zürich, Low-Shear 30) with a range of shear rates from 0.01 to 130 s⁻¹. Apparent viscosity was approximated using the power-law equation:

$$\mu = K|\dot{\gamma}|^{n-1} \quad (\text{A-1})$$

where K is a proportionality constant and n is the power-law index. In the method of Couette cylindrical viscometry, the shear rate $\dot{\gamma}$ for power-law fluids can be determined as

* A version of this appendix has been published. Eweh, W., H.A. Nass-El-Din and R.E. Hayes, 1992. *Journal of Canadian Petroleum Technology*, Vol.32, pp.39-48.

$$\dot{\gamma} = \frac{2\omega_o}{n(1-s^{2n})} \quad (\text{A-2})$$

where ω_o is the angular velocity of the outer cylinder and s is the ratio of the inner and outer radii of the cylinders.

A.2 Effect of Salinity on the Apparent Viscosity of Surfactant Solutions

Figure A-1 shows the apparent viscosity, μ , as a function of the shear rate, $\dot{\gamma}$, of surfactant solutions having 0.5 wt.% Neodol 25-3S and sodium chloride concentrations from 8 to 14 wt.% sodium chloride. At sodium chloride concentrations less than 10 wt.%, the apparent viscosity was independent of the shear rate; that is, Newtonian behaviour. At sodium chloride concentrations greater than 10 wt.%, the apparent viscosity significantly increased with increasing sodium chloride concentration and it reached a maximum value at nearly 13 wt.% sodium chloride. At sodium chloride concentrations greater than 13 wt.%, the apparent viscosity decreased with increasing sodium chloride concentration. The solid lines shown in Figure A-2 represent predictions based on the power-law model. Over the shear rate range tested, the experimental data fit very well with the model. Figure A-1 also shows that surfactant solutions containing a sodium chloride concentration from 11 to 14 wt.% had shear thinning behaviour at higher shear rates. Table A-1 depicts the variation of the power-law parameters with sodium chloride concentration. At sodium chloride concentrations less than 10 wt.%, the power-law index, n , was unity indicating a Newtonian fluid. The power-law index decreased with sodium chloride concentration and reached a minimum of 0.43 at a sodium chloride concentration of 13 wt.%. The power-law constant, K , showed the same variation with sodium chloride concentration as the low-shear Newtonian viscosity.

Figure A-2 shows the low-shear Newtonian viscosity of brine solutions containing from 0 to 20 wt.% sodium chloride with and without 0.5 wt.% Neodol 25-3S. At sodium chloride concentrations less than 6 wt.%, the surfactant solution viscosity was about the

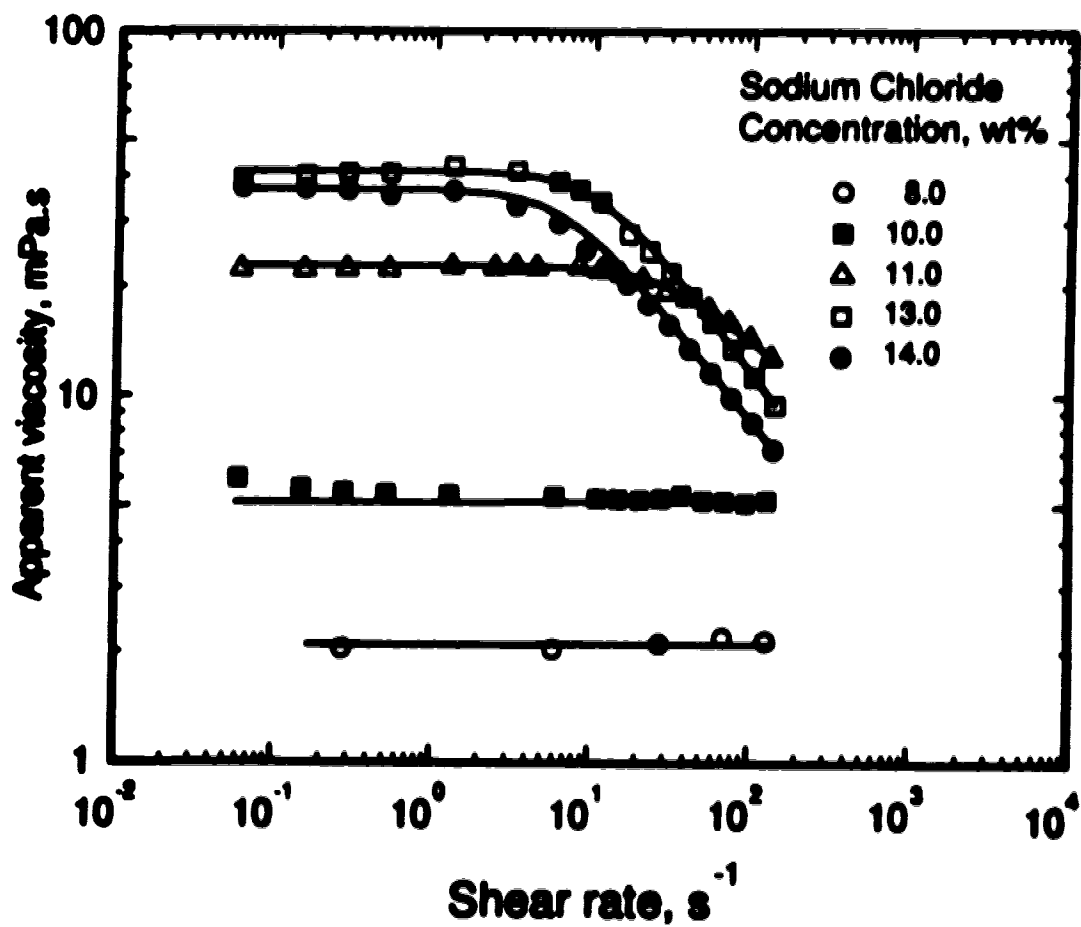


Figure A-1. Apparent viscosity as a function of shear rate for 0.5 wt.% Neodol 25-3S solutions containing various sodium chloride concentrations.

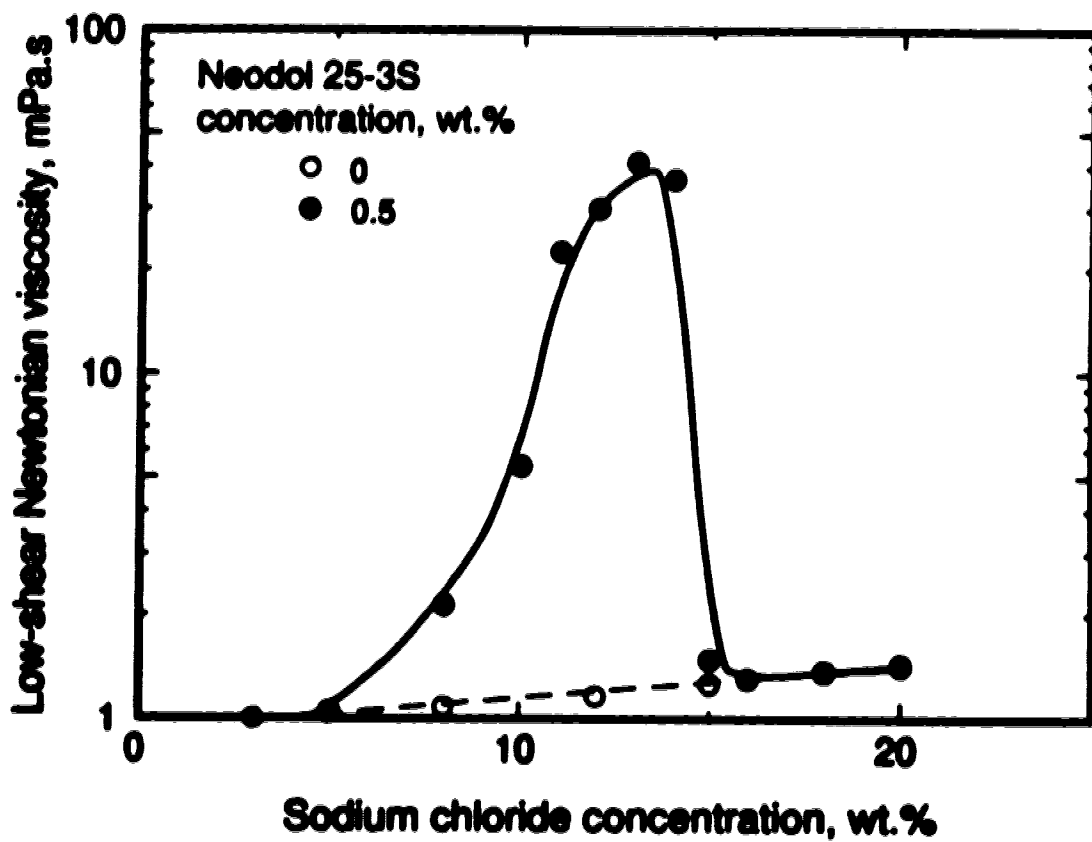


Figure A-2. Low-shear Newtonian viscosity of 0.5 wt.% Neodol 25-3S solutions as a function of sodium chloride concentration.

Table A-1. Effect of sodium chloride concentration on the power-law constant, K , and index, n , of surfactant solutions containing 0.5 wt.% Neodol 25-3S.

Sodium Chloride Concentration (wt%)	K (mPa s)^a	n
8	2.0	1.0 †
10	5.0	1.0 †
11	76.3	0.64
12	134.1	0.48
13	161.5	0.43
14	99.2	0.47

† Newtonian solution

same as that of the brine. When the sodium chloride concentration was further increased, the solution viscosity increased gradually to a maximum of 40 mPa s at 13 wt.% sodium chloride. A slight increase in sodium chloride concentration beyond 13 wt.% caused the solution to separate into two phases (one lean and the other rich in surfactant; similar to the results reported by Lawson, 1978). A sharp drop in viscosity was then observed. The sodium chloride concentration at which phase separation occurred is called the critical electrolyte concentration (c.e.c.) characteristic of the surfactant system.

The viscosity increase shown in Figures A-1 and A-2 is due to the electrolyte effect on the micellization of anionic surfactants (Anacker, 1979; Celik *et al.*, 1982; Lindman, 1987). According to Celik *et al.* (1982), an anionic surfactant (NaR) ionizes in water as follows:



where R^- represents the surfactant monomer and Na^+ is the counterion. Increasing the concentration of the surfactant above the critical micelle concentration, c.m.c., leads to the formation of micelles above the Krafft temperature:



where $\text{Na}_a\text{R}_b^{-(b-a)}$ is the ionic micelle, a is the number of counterions attached to the micelle and b is the number of surfactant monomers in the micelle. The surface charge of micelles is balanced by a diffuse atmosphere of counterions in the electrical double layer. At low counterion concentrations, there exists a very strong micelle-micelle repulsion, which acts as the stabilization force of the micelles in solution. An increase in the counterion concentration reduces the electrostatic repulsion, leading to:



where $(\text{NaR})_b$ is a micelle with a compact diffuse layer of counterions.

Chiu (1982) found that the size of micelles or aggregates increased as sodium chloride concentration was increased. At high enough surfactant concentration, these large micelles form a viscous isotropic phase (spherical units in a body-centred cubic arrangement), or form a liquid crystal phase; that is, transform from spherical to rod-like aggregates (Lindman, 1987; Rosenblatt, 1987; Mishic *et al.*, 1990). The aggregates are arranged in a compact and ordered form having minimum micelle-micelle repulsion, and are the cause of the dramatic increase in viscosity (Lindman, 1987). Increasing sodium chloride concentration further, the micelle size continues to increase giving rise to stronger van der Waals interaction forces until they become large enough to separate into two immiscible liquids, as follows (Chiu, 1982):



The viscosity of the surfactant solution dramatically decreases once the phases separate. Equations (A-4) to (A-6) indicate that the formation of surfactant aggregates is also a function of the surfactant concentration. Therefore, it is of interest to examine the relationship between solution viscosity and surfactant concentration. Figure A-3 shows the flow curves of surfactant solutions prepared in 12 wt.% sodium chloride at various surfactant concentrations. At low surfactant concentrations, the apparent viscosity was independent of the shear rate. As the surfactant concentration was increased, the apparent viscosity increased rapidly and became dependent on the shear rate. It should be mentioned that the shear thinning behaviour at surfactant concentrations of 2 and 10 wt.% could not be measured. This is because of the limitations of the viscometer used.

Figure A-4 summarizes the effects of surfactant and sodium chloride concentrations on the low-shear Newtonian viscosity. For all sodium chloride concentrations examined, viscosity increase was observed above a critical surfactant concentration. This critical surfactant concentration was found to decrease at higher sodium chloride concentrations.

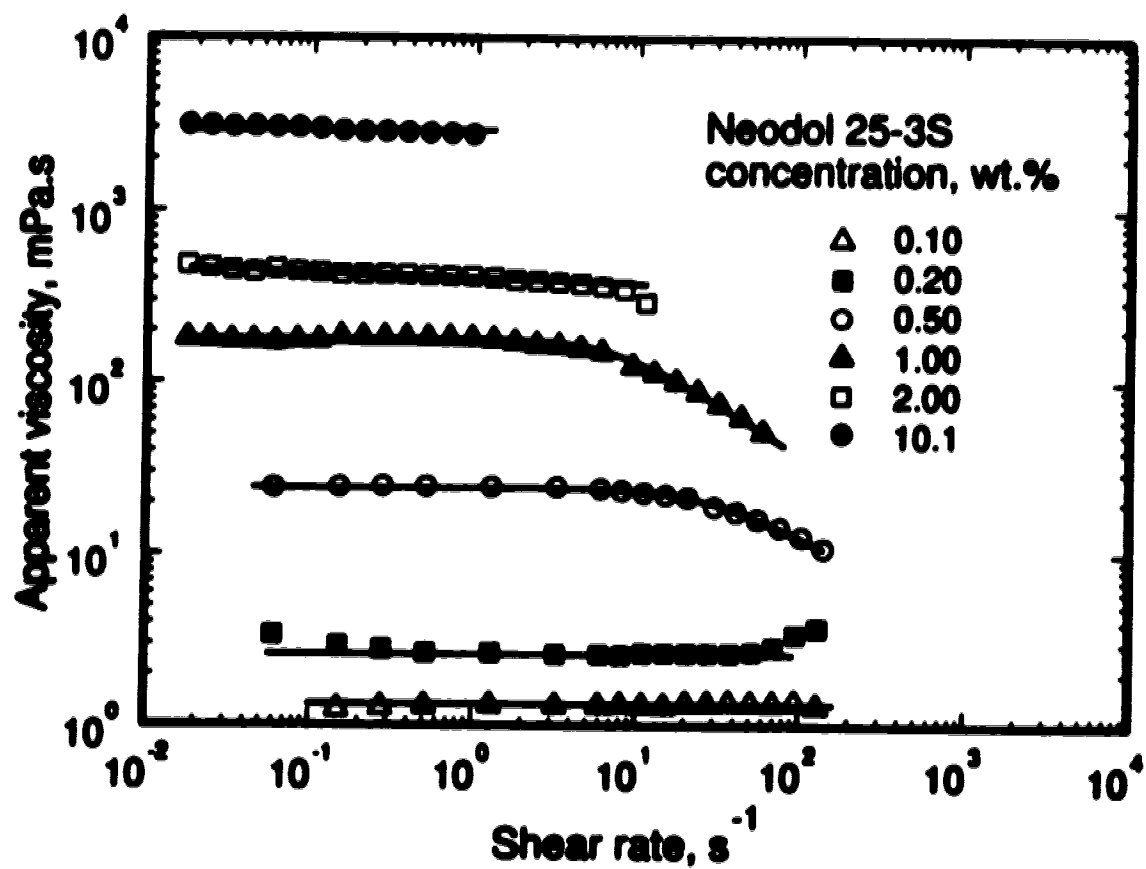


Figure A-3. Effect of surfactant concentration on the flow curves of surfactant solutions containing 12 wt.% sodium chloride.

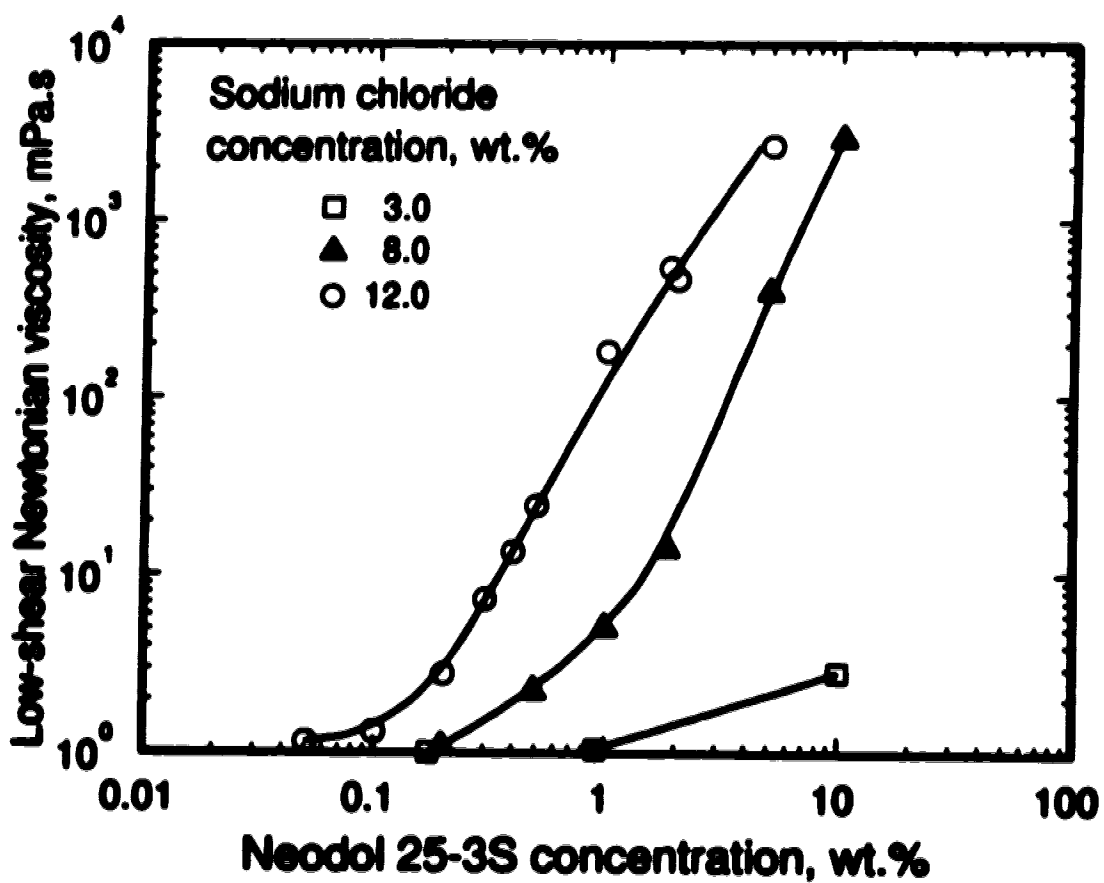


Figure A-4. Low-shear Newtonian viscosity of Neodol 25-3S solutions in 3, 8 and 12 wt.% sodium chloride brines as a function of surfactant concentration.

A.3 References

- Anacker, E.W., *Electrolyte Effect on Micellization*, in "Solutions Chemistry of Surfactants", Volume 1, K.L. Mittal (Ed.), Plenum Press, New York (1979) 67-77.
- Celik, M.S., E.D. Manev and P. Somasundaran, *Sulfonate Precipitation-Redissolution-Redeprecipitation in Inorganic Electrolytes*, in "Interfacial Phenomena in Enhanced Oil Recovery", AIChE Symp. Ser., No.212, Vol.78 (1982) 86-96.
- Chiu, Y.C., *Relationship of Oil Recovery Activity to Surfactant Aggregate Size in Petroleum Sulfonate Solutions*, in "Solution Behavior of Surfactants: Theory and Application Aspects", Vol.2, K.L. Mittal and E. Fendler (Eds.), Plenum Press, New York (1982) 1415-1440.
- Lawson, J.B., *The Adsorption of Non-ionic and Anionic Surfactants on Sandstone and Carbonate*, SPE Paper 7052 presented at the 5th Symposium on Improved Methods for Oil Recovery of the Society of Petroleum Engineers of AIME held in Tulsa, Oklahoma, April 16-19 (1978).
- Lindman, B., *Structural Aspects of Surfactant Micellar Systems*, in "Surfactants". Th.F. Tadros (Ed.), Academic Press, New York (1987) 83-109.
- Mishic, J.R., R.J. Nash and M.R. Fisch, *Liquid Crystal Phase Transition in Large Micelles*, *Langmuir*, **6** (1990) 915-919.
- Rosenblatt, C., *The Nematic Phase in the Micellar Liquid Crystal CsPFO + Water*, in "Physics of Complex and Supermolecular Fluids", S.A. Safran and N.A. Clark (Eds.), John Wiley & Sons, New York (1987) 373-386.

Appendix B

Mathematical Formulation of the Governing Transport Equations

B.1 General Description

At the macroscopic scale, transport of a soluble mass in porous media can be described by the general advection-dispersion equation, viz.,

$$\frac{\partial c}{\partial t} + \underline{u} \cdot \nabla c - \nabla \cdot (\underline{D} \cdot \nabla c) = 0 \quad (\text{B-1})$$

where c is the concentration of solute in the bulk solution, \underline{u} is the pore velocity, \underline{D} is the dispersion tensor and t is time. An approximate solution can be obtained by applying the finite element method through temporal and spatial discretizations.

The first step is to divide the entire solution domain Ω into m sub-domains or elements, Ω^e , as shown in Figure B-1. The unknown value of c can then be estimated by a trial value of \hat{c} , which is a linear combination of the global shape functions ψ over the entire solution domain (see Section B.2.1 for details):

$$c \approx \hat{c}(\underline{x}, t) = \sum_{i=1}^n \psi_i(\underline{x}) c_i(t) \quad (\text{B-2})$$

in which c_i are the unknown nodal values to be determined at position \underline{x} and time t , and n is the total number of nodes in the finite element network. Knowing that \hat{c} is an approximation of c , the solution obtained by substituting \hat{c} in Equation (B-1) is not likely

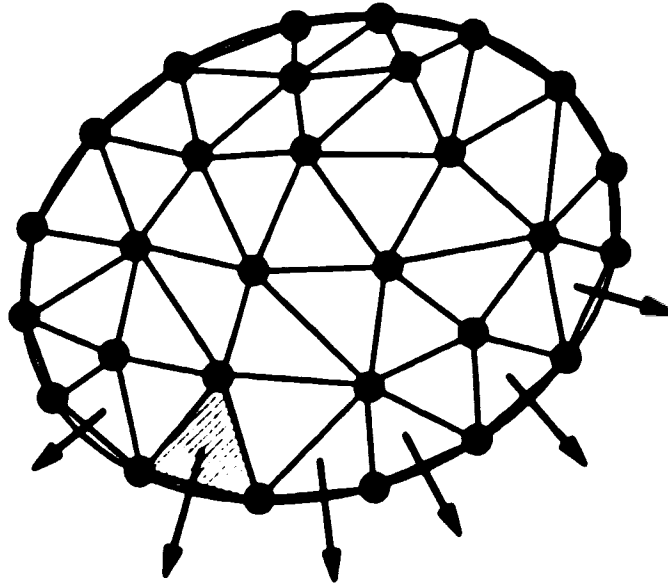


Figure B-1. Domain discretization in finite element.

to be exact and, hence, results in an error or residual denoted by ϵ :

$$\frac{\partial c}{\partial t} + \underline{u} \cdot \nabla c - \nabla \cdot (\underline{D} \cdot \nabla c) = \epsilon \quad (\text{B-3})$$

With the principles of variational calculus, the above governing equation can be expressed in a functional form such that the weighted integral of the residual over the solution domain is set to zero:

$$\int_{\Omega} [W \frac{\partial c}{\partial t} + W \underline{u} \cdot \nabla c - W \nabla \cdot (\underline{D} \cdot \nabla c)] d\Omega = 0 \quad (\text{B-4})$$

where W is the weighting function which is selected in such a way that the residual is minimal. Combining Equations (B-2) and (B-4) gives a set of simultaneous equations in the unknowns c_i for $i = 1, 2, \dots, n$.

For the Galerkin method, the weighting factor is chosen to be identical to the basis shape function: that is, $W = \psi$, and Equation (B-4) can be re-written as

$$\int_{\Omega} \left[\psi \frac{\partial c}{\partial t} + \psi \underline{n} \cdot \nabla c - \psi \nabla \cdot (\underline{D} \cdot \nabla c) \right] d\Omega = 0 \quad (\text{B-5})$$

The order of derivatives in this equation can then be reduced by applying Green's theorem (integration by parts) to the second-derivative term, such that:

$$\begin{aligned} \int_{\Omega} \left[\psi \frac{\partial c}{\partial t} + \psi \underline{n} \cdot \nabla c + \nabla \psi \cdot \underline{D} \cdot \nabla c \right] d\Omega \\ - \int_{\mathcal{S}} \psi \underline{D} \cdot \frac{\partial c}{\partial \underline{n}} d\mathcal{S} = 0 \end{aligned} \quad (\text{B-6})$$

where \underline{n} is the normal vector on boundary \mathcal{S} . Upon substitution of Equation (B-2), Equation (B-6) becomes

$$\begin{aligned} \int_{\Omega} \left[\psi_j \psi_i \frac{\partial c_i}{\partial t} + \psi_j \underline{n} \cdot \nabla \psi_i c_i + \nabla \psi_j \cdot \underline{D} \cdot \nabla \psi_i c_i \right] d\Omega \\ - \int_{\mathcal{S}} \psi_j \underline{D} \cdot \frac{\partial \psi_i}{\partial \underline{n}} c_i d\mathcal{S} = 0 \end{aligned} \quad (\text{B-7})$$

where the repeated subscripts i and j indicate the summation over all nodes. The expression can then be simplified and written in a matrix form for the unknowns c_i :

$$\mathbf{M}_j^a c_i + \mathbf{M}_j^b \frac{dc_i}{dt} = 0 \quad (\text{B-8a})$$

or

$$\mathbf{[M^a][c]} + \mathbf{[M^b]}\left[\frac{dc}{dt}\right] = 0 \quad (\text{B-8b})$$

where \mathbf{M}_j^a and \mathbf{M}_j^b are the coefficients for the j -th equation applied to the i -th node in the coefficient matrices $\mathbf{[M^a]}$ and $\mathbf{[M^b]}$ respectively. This is a system of first-order differential equations which can be solved iteratively following the method discussed in a later section, Section B.2.4. Detailed treatment of the boundary integral will be discussed in Section B.2.5.

On the other hand, since the integrals in Equation (B-6) contain only the first order derivatives of c , the requirement of continuity across the element interface will be automatically satisfied because of the use of quadratic basis functions. It is therefore possible to write the total functional as

$$\int_{\Omega} (\cdot) d\Omega - \int_{\partial} (\cdot) dS = \sum_{\Omega^e} \left[\int_{\Omega^e} (\cdot) d\Omega^e - \int_{\partial^e} (\cdot) dS^e \right] = 0$$

That is, Equation (B-6) for the entire solution domain can be reduced to form an element variation equation:

$$\int_{\Omega^e} \left[\psi \frac{\partial c}{\partial t} + \psi_{,i} \nabla c + \nabla \psi \cdot \underline{D} \cdot \nabla c \right] d\Omega^e - \int_{\partial^e} \psi \underline{D} \cdot \frac{\partial c}{\partial n} dS^e = Q^e \quad (\text{B-9})$$

subject to

$$\sum_{\Omega^e} Q^e = 0 \quad (\text{B-10})$$

where ψ is a basis function defined within the element or local domain, Ω^e . For the discretized domain, Figure B-1, a unique set of element matrix equations can then be written for $[c]^e$

$$[M^e][c]^e + [M^e] \left[\frac{dc}{dt} \right]^e = [Q]^e \quad (\text{B-11})$$

The final step is then to assemble the contributions of all the element equations into the global matrix equation, Equation (B-8b), with the appropriate initial and boundary conditions.

In the following sections, various approximations for the individual terms in Equation (B-6) will be discussed, Section B.2, and subsequently applied to obtain a solution for Equation (B-8b), Section B.3.

B.2 Numerical Approximation

B.2.1 Interpolation Functions for One-Dimensional Elements

Here we consider one-dimensional interpolation functions based on the discussion in Schwarz (1988, pp.54-56) and how to describe them in terms of the nodal variables. In the next section, this technique will be applied to evaluate two-dimensional elements.

It is assumed that the function $c(\xi)$ is a quadratic approximation of the form

$$c(\xi) = \beta_1 + \beta_2 \xi + \beta_3 \xi^2 \quad (\text{B-12})$$

This function is uniquely determined by three function values, which may be taken as the nodal values of the end-points (c_1 and c_2) and the mid-point (c_3) of the interval. For $\xi = 0$, where $c_1 = c_1$, the interpolation function about can be given as

$$c_1 = c_1, \quad c_2 = c_1 + \frac{1}{2}c_2 + \frac{1}{2}c_3, \quad \text{and} \quad c_3 = c_1 + c_2 + c_3$$

and inversion of these linear expressions leads to

$$\begin{bmatrix} \beta_1 \\ \beta_2 \\ \beta_3 \end{bmatrix} = \begin{bmatrix} 1 & 0 & 0 \\ -3 & 4 & -1 \\ 2 & -4 & 2 \end{bmatrix} \begin{bmatrix} c_1 \\ c_2 \\ c_3 \end{bmatrix} \quad (\text{B-13})$$

Substitution of Equation (B-13) into (B-12) gives $c(\xi)$ in terms of nodal basis functions $\psi_i(\xi)$ as

$$\begin{aligned} c(\xi) &= c_1(1 - 3\xi + 2\xi^2) + c_2(4\xi - 4\xi^2) + c_3(-\xi + 2\xi^2) \\ &= c_1\psi_1(\xi) + c_2\psi_2(\xi) + c_3\psi_3(\xi) = \sum_{i=1}^3 c_i \psi_i(\xi) \end{aligned} \quad (\text{B-14})$$

B.2.2 Interpolation Functions for Two-Dimensional Elements

Figure B-2a shows a general quadratic triangular element. Nodes are numbered in an anti-clockwise direction, first vertices to outline the geometry at $P_1(x,y)$, $P_2(x,y)$ and $P_3(x,y)$, and then midpoints of the sides at $P_4(x,y)$, $P_5(x,y)$ and $P_6(x,y)$. This general triangle can be mapped uniquely onto a standard or reference isosceles right-angle triangle in the ξ,η -coordinates or Ω^e , Figure B-2b, by means of a linear transformation:

$$\begin{aligned}x &= x_1 + (x_2 - x_1)\xi + (x_3 - x_1)\eta \\y &= y_1 + (y_2 - y_1)\xi + (y_3 - y_1)\eta\end{aligned}\tag{B-15}$$

with a short side length of unity. Similar to the one-dimensional geometries described above, a complete quadratic approximation of unknown $c(\xi,\eta)$ can be determined uniquely by a function containing six coefficients, $\beta_1, \beta_2, \dots, \beta_6$:

$$c(\xi,\eta) = \beta_1 + \beta_2\xi + \beta_3\eta + \beta_4\xi^2 + \beta_5\xi\eta + \beta_6\eta^2\tag{B-16}$$

The interpolation for the quadratic function produces a set of linear expressions defining the value at each node as summarized in Table B-1 (Schwarz, 1988, p.75). The coefficients in Equation (B-16) can thus be determined by using the inverse form of these linear relationships

$$[\beta] = [A][c]\tag{B-17}$$

where $[\beta] = [\beta_1, \beta_2, \dots, \beta_6]^T$ is the coefficient vector, $[c] = [c_1, c_2, \dots, c_6]^T$ is the vector for the unknown functions, and $[A]$ is the transformation matrix. For Equation (B-17), the unknown function $c(\xi,\eta)$ can be approximated in terms of the nodal values, c_1, c_2, \dots, c_6 for any given location at (ξ,η) within the standard triangle:

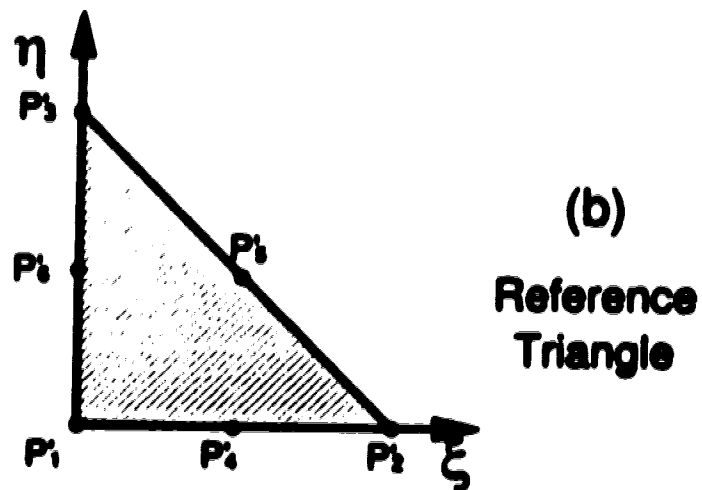
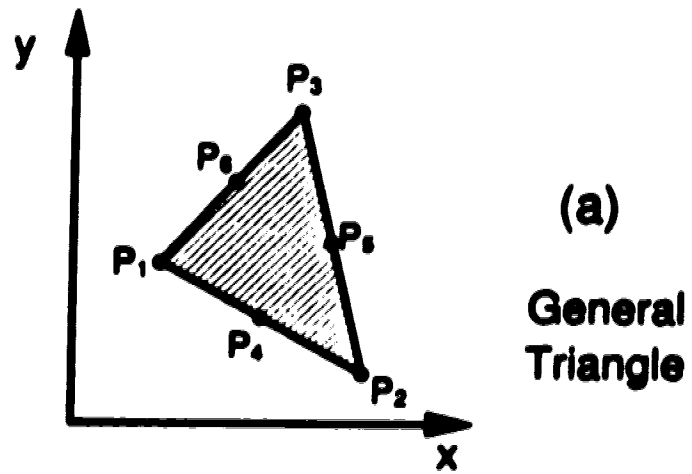


Figure B-2. (a) A typical quadratic triangular element and (b) its transformation to a reference triangle.

$$c_i(\xi, \eta) = \sum_{j=1}^6 c_j \psi_j(\xi, \eta) \quad (\text{B-18})$$

where

$$\begin{aligned} \psi_1 &= -\lambda(1-2\lambda), & \psi_4 &= 4\xi\lambda, \\ \psi_2 &= -\xi(1-2\xi), & \psi_5 &= 4\xi\eta, \\ \psi_3 &= -\eta(1-2\eta), & \psi_6 &= 4\eta\lambda \end{aligned} \quad (\text{B-19})$$

are called the interpolation or basis functions, and $\lambda = 1 - \xi - \eta$.

Table B-1 Interpolation results from Equation (B-16).

<i>i</i>	Coordinates		c_i
	ξ_i	η_i	
1	0	0	β_1
2	1	0	$\beta_1 + \beta_2 + \beta_6$
3	0	1	$\beta_1 + \beta_3 + \beta_6$
4	$\frac{1}{2}$	0	$\beta_1 + \frac{1}{2}\beta_2 + \frac{1}{2}\beta_6$
5	$\frac{1}{2}$	$\frac{1}{2}$	$\beta_1 + \frac{1}{2}\beta_2 + \frac{1}{2}\beta_3 + \frac{1}{4}\beta_4 + \frac{1}{4}\beta_5 + \frac{1}{2}\beta_6$
6	0	$\frac{1}{2}$	$\beta_1 + \frac{1}{2}\beta_3 + \frac{1}{2}\beta_6$

The domain integral in Equation (B-9) can thus be transformed to reference ξ, η -coordinates (in the standard triangle, Ω^e) by multiplying the Jacobian matrix, *J*

$$d\Omega^e = J d\Omega^e \quad (\text{B-20a})$$

or, for two-dimensional domain,

$$dx \, dy = \det \begin{pmatrix} \frac{\partial x}{\partial \xi} & \frac{\partial x}{\partial \eta} \\ \frac{\partial y}{\partial \xi} & \frac{\partial y}{\partial \eta} \end{pmatrix} d\xi \, d\eta \quad (\text{B-20b})$$

Similarly, other integrals and/or derivatives can be transformed from x,y - to ξ,η -coordinates by the chain rule.

B.2.3 Numerical Integration

From Equation (B-9), the local integral of the element variation equation, $\int_{\Omega^e} (\cdot) d\Omega^e$, in the two-dimensional domain can be evaluated using the Hammer Gaussian integration method (Dhatt and Touzot, 1984, p.259) in the reference coordinates, (ξ,η) :

$$\int_0^1 \int_0^1 g(\xi,\eta) \, d\xi \, d\eta \approx \sum_{k=1}^{n^e} w_k g(\xi_k, \eta_k) \quad (\text{B-21})$$

where $g(\xi_k, \eta_k)$ is the value of the function g at the integration point k , w_k is the weighting coefficient for the integration point k , and n^e is the number of integration points. Figure B-3 and Table B-2 show the locations of integration points and values of the weighting coefficients for a quadratic triangle with six integration points.

In the current study, the function $g(\xi_k, \eta_k)$ for the local integral of Equation (B-9) can be expressed as

$$g(\xi_k, \eta_k) = J_k \left[\psi \frac{\partial c}{\partial t} + \dots \right] \quad (\text{B-22})$$

where c is evaluated as $c(\xi_k, \eta_k)$ according to Equation (B-18), and J_k is the determinant of the Jacobian matrix at point k from Equation (B-20b).

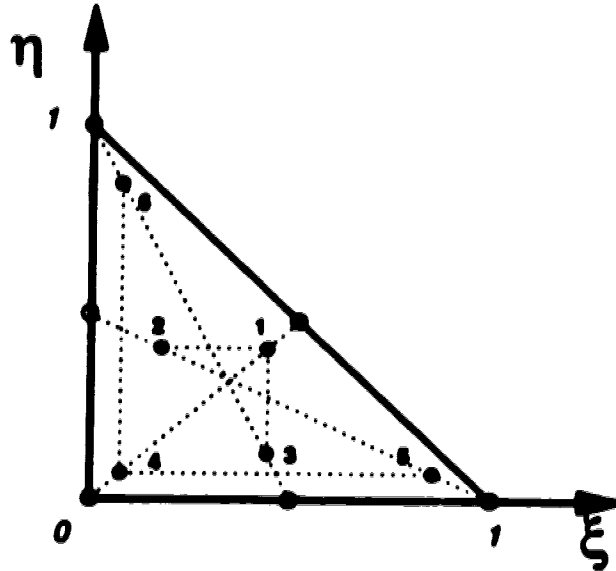


Figure B-3. Quadrature points for a triangular element.

Table B-2. Direct integration formulae for a triangle.

Number of points j	Coordinates		Weights w_j
	ξ_j	η_j	
1	a	a	0.111690794839005
2	$1 - 2a$	a	0.111690794839005
3	a	$1 - 2a$	0.111690794839005
4	b	b	0.054975871827661
5	$1 - 2b$	b	0.054975871827661
6	b	$1 - 2b$	0.054975871827661

$$a = 0.445948490915965, b = 0.091576213509771$$

B.2.4 Approximation of the Time Derivative

The time derivative term in Equation (B-6) or (B-9) was approximated using an implicit second-order Gear scheme (for $t \geq 2\Delta t$) or the Euler method:

$$\frac{\partial c}{\partial t} = \begin{cases} \frac{3c^{n+1} - 4c^n + c^{n-1}}{2\Delta t} & \text{for } n > 1 \quad (\text{Gear Scheme}) \\ \frac{c^{n+1} - c^n}{\Delta t} & \text{for } n = 1 \quad (\text{Euler Method}) \end{cases}$$

or

$$\frac{\partial c}{\partial t} = \frac{\theta_{+1}c^{n+1} + \theta_0c^n + \theta_{-1}c^{n-1}}{\Delta t} \quad (\text{B-23})$$

where θ_{+1} , θ_0 , and θ_{-1} are the time coefficients having values of 3/2, -2 and 1/2, respectively, when using the Gear scheme and 1, -1 and 0 when using the Euler method; and n is the number of time steps.

B.2.5 Boundary Conditions

In obtaining the solution of Equation (B-6), boundary conditions must be specified and resolved into an appropriate variational form for the boundary integral:

$$\int_S \nabla D \cdot \frac{\partial c}{\partial \mathbf{n}} dS \quad (\text{B-24})$$

Three types of boundary conditions are of practical interest: prescribed concentration (Dirichlet), prescribed material flux (Neumann), and prescribed concentration and material flux (Cauchy).

For the Dirichlet boundary value problems; that is, prescribed c along the boundary S , the boundary integral is simply set to zero. When the Neumann boundary condition is specified, prescribed values for $\partial c/\partial n$, the boundary integral may be evaluated directly as a separate function (independent on the unknown functions of c).

The Cauchy condition can be represented by

$$\begin{aligned} \underline{u}c - \underline{D} \cdot \frac{\partial c}{\partial n} &= \underline{u}C_s \\ \underline{D} \cdot \frac{\partial c}{\partial n} &= \underline{u}(c - C_s) \end{aligned} \quad (\text{B-25})$$

such that the boundary integral above can be expressed as

$$\int_S \underline{v} \underline{D} \cdot \frac{\partial c}{\partial n} dS = \int_S \underline{v} \underline{u}(c - C_s) dS \quad (\text{B-26})$$

which can be substituted directly into Equation (B-6).

B.3 Method of Solution

From the estimate for the time derivative term in Equation (B-23), both the values for c^n and c^{n-1} are either specified by the initial condition or evaluated from the previous time step. The new unknown values, c^{n+1} , can be approximated by expanding Equation (B-18):

$$\begin{aligned}
 c^{n+1} &= \sum_{i=1}^n \psi_i (c_i^{n+1} + \Delta c_i^{n+1}) \\
 \nabla c^{n+1} &= \sum_{i=1}^n \nabla \psi_i (c_i^{n+1} + \Delta c_i^{n+1})
 \end{aligned}
 \tag{B-27}$$

where c_i^{n+1} is the initial (guess) value at the i -th node, and Δc_i^{n+1} is the residual of the solution at the i -th node. Upon substituting into Equation (B-6) or (B-9), the residual values of Δc_i^{n+1} can then be solved by, in matrix form:

$$\mathbf{[M]} [\Delta c^{n+1}] = \mathbf{[F]}
 \tag{B-28}$$

where $\mathbf{[M]}$ is the global coefficient matrix and $\mathbf{[F]}$ is a global vector which is a function of the known values of c^n and c^{n+1} at all nodes determined in the previous time step(s). The solutions of Δc_i^{n+1} obtained can then be combined with c_i^{n+1} , and iterated (if necessary) until the calculated residuals become zero or within a reasonable tolerance. This method is similar to Newton's iterative scheme for a non-linear functions.

B.4 Adsorption Models

For an adsorbing soluble mass, the transport behaviour in porous media can be represented by the general equation for advection-dispersion-adsorption:

$$\frac{\partial c}{\partial t} + \left(\frac{1-\phi}{\phi} \right) \frac{\partial \Gamma^*}{\partial t} + \underline{u} \cdot \nabla c - \nabla \cdot (\underline{D} \cdot \nabla c) = 0
 \tag{B-29}$$

where ϕ is the porosity and Γ^* is the amount of adsorption.

Equilibrium adsorption models can be incorporated into the above expression by using a retardation factor, R (Bear, 1972). For example, in a dilute solution ($c \rightarrow 0$), the adsorption process can be approximated by Henry's law; that is, $\Gamma^* = \kappa c$, where κ is a

proportionality constant. Substituting $\partial\Gamma^*/\partial t$ into Equation (B-29) results in a "retarded" advection-dispersion equation:

$$R \frac{\partial c}{\partial t} + \underline{u} \cdot \nabla c - \nabla \cdot (\underline{D} \cdot \nabla c) = 0 \quad (\text{B-30})$$

where $R = 1 + \kappa(1-\phi)/\phi$, and the solution can be obtained by solving the following variational form as described earlier:

$$\int_{\Omega} [\psi R \frac{\partial c}{\partial t} + \psi \underline{u} \cdot \nabla c - \psi \nabla \cdot (\underline{D} \cdot \nabla c)] d\Omega = 0 \quad (\text{B-31})$$

Similarly, for the case of an equilibrium Langmuir-type adsorption, the amount of adsorption, Γ^* , can be determined from the adsorption isotherm; that is,

$$\Gamma^* = \frac{Q_s^* K c}{1 + K c} \quad (\text{B-32})$$

where K is the equilibrium ratio and Q_s^* is the maximum adsorption capacity, and $\partial\Gamma^*/\partial t$ can be expressed using the chain rule as

$$\frac{\partial\Gamma^*}{\partial t} = \frac{d\Gamma^*}{dc} \frac{\partial c}{\partial t} = \frac{Q_s^* K}{(1 + K c)^2} \frac{\partial c}{\partial t} \quad (\text{B-33})$$

The retardation factor, in this case, becomes a function of the unknown concentration, c , such that

$$R = 1 + \frac{1-\phi}{\phi} \frac{Q_s^* K}{(1 + K c)^2} \quad (\text{B-34})$$

For a kinetic adsorption process, the advection-dispersion equation is coupled with the adsorption rate expression. An iterative method may therefore be required. With a simple Langmuir-type kinetic adsorption process, the rate of adsorption can be represented by a reversible second-order rate expression:

$$\frac{\partial \Gamma^*}{\partial t} = k_a(Q_s^* - \Gamma^*)c - k_d \Gamma^* \quad (\text{B-35})$$

where k_a and k_d are the rate constants of adsorption and desorption, respectively. In this case, the transport equation and the adsorption rate equation can be rearranged to the weighted residual forms:

$$\int_{\Omega} \left[\psi \frac{\partial c}{\partial t} - \psi \left(\frac{1-\phi}{\phi} \right) \frac{\partial \Gamma^*}{\partial t} + \psi \underline{u} \cdot \nabla c - \psi \nabla \cdot (\underline{D} \cdot \nabla c) \right] d\Omega = 0 \quad (\text{B-36})$$

$$\int_{\Omega} \left[\psi \frac{\partial \Gamma^*}{\partial t} - \psi k_a (Q_s^* - \Gamma^*) c + \psi k_d \Gamma^* \right] d\Omega = 0$$

where the amount of adsorption is estimated by

$$\hat{\Gamma}^*(\underline{x}, t) = \sum_{i=1}^N \psi_i(\underline{x}) \Gamma_i^*(t) \quad (\text{B-37})$$

Solutions for the coupled equation are obtained by (1) solving the transport equation and adsorption kinetic expression independently using the iterative scheme mentioned above; that is, by assuming c_i^{n+1} and $\hat{\Gamma}_i^{n+1}$; and then (2) iterating between the transport equation and kinetic adsorption expression.

If the adsorption model is a combination of more than one kinetic expression (for example, two-site or bilayer model), the equations for the adsorption kinetics must be solved as a coupled equation. That is, the solutions for $\hat{\Gamma}_1^*$, $\hat{\Gamma}_2^*$, ..., $\hat{\Gamma}_N^*$ must first be evaluated and combined as:

$$\hat{\Gamma}^* = \sum_{i=1}^N \hat{\Gamma}_i^*$$

where N is the number of adsorption kinetic expressions. The obtained value of $\hat{\Gamma}^*$ can then be substituted into the transport equation. The solutions for c and $\hat{\Gamma}^*$ are then computed by repeatedly iterating between the coupled adsorption kinetic expressions and the transport equation.

B.5 References

Bear, J., "Dynamics of Fluids in Porous Media", Dover Pub., Inc., New York (1972).

Dhatt, G., and G. Touzot, "The Finite Element Method Displayed", John Wiley & Sons, Chichester (1984).

Schwarz, H.R., "Finite Element Methods", J.R. Whiteman (Trans. Ed.), Academic Press, London (1988).

Appendix C

Summary of Experimental Data

Detailed experimental conditions, core characteristics and measured concentration profiles of the radial coreflows are summarized in this appendix.

C.1 Experimental run no. 91-042**EXPERIMENTAL SPECIFICATIONS**

Solution contents:	0.194	wt.% Neodol 25-3S
	3.0	wt.% NaCl
	6.40	pH (Injected)
Injection rate:	20	mL/h
Total Injection:	2.99	PV

CORE CHARACTERISTICS

Core ID:	WK-55	
Weight:	438.62	g
Thickness:	34.85	mm
Diameter:	88.30	mm
Wellbore diameter:	3.40	mm
Pore volume:	47.57	cm ³
Porosity:	22.32	%

Effluent PV	Tracer C/C ₀	Surfactant C/C ₀	Effluent PV	Tracer C/C ₀	Surfactant C/C ₀
0.009	0.0001	0.0000	6.482	0.0009	
0.122	0.0002	0.0000	6.589		0.0197
0.228	0.0002	0.0000	6.695	0.0006	
0.334	0.0002	0.0000	6.801		
0.441	0.0004	0.0000	6.907	0.0007	0.0176
0.546	0.0006	0.0000	7.014		
0.653	0.0068	0.0000	7.120	0.0004	
0.759	0.0558	0.0000	7.227		0.0173
0.865	0.2026	0.0000	7.334	0.0003	
0.971	0.4317	0.0000	7.440		
1.077	0.6358	0.0042	7.547	0.0002	
1.183	0.8000	0.0399	7.653		0.0127
1.290	0.8897	0.1390	7.760	0.0001	
1.396	0.9420	0.2407	7.866		
1.502	0.9646	0.3634	7.973	0.0002	
1.608	1.0016	0.4237	8.080		0.0133
1.714	1.0010	0.5225	8.186	0.0001	
1.820	1.0036	0.5931	8.292		
1.926	1.0166		8.406	0.0003	0.0113
2.033	1.0244	0.7001			
2.139	1.0076	0.7356			
2.246	0.9953	0.7863			
2.352	1.0095	0.8288			
2.458	1.0057	0.8413			
2.563	1.0265	0.8556			
2.670	1.0120	0.8734			
2.776	1.0259	0.8743			
2.883	0.9868	0.9072			
2.990	1.0247	0.8968			
3.096	1.0207	0.9132			
3.202	1.0049	0.9384			
3.307	1.0067				
3.413	0.9791	0.9271			
3.518	0.9996	0.9206			
3.623	1.0060	0.9202			
3.729	1.0288				
3.834	0.9649	0.8881			
3.940	0.8170	0.7651			
4.045	0.6058	0.6576			
4.151	0.3968	0.4397			
4.256	0.2359	0.2972			
4.362	0.1340	0.2296			
4.468	0.0726	0.1738			
4.574	0.0400	0.1268			
4.679	0.0235	0.1008			
4.785	0.0146	0.0924			
4.891	0.0092	0.0778			
4.997	0.0061	0.0655			
5.103	0.0040	0.0523			
5.209	0.0031	0.0492			
5.315	0.0022	0.0490			
5.421	0.0018				
5.527	0.0015	0.0412			
5.633	0.0013				
5.738	0.0018	0.0412			
5.843	0.0008				
5.951	0.0008	0.0277			
6.058	0.0010				
6.164	0.0008	0.0278			
6.270	0.0007				
6.376		0.0255			

C.2 Experimental run no. 90-009**EXPERIMENTAL SPECIFICATIONS**

Solution contents:	0.463	wt. % Neodol 25-3S
	3.0	wt. % NaCl
	7.08	pH (injected)
Injection rate:	20	mL/h
Total injection:	3.07	PV

CORE CHARACTERISTICS

Core ID:	WK-15	
Weight:	438.19	g
Thickness:	35.20	mm
Diameter:	88.10	mm
Wellbore diameter:	3.65	mm
Pore volume:	47.25	cm ³
Porosity:	22.06	%

Effluent PV	Tracer C/C ₀	Surfactant C/C ₀	Effluent PV	Tracer C/C ₀	Surfactant C/C ₀
0.062	0.0001	0.0000	7.782	0.0002	0.0076
0.041	0.0000	0.0000	7.997		0.0068
0.145	0.0000	0.0000	8.211	0.0002	0.0068
0.249	0.0000	0.0000	8.368		0.0047
0.352	0.0001	0.0000	8.471		0.0046
0.455	0.0002	0.0000	8.579	0.0005	0.0042
0.596	0.0215	0.0015	8.687		0.0038
0.760	0.0509	0.0021	8.794		0.0044
0.848	0.1860	0.0062	8.902		0.0030
0.914	0.3182	0.0333	9.009	0.0002	0.0032
1.023	0.5441	0.1316	9.116		0.0042
1.130	0.7299	0.2897	9.224		0.0084
1.236	0.8726	0.4525	9.331		0.0386
1.344	0.9213	0.6037	9.438	0.0001	0.1129
1.452	0.9697	0.7120	9.545		0.1927
1.560	0.9743	0.7849	9.652		0.2049
1.668	1.0018	0.8688	9.759		0.1806
1.776	1.0039	0.8643	9.866	0.0004	0.1454
1.884	1.0063	0.9084	9.973		0.0973
1.992		0.9216	10.080		0.0704
2.100	0.9984	0.9049	10.187		0.0434
2.208	1.0242	0.9434	10.294	0.0003	0.0305
2.317		0.9705	10.401		0.0230
2.425	1.0371	0.9736	10.508		0.0147
2.533	1.0086	0.9660	10.621		0.0121
2.640	0.9846	0.9715	10.734	0.0004	0.0127
2.749	0.9957	0.9715	10.841		0.0096
2.857	1.0205	0.9740	10.949		0.0094
2.965	1.0239	1.0062	11.055		0.0078
3.073	0.9999	1.0003	11.162	0.0003	0.0079
3.181	1.0090	0.9986	11.269		0.0064
3.295	1.0069	0.9903	11.376		0.0102
3.403	1.0467	0.9778	11.483		0.0240
3.511	1.0295	0.9979	11.590	0.0002	0.0461
3.619	1.0091	0.9910	11.696		0.0553
3.727	1.0138	0.9646	11.803		0.0591
3.834	0.9644	1.0021	11.910		0.0509
3.942	0.9679	0.9362	12.017	-0.0000	0.0401
4.049	0.9123	0.8466	12.123		0.0303
4.157	0.7300	0.6530	12.230		0.0215
4.264	0.5338	0.4962	12.337		0.0155
4.372	0.3459	0.3289	12.443	-0.0000	0.0147
4.480	0.1979	0.2089	12.550		0.0107
4.587	0.1082	0.1631	12.657		0.0078
4.695	0.0728	0.1055			
4.803	0.0297	0.0788			
4.910	0.0161	0.0540			
5.017	0.0094	0.0470			
5.125	0.0057	0.0420			
5.232	0.0040	0.0456			
5.340		0.0274			
5.448	0.0008	0.0228			
5.554		0.0190			
5.668	0.0004	0.0144			
5.782		0.0128			
5.895	0.0003	0.0117			
6.010		0.0096			
6.123	0.0002	0.0076			
6.238		0.0074			
6.353	0.0002	0.0071			
6.468		0.0076			

C.3 Experimental run no. 90-022**EXPERIMENTAL SPECIFICATIONS**

Solution contents:	0.910	wt.% Neodol 25-3S
	3.0	wt.% NaCl
	6.18	pH (injected)
Injection rate:	20	mL/h
Total injection:	3.23	PV

CORE CHARACTERISTICS

Core ID:	WK-32	
Weight:	434.85	g
Thickness:	34.93	mm
Diameter:	88.29	mm
Wellbore diameter:	3.51	mm
Pore volume:	47.03	cm ³
Porosity:	22.03	%

Effluent PV	Tracer C/C ₀	Surfactant C/C ₀	Effluent PV	Tracer C/C ₀	Surfactant C/C ₀
0.037	0.0002	0.0000	7.994	0.0001	0.0045
0.073	0.0001	0.0000	8.151		
0.100	0.0001	0.0000	8.309		0.0035
0.207	0.0001	0.0000	8.543	0.0001	0.0039
0.396	0.0015	0.0005	8.743		
0.506	0.0037	0.0019	8.871		0.0033
0.617	0.0154	0.0059	9.032		
0.727	0.0585	0.0158	9.188	-0.0001	0.0031
0.838	0.1834	0.0497			
0.949	0.3926	0.1439			
1.061	0.6463	0.3038			
1.172	0.8185	0.5124			
1.284	0.9458	0.6603			
1.396	1.0020	0.8045			
1.507	1.0108	0.8669			
1.619	1.0506	0.9189			
1.732	1.0560	0.9549			
1.845	1.0629	0.9828			
1.959	1.0723	0.9878			
2.074	1.0661	0.9909			
2.188	1.0587	1.0190			
2.303	1.0680	1.0197			
2.419	1.0702	0.9742			
2.535	1.0747	1.0201			
2.651	1.0381	0.9957			
2.769	1.0359	1.0006			
2.886	1.0622	1.0035			
3.005	1.0445	1.0331			
3.123	1.0631	1.0217			
3.225	1.0373	1.0051			
3.323	1.0367	1.0141			
3.433	1.0249	1.0476			
3.543	1.0233	1.0400			
3.655	1.0146	1.0605			
3.766	1.0568	1.0098			
3.878	1.0079	1.0255			
3.991	1.0033	0.9805			
4.106	0.9281	0.8700			
4.220	0.7899	0.7133			
4.337	0.5534	0.4923			
4.454	0.3419	0.3172			
4.573	0.1861	0.1864			
4.696	0.0890	0.1029			
4.822	0.0392	0.0756			
4.949	0.0174	0.0492			
5.079	0.0078	0.0371			
5.208	0.0041	0.0289			
5.340	0.0022	0.0209			
5.473	0.0014	0.0165			
5.608	0.0010	0.0140			
5.820		0.0121			
6.102	0.0002	0.0106			
6.390		0.0079			
6.688	0.0003	0.0064			
6.915					
7.069		0.0053			
7.223					
7.377	0.0001	0.0051			
7.532					
7.685		0.0037			
7.839					

C.4 Experimental run no. 91-046**EXPERIMENTAL SPECIFICATIONS**

Solution contents:	0.209	wt.% Neodol 25-3S
	8.0	wt.% NaCl
	6.00	pH (injected)
Injection rate:	20	mL/h
Total injection:	2.91	PV

CORE CHARACTERISTICS

Core ID:	WK-58	
Weight:	432.30	g
Thickness:	35.10	mm
Diameter:	88.42	mm
Wellbore diameter:	3.44	mm
Pore volume:	50.93	cm ³
Porosity:	23.67	%

Effluent PV	Tracer C/C _o	Surfactant C/C _o	Effluent PV	Tracer C/C _o	Surfactant C/C _o
0.017	0.0001	0.0000	6.097		0.0314
0.127	0.0001	0.0000	6.196		
0.228	0.0000	0.0000	6.295	0.0004	
0.328	0.0001	0.0000	6.395		0.0261
0.426	0.0001	0.0000	6.494		
0.526	0.0005	0.0000	6.593	0.0002	
0.625	0.0096	0.0000	6.692		0.0268
0.724	0.0569	0.0000	6.791		
0.824	0.1693	0.0000	6.891	0.0002	
0.923	0.3513	0.0000	6.990		0.0234
1.022	0.5414	0.0000	7.090	0.0002	
1.121	0.7011	0.0000	7.189		
1.220	0.8412	0.0000	7.289	0.0002	0.0187
1.319	0.9094	0.0000	7.388		
1.418	0.9388	0.0000	7.488	0.0002	
1.517	0.9590	0.0000	7.587		0.0204
1.616	0.9635	0.0165	7.687		
1.715	0.9917	0.0337	7.786		
1.814	1.0007	0.0579	7.886		0.0140
1.914	0.9863	0.1001			
2.013	1.0083	0.1499			
2.112	1.0142	0.2227			
2.212	0.9932	0.3102			
2.311	1.0078	0.3781			
2.410	1.0206	0.4281			
2.510	1.0136	0.4886			
2.609	1.0108	0.5620			
2.709	0.9978	0.6044			
2.808	0.9920	0.6613			
2.907	0.9722	0.6895			
3.006	1.0070				
3.105	0.9957	0.7291			
3.205	1.0053	0.7319			
3.304	1.0110	0.7605			
3.404	0.9928	0.7666			
3.504	0.9946				
3.603	0.9778	0.7424			
3.703		0.6645			
3.803	0.8312	0.5818			
3.902	0.6751	0.4887			
4.002	0.4712	0.2970			
4.102	0.2901	0.2130			
4.202	0.1679	0.1806			
4.301	0.0940	0.1525			
4.401	0.0499	0.1230			
4.501	0.0273	0.1080			
4.601	0.0162	0.0901			
4.701	0.0099	0.0799			
4.801	0.0062	0.0702			
4.900	0.0041	0.0631			
5.000	0.0029	0.0642			
5.100	0.0025	0.0624			
5.200	0.0019	0.0533			
5.300	0.0014	0.0483			
5.400	0.0011				
5.500		0.0445			
5.600	0.0010				
5.700		0.0402			
5.800	0.0007				
5.899		0.0366			
5.998	0.0006				

C.5 Experimental run no. 91-045**EXPERIMENTAL SPECIFICATIONS**

Solution contents:	0.453	wt.% Neodol 25-3S
	8.0	wt.% NaCl
	6.00	pH (injected)
Injection rate:	20	mL/h
Total Injection:	2.91	PV

CORE CHARACTERISTICS

Core ID:	WK-56	
Weight:	432.71	g
Thickness:	35.00	mm
Diameter:	88.20	mm
Wellbore diameter:	3.50	mm
Pore volume:	49.66	cm ³
Porosity:	23.26	%

Effluent PV	Tracer C/C ₀	Surfactant C/C ₀	Effluent PV	Tracer C/C ₀	Surfactant C/C ₀
-0.005	-0.0001	0.0000	6.132		0.0147
0.096	-0.0003	0.0000	6.233		
0.197	-0.0001	0.0000	6.334	0.0005	
0.298	0.0000	0.0000	6.434		0.0112
0.398	-0.0001	0.0000	6.535		
0.499	0.0012	0.0000	6.636	0.0005	
0.599	0.0156	0.0000	6.737		0.0096
0.700	0.0671	0.0000	6.838		
0.800	0.1774	0.0000	6.957	0.0002	
0.901	0.3344	0.0000	7.093		0.0087
1.001	0.5016	0.0187	7.227	0.0003	
1.102	0.6575	0.0760	7.360		
1.202	0.7760	0.1335	7.494	0.0002	0.0074
1.302	0.8627	0.2401	7.628		
1.402	0.9207	0.3164	7.761	0.0003	
1.503	0.9783	0.4179	7.895		0.0071
1.603	0.9703	0.5187			
1.703	0.9910	0.5981			
1.804	1.0221	0.6392			
1.904	0.9819	0.6843			
2.004	0.9964	0.7451			
2.105	1.0275	0.7627			
2.205	1.0112				
2.306	1.0192	0.8093			
2.406	1.0181	0.8164			
2.507	1.0331	0.8164			
2.607	1.0055	0.8474			
2.708	0.9909	0.8631			
2.808	1.0168	0.8787			
2.909	1.0176	0.9078			
3.009	0.9978	0.8619			
3.110	0.9804	0.9164			
3.211	1.0406	0.8851			
3.311	1.0102	0.8851			
3.412	1.0119	0.8985			
3.513	1.0129	0.8799			
3.614	0.9786	0.8198			
3.714		0.6772			
3.814	0.7502	0.5366			
3.915	0.6012	0.4179			
4.015	0.4577	0.3172			
4.116	0.3447	0.2280			
4.217	0.2349	0.1493			
4.318	0.1517	0.1341			
4.419	0.0942	0.0927			
4.520	0.0547	0.0660			
4.621	0.0325	0.0607			
4.722	0.0184	0.0531			
4.823	0.0118	0.0432			
4.923	0.0078	0.0343			
5.024	0.0051				
5.125	0.0040	0.0288			
5.225	0.0028				
5.326	0.0021	0.0206			
5.426	0.0018				
5.527		0.0184			
5.628	0.0013				
5.729					
5.829	0.0009	0.0172			
5.930					
6.031	0.0006				

C.6 Experimental run no. 90-010**EXPERIMENTAL SPECIFICATIONS**

Solution contents:	0.991	wt.% Neodol 25-3S
	8.0	wt.% NaCl
	6.36	pH (injected)
Injection rate:	20	mL/h
Total injection:	2.96	PV

CORE CHARACTERISTICS

Core ID:	WK-17	
Weight:	435.34	g
Thickness:	35.30	mm
Diameter:	88.15	mm
Wellbore diameter:	3.40	mm
Pore volume:	49.306	cm ³
Porosity:	22.92	%

Effluent PV	Tracer C/C ₀	Surfactant C/C ₀	Effluent PV	Tracer C/C ₀	Surfactant C/C ₀
-0.044	0.0000	0.0000	7.470	0.0002	0.0067
0.068	0.0000	0.0000	7.675		0.0061
0.171	0.0000	0.0000	7.880	0.0001	0.0071
0.274	0.0000	0.0000	8.085		0.0057
0.377	0.0011	0.0000			
0.481	0.0043	0.0013			
0.584	0.0129	0.0034			
0.687	0.0460	0.0070			
0.790	0.1395	0.0211			
0.894	0.3044	0.0630			
0.997	0.4814	0.1481			
1.099	0.6905	0.2840			
1.202	0.8420	0.4502			
1.306	0.9412	0.5812			
1.409	1.0112	0.6699			
1.512	0.9890	0.7410			
1.615	0.9607	0.7602			
1.718	1.0043	0.8315			
1.821	0.9766	0.8539			
1.924	0.9783	0.8681			
2.027	0.9706	0.8966			
2.130	0.9872	0.9114			
2.234	0.9502	0.9306			
2.337	0.9886	0.9273			
2.440	0.9909	0.9221			
2.544	1.0005	0.9609			
2.647	1.0167	0.9477			
2.750	1.0129	0.9856			
2.853	1.0045	0.9523			
2.957	0.9879	0.9629			
3.061	0.9932	0.9817			
3.166	0.9960	0.9566			
3.269	1.0065				
3.372	0.9984	0.9797			
3.476	0.9777	0.9382			
3.579	0.9662	0.8892			
3.682	0.9285	0.7728			
3.785	0.8876	0.6795			
3.888	0.6438	0.5498			
3.991	0.6078	0.4643			
4.094	0.4701	0.3803			
4.197	0.3825	0.3100			
4.301	0.2832	0.2440			
4.405	0.2266	0.2052			
4.508	0.1657	0.1538			
4.611	0.1265	0.1215			
4.714	0.0691	0.0976			
4.817	0.0613	0.0723			
4.920	0.0403	0.0664			
5.023	0.0276	0.0535			
5.196		0.0445			
5.421	0.0070	0.0247			
5.627		0.0205			
5.832	0.0016	0.0189			
6.037		0.0153			
6.242	0.0002	0.0130			
6.447		0.0111			
6.652	0.0003	0.0116			
6.856		0.0098			
7.061	0.0001	0.0088			
7.265		0.0076			

C.7 Experimental run no. 90-021**EXPERIMENTAL SPECIFICATIONS**

Solution contents:	0.173	wt.% Neodol 25-3S
	12.0	wt.% NaCl
	5.99	pH (injected)
Injection rate:	20	mL/h
Total injection:	2.88	PV

CORE CHARACTERISTICS

Core ID:	WK-30	
Weight:	435.04	g
Thickness:	34.95	mm
Diameter:	88.32	mm
Wellbore diameter:	3.53	mm
Pore volume:	47.93	cm ³
Porosity:	22.42	%

Effluent PV	Tracer C/C _o	Surfactant C/C _o	Effluent PV	Tracer C/C _o	Surfactant C/C _o
0.041	-0.0002	0.0000	7.217	0.0000	0.0155
0.057	-0.0001	0.0000	7.414		0.0120
0.150	-0.0001	0.0000	7.613	-0.0001	0.0111
0.260	0.0000	0.0000	7.813		0.0135
0.360	0.0005	0.0000			
0.460	0.0017	0.0000			
0.561	0.0046	0.0000			
0.660	0.0274	0.0000			
0.761	0.1050	0.0000			
0.861	0.2405	0.0000			
0.962	0.4405	0.0000			
1.062	0.6097	0.0000			
1.162	0.7305	0.0000			
1.261	0.8225	0.0000			
1.361	0.8890	0.0000			
1.461		0.0000			
1.560	0.9011	0.0000			
1.660		0.0000			
1.760		0.0000			
1.860	0.9650	0.0064			
1.961	0.9821	0.0070			
2.062	0.9562	0.0057			
2.164	0.9643	0.0007			
2.266	0.9736	0.0157			
2.369	0.9643	0.0157			
2.471	0.9809	0.0225			
2.573		0.0319			
2.674	0.9710	0.0451			
2.775	0.9529	0.0579			
2.875	0.9518	0.0640			
2.967	0.9645	0.0919			
3.059	0.9732	0.1066			
3.160	0.9807	0.1345			
3.262	0.9815	0.1509			
3.364	0.9216	0.1879			
3.466		0.2198			
3.560	0.8892	0.2274			
3.669	0.8874	0.2075			
3.771	0.8626	0.1533			
3.872		0.1364			
3.974	0.5441	0.1064			
4.075	0.3939	0.0830			
4.176	0.2424	0.0696			
4.277	0.1420	0.0543			
4.378	0.0822	0.0477			
4.480	0.0441	0.0462			
4.581	0.0250	0.0371			
4.682	0.0142	0.0363			
4.783	0.0080	0.0409			
4.884	0.0054	0.0350			
5.032		0.0292			
5.231	0.0014	0.0167			
5.430		0.0235			
5.631	0.0007	0.0260			
5.832		0.0173			
6.033	0.0002	0.0200			
6.231		0.0101			
6.428	0.0001	0.0142			
6.626		0.0172			
6.823	-0.0002	0.0123			
7.020		0.0072			

C.8 Experimental run no. 90-006**EXPERIMENTAL SPECIFICATIONS**

Solution contents:	0.485	wt. % Neodol 25-3S
	12.0	wt. % NaCl
	6.12	pH (injected)
Injection rate:	20	mL/h
Total injection:	2.86	PV

CORE CHARACTERISTICS

Core ID:	WK-37	
Weight:	460.99	g
Thickness:	38.65	mm
Diameter:	88.40	mm
Wellbore diameter:	3.45	mm
Pore volume:	49.95	cm ³
Porosity:	22.24	%

Effluent PV	Tracer C/C ₀	Surfactant C/C ₀	Effluent PV	Tracer C/C ₀	Surfactant C/C ₀
0.030	0.0000	0.0000	7.192	0.0002	0.0092
0.069	0.0000	0.0000	7.391		0.0072
0.167	0.0001	0.0000	7.589	0.0001	0.0093
0.267	0.0017	0.0000	7.788		0.0086
0.367	0.0060	0.0000			
0.467	0.0125	0.0035			
0.567	0.0125	0.0047			
0.666	0.0583	0.0088			
0.765	0.1451	0.0095			
0.864	0.2885	0.0196			
0.963	0.4516	0.0214			
1.062	0.5961	0.0364			
1.162	0.7366	0.0504			
1.261	0.8393	0.0993			
1.361	0.9002	0.1534			
1.462	0.9597	0.2368			
1.561	0.9947	0.3095			
1.661	0.9810	0.3846			
1.760	0.9939	0.4874			
1.860	0.9788	0.5386			
1.959	1.0034	0.6157			
2.058	0.9909	0.6666			
2.158	1.0156	0.7541			
2.257	1.0156	0.7737			
2.357	0.9557	0.7929			
2.457	1.0437	0.7720			
2.558	1.0089	0.8309			
2.657	0.9959	0.7918			
2.757	1.0508	0.8201			
2.857	1.0138	0.8387			
2.957	1.0043	0.8663			
3.072	0.9924	0.8388			
3.172	1.0051	0.8171			
3.272	1.0014	0.7797			
3.373	0.9342	0.7460			
3.473	0.8834	0.7006			
3.574	0.8250	0.6521			
3.674	0.7686	0.5648			
3.774	0.7259	0.5049			
3.873	0.6322	0.4160			
3.971	0.5755	0.3668			
4.070	0.4954	0.3132			
4.168	0.3993	0.2728			
4.267	0.3123	0.1994			
4.366	0.2300	0.1664			
4.465	0.1624	0.1316			
4.564	0.1125	0.1054			
4.664	0.0777	0.0798			
4.764	0.0497	0.0759			
4.863	0.0334	0.0592			
5.012		0.0486			
5.209	0.0128	0.0377			
5.406		0.0302			
5.603	0.0042	0.0218			
5.801		0.0181			
6.000	0.0006	0.0154			
6.198		0.0133			
6.396	0.0002	0.0111			
6.595		0.0107			
6.794	0.0002	0.0097			
6.993		0.0081			

C.9 Experimental run no. 90-018**EXPERIMENTAL SPECIFICATIONS**

Solution contents:	1.058	wt.% Neodol 25-3S
	12.0	wt.% NaCl
	6.07	pH (injected)
Injection rate:	20	mL/h
Total injection:	2.90	PV

CORE CHARACTERISTICS

Core ID:	WK-27	
Weight:	434.60	g
Thickness:	34.93	mm
Diameter:	88.08	mm
Wellbore diameter:	3.43	mm
Pore volume:	48.82	cm ³
Porosity:	22.99	%

Effluent PV	Tracer C/C ₀	Surfactant C/C ₀	Effluent PV	Tracer C/C ₀	Surfactant C/C ₀
-0.064	0.0001	0.0000	7.305	0.0437	0.0516
0.037	0.0002	0.0000	7.500		0.0499
0.130	0.0000	0.0000	7.712	0.0344	0.0445
0.241	0.0006	0.0000	7.916		0.0421
0.343	0.0024	0.0010			
0.444	0.0103	0.0065			
0.545	0.0401	0.0121			
0.646	0.1079	0.0232			
0.747	0.1993	0.0413			
0.849	0.3043	0.0879			
0.950	0.4268	0.1369			
1.051	0.5774	0.2021			
1.153	0.7062	0.2910			
1.254	0.8403	0.4053			
1.357	0.9389	0.5439			
1.459	0.9742	0.7269			
1.562	1.0101	0.8025			
1.664	1.0001	0.8292			
1.767	0.9895	0.8439			
1.871	0.9926	0.8839			
1.974	1.0046	0.9010			
2.076		0.9226			
2.179	0.9865	0.9213			
2.282	0.9877	0.9200			
2.384	0.9794	0.9154			
2.487	0.9845	0.9423			
2.590	1.0303	0.9568			
2.693	1.0142	0.9545			
2.795	0.9966	0.9426			
2.895		0.9730			
2.996	1.0333	0.9472			
3.079	1.0232	0.9793			
3.181	0.8964	0.7321			
3.284	0.8964	0.5692			
3.386	0.5537	0.4417			
3.489	0.5099	0.3871			
3.592	0.4623	0.3403			
3.695	0.4044	0.3014			
3.797	0.3841	0.2887			
3.900	0.3456	0.2450			
4.003	0.3302	0.2305			
4.106	0.2934	0.2183			
4.209	0.2813	0.1914			
4.311	0.2638	0.1919			
4.413	0.2550	0.1765			
4.514	0.2322	0.1760			
4.614	0.2357	0.1632			
4.715	0.2198	0.1530			
4.816	0.2098	0.1423			
4.917	0.1884	0.1241			
5.068		0.1192			
5.270	0.1443	0.1005			
5.472		0.0948			
5.675	0.1194	0.0868			
5.878		0.0775			
6.082	0.0926	0.0758			
6.287		0.0702			
6.491	0.0723	0.0669			
6.695		0.0627			
6.899	0.0363	0.0578			
7.102		0.0538			

C.10 Experimental run no. 90-025**EXPERIMENTAL SPECIFICATIONS**

Solution contents:	1.848	wt.% Neodol 25-3S
	12.0	wt.% NaCl
	6.33	pH (injected)
Injection rate:	20	mL/h
Total injection:	2.97	PV

CORE CHARACTERISTICS

Core ID:	WK-039	
Weight:	444.39	g
Thickness:	35.30	mm
Diameter:	88.35	mm
Wellbore diameter:	3.20	mm
Pore volume:	47.63	cm ³
Porosity:	22.04	%

Effluent PV	Tracer C/C ₀	Surfactant C/C ₀	Effluent PV	Tracer C/C ₀	Surfactant C/C ₀
-0.040	-0.0000	0.0000	7.505	0.0668	0.0502
0.058	-0.0001	0.0000	7.714		0.0447
0.160	0.0000	0.0000	7.924	0.0600	0.0430
0.263	0.0006	0.0000	8.133		0.0423
0.366	0.0018	0.0020	8.343	0.0523	0.0384
0.470	0.0030	0.0022	8.552		0.0377
0.574	0.0095	0.0053	8.762	0.0454	0.0378
0.678	0.0358	0.0144	8.972		0.0343
0.782	0.1163	0.0369	9.181		0.0390
0.886	0.2780	0.0590	9.391		
0.990	0.5023	0.1794	9.587		
1.094	0.6899	0.3815			
1.198	0.8779	0.6399			
1.301	0.9032	0.7203			
1.404	0.9432	0.8100			
1.508	1.0127	0.8591			
1.612	1.0067	0.8535			
1.716	1.0005	0.9012			
1.821	1.0137	0.9809			
1.925	1.0043	0.9106			
2.029	1.0146	0.9134			
2.133	1.0153	0.9593			
2.238	1.0043	0.9478			
2.342	0.9945	0.9468			
2.446	1.0109	0.9123			
2.550	1.0024	0.9861			
2.655	1.0317	0.9600			
2.759	1.0107	0.9600			
2.863	1.0223	0.9527			
2.968	1.0133	0.9235			
3.072	0.9598	0.9656			
3.176	0.9347	0.9266			
3.280	0.7096	0.5588			
3.375	0.4777	0.3514			
3.481	0.3705	0.2550			
3.585	0.3144	0.1917			
3.690	0.2720	0.1917			
3.795	0.2542	0.1634			
3.900	0.2436	0.1570			
4.005	0.2132	0.1390			
4.110	0.1880	0.1307			
4.215	0.1880	0.1239			
4.320	0.1622	0.1114			
4.425	0.1613	0.1093			
4.529	0.1434	0.0993			
4.634	0.1377	0.0899			
4.740	0.1295	0.0864			
4.845	0.1210	0.0804			
4.950	0.1160	0.0785			
5.056	0.1154	0.0636			
5.162		0.0617			
5.268	0.0975	0.0587			
5.373		0.0689			
5.479	0.0912	0.0525			
5.584		0.0554			
5.689	0.0952	0.0561			
5.794		0.0484			
5.899	0.0831	0.0454			
6.004		0.0499			
6.109	0.0729	0.0504			
6.214		0.0483			

C.11 Experimental run no. 90-014**EXPERIMENTAL SPECIFICATIONS**

Solution contents:	0.485	wt.% Neodol 25-3S
	8.0	wt.% NaCl
	2.37	pH (injected)
Injection rate:	20	mL/h
Total injection:	2.89	PV

CORE CHARACTERISTICS

Core ID:	WK-35	
Weight:	435.65	g
Thickness:	35.05	mm
Diameter:	88.32	mm
Wellbore diameter:	3.56	mm
Pore volume:	47.95	cm ³
Porosity:	22.37	%

Effluent PV	Tracer C/C ₀	Surfactant C/C ₀	Effluent PV	Tracer C/C ₀	Surfactant C/C ₀
-0.053	-0.0001	0.0000	7.407	0.0001	
0.034	0.0001	0.0000	7.611		0.0160
0.136	0.0000	0.0000	7.815	0.0002	
0.238	0.0000	0.0000	8.018		0.0151
0.341	0.0000	0.0000			
0.443	0.0000	0.0000			
0.544	0.0000	0.0000			
0.645	0.0295	0.0000			
0.746	0.1182	0.0000			
0.848	0.2380	0.0310			
0.950	0.4151	0.0620			
1.051	0.5881	0.0967			
1.153	0.7302	0.1471			
1.255	0.8262	0.2344			
1.357	0.9272	0.3225			
1.459	0.9576	0.4156			
1.561	1.0114	0.4769			
1.663		0.5493			
1.764		0.6193			
1.866		0.6532			
1.967	1.0238	0.7077			
2.069	0.9943	0.7378			
2.171	0.9988	0.7754			
2.273	1.0196	0.8106			
2.376	0.9800	0.8309			
2.478	1.0307	0.8495			
2.580	1.0003	0.8650			
2.682		0.8948			
2.783	1.0157	0.9046			
2.885	1.0240	0.9009			
3.031	0.9827	0.9151			
3.177	0.9833	0.9131			
3.280	0.9942	0.9053			
3.383	0.9685	0.9463			
3.486	0.9571	0.8996			
3.588		0.9023			
3.691		0.8278			
3.793	0.8511	0.7764			
3.895	0.7269	0.6762			
3.997	0.5601	0.5479			
4.100	0.3784	0.4041			
4.202		0.3168			
4.304		0.2307			
4.407	0.0809	0.1652			
4.510	0.0448	0.1453			
4.613	0.0225	0.1232			
4.715	0.0128	0.0927			
4.818	0.0076	0.0868			
4.920	0.0052	0.0712			
5.023	0.0036	0.0628			
5.176		0.0590			
5.278	0.0015	0.0432			
5.380		0.0403			
5.483	0.0007	0.0334			
5.586		0.0288			
5.689	0.0003	0.0273			
5.792		0.0298			
5.895	0.0003	0.0223			
5.998		0.0238			
7.001	-0.0002	0.0287			
7.204		0.0188			

C.12 Experimental run no. 91-043**EXPERIMENTAL SPECIFICATIONS**

Solution contents:	0.520	wt.% Neodol 25-3S
	8.0	wt.% NaCl
	12.53	pH (injected)
Injection rate:	20	mL/h
Total injection:	3.06	PV

CORE CHARACTERISTICS

Core ID:	WK-52	
Weight:	432.63	g
Thickness:	34.85	mm
Diameter:	88.35	mm
Wellbore diameter:	3.35	mm
Pore volume:	48.92	cm ³
Porosity:	22.93	%

Effluent PV	Tracer C/C ₀	Surfactant C/C ₀	Effluent PV	Tracer C/C ₀	Surfactant C/C ₀
0.036	0.0003	0.0000	6.374	0.0017	
0.171	0.0002	0.0000	6.478		0.0139
0.275	0.0002	0.0000	6.581		
0.378	0.0005	0.0000	6.684	0.0013	
0.481	0.0003	0.0000	6.787		0.0117
0.584	0.0012	0.0000	6.890		
0.686	0.0138	0.0000	6.993	0.0010	
0.789	0.0784	0.0000	7.095		0.0108
0.892	0.2519	0.0000	7.198		
0.996	0.4903	0.0481	7.301	0.0008	
1.099	0.6930	0.2035	7.404		0.0096
1.202	0.8505	0.3829	7.506		
1.306	0.9881	0.5374	7.610	0.0008	
1.409	0.9860	0.6343	7.713		
1.512	0.9840	0.6909	7.816		0.0081
1.615	0.9976	0.7510	7.919	0.0006	
1.719	1.0211	0.8013	8.022		
1.822	1.0145	0.8217	8.125		
1.925	0.9876	0.8509	8.228	0.0005	0.0070
2.028	1.0072	0.8743			
2.131	1.0322	0.8818			
2.234	0.9873	0.8822			
2.337	1.0119	0.8973			
2.441	0.9751	0.9048			
2.544	1.0009	0.9177			
2.648	1.0074	0.8937			
2.752	1.0078	0.9190			
2.856	1.0002	0.9183			
2.960	0.9862	0.9334			
3.060	1.0093	0.9387			
3.161	1.0002	0.9348			
3.265	0.9933	0.9269			
3.369	0.9951	0.9259			
3.472	1.0117	0.9410			
3.576	1.0280	0.9377			
3.679	0.9895	0.8910			
3.783	0.9459	0.8061			
3.887	0.8664	0.6508			
3.990	0.7244	0.5269			
4.094	0.5655	0.3954			
4.197	0.4311	0.3201			
4.301	0.2926	0.2406			
4.405	0.1803	0.1647			
4.508	0.1211	0.1407			
4.612	0.0815	0.1083			
4.715	0.0578	0.0975			
4.819	0.0404	0.0723			
4.922	0.0278	0.0574			
5.027	0.0196	0.0454			
5.130	0.0134	0.0386			
5.234	0.0099	0.0305			
5.338		0.0291			
5.441	0.0059				
5.545		0.0215			
5.649					
5.753	0.0038	0.0235			
5.856					
5.960		0.0198			
6.063	0.0023				
6.167		0.0153			
6.271					

C.13 Experimental run no. 90-020**EXPERIMENTAL SPECIFICATIONS**

Solution contents:	0.471	wt.% Neodol 25-3S
	8.0	wt.% NaCl
	6.44	pH (Injected)
Injection rate:	5	mL/h
Total Injection:	2.80	PV

CORE CHARACTERISTICS

Core ID:	WK-32	
Weight:	434.59	g
Thickness:	35.05	mm
Diameter:	88.21	mm
Wellbore diameter:	3.58	mm
Pore volume:	48.76	cm ³
Porosity:	22.80	%

Effluent PV	Tracer C/C ₀	Surfactant C/C ₀	Effluent PV	Tracer C/C ₀	Surfactant C/C ₀
0.049	0.0000	0.0000	6.029		0.0230
0.051	0.0002	0.0000	6.127		0.0225
0.155	0.0020	0.0027	6.226	0.0008	0.0200
0.262	0.0074	0.0142	6.326		0.0202
0.369	0.0204	0.0118	6.425		0.0181
0.477	0.0439	0.0230	6.525		
0.587	0.0962	0.0360	6.624	0.0004	0.0163
0.696	0.2163	0.0486	6.723		
0.805	0.3017	0.0659	6.821		0.0160
0.910	0.4370	0.0791	6.919		
1.014	0.5958	0.0978	7.018		0.0147
1.117	0.6714	0.1198	7.118		
1.218	0.7656	0.1389	7.218		0.0122
1.318	0.8065	0.1981	7.318		
1.417	0.9471	0.2618	7.418	0.0002	0.0128
1.516	0.8936	0.3672	7.520		
1.613	0.9523	0.4350	7.622		0.0107
1.710	0.9300	0.5178	7.724		
1.807	0.9493	0.6065	7.826	0.0001	0.0105
1.904	0.9552	0.6794			
2.002		0.7347			
2.101	0.9586	0.7769			
2.200	1.0035	0.8076			
2.300	0.9298	0.8434			
2.399	0.9534	0.8676			
2.499	0.9849	0.8874			
2.598	1.0073	0.8956			
2.696		0.9147			
2.795	0.9973	0.9338			
2.891	0.9766	0.9406			
2.948	0.9971	0.9542			
3.048	0.9391	0.9788			
3.148	0.9533	0.9385			
3.248	0.9479	0.9003			
3.347	0.9725	0.8959			
3.445	0.8879	0.8792			
3.544		0.8383			
3.643	0.8077	0.7919			
3.742	0.6935	0.6355			
3.840	0.5691	0.5315			
3.937	0.4579	0.3982			
4.035	0.3878	0.3239			
4.132	0.3075	0.2386			
4.230	0.2353	0.1820			
4.328	0.1917	0.1548			
4.426	0.1437	0.1345			
4.525		0.1094			
4.626	0.0888	0.0924			
4.726	0.0660	0.0788			
4.827	0.0465	0.0360			
4.928		0.0603			
5.031	0.0270	0.0510			
5.133	0.0181	0.0488			
5.232		0.0405			
5.331	0.0113	0.0391			
5.430	0.0088	0.0344			
5.530	0.0063	0.0312			
5.631	0.0048	0.0273			
5.731	0.0032	0.0303			
5.831	0.0027	0.0275			
5.931		0.0258			

C.14 Experimental run no. 91-044**EXPERIMENTAL SPECIFICATIONS**

Solution contents:	0.453	wt.% Neodol 25-3S
	8.0	wt.% NaCl
	6.00	pH (injected)
Injection rate:	120	mL/h
Total injection:	2.94	PV

CORE CHARACTERISTICS

Core ID:	WK-51	
Weight:	434.71	g
Thickness:	34.90	mm
Diameter:	88.30	mm
Wellbore diameter:	3.35	mm
Pore volume:	49.31	cm ³
Porosity:	23.11	%

Effluent PV	Tracer C/C ₀	Surfactant C/C ₀	Effluent PV	Tracer C/C ₀	Surfactant C/C ₀
0.001	0.0000	0.0000	6.185		
0.098	0.0001	0.0000	6.286		
0.199	0.0002	0.0000	6.388	0.0008	0.0104
0.300	0.0001	0.0000	6.490		
0.402	0.0001	0.0000	6.591		
0.503	0.0002	0.0000	6.693	0.0005	
0.604	0.0041	0.0000	6.794		0.0089
0.705	0.0347	0.0000	6.896		
0.806	0.1355	0.0028	6.997	0.0006	
0.907	0.3080	0.0346	7.099		
1.008	0.5167	0.1017	7.200		0.0059
1.109	0.6973	0.1871	7.302	0.0006	
1.210	0.8115	0.2590	7.404		
1.312	0.9104	0.3735	7.505		
1.413	0.9630	0.4720	7.607	0.0004	0.0054
1.514	0.9880	0.5623	7.708		
1.615	0.9891	0.5989	7.810		
1.717	0.9857	0.6560	7.911	0.0004	
1.818	0.9654	0.7269	8.013		0.0069
1.919	1.0011	0.7313			
2.021	1.0107	0.7440			
2.122	1.0018	0.7590			
2.224	1.0253	0.7918			
2.325	0.9954	0.8019			
2.427	0.9907	0.8063			
2.528	1.0192	0.8317			
2.630	0.9951	0.8071			
2.731	0.9792	0.8310			
2.833	1.0035	0.8310			
2.935	0.9989	0.8440			
3.036	1.0107	0.8414			
3.136	1.0239	0.8653			
3.238	0.9988	0.8627			
3.340	0.9970	0.8750			
3.442	1.0168	0.8459			
3.543	0.9998	0.8049			
3.645	0.9579	0.6963			
3.746	0.8448	0.5795			
3.848	0.7088	0.4354			
3.949	0.5966	0.3608			
4.051	0.4289	0.2836			
4.152	0.3310	0.2231			
4.254	0.2433	0.1743			
4.356	0.1651	0.1416			
4.458	0.1051	0.0961			
4.559	0.0677	0.0749			
4.660	0.0427	0.0607			
4.762	0.0284	0.0524			
4.863	0.0192	0.0394			
4.965	0.0145	0.0362			
5.067	0.0107				
5.168	0.0083				
5.270	0.0067	0.0201			
5.372	0.0052				
5.474	0.0044	0.0161			
5.575	0.0034				
5.676	0.0029				
5.778	0.0022	0.0134			
5.880	0.0019				
5.981	0.0015				
6.083	0.0014	0.0093			

C.15 Experimental run no. 91-036**EXPERIMENTAL SPECIFICATIONS**

Solution contents:	0.501	wt.% Triton X-100
	3.0	wt.% NaCl
	5.80	pH (injected)
Injection rate:	20	mL/h
Total injection:	5.99	PV

CORE CHARACTERISTICS

Core ID:	DS-03	
Weight:	432.22	g
Thickness:	35.10	mm
Diameter:	88.38	mm
Wellbore diameter:	3.80	mm
Pore volume:	48.82	cm ³
Porosity:	22.71	%

Effluent PV	Tracer C/C ₀	Surfactant C/C ₀	Effluent PV	Tracer C/C ₀	Surfactant C/C ₀
0.031	0.0001	0.0054	6.197	0.9575	0.9885
0.071	0.0002	0.0057	6.301	0.9723	0.9833
0.173	0.0001	0.0052	6.404	0.9823	0.9847
0.274	0.0000	0.0054	6.508	0.9898	0.9824
0.376	0.0001	0.0048	6.611	0.9810	0.9841
0.479	0.0001	0.0046	6.714	0.9898	0.9803
0.580	0.0007	0.0047	6.817	0.9607	0.9567
0.682	0.0117	0.0045	6.920	0.8878	0.8639
0.784	0.0755	0.0047	7.023	0.7113	0.6888
0.886	0.2360	0.0044	7.126	0.4946	0.5348
0.988	0.4713	0.0048	7.229	0.2660	0.3915
1.089	0.6982	0.0048	7.331	0.1403	0.2841
1.191	0.8524	0.0052	7.434	0.0739	0.2141
1.294	0.9277	0.0061	7.537	0.0410	0.1679
1.396	0.9690	0.0059	7.640	0.0242	0.1377
1.497	0.9992	0.0067	7.743	0.0149	0.1024
1.599	1.0097	0.0077	7.846	0.0093	0.0923
1.701	1.0123	0.0084	7.949	0.0061	0.0833
1.803	1.0076	0.0121	8.052	0.0043	0.0767
1.906	1.0135	0.0299	8.154		0.0712
2.007	1.0084	0.0813	8.257	0.0021	0.0663
2.109	0.9820	0.1883	8.360		0.0621
2.212		0.3325	8.462	0.0012	0.0588
2.314	1.0108	0.4715	8.565		0.0558
2.416		0.5823	8.668	0.0011	0.0534
2.518	1.0119	0.6774	8.771		0.0514
2.620		0.7511	8.874	0.0009	0.0494
2.721	0.9870	0.8021	8.976		0.0473
2.823		0.8393	9.079	0.0008	0.0462
2.925	0.9971	0.8643	9.182		0.0448
3.027		0.8891	9.284	0.0007	0.0440
3.128	0.9588	0.9076	9.387		0.0426
3.230		0.9202	9.489	0.0005	0.0416
3.332	1.0142	0.9313	9.591		0.0407
3.434		0.9406	9.693	0.0006	0.0398
3.536	0.9801	0.9465	9.796		0.0393
3.639		0.9585	9.898	0.0004	0.0385
3.742	0.9940	0.9601	10.001		0.0379
3.845		0.9652	10.103	0.0002	0.0376
3.948	1.0091	0.9704	10.206		0.0376
4.051		0.9771	10.308	0.0005	0.0367
4.153	0.9894	0.9770	10.411		0.0362
4.256		0.9779	10.514	0.0003	0.0359
4.359	0.9996	0.9819	10.616		0.0353
4.461		0.9863	10.719	0.0003	0.0349
4.559	0.9868	0.9865	10.821		0.0347
4.657		0.9884	10.924	0.0003	0.0342
4.760	0.9802	0.9942	11.016		0.0345
4.862		0.9950			
4.965	0.9751	0.9949			
5.067		0.9901			
5.169	0.9741	0.9945			
5.272		0.9922			
5.374	0.9653	0.9954			
5.476		0.9954			
5.579	0.9681	0.9951			
5.681		0.9984			
5.784	0.9626	0.9988			
5.886		0.9963			
5.989	0.9616	1.0082			
6.092	0.9795	1.0071			

C.16 Experimental run no. 91-034**EXPERIMENTAL SPECIFICATIONS**

Solution contents:	0.472	wt.% Triton X-100
	8.0	wt.% NaCl
	6.00	pH (injected)
Injection rate:	20	mL/h
Total injection:	6.39	PV

CORE CHARACTERISTICS

Core ID:	DS-01	
Weight:	434.90	g
Thickness:	35.04	mm
Diameter:	88.55	mm
Wellbore diameter:	3.45	mm
Pore volume:	44.25	cm ³
Porosity:	20.54	%

Effluent PV	Tracer C/C ₀	Surfactant C/C ₀	Effluent PV	Tracer C/C ₀	Surfactant C/C ₀
0.012	0.0000	0.0000	6.934	0.9490	0.9683
0.103	0.0001	0.0000	7.037	0.9798	0.9698
0.216	0.0001	0.0000	7.143	0.9484	0.9242
0.328	0.0000	0.0000	7.256	0.8766	0.8154
0.441	0.0002	0.0000	7.369	0.6890	0.6667
0.553	0.0007	0.0000	7.482	0.4966	0.5240
0.666	0.0162	0.0000	7.596	0.3624	0.4107
0.779	0.1076	0.0023	7.709	0.2416	0.3152
0.892	0.2949	0.0023	7.822	0.1645	0.2434
1.004	0.5065	0.0022	7.935	0.1142	0.1927
1.117	0.6817	0.0023	8.048	0.0711	0.1532
1.230	0.7975	0.0023	8.161	0.0540	0.1269
1.343	0.8932	0.0024	8.274	0.0416	0.1095
1.455	0.9399	0.0025	8.387	0.0325	0.0946
1.567	0.9852	0.0026	8.500	0.0243	0.0835
1.679	0.9990	0.0029	8.613	0.0196	0.0739
1.791	0.9731	0.0054	8.726	0.0165	0.0666
1.904	1.0459	0.0204	8.839	0.0131	0.0607
2.017	1.0459	0.0561	8.951	0.0111	0.0555
2.130	1.0239	0.1061	9.064		0.0515
2.243		0.1712	9.177	0.0077	0.0474
2.356	1.0052	0.2506	9.290		0.0443
2.469		0.3341	9.403	0.0058	0.0417
2.582	1.0074	0.4128	9.516		0.0402
2.696		0.4830	9.629	0.0042	0.0377
2.809	0.9876	0.5440	9.742		0.0359
2.971			9.854	0.0032	0.0342
3.162	0.9909	0.6758	9.967		0.0329
3.259		0.7467	10.080	0.0024	0.0313
3.326	1.0251	0.7766	10.193		0.0305
3.439		0.8083	10.306	0.0018	0.0294
3.552	1.0025	0.8333	10.419		0.0285
3.665		0.8550	10.531	0.0015	0.0275
3.778	0.9724	0.8734	10.642		0.0269
3.891		0.8876	10.753	0.0010	0.0262
4.003	0.9749	0.8983	10.863		0.0255
4.116		0.9130	10.973	0.0009	0.0246
4.229	0.9799	0.9193	11.083		0.0244
4.342		0.9321	11.196	0.0007	0.0237
4.455	0.9866	0.9355			
4.568		0.9424			
4.681	0.9920	0.9514			
4.795		0.9506			
4.908	0.9811	0.9615			
5.021		0.9657			
5.134	1.0109	0.9664			
5.248		0.9682			
5.361	0.9865	0.9742			
5.427		0.9758			
5.494	0.9632	0.9800			
5.607		0.9805			
5.720	0.9946	0.9809			
5.833		0.9854			
5.946	0.9851	0.9858			
6.059		0.9883			
6.173	0.9719	0.9879			
6.286		0.9908			
6.385	0.9848	0.9908			
6.484		0.9754			
6.597	0.9888	0.9587			
6.767	0.9754	0.9581			

C.17 Experimental run no. 91-035**EXPERIMENTAL SPECIFICATIONS**

Solution contents:	0.490	wt.% Triton X-100
	12.0	wt.% NaCl
	7.32	pH (injected)
Injection rate:	20	mL/h
Total injection:	6.21	PV

CORE CHARACTERISTICS

Core ID:	DS-02	
Weight:	430.18	g
Thickness:	34.75	mm
Diameter:	88.33	mm
Wellbore diameter:	3.30	mm
Pore volume:	49.75	cm ³
Porosity:	21.98	%

Effluent PV	Tracer C/C ₀	Surfactant C/C ₀	Effluent PV	Tracer C/C ₀	Surfactant C/C ₀
0.016	0.0000	0.0000	6.421	0.9328	0.9569
0.058		0.0000	6.529	0.9931	0.9647
0.111	0.0001	0.0000	6.637	0.9321	0.9641
0.219	0.0000	0.0000	6.745	0.9532	0.9712
0.325	0.0000	0.0000	6.852	0.9674	0.9782
0.431	0.0002	0.0009	6.960	0.9382	0.9623
0.536	0.0002	0.0011	7.068	0.9607	0.8949
0.642	0.0056	0.0011	7.175	0.8421	0.7540
0.748	0.0522	0.0010	7.283	0.6378	0.5759
0.855	0.2001	0.0010	7.390	0.4348	0.4300
0.962	0.4249	0.0009	7.496	0.2625	0.3025
1.069	0.6373	0.0007	7.602	0.1498	0.2108
1.176	0.7864	0.0009	7.709	0.0811	0.1510
1.282	0.8890	0.0009	7.817	0.0417	0.1118
1.389	0.9385	0.0009	7.924	0.0238	0.0943
1.497	0.9710	0.0013	8.032	0.0124	0.0784
1.604	0.9935	0.0011	8.139	0.0070	0.0661
1.710	1.0068	0.0016	8.246	0.0046	0.0572
1.816		0.0014	8.354	0.0026	0.0499
1.923	1.0319	0.0015	8.462		0.0444
2.029	1.0164	0.0025	8.569	0.0013	0.0403
2.136	1.0204	0.0105	8.677		0.0373
2.243	1.0134	0.0416	8.784	0.0008	0.0336
2.349	1.0031	0.0986	8.892		0.0312
2.456	0.9976	0.1720	9.000	0.0009	0.0291
2.563	0.9834	0.2707	9.107		0.0274
2.671	1.0030	0.3738	9.215	0.0005	0.0260
2.778	0.9988	0.4699	9.323		0.0246
2.886	1.0090	0.5524	9.430	0.0005	0.0234
2.993	1.0120	0.6296	9.538		0.0222
3.100		0.6955	9.646	0.0004	0.0213
3.207	0.9776	0.7435	9.753		0.0207
3.315		0.7912	9.861	0.0006	0.0199
3.422	0.9872	0.8202	9.968		0.0195
3.529		0.8444	10.076	0.0005	0.0186
3.637	0.9819	0.8669	10.183		0.0180
3.744		0.8873	10.291	0.0005	0.0183
3.852	0.9787	0.9034	10.398		0.0168
3.959		0.9141	10.505	0.0006	0.0166
4.066	0.9240	0.9260	10.612		0.0164
4.174		0.9340	10.719	0.0004	0.0157
4.281	0.9414	0.9442	10.827		0.0152
4.388		0.9463	10.934	0.0004	0.0152
4.495	0.9647	0.9541	11.041		0.0150
4.603		0.9601	11.148	0.0003	0.0146
4.710	0.9567	0.9673	11.256		0.0148
4.818		0.9700	11.364	0.0003	0.0140
4.926	0.9792	0.9659	11.471		0.0138
5.033		0.9775			
5.141	0.9585	0.9804			
5.248		0.9813			
5.356	0.9287	0.9840			
5.464		0.9877			
5.571	0.9645	0.9908			
5.679		0.9883			
5.787	0.9578	0.9930			
5.895		0.9931			
6.002	0.9934	0.9937			
6.110		0.9943			
6.212	0.9431	0.9986			
6.314	0.9642	0.9723			

C.18 Experimental run no. 91-041**EXPERIMENTAL SPECIFICATIONS**

Solution contents:	0.505	wt.% Triton X-100
	3.0	wt.% NaCl
	6.00	pH (injected)
Injection rate:	80	mL/h
Total injection:	6.86	PV

CORE CHARACTERISTICS

Core ID:	DS-06	
Weight:	434.28	g
Thickness:	34.93	mm
Diameter:	88.43	mm
Wellbore diameter:	3.28	mm
Pore volume:	46.06	cm ³
Porosity:	21.50	%

Effluent PV	Tracer C/C ₀	Surfactant C/C ₀	Effluent PV	Tracer C/C ₀	Surfactant C/C ₀
0.026	0.0001	0.0036	6.648	0.9959	0.9716
0.084	0.0001	0.0037	6.755		0.9755
0.195	0.0002	0.0033	6.863	1.0043	0.9768
0.305	0.0001	0.0030	6.971		0.9678
0.414		0.0029	7.083	1.0302	0.9633
0.524	0.0023	0.0028	7.191	1.0253	0.9634
0.634	0.0285	0.0025	7.298	1.0126	0.9681
0.744	0.1192	0.0025	7.405	0.9973	0.9704
0.854	0.2755	0.0025	7.188	1.0081	0.9551
0.964	0.4464	0.0025	7.296	0.9998	0.9008
1.073	0.6067	0.0027	7.728	0.8911	0.8116
1.182	0.7406	0.0029	7.835	0.7528	0.6889
1.292	0.8541	0.0070	7.942	0.5900	0.5614
1.402	0.8809	0.0239	8.049	0.4362	0.4474
1.511	0.9313	0.0602	8.156	0.3102	0.3549
1.621	0.9665	0.1102	8.264	0.2054	0.2805
1.731	0.9853	0.1688	8.371	0.1374	0.2220
1.840	0.9935	0.2333	8.478	0.0928	0.1779
1.950	1.0042	0.3008	8.585	0.0606	0.1459
2.059	0.9944	0.3709	8.691	0.0419	0.1231
2.169	1.0065	0.4390	8.797	0.0285	0.1018
2.278	1.0198		8.903	0.0194	0.0949
2.388	1.0161	0.5779	9.010	0.0143	0.0848
2.497	0.9998	0.6354	9.116		0.0766
2.607		0.6850	9.222	0.0084	0.0704
2.717	0.9994	0.7283	9.328		0.0648
2.826		0.7652	9.434	0.0058	0.0610
2.935	1.0140	0.7935	9.541		0.0567
3.045		0.8199	9.647	0.0041	0.0537
3.155	0.9893	0.8423	9.753		0.0509
3.264		0.8571	9.859	0.0033	0.0488
3.374	1.0001	0.8693	9.965		0.0468
3.483		0.8823	10.071	0.0027	0.0451
3.592	0.9981	0.8907	10.178		0.0435
3.702		0.9031	10.284	0.0023	0.0420
3.812	0.9807	0.9143	10.391		0.0409
3.921		0.9201	10.497	0.0019	0.0399
4.031	0.9920	0.9264	10.603		0.0386
4.141		0.9322	10.709	0.0017	0.0377
4.250	1.0055	0.9360	10.815		0.0368
4.359		0.9435	10.921	0.0015	0.0360
4.469	1.0014	0.9443	11.027		0.0354
4.579		0.9450	11.133	0.0013	0.0353
4.688	1.0058	0.9543	11.239		0.0341
4.798		0.9584	11.346	0.0010	0.0337
4.907	1.0002	0.9577	11.452		0.0332
5.017		0.9626	11.559	0.0010	0.0330
5.126	0.9927	0.9657	11.665		0.0324
5.236		0.9652	11.771	0.0009	0.0317
5.346	1.0216	0.9664	11.877		0.0314
5.455		0.9715	11.983	0.0007	0.0310
5.564	1.0223	0.9727	12.090		0.0306
5.674		0.9746	12.196	0.0010	0.0304
5.783	0.9937	0.9756	12.302		0.0300
5.893		0.9779			
6.003	1.0101	0.9793			
6.111		0.9706			
6.219	0.9980	0.9640			
6.326		0.9667			
6.434	0.9978	0.9704			
6.541		0.9696			

C.19 Experimental run no. 91-033**EXPERIMENTAL SPECIFICATIONS**

Solution contents:	0.488	wt.% Triton X-100
	8.0	wt.% NaCl
	6.00	pH (injected)
Injection rate:	80	mL/h
Total injection:	6.87	PV

CORE CHARACTERISTICS

Core ID:	WK-47	
Weight:	443.91	g
Thickness:	35.23	mm
Diameter:	88.37	mm
Wellbore diameter:	3.55	mm
Pore volume:	46.29	cm ³
Porosity:	21.46	%

Effluent PV	Tracer C/C ₀	Surfactant C/C ₀	Effluent PV	Tracer C/C ₀	Surfactant C/C ₀
0.025	0.0001	0.0000	6.652	0.9984	0.9592
0.199	0.0000	0.0000	6.760		0.9602
0.318	0.0001	0.0000	6.869	1.0072	0.9602
0.442	0.0008	0.0000	6.976	0.9737	0.9372
0.562	0.0089	0.0000	7.081	0.9806	0.9158
0.671	0.0372	0.0000	7.189	0.9814	0.9117
0.781	0.1311	0.0059	7.297	0.9894	0.9127
0.863	0.2546	0.0056	7.406	0.9950	0.9143
0.925	0.3764	0.0053	7.514	1.0209	0.9083
1.029	0.5469	0.0054	7.622	0.9867	0.8662
1.150	0.7655	0.0074	7.730	0.9131	0.7777
1.258	0.8893	0.0109	7.837	0.7848	0.6407
1.366	0.9608	0.0157	7.945	0.6312	0.4944
1.474	1.0093	0.0215	8.053	0.4345	0.3837
1.581	1.0200	0.0277	8.161	0.2638	0.2845
1.689	1.0086	0.0387	8.269	0.1476	0.2105
1.797	1.0466	0.0627	8.376	0.0830	0.1592
1.905	1.0319	0.1057	8.484	0.0456	0.1259
2.012	1.0254	0.1626	8.591	0.0285	0.1018
2.121	1.0197	0.2321	8.699	0.0192	0.0861
2.229	0.9895	0.3061	8.807	0.0134	0.0747
2.337	0.9826	0.3856	8.914	0.0092	0.0656
2.445	1.0099	0.4596	9.022	0.0064	0.0580
2.553	1.0119	0.5231	9.130	0.0048	0.0522
2.661	0.9894	0.5864	9.237	0.0033	0.0473
2.768	0.9761	0.6427	9.345	0.0027	0.0433
2.875	0.9560	0.6852	9.452	0.0016	0.0402
2.983	0.9966	0.7217	9.560	0.0015	0.0376
3.090	1.0260	0.7521	9.668	0.0010	0.0351
3.198	1.0083	0.7799	9.775		0.0331
3.306		0.7959	9.883	0.0008	0.0313
3.414	1.0048	0.8157	9.991		0.0299
3.523		0.8332	10.098	0.0007	0.0288
3.633	0.9725	0.8395	10.206		0.0273
3.740		0.8515	10.313	0.0006	0.0263
3.848	0.9885	0.8772	10.421		0.0252
3.955		0.8726	10.528	0.0006	0.0245
4.063	0.9892	0.8807	10.636		0.0237
4.174		0.8909	10.744	0.0003	0.0229
4.285	1.0000	0.8966	10.852		0.0224
4.392		0.9011	10.960	0.0003	0.0217
4.500	0.9894	0.9044	11.068		0.0212
4.608		0.9041	11.175	0.0004	0.0206
4.716	0.9804	0.9166	11.283		0.0202
4.824		0.9221	11.391	0.0003	0.0197
4.932	0.9824	0.9250	11.499		0.0193
5.040		0.9293	11.606	0.0004	0.0189
5.147	0.9905	0.9327	11.714		0.0187
5.255		0.9358	11.822	0.0002	0.0184
5.363	1.0066	0.9420			
5.470		0.9406			
5.578	0.9788	0.9425			
5.685		0.9471			
5.793	0.9842	0.9479			
5.900		0.9498			
6.007	1.0074	0.9539			
6.114		0.9504			
6.221	1.0097	0.9548			
6.329		0.9568			
6.437	0.9785	0.9572			
6.544		0.9448			

C.20 Experimental run no. 91-039**EXPERIMENTAL SPECIFICATIONS**

Solution contents:	0.495	wt.% Triton X-100
	3.0	wt.% NaCl
	6.00	pH (injected)
Injection rate:	120	mL/h
Total Injection:	7.19	PV

CORE CHARACTERISTICS

Core ID:	DS-04	
Weight:	430.00	g
Thickness:	35.17	mm
Diameter:	88.43	mm
Wellbore diameter:	3.45	mm
Pore volume:	48.47	cm ³
Porosity:	22.47	%

Effluent PV	Tracer C/C ₀	Surfactant C/C ₀	Effluent PV	Tracer C/C ₀	Surfactant C/C ₀
-0.029	0.0002	0.0078	6.378	0.9975	0.9905
0.073	0.0001	0.0074	6.483		0.9896
0.178	0.0002	0.0069	6.588	0.9883	0.9902
0.283	-0.0000	0.0060	6.693		0.9922
0.389	-0.0001	0.0054	6.797	0.9911	0.9920
0.494	0.0001	0.0048	6.902		0.9865
0.599	0.0027	0.0045	7.007	1.0181	0.9951
0.705	0.0266	0.0042	7.111		1.0029
0.810	0.1091	0.0038	7.193	1.0217	0.9970
0.915	0.2829	0.0036	7.279	1.0123	0.9656
1.022	0.5567	0.0035	7.389	1.0322	0.9326
1.129	0.7734	0.0036	7.495	1.0095	0.9179
1.235	0.9197	0.0040	7.601	1.0202	0.9392
1.340	0.9673	0.0088	7.707	0.9391	0.9422
1.445	0.9739	0.0251	7.812	1.0506	0.9052
1.550	1.0080	0.0559	7.918	0.9808	0.9303
1.655	0.9791	0.1089	8.024	0.9806	0.8557
1.760	0.9802	0.2083	8.129	0.8952	0.7252
1.865	0.9982	0.3414	8.235	0.6663	0.5635
1.969		0.4502	8.340	0.4359	0.4453
2.074	1.0077	0.5379	8.446	0.2406	0.3175
2.179	1.0080	0.6167	8.551	0.1213	0.2346
2.284	0.9915	0.6792	8.657	0.0617	0.1782
2.389	1.0072	0.7302	8.762	0.0353	0.1416
2.494		0.7568	8.868	0.0224	0.1156
2.599	1.0072	0.7944	8.973	0.0156	0.1038
2.704		0.8262	9.079	0.0112	0.0916
2.809	1.0188	0.8431	9.184	0.0081	0.0820
2.914		0.8549	9.290	0.0064	0.0745
3.019	0.9821	0.8751	9.395		0.0683
3.124		0.8891	9.501	0.0041	0.0633
3.229	0.9895	0.8900	9.606		0.0593
3.334		0.9086	9.711	0.0031	0.0558
3.439	0.9871	0.9144	9.816		0.0526
3.544		0.9232	9.922	0.0019	0.0501
3.649	0.9863	0.9315	10.028		0.0479
3.754		0.9284	10.133	0.0021	0.0460
3.859	0.9978	0.9343	10.239		0.0443
3.964		0.9494	10.344	0.0016	0.0428
4.068	1.0133	0.9467	10.450		0.0412
4.173		0.9535	10.555	0.0013	0.0402
4.280	1.0098	0.9559	10.661		0.0391
4.388		0.9538	10.766	0.0011	0.0381
4.493	0.9766	0.9586	10.872		0.0371
4.598		0.9635	10.977	0.0009	0.0362
4.703	1.0106	0.9558	11.083		0.0355
4.808		0.9672	11.188	0.0008	0.0348
4.912	1.0081	0.9698	11.294		0.0340
5.017		0.9703	11.400	0.0009	0.0334
5.122	1.0001	0.9701	11.505		0.0328
5.226		0.9766	11.611	0.0008	0.0325
5.331	1.0189	0.9839	11.717		0.0321
5.436		0.9846	11.823	0.0007	0.0316
5.541	0.9911	0.9875	11.928		0.0310
5.646		0.9795	12.034	0.0007	0.0305
5.750	0.9854	0.9783	12.139		0.0303
5.855		0.9866	12.244	0.0007	0.0298
5.960	0.9979	0.9864	12.328		0.0297
6.065		0.9855			
6.169	0.9875	0.9883			
6.274		0.9633			

C.21 Experimental run no. 91-040**EXPERIMENTAL SPECIFICATIONS**

Solution contents:	0.504	wt.% Triton X-100
	3.0	wt.% NaCl
	12.00	pH (injected)
Injection rate:	20	mL/h
Total injection:	6.38	PV

CORE CHARACTERISTICS

Core ID:	DS-05	
Weight:	430.07	g
Thickness:	34.89	mm
Diameter:	88.39	mm
Wellbore diameter:	3.28	mm
Pore volume:	47.48	cm ³
Porosity:	22.21	%

Effluent PV	Tracer C/C ₀	Surfactant C/C ₀	Effluent FV	Tracer C/C ₀	Surfactant C/C ₀
-0.035	-0.0001	0.0027	6.380	0.9895	0.9955
0.065	-0.0003	0.0027	6.450	0.9864	1.0116
0.171	-0.0002	0.0028	6.557	0.9705	0.9929
0.276	0.0001	0.0027	6.662	1.0055	0.9968
0.381	-0.0002	0.0027	6.768	0.9671	0.9898
0.486	0.0000	0.0028	6.874	0.9822	0.9976
0.592	0.0028	0.0028	6.979	0.9913	0.9922
0.697	0.0306	0.0027	7.085	0.9783	0.9806
0.802	0.1246	0.0027	7.191	0.9563	0.9390
0.907	0.3038	0.0032	7.297	0.8355	0.8238
1.013	0.5280	0.0036	7.403	0.6627	0.6660
1.118	0.7066	0.0043	7.508	0.4575	0.5111
1.223	0.8339	0.0051	7.614	0.2874	0.3790
1.329	0.9121	0.0087	7.720	0.1766	0.2752
1.434	0.9382	0.0263	7.826	0.1022	0.2026
1.539	0.9574	0.0794	7.932	0.0618	0.1551
1.645	0.9573	0.1742	8.038	0.0366	0.1238
1.750	0.9735	0.3088	8.145	0.0225	0.1048
1.856	0.9943	0.4434	8.251	0.0146	0.0927
1.961	0.9664	0.5564	8.356		0.0814
2.067	0.9764	0.6568	8.462	0.0097	0.0727
2.172	1.0018	0.7348	8.568		0.0659
2.278	0.9871	0.7885	8.674	0.0071	0.0603
2.384	0.9905	0.8320	8.780		0.0563
2.489		0.8708	8.885	0.0040	0.0525
2.595	1.0085	0.8996	8.991		0.0497
2.701		0.9151	9.097	0.0027	0.0471
2.807	0.9846	0.9330	9.203		0.0449
2.913		0.9403	9.310	0.0017	0.0430
3.019	1.0042	0.9451	9.416		0.0416
3.125		0.9592	9.521	0.0010	0.0405
3.231	0.9932	0.9626	9.627		0.0393
3.337		0.9725	9.733	0.0010	0.0380
3.442	0.9872	0.9721	9.839		0.0369
3.548		0.9741	9.945	0.0008	0.0359
3.654	0.9958	0.9807	10.050		0.0351
3.760		0.9861	10.155	0.0004	0.0343
3.867	0.9933	0.9847	10.261		0.0336
3.973		0.9847	10.366	0.0005	0.0331
4.081	0.9721	0.9918	10.471		0.0324
4.190		0.9812	10.577	0.0004	0.0319
4.298	0.9695	0.9905	10.683		0.0323
4.404		0.9966	10.788	0.0006	0.0307
4.511	0.9674	0.9947	10.894		0.0302
4.617		0.9930	11.000	0.0004	0.0299
4.723	0.9820	0.9953	11.105		0.0295
4.829		0.9905	11.211	0.0002	0.0292
4.935	0.9901	0.9934	11.316		0.0289
5.041		0.9961	11.397	0.0002	0.0286
5.148	1.0050	0.9997			
5.255		0.9940			
5.360	0.9843	0.9952			
5.466		0.9958			
5.572	0.9892	0.9912			
5.677		0.9827			
5.782	0.9878	0.9950			
5.888					
5.994	0.9795	0.9935			
6.099					
6.205	1.0053	0.9986			
6.311					

C.22 Experimental run no. 91-038**EXPERIMENTAL SPECIFICATIONS**

Solution contents:	0.498	wt.% Triton X-100
	8.0	wt.% NaCl
	12.00	pH (injected)
Injection rate:	20	mL/h
Total injection:	6.79	PV

CORE CHARACTERISTICS

Core ID:	WK-48	
Weight:	447.40	g
Thickness:	35.40	mm
Diameter:	88.30	mm
Wellbore diameter:	3.50	mm
Pore volume:	43.15	cm ³
Porosity:	19.94	%

Effluent PV	Tracer C/C ₀	Surfactant C/C ₀	Effluent PV	Tracer C/C ₀	Surfactant C/C ₀
-0.042	0.0001	0.0161	7.034	0.9812	1.0001
0.075	0.0000	0.0134	7.149	0.9522	0.9997
0.191	0.0000	0.0117	7.265	0.9848	0.9947
0.307	0.0000	0.0097	7.380	1.0026	0.9772
0.423	0.0001	0.0115	7.495	0.9600	0.9196
0.540	0.0008	0.0091	7.610	0.8822	0.8071
0.658	0.0164	0.0074	7.725	0.6699	0.6250
0.773	0.1014	0.0070	7.840	0.4563	0.4730
0.890	0.2980	0.0066	7.956	0.2929	0.3495
1.006	0.5260	0.0063	8.071	0.1808	0.2531
1.122	0.7202	0.0060	8.186	0.1121	0.1899
1.238	0.8384	0.0060	8.302	0.0663	0.1433
1.353	0.9325	0.0061	8.417	0.0402	0.1134
1.469	0.9437	0.0070	8.533	0.0217	0.0949
1.585	0.9891	0.0110	8.648	0.0133	0.0804
1.701	0.9888	0.0267	8.764	0.0083	0.0709
1.817	0.9701	0.0649	8.879	0.0055	0.0623
1.932	1.0074	0.1265	8.995	0.0038	0.0564
2.074	0.9910	0.2239	9.110	0.0029	0.0514
2.215	0.9995	0.3491	9.226		0.0472
2.331	0.9916	0.4632	9.341	0.0017	0.0466
2.447	0.9781	0.5576	9.457		0.0406
2.562	0.9658	0.6436	9.572	0.0009	0.0381
2.678	0.9935	0.7124	9.688		0.0361
2.794		0.7532	9.804	0.0009	0.0342
2.909	0.9709	0.8086	9.920		0.0325
3.025		0.8353	10.035	0.0006	0.0310
3.141	0.9719	0.8650	10.151		0.0298
3.257		0.8883	10.267	0.0008	0.0288
3.373	0.9747	0.8984	10.383		0.0277
3.488		0.9155	10.499	0.0006	0.0268
3.603	1.0350	0.9299	10.615		0.0262
3.719		0.9408	10.731	0.0003	0.0253
3.835	0.9870	0.9429	10.847		0.0246
3.951		0.9444	10.963	0.0004	0.0241
4.066	0.9596	0.9503	11.079		0.0233
4.182		0.9442	11.196	0.0003	0.0229
4.298	0.9822	0.9622	11.312		0.0225
4.414		0.9473	11.427	0.0002	0.0219
4.530	1.0050	0.9524	11.543		0.0214
4.646		0.9462	11.660	0.0002	0.0211
4.752	0.9795	0.9704	11.775		0.0208
4.861		0.9658	11.891	0.0001	0.0203
4.981	0.9891	0.9668	12.007		0.0198
5.097		0.9686	12.124	0.0003	0.0194
5.213	0.9947	0.9762	12.240		0.0191
5.328		0.9769	12.356	0.0002	0.0187
5.444	0.9696	0.9674	12.458		0.0185
5.560		0.9795			
5.675	0.9622	0.9753			
5.791		0.9812			
5.907	0.9726	0.9829			
6.022		0.9888			
6.138	1.0173	0.9738			
6.253		0.9816			
6.369	0.9971	0.9858			
6.485		0.9819			
6.601	0.9712	0.9779			
6.698		0.9931			
6.791	0.9885	0.9876			
6.915	0.9875	0.9988			